UNIVERSIDAD CARLOS III DE MADRID

DOCTORAL THESIS

ADAPTIVE MICRO-OPTICAL PHASE MODULATORS BASED ON LIQUID CRYSTAL TECHNOLOGY

AUTHOR

José Francisco Algorri Genaro

SUPERVISOR

Virginia Urruchi del Pozo

Departamento de Tecnología Electrónica

Leganés, Junio de 2015

Universidad Carlos III de Madrid
www.uc3m.es

DOCTORAL THESIS

ADAPTIVE MICRO-OPTICAL PHASE MODULATORS BASED ON LIQUID CRYSTAL TECHNOLOGY

AUTHOR

José Francisco Algorri Genaro

SUPERVISOR

Virginia Urruchi del Pozo

Firma del Tribunal Calificador:

Firma

Presidente: Ignacio Raúl Matías Maestro

Vocal: Dimitrios Zografopoulos

Secretario: Isabel Pérez Garcilópez

Calificación:

Leganés, de de

ACKNOWLEDGES

En primer lugar, deseo expresar mi más sincero agradecimiento a mi directora de tesis, Virginia Urruchi, por la confianza depositada en mí para el desarrollo de este proyecto. También agradecerle su esfuerzo y apoyo científico, que han sido fundamentales para culminar este trabajo. Trabajo el cual ha sido desarrollado en el marco de los proyectos TEC2009-13991-C02-01 financiado por el Ministerio de Ciencia e Innovación y FACTOTEM2 S2009/ESP-1781 financiado por la Comunidad de Madrid.

Mi agradecimiento a todos los que forman parte del grupo de Displays y Aplicaciones Fotónicas de la UC3M por sus consejos y apoyo durante estos años. También agradecerle al grupo de investigación de Cristales Líquidos de la Universidad Politécnica de Madrid (CEMDATIC), por cedernos el uso de sus instalaciones para la fabricación de los dispositivos de cristal líquido, así como su ayuda inestimable en el desarrollo de estos. En especial, mi agradecimiento a Noureddine Bennis por estar siempre disponible a la hora de fabricar dispositivos.

I would also thanks to Professors Gordon Love and Shin-Tson Wu, from Durham University and Central Florida University, for giving me the opportunity to know an alternative way of research. The stays in both research groups give me much inspiration to continue with this work.

Agradecer a mi familia por estar siempre apoyándome y allanarme el camino hasta aquí. Sin su apoyo nada de esto hubiese sido posible.

Por último, deseo dedicar este trabajo a la segunda persona que más lo ha sufrido, Marta. Su alegría y optimismo hacen que a su lado la vida sea más fácil. Gracias por tu apoyo incondicional.

ABSTRACT

Thanks to the commercial success of some stereoscopic film productions, three-dimensional (3D) vision has acquired great importance in audiovisual industry in the past ten years. This great commercial impact has produced an exponentially increase in 3D vision research. The technological transfer to commercial applications is bigger than in any other field. This thesis began with the project "Advanced Devices of Liquid Crystal and Electroluminescent Organic Diodes. Hybrid Applications for 3D Vision" funded by the Spanish government. The goal of this project was the development of optical devices to achieve 3D vision in portable devices without glasses or external elements. In the last year, the use of portable devices has grown rapidly. Everything indicates that in the near future most of the multimedia content will be displayed in mobiles or tablets. For achieve 3D vision in these kind of devices, some aspects have to be taken into account. As the observer usually has the device in his own hands, the 3D distance is considerably lower than with big displays. As every observer has different physical characteristics a tunability of this distance is especially required for a useful device. Another characteristic of these devices is the possibility of vertical and horizontal viewings; a rotation of the optical axis would be necessary to achieve this function.

In order to achieve the goals of this project, solutions based on liquid crystal are considered. Specifically, adaptive micro-optical phase modulators based on liquid crystal technology are researched in depth. Liquid crystals are anisotropic materials whose optical axes are parallel to the average direction of the molecular orientation. By supplying a relatively low voltage the liquid crystal molecules are reoriented and the effective refractive index of the liquid crystal is modified. The gradient of the refractive index varies spatially the phase delay experienced by an impinging wavefront of a light beam. By using this effect, any refractive optical element may be reproduced with the proper voltage gradient applied to the sample. This is the main operating principle of the micro-optical phase modulators proposed in this thesis. However, the fabrication of phase modulators based on liquid crystals at micrometric scale (tunable microlenses) implies a technological challenge. In order to achieve proper designs, some characteristics such as anisotropy or dispersion and the knowledge of the molecular directions inside a device is essential for predicting the electro-optic response as a function of external stimulus. As original contribution of this thesis, a novel algorithm to solve the position of a nematic liquid crystal molecular director is proposed. Once the liquid crystal is completely characterized, the developing of a specific model to know the electro-optic response of the micro-optical phase modulators is also relevant. Another original contribution is a novel equivalent electric circuit for modeling liquid crystal microlenses. An interesting feature of the model is that it provides an analytical solution for microlenses with modal and hole-patterned electrode schemes, by using a simple software tool. The required driving scheme (modal or hole-patterned) can be predicted. These theories have been validated by experimental results. For more complex devices, the equations are solved by Finite Element Method.

As commented above, the fabrication of the proposed devices is a critical step. A high resolution photolithography is necessary in order to build the micro-electrodes. Also evaporation of nanometric layers is necessary. Accuracy, cleaning, and timing are decisive. For these reasons, a clean room specifically designed for the fabrication of liquid crystal devices is used (R&D Center CEMDATIC from Universidad Politécnica de Madrid). As original contribution, a new manufacturing protocol is proposed to make the first set of modal microlens arrays. As a first step

simple devices (monopixel cells) are fabricated in order to do a complete study of the liquid crystal electro-optical behavior. The characterization of the liquid crystal electro-optical parameters is determinant in order to design more complex devices. Refractive index and permittivity are the most important features considered. These parameters have been characterized to validate the proposed theoretical modelling of the liquid crystal molecular position.

At a more advanced stage of the work of thesis, the knowledge of the liquid crystal characteristics has made possible designs of more complex devices that can fulfill the goals of the initial project. These devices have required special fabrication processes as well as a special characterization set-up especially in terms of size resolution or arrangement complexity. A custom micropositioner is developed and control software is programmed in relation to these tasks. The software automates the characterization process giving directly measured results of: phase modulation, focal distance, thickness or aberrations. These results have made it possible to validate experimentally the proposed electrical modeling for micro-optical devices.

Demonstration of the viability of the liquid crystal lenticular technology has been carried out for an autostereoscopic application. In addition to fulfill the project goals, two of the typical problems of this kind of systems have been solved by each devising solutions provided in this work of thesis. In this sense, the temperature dependence of lenticular arrays has been assessed by a novel temperature sensor. Also, aberrations (a big problem of optical devices) have been compensated through conceiving special phase-delayed waveforms to switch the devices. And a further advanced proposal has been focused on the next generation of autostereoscopic portable devices. This scheme provides the observer with the option of changing between horizontal and vertical views through his portable autostereoscopic display.

Finally, last research contributions of this work of thesis have taken advantage of the deep knowledge of the electro-optical properties of lenticular devices for autostereoscopic applications, to guide the design of refined micro-optical phase modulators. Adaptive axicons and optical vortices are specially emphasized because their relevance from both, the scientific and technological point of view. Indeed, these devices may be used in many practical applications such as optical tweezers, particle trapping, optical communications, etc.

RESUMEN

Gracias al éxito comercial de algunas producciones estereoscópicas, la visión tridimensional (3D) ha adquirido gran importancia en la industria audiovisual en los últimos diez años. Este gran impacto comercial ha producido un aumento exponencial en la investigación de la visión 3D. La transferencia tecnológica hacia aplicaciones comerciales es más grande que en cualquier otro campo. Esta tesis se inició con el proyecto de investigación "Dispositivos avanzados de cristal líquido y diodos orgánicos electroluminiscentes. Aplicaciones híbridas para visión 3D", financiado por el gobierno español. El objetivo de este proyecto consistía en el desarrollo de dispositivos ópticos para lograr visión 3D en dispositivos portátiles sin necesidad de gafas o elementos externos. En este último año, el uso de dispositivos portátiles ha crecido enormemente. Todo indica que en un futuro próximo la mayor parte del contenido audiovisual se mostrará en móviles o "tablets". Para lograr la visión 3D en este tipo de dispositivos se tienen que tener en cuenta algunos aspectos. El usuario suele tener el dispositivo en sus propias manos, por ello la distancia de visión 3D es considerablemente menor que en pantallas grandes. Como cada usuario tiene diferentes características físicas se hace especialmente necesaria una capacidad de ajuste de esta distancia. Otra característica de estos dispositivos es la posibilidad de visión vertical y horizontal; una rotación del eje óptico será necesaria para lograr esta función.

Con el fin de alcanzar los objetivos de este proyecto, se consideran soluciones basadas en cristal líquido. En concreto, moduladores adaptativos de fase micro-ópticos basados en tecnología de cristal líquido. Los cristales líquidos son materiales anisótropos cuyos ejes ópticos son paralelos a la dirección media de la orientación molecular. Mediante la aplicación de un voltaje relativamente bajo las moléculas de cristal líquido se reorientan y el índice de refracción efectivo del cristal líquido se modifica. El gradiente del índice de refracción varía espacialmente el retardo de fase experimentado por un frente de onda incidente. Mediante el uso de este efecto, cualquier elemento óptico refractivo puede ser reproducido mediante un gradiente de tensión adecuado aplicado a la muestra. Este es el principio de funcionamiento de los moduladores de fase micro-ópticos propuestos en esta tesis. Sin embargo, la fabricación de moduladores de fase basados en cristal líquido a escala micrométrica (microlentes sintonizables) implica un reto tecnológico. A fin de lograr diseños adecuados, algunas características como anisotropía o dispersión y el conocimiento de las direcciones moleculares dentro del dispositivo es esencial para predecir la respuesta electro-óptica en función de un estímulo externo. Como aportación original de esta tesis, se propone un nuevo algoritmo para resolver el director molecular de un cristal líquido nemático. Una vez que el cristal líquido está completamente caracterizado, es necesario el desarrollo de un modelo específico para saber la respuesta electro-óptica de los moduladores de fase micro-ópticos. Otra contribución original, consiste en un circuito eléctrico equivalente para el modelado de microlentes de cristal líquido. Una característica interesante del modelo es que proporciona una solución analítica para microlentes con esquemas de electrodos modales y "hole patterned". Se puede predecir la topología necesaria en función de los parámetros de construcción. Estas teorías han sido validadas por resultados experimentales. Para los dispositivos más complejos, las ecuaciones se resuelven por el método de elementos finitos.

Como se ha comentado anteriormente, la fabricación de los dispositivos propuestos es un proceso complejo. Es necesario realizar fotolitografía de alta resolución para construir el micro-electrodo. También es necesaria la evaporación de capas nanométricas. La precisión, la limpieza, y los tiempos son críticos. Por estas razones, se utiliza una sala blanca diseñada específicamente para

la fabricación de dispositivos de cristal líquido (CEMDATIC de la Universidad Politécnica de Madrid). Como aportación original, se propone un nuevo protocolo de fabricación para hacer microlentes modales. Como primer paso se fabrican dispositivos sencillos (células monopixel) con el fin de hacer un estudio completo del comportamiento electro-óptico del cristal líquido. La caracterización de los parámetros electro-ópticos de cristal líquido es determinante para diseñar dispositivos más complejos. El índice de refracción y la permitividad son las características más importantes. Estos parámetros se han caracterizado para validar el modelo teórico de la posición molecular de cristal líquido.

En una etapa más avanzada, el conocimiento de las características del cristal líquido ha hecho posible el diseño de dispositivos más complejos que cumplen los objetivos iniciales del proyecto. Estos dispositivos han requerido procesos de fabricación complejos, así como montajes de caracterización determinados. Se ha desarrollado un microposicionador y un software de control. El software automatiza el proceso de caracterización dando resultados de: modulación de fase, distancia focal, grosor o aberraciones. Estos resultados han permitido validar experimentalmente el modelado eléctrico propuesto para dispositivos micro-ópticos.

La demostración de la viabilidad de la tecnología propuesta se ha llevado a cabo mediante un dispositivo autoestereoscópico. Además de cumplir con los objetivos del proyecto, se han resuelto dos de los problemas típicos de este tipo de sistemas. En este sentido, la dependencia de la temperatura de los dispositivos de cristal líquido lenticulares puede medirse mediante novedosos sensores. Además, las aberraciones (un gran problema de los dispositivos ópticos) se han compensado a través de formas de onda eléctrica determinadas. Además, una novedosa propuesta se ha centrado en la próxima generación de dispositivos portátiles autoestereoscópicos. Este dispositivo ofrece al observador la opción de cambiar entre vistas horizontal y vertical a través de su pantalla autoestereoscópica portátil.

Finalmente, los últimos aportes de investigación de este trabajo de tesis se han aprovechado del profundo conocimiento de las propiedades electro-ópticas de los dispositivos lenticulares para aplicaciones autoestereoscópicas. Se pueden destacar los axicones adaptativos y vórtices ópticos por su relevancia tanto desde el punto de vista científico como tecnológico. De hecho, estos dispositivos pueden ser utilizados en muchas aplicaciones prácticas, tales como pinzas ópticas, comunicaciones ópticas, etc.

TABLE OF CONTENTS

FIGURES AND TABLES

ACRONYMS

Acronym	Definition
2D	Two Dimensions
3D	Three Dimensions
AC	Alternating Current
BTN	Bistable Twisted Nematic
Bvp4c	Boundary Value Problem Solver
CCD	Coupled Charged Device
EEC	Equivalent Electrical Circuit
CEMDATIC	Centro de Materiales y Dispositivos Avanzados
CPE	Constant Phase Element
DC	Direct Current
DHF	Deformed Helix Ferroelectric
OAM	Orbital Angular Momentum
ODE	Ordinary Differential Equation
FEM	Finite Element Method
FLC	Ferroelectric Liquid Crystal
GDAF	Displays and Photonic Applications Group
GRIN	Graded Index
ITO	Indium Tin Oxide
LC	Liquid Crystal
LCD	Liquid Crystal Display
MEMS	Micro-Electro-Mechanical Systems
OLED	Organic Light Emisor Diode
PC	Personal Computer
PEDOT	Poly(3,4-ethylenedioxythiophene)
SLM	Spatial Light Modulator

1. Introduction

Adaptive micro-optical phase modulators based on liquid crystal technology; the title of this thesis covers a wide range of devices designed and manufactured in order to control the optical path of each ray of light passing through them. This thesis was from the beginning closely linked to the Project "Advanced Devices of Liquid Crystal and Electroluminescent Organic Diodes. Hybrid Applications for 3D Vision" funded by the Spanish government. This Project was aiming at the development of optical devices based on liquid crystals to achieve 3D vision in portable devices without glasses or external elements. This chapter briefly discusses actual technologies to achieve 3D vision. In this thesis, it is proposed the use of adaptive micro-optical phase modulators based on liquid crystal technology (tunable microlenses) for this application. For this reason, a brief state of the art of liquid crystal lenses is presented. The deep knowledge of the electro-optical properties of these devices have led to design other original devices to control the phase of light (axicons, prisms microaxicon arrays, optical vortices, etc.). Among these, adaptive axicons and optical vortices are relevant from both, the scientific and the technological point of view. For this reason, these devices are also introduced in this chapter. Finally, an outlook of the presented work is included.

1.1. Brief historical overview of liquid crystals

Since 1888, the physiologist F. Reinitzer and physicist O. Lehmann described the unusual characteristics of liquid crystals (LC) [1], up to more than 80 years later, they remained as a pure scientific curiosity. In spite of this, some researchers remained interested in them. This is the case of Daniel Vorländer that synthetize the majority of the currently known LCs until his retirement in 1935, J. Friedel that proposed its classification and V. K. Freedericksz and V. Zolina that studied their unusual electrical and optical properties [2]. During the last century, and until the beginning of the 1960s, only a small group of researchers studied the LCs. In parallel, a rapid development of electronics and a continuous miniaturization of this one was going on.

The technology went from electronic valves to transistors. After this, integrated circuits emerged and subsequently an increase of the integration. The final problem to overcome was the need for a small device capable of acting as an interface between the electronic world and human-being. Until then, only the bulky cathode-ray tube fulfilled this mission.

It was in 1958 when Glen Brown, an US scientist, published an article titled "The Mesomorphic State" on the journal Chemical Reviews [3]. This, reminded the scientific community the effects revealed years ago by V. K. Freedericksz and V. N. Tsvetkov. Along with the pioneering work of R. Williams and subsequently of G. H. Heilmeier [4], triggered a great revolution around this forgotten material. Screens with pixels based on LC appeared and the investigation in its physical and chemical properties revived. This in-depth study of its structure and fluidity, led to the creation of new substances in which new phenomena caused by external forces (electric field, magnetic, temperature) was observed. Through the works of scientists of different disciplines and countries (Russia, France, USA, UK), the science of LCs acquired an important role in the electronic world during the following years.

Figure 1. First clock based on LC technology, 1972.

In the next decade a significant step occurred. Swiss watchmaker BWC announced its clock based on LC technology, being the first in history, in 1971 (Figure 1). This clock was sold at a price of 1100 Deutschmarks and used the Dynamic Scattering principle to drive the display. That same year M. Schadt and W. Helfrich described a new electro-optic effect of nematic LCs, known as twist effect or TN (twisted nematic) mode [5]. The TN mode is produced by turning the alignment of one of the substrates at a certain angle with respect to each other. The molecules acquire a helical pattern. A controlled rotation of the polarization of the light passing through the LC cell is produced. By using this effect, it was possible to build a liquid crystal display (LCD), characterized by its low consumption, low voltage control, high contrast and quite small response time [6]. Thanks to the absence of electrochemical degradation of the material, high life times were achieved [7]. From the ubiquitous wristwatch and the pocket calculator, until advanced television displays, LCDs can be found in all sorts of electronic devices requiring to display certain information. New technologies for these new applications were developed. In 1983 researchers from Switzerland, invented the super-twisted nematic (STN) structure [8], with molecular turns of more than 90°, for passive matrix addressed LCDs. In 1990, the use of interdigital electrodes on one glass substrate only to produce an electric field essentially parallel to the glass substrates was proposed [9]. This technique was called in plane switching (IPS).

In the 1990s, engineers at Hitachi developed active control schemes (active-matrix addressing, Figure 2). This produced a definitive step toward the high resolution displays [10]. This fact give rise to a market of billions of euros. In 2007, LCD televisions surpassed CRTs in worldwide sales for the first time. Liquid crystal displays currently monopolized the market; other technologies such as plasma displays in large format, Quantum Dots or organic light emitting diode (OLED) technology in small formats competing to carve a niche. In recent years OLED technology is succeeded in overcoming the technological issues of quality and durability. In the near future maybe will be able to cope, and even completely overcome LC technology. This possible scenario does not mean the end of LCs. In 2009 a meeting took place in Europe in order to explore the new and more promising lines of research on LCs for the next few years. The main objective was to obtain an overview of current projects and contribute to define a report that will determine new projects for the future [11]. None of the research lines were related to the development of displays.

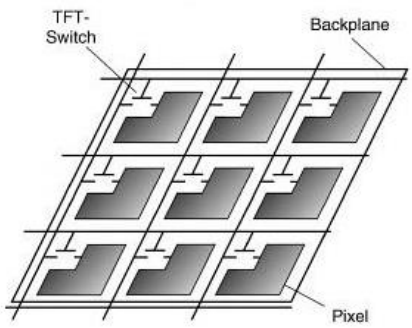

Figure 2. Active-matrix based on thin film transistor (TFT) [10]**.**

In short, LCs have been the subject of numerous developments during the past 50 years. In some areas have competed with other materials, but in other cases, their anisotropic properties easily modifiable through the application of external fields (mechanical, electric or magnetic) are unique. Another great advantage is the deep knowledge of their features and parameters. Therefore, now and in the future LCs will be the protagonists of a multitude of applications, mostly non-related with displays. Today, there are wide variety of research lines open. Among these, the following would seem to be particularly noteworthy:

- *Optical Communications:* LC can be used to work as almost any of the components of an optical communication network. They can work as modulators, switches, multiplexers, waveguides, filters (both in visible as in-band optical communication), attenuators, equalizers, etc. [12]. Also some devices for the aerospace industry or astronomy (filters, beam deflection, flat lenses, etc.) are being developed [13].

- *Microwave:* The use of LC to control or modify signals at millimeter and micrometer frequencies is a recent research line in which several devices have been proposed. For example, antennas [14], phase shifters [15], filters [16], etc.

- *Nanotechnology:* Interaction of nanoparticles and carbon nanotubes with LC [17]. Recent works have shown the possibility to perform stable and homogeneous mixtures of LC and nanoparticles (e.g. carbon nanotubes, gold nanoparticles). For example, we have demonstrated the mixture of LC and carbon nanotubes [18]. Although these mixtures are mainly developed to produce controlled changes in the electro-optical properties of LC [19], they could be also used to modify the behavior of the nanoparticles [20]. In particular, the interaction of light and metallic nanoparticles (e.g. gold or silver) presents an interesting phenomenon, known as Localized Surface Plasmon Resonance (LSPR). This phenomenon, which produces a strong enhancement of both the absorption and scattering of the nanoparticle, is currently used for a wide range of sensors. This fact is possible due to the high dependence of the resonant frequency with any change of the surrounding medium.

This change could be produced by the presence of an analyte, this is the case of plasmon-based biosensors [21], or by an active medium, such as LCs.

- *Medicine, Biology, and biochemistry:* In addition to medical applications in the ophthalmic field [22], it should not be forgotten that LC is an organic compound of which new compounds and phases have to be discovered [23]. Moreover, the orientation of LCs is extraordinarily sensitive to the change of the surface which they are in contact with. The surface-induced local order can be amplified over several tens of micrometers in the LC bulk due to the long-range interaction of LCs. The general idea is to prepare an LC cell with a constant homogeneous or homeotropic alignment all over the active surface. Orienting the cell adequately, it can be made completely dark between crossed polarizers. Adding an analyte that allows any kind of binding with the existing components (the LC or the alignment surface), the LC orientation will be affected by the presence of microparticles like bacteria, introducing disorder in the area around. The optical amplification of LCs makes them a unique optical probe for imaging the molecular ordering and chemical patterns of organic surfaces and sensing the chemical reactions such as enzymatic reactions, DNA hybridization, ligand–receptor bindings, and peptide–lipid interactions at the LC/aqueous interface [24].
- *Security:* Liquid crystal devices based on different alignments that confer them special characteristics of visualization. Depending on dye and concentration, LCs are either oriented by surface conditioning or stabilized in volume by gelification. Based on the same principles, it has been possible to create latent images into the dye-doped LC. Images are made permanent by gelification or polymerization and can be made visible by placing a polarizer either behind or in front of the cell. The most interesting characteristic of these devices is that the latent image made visible by the polarizer is different with the polarizer in front of the sample or behind the sample (Figure 3) [25]. Moreover, several latent images may be induced on each side. The result is a customized label of arbitrary size whose unique characteristics made it interesting for authentication of documents, goods or objects.

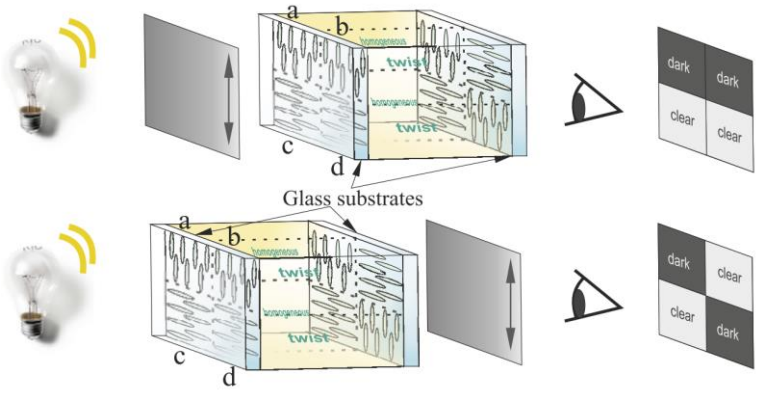

Figure 3. Operation principle of a safety device based on different alignments and absorbing dyes [25].

- *Metamaterials:* An old physic theory that has been able to be implemented in recent years thanks to constructive and design advances. The construction of nanometric structures (in the case of optical applications) allows to achieve unusual properties such as negative refractive index. The LC modify the resonances of these structures [26].

- *Sensors*: This is a very open field only limited by the imagination of researchers. The variation of the LC characteristics with different physical parameters such as deformation, electrical and magnetic fields, pressure and temperature, in addition with the easy integration with fiber-optic, makes them ideal candidates for the development of distributed sensors [27]. In recent years, LCs are also used in the temperature sensing field due to their interesting characteristics. It has been shown that their properties are also quite dependent on the temperature, through a high thermo-optic coefficient [28]. Taking advantage of this effect, LCs are currently used in the design of new temperature sensors. For example, in Fabry-Perot systems [29], photonic crystal fibers [30] and chiral nematic polymer networks [31]. In this thesis, some original contributions to the field of temperature sensors has been made. For example, a novel structure based on three electrodes and a high resistivity layer [32], a micrometric structure to measure the temperature in autostereoscopic devices based on LC [33] [34], sensors based on mixtures of LC and metallic NP in a Fabry-Perot [35] or fiber optic cavity [36].
- *Optical phase modulators:* An optical phase modulator is an optical element which can be used to control the optical phase of light. In this area much research has been done in recent years. A large number of techniques and processes has been proposed. Today, continues to be a hot research topic, for example in ophthalmological applications, tunable zooms [37], beam steering [38], correction of aberrations [39], astronomy [40], 3D vision applications [41], etc. In this thesis, some original contributions to the field of optical phase modulators based on LC have been made. For example, novel LC microlenses for an autostereoscopic application [42], novel aberrations correctors for rectangular apertures [43], micro-axicon arrays [44], novel microlens arrays with rotary capability [45], a tunable array of optical elements [46], optical vortices [47], lensacons and logarithmic axicons [48], etc.

1.2. Micro-optical phase modulators based on liquid crystals

As commented above, this thesis was from the beginning closely linked to the Project "Advanced Devices of LC and Electroluminescent Organic Diodes. Hybrid Applications for 3D Vision". This Project was aiming at the development of optical devices based on LCs to achieve 3D vision without glasses or external elements. For this reason, a brief state of the art of the actual technologies to achieve 3D vision is presented in this section.

As original contribution, in this thesis novel LC micro-optical phase modulators (tunable microlenses) are proposed to achieve the goals of the project (spatial multiplexing, switching between modes and tunable 3D distance) [42]. Modal LC microlenses are proposed and experimentally demonstrated for the first time [49]. Also a novel theory governing this type of systems and hole patterned lenses is proposed and experimentally validated [50] [51]. New analytical expressions for designing LC microlenses are also proposed [52]. Thus far, only experimental studies have been conducted on LC microlenses. The analytical expressions developed in this thesis depend on various manufacturing parameters and can be used to design microlenses with specific focal lengths and a parabolic phase profile. The required driving scheme (modal or hole-patterned) can be predicted. These theories have been validated by experimental results. Also additional original proposals have been made in order to solve some problems caused by using LC lenticular lenses in autostereoscopic devices. For example, to rotate the optical power [45], sense the temperature [34] [33] or compensate aberrations [43] in autostereoscopic systems

(but not limited to). A careful review of the most important topologies of LC lenses has been carried out in sub-section 1.2.2.

In parallel to the tasks strictly linked to the generation of the devices proposed in the mentioned project, a number of original phase modulating devices have also been proposed (axicons [48], prisms [46], microaxicon arrays [44] , optical vortices [47], etc.). A brief state of the art of these technologies is presented in sub-section 1.2.3.

1.2.1. Auto-stereoscopic devices based on liquid crystals

More than 170 years ago, Charles Wheatstone demonstrated the first stereoscope to the Royal Society (1838) [53]. He illustrated the basic principle of stereoscopic vision, the brain's capacity to achieve depth perception from different images. He combined mirrors to present separate images representing different perspectives of the same object for each eye (Figure 4). In the early 1900s, a new theory based on lenticular lenses applied this concept, but it was not until 1930 when the first "lenticular" images were produced by Victor Anderson. These images were of poor quality due to the production methods available at the time. In the 1950s, 3D vision were attempted to be displayed in some cinemas by using anaglyphs. The low quality of the content led to a decrease in the interest. In the 1970s, the system was improved thanks to the patented system of Stephen Gibson "Deep Vision"; red-cyan anaglyphs could reproduce the color of the skin better than the red-blue or red-green anaglyphs. Despite this, it was not until the 1980s when better results were achieved thanks to the IMAX high resolution displays and the use of linearly polarized glasses. The introduction of these systems produced a great commercial impact that increase the interest of the research groups in this field.

Figure 4. First stereoscopic device.

Currently, 3D technology can be classified into two major groups: one requiring the help of external means, normally glasses (stereoscopic) and another that allows the generation of 3D vision without the need for them (autostereoscopic). As can be deduced, the use of autostereoscopic devices is the objective of current research groups. Even though these systems were investigated for the first time by Frank Ives (1903) and by Gabriel Lippman (1908), using a barrier system and microlens, respectively, the technological limitations stopped the development of these systems. More recently, this technology has improved considerably, primarily due to new manufacturing processes, advanced photolithography techniques and the reduction of production costs. Furthermore, this technology can now display both 3D and different styles of animated visual effects without the need of special viewing glasses.

Interest has arisen in applying this technology, known as spatial multiplexing to different areas, such as cinema, television, virtual prototyping, and medical imaging. At present, most commercial 3D autostereoscopic devices use the spatial multiplexing technique (Figure 5). The operating principle is based on the optimization of two aspects: the correct capture of the necessary stereogram for display on the screen and the correct visualization of these images by the user. The stereograms consist of two images (corresponding to the same scene viewed from two different angles) that are intertwined in columns of pixels. At this point, a system capable of directing each

column of pixels to the corresponding eye is necessary. Then, the brain interprets the signals and generates a stereoscopic response.

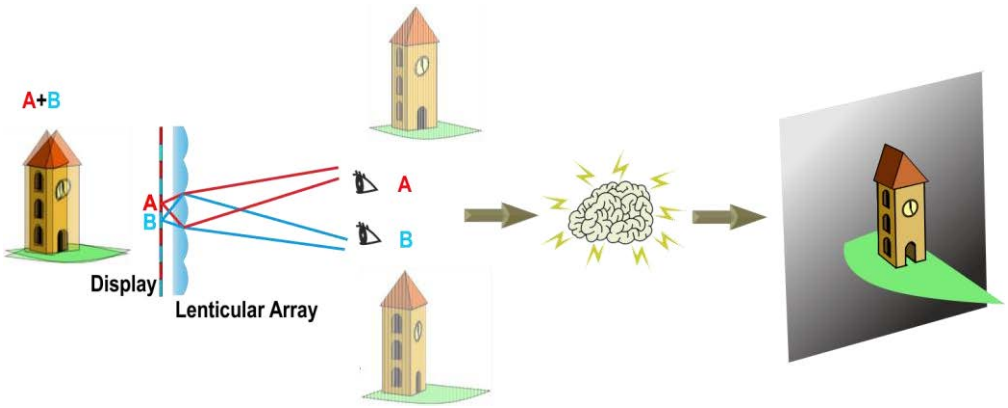

Figure 5. 3D effect using an autostereoscopic system based on spatial multiplexing.

There are two main approaches to achieve this function: parallax barriers [1] and lenticular systems [2]. A parallax barrier consists of masks that contain vertical apertures to cover the light at certain angles. The barrier can be considered a mature technology because commercial devices have been produced. For example, dynamic barriers based on LCDs are used to generate black and white columns. Despite its maturity, this technology has considerable drawbacks [3] such as lower brightness, small viewing angles, and crosstalk, which is caused by diffraction and is difficult to suppress. To improve the function of this system, lenticular technology can be used. As original contribution, in this thesis it is proposed the use of a LC lenticular lens manufactured from novel materials to resolve the main drawback of lenticular technology, the tunability of the 3D distance.

Parallax barriers and fixed lenticular systems (no based on LC), can already be found in commercial products. Recently (January 6-9, 2015), Toshiba presented at the "2015 International Consumer Electronics Show" in Las Vegas a new display using LC lenses. Despite this, the information of the technology behind is still unknown. This will be probably the first commercial display using LC lenses. Table 1 shows also two representative examples of 3D displays already on the market, developed by Sharp and Toshiba. Companies dominating the development, distribution and global marketing of 3D displays are usually located in Japan and South Korea.

PRODUCT	COMPANY	TECHNOLOGY	RESOLUTION	MODE	YEAR
	Sharp 3.4" (3DS)	Dynamic parallax	480x854	2D/3D	2011
	Toshiba 55" (55ZL2G)	Fixed Lenticular array	3840 x 2160 (4K)	2D/3D	2012
?	Toshiba 15" (?)	LC Lenticular array	?	2D/3D/4K	2015?

Table 1. Commercial examples of autostereoscopic devices based on spatial multiplexing.

The device of Sharp uses a dynamic parallax barrier that only a few years ago was in the research stage. It is based on the use of LCs and has many advantages such as 2D/3D switching, multiple views, variable focal length, work area, etc. In the case of the Toshiba display, is based on a set of microlens of high quality, manufactured probably with some kind of resin or polymer. This display uses a specific eight-core processor that allows calculations of the required views as a function of the number of observers. Some common disadvantages of spatial multiplexing systems have been solved in different ways:

- The resolution loss is solved through very high resolution displays (QFHD, 3840x2160 pixels). Moreover, the lenses are placed with a small angle to distribute the resolution loss vertically and horizontally [54].
- Another common problem is the non-uniformity of the light coming from pixels. The problem is caused by the darker spaces of the pixels which generate bright and dark areas. An observer looking at different angles will notice a change in the image brightness under certain positions. There are three methods to solve this, place the lenses with a certain angle, adapt the focal distance and modify the width of the lenses to obtain fractionated views [55] .
- Another big problem are aberrations caused by manufacturing defects. These cause a not uniform distribution of the intensity. However, thanks to improvements in various processes, the non-uniformity can be reduced to values less than 5% for which the bands are hardly noticeable.

Previous systems are patented or commercially available. However, there are still many problems to be solved. This makes the autostereoscopic vision a topical issue in which there are numerous research resources. In the field of lenticular arrays the possibility of using LC lenses is being investigated. Probably, one of the following topologies is part of the new display of Toshiba. Within the LC lenses should distinguish between the active (birefringent active) and passive (activated by polarization) (Figure 6). In the active case it is important to note the high voltage switching >30V that hinder the multiplexing of 2D and 3D areas. In the passive case low voltages are required to commute, have good behavior when there is a pressure from surface and have lower minimum distances in multi-view vision. The only disadvantage is its increased thickness, which has been compensated with different topologies.

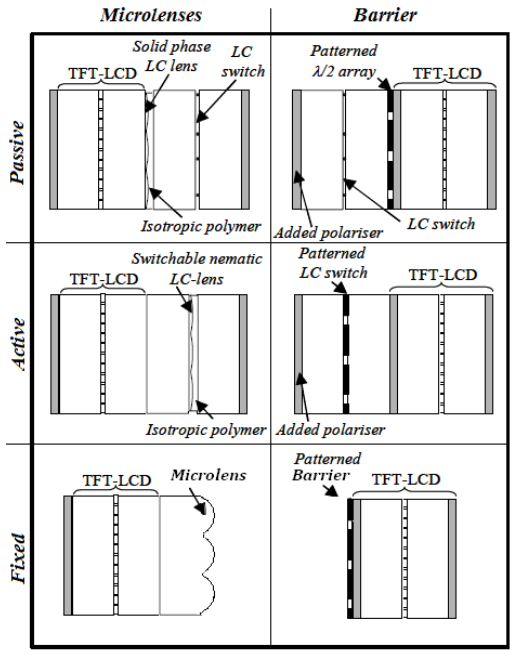

Figure 6. Microlenses and parallax barriers, fixed and based on LC.

This review is summarized in Table 2. Data collected are the best found for each of them. It must be borne in mind that fixed microlens technologies and fixed barriers can be found implemented in commercial products, while devices based on LC are still part of the research field. Given the great commercial impact of these technologies they will be probably marketed in a short time.

	Fixed parallax	Dynamic parallax	Passive parallax	Fixed lenses	Active lenses	Passive lenses
Brightness 2D*	45%	45-85%	45%	>95%	>95%	>95%
Brightness 3D*	45%	<20%	<20%	>95%	>95%	>95%
Contrast	1:1000	-	-	1:1500	-	-
Crosstalk	>2-3%	>2-3%	>2-3%	<1%	<1%	<1%
Thickness	0.5mm	1.13mm	1.65mm	0.7mm	1mm	1.1mm
Voltage 2D	-	0V	0V	-	>30V	0V
Voltage 3D	-	3.3V	3.3V	-	0V	3.3V
Switching time	-	<100ms	<100ms	-	~seconds	<100ms
Multiplexing of 2D/3D areas	-	Differences x3-x5 in brightness	Differences x2 in brightness	-	High Voltage	Yes

*Over a maximum brightness of 500cd/m^2

Table 2. Comparison between different autostereoscopic technologies.

In this study, different existing technologies for autostereoscopic applications have been presented. It has been found that the only system that allows a tuning of the 3D distance is the method of dynamic parallax barrier with the disadvantages that this system entails. Devices that employ LC lenses only are designed for 2D/3D operation and usually are based on curved surface (explained in next section). There are numerous techniques for manufacture LC lenses that are also detailed in the next section. As original contribution, in this thesis it is proposed a LC microlens to achieve a 3D tunable distance in small displays [42]. Some problems mentioned above as aberrations, are solved by other original contribution, an aberration compensator for rectangular apertures [43]. The dependence of the LC birefringence with temperature is solved by a temperature sensor for this type of structures [34] [33]. Unlike other proposed systems, modal LC lenses have a wide range of focal length tunability, so this system could adjust the 3D distance over a wide range. Other improvement over other proposed LC lenses or the fixed lenticular systems is the capability of switching between horizontal and vertical vision for portable devices [45].

1.2.2. Adaptive liquid crystal lenses

A homogeneous conventional lens has two physical characteristics that contribute to the way in which such lens modify a wavefront passing through it: the difference between the refractive index of the lens material and the surrounding environment, and the curvature of their interfaces. In addition, it is known that when light travels through a non-homogeneous medium, the wavefronts decrease its speed in the optically dense regions and are accelerated in areas of lower density. Therefore, it should be possible to design a lens without curvature but with a material that has a gradient in the refractive index; this device is known as GRIN (Gradex Index) lens. In this thesis, the used material is a LC. Particularly, LC lenses with electrically controllable focal length have been reported to show many feasible approaches. Liquid crystal lenses share their applications with

conventional fixed lenses, but the first ones have shown some advantages such as small size, light weight, low driving voltages, low power consumption and transmissive/reflective operation modes. Many of the topologies proposed for LC lenses are based on generating a gradual voltage across the lens capable of reproducing a parabolic refractive index gradient in the LC layer, so mimicking the optical behavior of a conventional lens.

At the end of the seventies were carried out some pioneer research which gave rise to the first proposals of adaptive lenses. For example, Berreman *et al.* (with patent application in 1977 [56]) and Sato *et al.* in 1979 [57] (Figure 7). The first adaptive lens was formed by a cavity with a certain curvature filled with LC. This device had low response times, due to the LC layer thickness. In addition, another problem was the molecular orientation homogeneity in this thick and curved layers. This is the reason why this particular technique was not further developed.

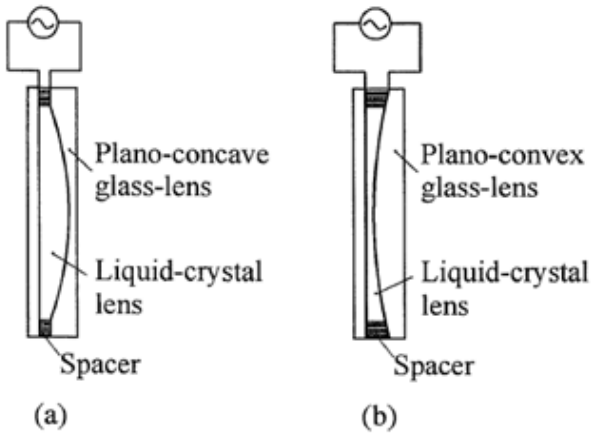

Figure 7. First proposals of LC lenses. (a) Plano-concave lens (b) Plano-convex lens [57]**.**

Two years later, in 1981 [58] a Syracuse University group made a LC cylindrical lens with electronic control working as an adaptive optical element. This type of lens employed a large number of electrodes to achieve a proper voltage gradient. This new concept of lens gave rise to other research works [59] and subsequently spherical lenses [60]. At the end of the eighties, new research works demonstrated LC lenses at micrometric scale. First references are from Sato *et al.* [61], [62]. In this time, the first Fresnel lenses were also proposed [63]. This configuration reduced the necessary thickness and increased the diameters.

Despite LC lenses were first reported more than 30 years ago, they remain as an active field of research even today. In general, the applications of LC lenses, regardless of whether they are or not microlenses, are as numerous as it can be the application of fixed lenses or GRIN lenses with the great advantage of weight and volume reduction and tunable focal distance by voltage. For example, LC lenses have been proposed to work in imaging systems of portable devices. In this field, LC lenses can help to realize auto-focusing system and optical zoom system for the portable devices, such as cell phones and cameras [64]. Also has been proposed for pico-projection systems, helping to electrically adjust the focusing properties of the projected image without mechanically adjusting position of a projection lens [65]. In the case of a holographic projection system, a LC lens can help to correct the mismatch of chromatic image size which is important for the full-color holographic projection system [66]. Liquid crystal lenses can also be used as a concentrator and a sun tracker in a concentrating photovoltaic (CPV) system [67].

It is worth mentioning the field of bio-optics. For example, it should be noted the use of lenses for medical instrumental in applications like endoscopy. A LC lens can be adopted to electrically enlarge the depth-of-field of the endoscopic system [68]. Moreover, for the ophthalmic lenses, the lens power of LC lenses is not only electrically tunable, but also can be positive or negative. Liquid crystal lenses can correct myopia. Commercial glasses based on LC lenses were developed in 2011. They have a switchable focal distance [69] (Figure 8). This development solves the problem that

have some patients requiring different types of glasses for different activities. Unfortunately, the company went bankrupt this year due to a high rate of return (battery issues and some defective devices). Liquid crystal lenses can also be a kind of "extra-artificial crystalline lens" to compensate the degradation of the crystalline lens of aging eyes or the eye accommodation [70].

Figure 8. Commercial LC glasses with tunable focus (PixelOptics) [69]**.**

In short, in recent years there has been lots of developments tailored to the needs of different applications. Over this period, many new topologies have been proposed, such as polymer gel stabilization, patterned electrode, curved surface, Fresnel lens, immersed lens, or modal control. Between them, it should be noted patterned electrode, curved surface and modal control.

Patterned electrode

As commented above, patterned electrode technique was the first proposed method to obtain LC lenses. Despite this, this technique has reinvented itself and is still present in many novel proposals. Below, some proposals based on this technique are briefly discussed. In the beginning, only a series of electrodes in contact with the LC were used to create a voltage gradient [71]. The first microlenses were fabricated by T. Nose and S. Sato in 1989 using hole patterned technique [61]. This technique is made up by several patterned circular holes in the upper electrode (Figure 9). Years later, other models were proposed. They were based on the inclusion of a dielectric between the electrode and the LC layer. This technique, known as dual voltage was proposed in 2004 [72]. The main disadvantage is the high operating voltage caused by the space between the electrode and the LC (>50V).

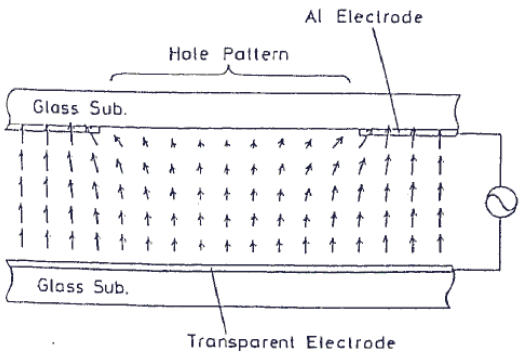

Figure 9. First LC microlens (1989) based on hole patterned technique [61]**.**

In recent years, a lot of research works based on this technology have been presented. For example, tetragonally hole-patterned electrodes [73]. In this work, each LC cell in the lens array behaves like cylindrical or spherical lens by electrically adjusting the applied voltages. Another recent proposal is a LC lens with two divided and double circularly hole-patterned electrodes [74]. The radially and axial symmetrically distributed refractive index of the hole-patterned aperture can be obtained by controlling the two divided circularly hole-patterned electrodes in addition to the

double circularly hole-patterned electrodes. Polarization independent adaptive microlens with a blue-phase LC has also been proposed [75]. Also, circular hole-patterned electrodes with tunable coaxial bifocals (CB) synthesized via photopolymerization of LC cells [76] consisting on two types of tunable CB LC lenses fabricated via different photocurable processes has been recently demonstrated. Another recent proposal has been a hole patterned electrode structure with ultrathin glass slab [77]. As can be seen, there is still a lot of research in this topology.

As original contribution, in this thesis it is proposed a hole patterned lens based on orthogonal electrodes and complex electrical signals to achieve a cylindrical LC microlens array with rotary optical power and tunable focal length [45]. Also a novel electrical model and an analytical method to design this type of lenses are proposed [51] [52]. Another original contribution is the proposal of this type of lenses to work in autostereoscopic devices, demonstrating the tunable focal distance, the deviation of images [78] and the 3D tunable distance (section 5.2.3). Another technique usually used in autostereoscopic applications is the curved surface, explained below.

Curved surface

In this category are included all lenses having at least a non-planar surface. The following list is based on the type of material used in the fabrication:

- *Curved ITO*: Consists of a curved electrode of indium titanium oxide (ITO). This structure has the same problems as dual-voltage lenses but requiring a complex fabrication process [79]. For these reasons are the less relevant.

- *Curved glass*: This lenses work as the first LC lenses [80]. It would appear, however, that this old design was overpassed by new technologies, but surprisingly is still used. The main reason is the application of this design to 3D vision devices. As commented above, this particular technique was not further developed because it had low response times and homogeneity problems. New proposals are designed to work as microlenses. This reduce the necessary thickness. Moreover, techniques of LC multilayers reduce more the thickness and the inhomogeneity (Figure 10) [81].

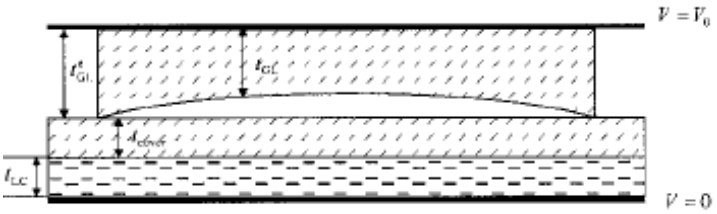

Figure 10. Multilayer LC lens [81]**.**

- *Curved Photoresin*: The photoresin has a spherical or cylindrical shape and is surrounded by the LC layer [82]. The main disadvantage is the complex fabrication process. Another option is to produce spherical cavities of photoresin and filled them with LC. This topology has been proposed to work in autostereoscopic devices with switchable 2D/3D mode:

  - ✓ *Active birefringent lenses*: A typical structure is shown in Figure 11 [83]. The cavity formed by the photoresin is filled with LC. Unswitched, a polarized light is affected by the extraordinary refractive index, greater than the photoresin (a positive lens is formed). When the LC is switched by an external electrical field the polarized light is affected by the ordinary refractive index, similar to the photoresin (the light passes through without deviation). The main disadvantage is the high operating voltage (50-100V).

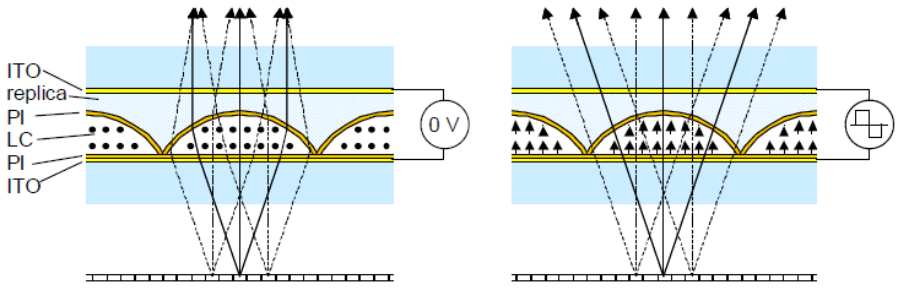

(a) Without voltage. **(b) With voltage.**

Figure 11. Active birefringent lens [83]**.**

- ✓ *Polarization Activated Microlenses*: In this structure two LC layers are used (Figure 12) [84]. One act as the lens (nematic LC) and the other control the polarization (TN LC). The TN LC cell change the polarization of the incoming light so it is affected by the extraordinary or ordinary refractive index of the nematic LC layer. This reduce considerably the operating voltage (only the TN cell is switched) but complicates the fabrication process. This structure has been proposed to work in a switchable 2D/3D mobile phone display [85].

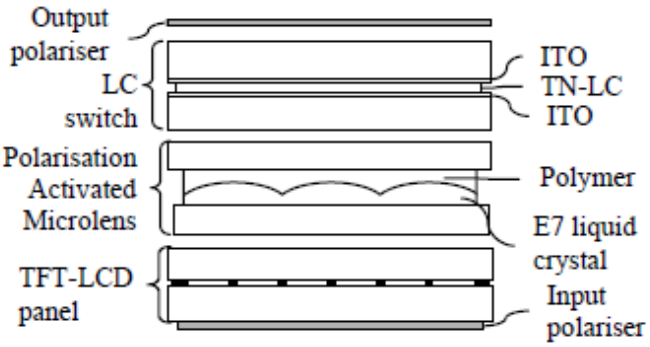

Figure 12. Polarization activated microlens [84]**.**

In summary, the curved surface topology has the problems of high operating voltage or complex fabrication process. On the other hand, the patterned electrode technique is based on voltage distribution through a dielectric layer. In one case, the electrodes are separated from the LC by a thin glass. This method usually employs two high-voltage controls (> 50 V). The other case surpasses these limitations and places the electrodes directly onto the LC surface. The optical properties depend on the relation between the lens aperture and the LC thickness and require lenses smaller than 250 µm. For larger diameters, the necessary thickness would be problematic. A technique that overcomes these aspects and simultaneously operates with only one low voltage is modal control. The fabrication of modal lenses at micrometric scale implies a technological challenge. In fact, no modal lenses in this scale has been proposed in the literature before to this thesis.

Modal control

Modal control technique has become an alternative for lens design because overpasses the main drawbacks of previous techniques. The main advantage is the driving method, with only one voltage control at low values. First research on modal control was reported by A.F. Naumov *et al.* [86]. This technique consists of generating a radial graded refractive index across the lens aperture by using a layer of high sheet resistance (MΩ/sq), deposited onto the pattern electrode, as a control electrode. Sheet resistance of the control electrode is a key design parameter. Its value must be in the range 100 kΩ/sq to few MΩ/sq for lens diameters on the order of millimeters [87]. This layer creates a voltage divider with the LC impedance causing a hyperbolic voltage gradient across the

lens aperture [17]. Different materials have been reported to act as a control electrode layer, PEDOT [88], thin ITO layers [89] (max. 10 MΩ/sq [90]) or titanium oxide films [91].

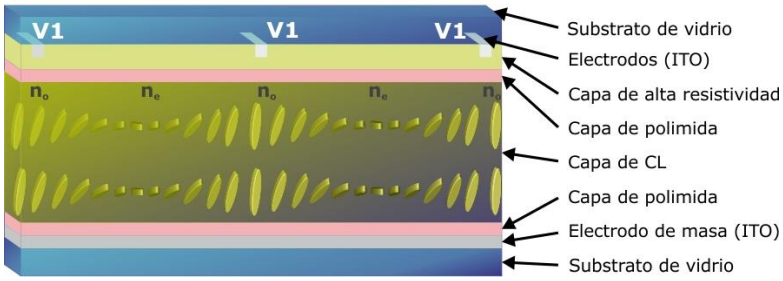

Figure 14. Simplified depiction of a modal LC cylindrical lens with applied voltage.

It is not a simple task indeed to obtain exact thicknesses of the high impedance layer; setting a thickness value must offer a good compromise between impedance (which affects lens refractive index gradient) and transparency (which concerns on lens quality). On the other hand, control voltages must be amplitude, frequency and shape optimized. Due to the capacitive effect of the LC, LC layer impedance is frequency dependent. In addition, one of the main drawbacks of systems using these optical arrangements is the generation of aberrations. So, the suitable choice of the voltage shape (set of harmonics) can minimize phase aberrations caused by both, the non-ideal distribution of the electric field and the nonlinear electro-optic response of the LC with voltage [91]. For this reason, some systems that control the frequency , amplitude and duty cycle have been proposed to control the phase profile [92]. Also novel structures, based on symmetric electrodes, have been proposed to reduce aberrations [88]. One worth mentioning application is a wavefront modulator based on modal control technique [39]. Also a modal LC lens is commercially available at Flexible Optical B.V. [93] (Figure 13).

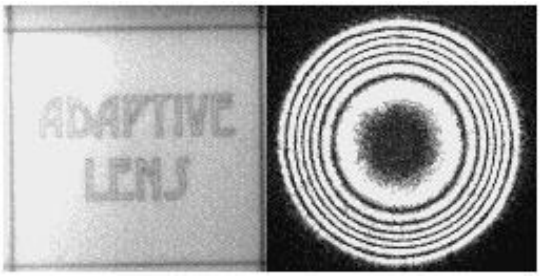

Figure 13. Commercial modal LC lens [93]**.**

However, the fabrication of modal lenses at micrometric scale implies a technological challenge. The main problems are difficulties in finding layers of 0.1–1 GΩ and the fact that, at some point, the fringe fields distributed by LC are sufficient to create a voltage distribution without the need of a high-resistivity layer. As original contribution, in this thesis modal LC microlenses are proposed and experimentally demonstrated for the first time [49]. Also a novel theory governing this type of systems is proposed and experimentally validated [50].

1.2.3. Other micro-optical phase modulators

Other LC based devices working as micro-optical phase modulators have been developed as a part of this thesis. Although the main aim of this work was the manufacturing and characterization of LC lenses to work in autostereoscopic devices, the deep knowledge of the electro-optical properties of these devices have led to design other original devices to control the phase of light. Among these, adaptive axicons and optical vortices are relevant from both, the scientific and the technological point of view. Indeed, these devices may be used in many practical applications such as optical tweezers, particle trapping and optical communications.

Axicons and microaxicons

The term axicon was first proposed by J. Mcleod in 1954 (from Greek: "axis image"). In the referred work, a glass cone was first studied to image a point source into a line focus. The main advantage over traditional optical lenses is that axicons produce a field distribution that is proportional to the zero order Bessel function (J_0). In the near field, these beams are characterized by a bright central part surrounded by concentric rings of decreasing intensity. The energy density in the central part of the Bessel beam is high and the focus depth (distance of the preservation) is greater than for Gaussian beams. For this reason, they are also known as non-diffracting Bessel beam (Gaussian beams are broadened and blurred by the diffraction). The use of axicons has attracted considerable interest in the last few years due to their wide range of applications in different fields. Some properties are self-reconstruction and the appearance of longitudinal components of the field vectors. In the near field, these beams are characterized by a high intensity spot surrounding by rings with a decreasing intensity. The applications are varied and numerous, for example precision alignment for large telescopes [94], laser machining [95], medical applications [96] [97], commercial applications [98], optical tweezers [99], atom optics [100], etc.

Yet, one of the impediments for the broad use of these optical elements is the fabrication cost, usually based on processes that use diamond turning from solid materials such as BK7 glass or fused silica. Some works have proposed the use of LC. For example, the generation of axicons of several millimeters, based on modal control technique, has been proposed in ref. [48]. As original contribution, in this thesis, a structure based on six electrodes and modal control technique has been proposed to generate an array of four optical elements that can also produce four axicons of several millimeters [46].

The use of microaxicons in arrays also has important applications such as, for example, ultrafast optical communications [101], generation of femtosecond Bessel beams [102], non-diffracting "flying images" [103], high-resolution optical coherence tomography [97], etc. Despite this, few works in the literature have demonstrated the fabrication of microaxicon arrays. Some of them use laser direct writing using two-photon polymerization [104], thin-film deposition methods [105] or by using masks based on LC displays [106]; these methods tend to have limitations on the axicon profile height and thus the axicon angle. To overcome these drawbacks, another technique based on using a multistep micromolding process [107], has been recently proposed. In general, the proposed ideas use complex fabricating processes. Moreover there is not a possible reconfiguration of the final device.

The parameters defining an axicon are the aperture diameter (d) and the wedge angle (γ). In order to increase the non-diffractive distance of a Bessel beam (z_{max}) one of these two parameters have to be modified ($z_{max} \sim d/\gamma$). Until now, these parameters were modified in the fabrication process. As commented above, the fabrication processes proposed until now produce limitations in the microaxicon parameters. One solution is the use of liquid-crystal-on-silicon spatial light modulators (LCoS-SLMs) [108]. Despite this, the main problem is the characteristic structure, based on pixels surrounded by opaque areas, causing losses of light efficiency and possible aliasing in the case of micro-optical systems. Also, they have residual phase distortions and a limited resolution [108].

To solve these problems, as original contribution of this thesis, a tunable microaxicon array with tunable aperture and wedge angle is proposed and experimentally demonstrated [44]. This device is simple and reconfigurable by low voltage signals. The proposed structure is capable of generate tunable axicons (hundreds of elements) with micrometric size, simple control (four control

voltages), low voltage and totally reconfigurable. The near field measurements demonstrate the generation of a non-diffracting Bessel beam array. Moreover this array is tunable both in phase amplitude and focus position. This device could contribute to developing new applications and to reducing the fabrication costs of the current devices.

Optical vortices

There are two forms of light rotation that are typically considered to describe a light beam: the first one is the dynamical rotation of the electric and magnetic fields around the propagation direction, and the second one is related to the dynamical rotation of light rays around the main beam axis. These two rotations are associated with two forms of angular momentum, namely spin and orbital angular momentum (OAM).

Over the last decade, helical wavefronts have been amongst the most extensively studied complex phase-shapes of light. Light beams with an azimuthal phase dependence of $e^{-il\Phi}$, where l is the topological charge, have an OAM associated with them, and when focused, they form rings instead of points in the focal plane. In recent years, the number of applications of this phenomenon has grown exponentially. It has been applied to beam shaping [109], optical tweezers [110], atom manipulation [111], free-space communication [112], and fiber optics communications with new types of fibers [113], among others. Optical vortices are usually generated using spiral phase plates (SPPs) [114] or computer generated holograms (CGHs) [115]. CGHs are created by digitally generating holographic interference patterns that are mathematically computed. Blazed forked gratings have been used to concentrate more energy in the first diffraction order [116]. Nonetheless, the fabrication of CGHs remains a difficult task. SPPs linearly vary the length of the optical path through an axially variable thickness. Owing to fabrication limitations, SPPs usually have discrete phase values. Another important disadvantage of SPPs is the absence of reconfigurability, which means that the topological charges and operating wavelengths are fixed. To solve this problem, spatial light modulators (SLM) have been proposed as alternatives to SPP [117]. This solution is not ideal because the SLM's characteristic structure, based on pixels surrounded by opaque areas, causes loss of light efficiency. Moreover, to separate the diffraction orders, the phase pattern should be combined with a blazed grating pattern. Recently, a novel device for generating a reconfigurable optical vortex has been proposed and demonstrated [118]. This device uses LC and pie slices of ITO) to generate quantized spiral phase steps. Although its reported efficiency is better than that of SLM (500 times greater diffraction efficiency), the device does not adhere to the concept of an ideal SPP as it generates quantized phase. Moreover, the fan out and the determination of the voltage required at each electrode complicates the use of the final device.

In this thesis as original contribution, a novel structure based on modal control technique has been proposed and theoretically studied. As commented above, the use of a high resistivity layer (modal control) for designing LC lenses, micro-axicon arrays or arrays of optical elements have been demonstrated. The proposed structure in this thesis can generate a continuous voltage with a SPP shape, which is completely reconfigurable by using low voltages. This device is capable of generating several OAM modes. Its fabrication cost is low, and its application in optical tweezers or OAM mode division multiplexing would reduce complexity and improve efficiency, allowing transmissions over longer distances.

1.3. Thesis overview

1.3.1. Motivation and objectives

Thanks to the commercial success of some stereoscopic film productions, 3D vision has acquired great importance in audiovisual industry in the past ten years. This great commercial impact has produced an exponentially increase in 3D vision research. The technological transfer to commercial applications is bigger than in any other field. In the last year, the use of portable devices has grown rapidly. Everything indicates that in the near future most of the multimedia content will be displayed in mobiles or tablets. For this reason, many experimental and theoretical research groups worldwide have actively worked on alternative solutions for 3D vision in portable devices in which no external devices are required. For these kind of devices, some aspects have to be taken into account:

- The observer usually has the device in his own hands, so the 3D distance is considerably lower than with big displays. This requires a higher optical power.
- Every observer has different physical characteristics; so a tunability of this distance is especially required for a useful device.
- Aberrations of the optical elements used in this type of systems is a problem that has to be solved in order to reduce the crosstalk.
- The ability to display vertical, as well as horizontal, views is an added value of autostereoscopic displays.

Liquid crystal (LC) materials were chosen as excellent candidates to implement alternative solutions: first, for mitigating some of the identified drawbacks; then, for creating new gadgets that add new capabilities that are not trading in the market currently. Liquid crystals modify the phase delay between spatially different regions of the sample causing beam steering or light focusing/defocusing. However, the use of LC as optical phase modulators (LC lenses) implies a technological challenge at micrometric scale. In order to develop successfully this project a set of objectives were initially determined. The objectives were classified into two categories: The basic objectives and the advanced ones. Basic objectives associated with the establishment of the theoretical assumptions that underlie the operation of the LC devices. Advanced objectives related to the practical implementation of devices.

The basic objectives are listed below:

- To explore the **current theory** about the electro-optical behavior of different LC lens technologies and topologies associated with them. To study the scope of these technologies in terms of focal distance, tunability, etc.
- To contribute to expand the current fundamentals by designing an **electrical model** in order to predict the LC driving voltage as a function of t**he constructive parameters** (ε, Δn, thickness, diameter, etc.) of the lenses. This model will help to design the lenses and save time in fabrication of test samples.

- To **study in depth the electro-optical characteristics** of the liquid crystal materials. The parameters obtained as a result will be introduced as input hypothesis in the electrical model
- To develop an own **simulation tool** of the LC itself and the LC inside the proposed micro-optical phase modulators.

The advanced objectives are summarized below:

- To **design a set of microlenses** that fulfills the objectives of the project, by using all the theories and the simulation program. To determine the **best topology** for the application under investigation.
- **To fabricate** the designed microlenses.
- **To characterize** them both individually and in array configurations. Different set-ups will be designed in order to characterize different parameters (phase, focal distance, etc.). An **automatized system** will be required.
- To develop and characterize a **prototype for autostereoscopic vision**. To **explore the final performance** of the system and the possibilities of **improvement of its features against not tunable** current devices.
- **To validate** the electrical and simulation models by experimental measurements.
- **To explore** other possibilities based on similar topologies to control and modify the phase of light.

1.3.2. Description of chapters

A brief revision of the actual technologies to achieve 3D vision, LC lenses and other adaptive micro-optical phase modulators has been carried out. This thesis is divided in six more chapters. It begins with a description of the classic theory of LC and an original theory to model the tunable microlenses that has been proposed for this work of thesis. These theories have been contrasted with the practical operation of the proposed devices and found that the optical behavior can be predicted. After this, other LC devices working as micro-optical phase modulators are presented. Finally, the most important results are summarized.

Chapter II. Theory of liquid crystal micro-optical devices: The theory of nematic LC is explained in this chapter. In order to characterize the electro-optical properties of nematic LCs, it is necessary a deep knowledge of the optical and electrical parameters that define them. Moreover, knowledge of the molecular directions in a determined sample is essential for predicting the electro-optic response as a function of external stimulus. The theory governing this behavior as well as an original algorithm to estimate these directions is explained in detail. Once the theory of LC is detailed, the developing of an original model to know the electro-optic response of the micro-optical phase modulators is proposed and explained. An interesting feature of the model is that it provides an analytical solution for microlenses with modal and hole-patterned electrode schemes, by using a simple software tool. Finally, the results of this model are presented.

Chapter III. Design and fabrication of micro-optical devices: Different aspects of the design of micro-optical phase modulators are addressed in this chapter. Firstly, the design of the electrode pattern for the autostereoscopic application is detailed. The fabrication of a modal lens implies a technological challenge at micrometric scale. For this reason, a brief discussion of different technologies to achieve the high resistivity layer is carried out. As original contribution a new

manufacturing protocol is proposed to obtain the first modal microlens array. The fabrication protocol will also be examined because accuracy, cleaning, and timing are critical. The clean room infrastructure, for the fabrication of LC devices, of R&D Center CEMDATIC from Universidad Politécnica de Madrid, is presented. At the end of the chapter, it is summarized a list of the fabricated samples.

Chapter IV. Electro-optic characterization of nematic liquid crystals: This chapter is dedicated to the experimental study of the nematic LC material. One of the most important things in order to design and manufacture LC devices is to have a deep knowledge of the LC electro-optical parameters. Among them, optical anisotropy (birefringence) is determinant. This feature has been characterized in order to validate the proposed theoretical modelling of the molecular position presented in chapter II. Another important parameter is the wavelength dependence of the birefringence (dispersion). Also, the impedance is characterized by electrical impedance spectroscopy (EIS). By using these results an equivalent electric circuit (EEC) for a broadband frequency is presented. With these results, the solution of the proposed theoretical modelling of the molecular position is also demonstrated.

Chapter V. Adaptive micro-optical lenticular arrays: The key parameter for designing a lenticular array is the focal length of each individual optical element. For this reason, the equations governing the lenticular arrays are presented. Due to the micrometric size of each microlens embedded in the lenticular array, special optical components are necessary in order to characterize them. In this thesis, the control and characterization software and the micropositioner are custom fabricated. This software automatizes the characterization process giving directly important results as phase modulation, focal distance or thickness. In this chapter, the experimental set-up, the control software and the characterization results are described. By comparison of the experimental results with the theoretical predictions, the electrical model presented in chapter II is validated. Finally, the viability of liquid crystal lenticular technology for an autostereoscopic application is demonstrated. Additionally, some solutions for sensing the temperature dependence and aberrations are proposed and experimentally demonstrated.

Chapter VI. Adaptive micro-optical phase modulators: By using an advanced configuration of the patterned electrode proposed in the previous chapter for an autostereoscopic display, other devices based on LC technology working as micro-optical phase modulators have been developed. The first device is a solution for one typical problem of portable autostereoscopic devices. For these kind of devices, some aspects have to be taken into account. An important issue is the ability to display vertical, as well as horizontal, views and the need to change the 3D distance for different observers. As original contribution of this work of thesis a microlens array with rotary axis and tunable capability is proposed and experimentally demonstrated.

Other micro-optical phase modulators with the same electrode arrangement or with other advanced configuration are proposed and described in this chapter: adaptive axicons and optical vortices. Indeed, these devices may be used in many practical applications such as optical tweezers, particle trapping and optical communications.

Chapter VII. Conclusions and future research lines: A brief summary of the results of the research presented in the thesis and a discussion about the possibilities for future developments.

2. Theory of liquid crystal micro-optical devices

Liquid crystals are anisotropy materials whose optical axis are parallel to the average direction of the molecular orientation. By supplying a relatively low voltage the LC molecules are reoriented and the effective refractive index of the liquid crystal is modified. The gradient of the refractive index spatially varies the phase delay experienced by an impinging wavefront of a light beam. In order to achieve proper designs, some characteristics such as anisotropy or dispersion have to be studied in detail. Moreover, knowledge of the molecular directions inside a device is essential for predicting the electro-optic response as a function of external stimulus. As original contribution, a novel algorithm to solve the position of a nematic liquid crystal molecular director is proposed. Once the liquid crystal is completely characterized, the developing of a specific model to know the electro-optic response of the micro-optical phase modulators is also very important. Another original contribution detailed in this section is a novel equivalent electric circuit for modeling liquid crystal microlenses. An interesting feature of the model is that it provides an analytical solution for microlenses with modal and hole-patterned electrode schemes, by using a simple software tool. The required driving scheme (modal or hole-patterned) can be predicted. These theories has been validated by experimental results. For more complex devices, the equations are solved by Finite Element Method.

2.1. Electro-optical properties of liquid crystals

Liquid crystals are a special kind of material having both solid and liquid characteristics at the same time. These ones have a certain molecular order but their molecules may also flow like a liquid. This results in dynamic changes in the physical properties of the material as a result of external disturbances. The molecules that make up a LC mixture may be discotic (disk-shaped) or calamitic (rod-shaped). The latter are used for most applications [Figure 15 (a)].

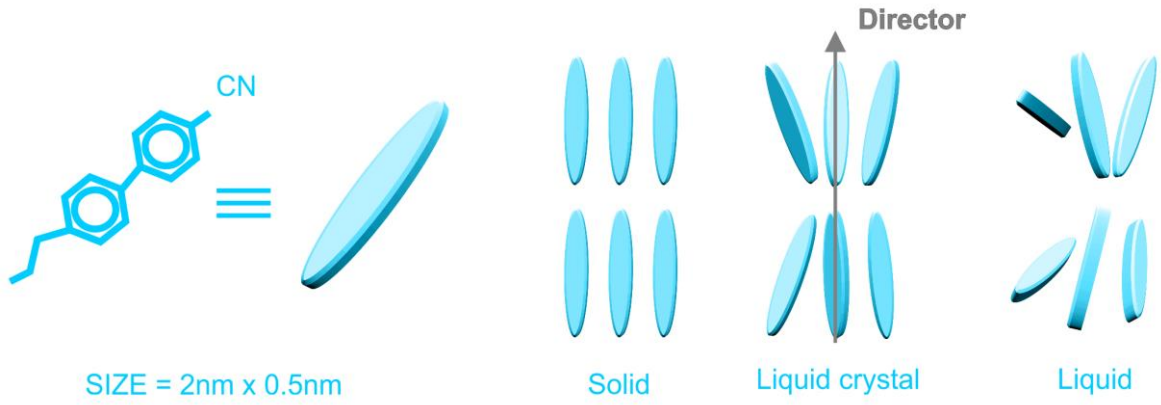

(a) Calamitic molecule. (b) Molecular phases of LC.

Figure 15. Molecular structure of LCs.

Between the solid and liquid state LCs have one or several intermediate states. They can have positional (whether molecules are arranged in any sort of ordered lattice) and orientational order (whether molecules are mostly pointing in the same direction). These intermediate states are called mesophases. The transition between states can be produced by temperature (thermotropic) or solvents (lyotropic). The most widely used are thermotropic LCs. They have two transitions [Figure 15 (b)]: to pass from solid to LC (melting point) and from LC to isotropic (clearing point). These two “melting points” were first discovered by the Austrian botanical physiologist Friedrich Reinitzer in 1888. Some years later, in 1922, M.G. Friedel described the three phases of the thermotropic LCs: smectic, originates from the Latin word "smecticus", meaning cleaning or having soap like properties; nematic, originates from the Greek νήμα (nema), which means "thread"; and chiral nematic usually called cholesteric because it was first observed for cholesterol derivatives.

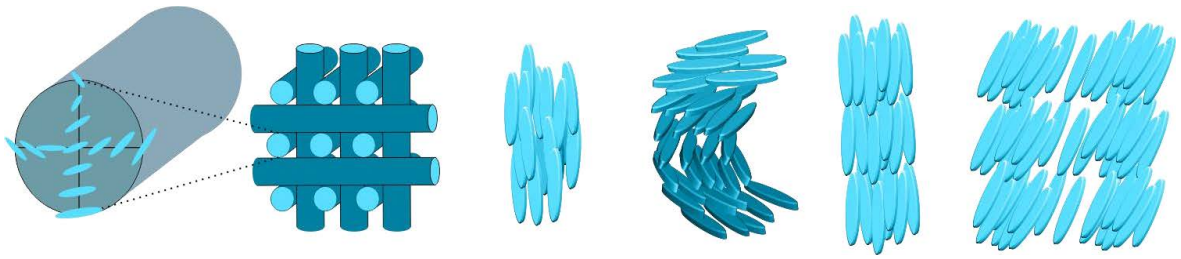

(a) Blue-phase (b) Nematic (c) Cholesteric (d) Smectic A (e) Smectic C

Figure 16. Thermotropic LC mesophases.

Each phase is related to a certain temperature range (Figure 16). Their main difference is the molecular ordering. The smectic mesophase is produced at a lower temperature than nematic mesophase. In smectic mesophase, the molecules are positioned in layers. In each plane the local order is nematic but change between layers. The structure has, therefore, orientational and positional order. There are different smectic phases (A, B, etc.) but the most used are A (SmA, normal orientation to the layers) and C (SmC, with an inclination relative to the normal of the layers). In particular, among C types there are the quiral C smectic (ferroelectric and anti-ferroelectric). The applications of these mesophases have remained in the research field [119][120].

Another special case occurs when the director in each layer is twisted with respect to those above and below. The directors form in a continuous helical pattern around the normal layer. This mesophase is called chiral nematic phase and exhibits chirality (handedness). As commented above, the common name is cholesteric because it was first observed for cholesterol derivatives. This is the most used phase to measure the temperature [121]. These LCs have a helical configuration that results in a material with a high light rotatory power. This fact is their main operation principle; for wavelengths $\lambda = n \cdot p$, where n is refractive index and p the helical pitch, the light is selectively reflected. This type of sensor takes advantage of the temperature dependence of the LC helical pitch as a sensing magnitude. The output parameter is the reflected wavelength when a white light strikes the sensor. Temperature-color transducers are usually manufactured on flexible substrates [31]. These kinds of sensors are cheap, easy to measure by means of a fiber optic link, and can be used in situations requiring sensors that do not emit any kind of electrical or electromagnetic signals. They have been proposed for use in medical applications [122], food processing [123], etc.

Recently a new phase has emerged in the research field of LCDs. Blue phases are LC phases that appear in the temperature range between a chiral nematic phase and an isotropic liquid phase. The temperature range is very small (~2º) and for this reason it has not been used until now. The discovery of stabilized blue phases over a temperature range of more than 60º [124] opened up endless possibilities. Polymer-stabilized blue phase LC (PS-BPLC) is a promising material to replace the widely used nematic LC and to overcome the emerging OLED technology. This special mesophase of the chiral doped nematic LC has several advantageous characteristics. For example, the structure gives it three important features: a microsecond response time (approximately ten times faster than nematic LC) due to the double-twist cylinder diameter and short coherence length, an optical isotropic voltage-off state due to the three-dimensional lattice structure and a multi-domain voltage-on state structure. The fast response time reduces motion blurs as well as enables color-sequential display [125]. The latter improves the optical efficiency, the resolution and the color gamut [126]. The isotropic voltage-off state produces high contrast ratios and the multi-domain voltage-on state a wide and symmetric viewing angle [127]. Another remarkable feature is the self-assembly of these structures that eliminates the need for an alignment layer and in consequence simplifies the fabrication process. Since Samsung Co. demonstrated a BP-LCD prototype at the 2008 SID exhibition, several research groups, both academic and industry, have been focused on improving the characteristics of a prospective BP-LCD. Two major challenges need to be overcome before makes the widespread application a reality; these are the low optical efficiency and the high operating voltage. One of the proposals with better performance has been proposed by the author [128]. It is a micro-optical phase modulator based on PS-BPLC. The detail of this invention can be found in the mentioned reference.

Finally, the nematic mesophase is the most used both in commercial and research applications. The main reason is the strong presence of the nematic LCs in the manufacturing processes (the main component in actual displays). In this thesis, all of the proposed and manufactured devices

use nematic LC. For this reason, this mesophase is studied in depth. The nematic mesophase is the less ordered and the one produced at the higher temperature. The long axis of the molecules are parallel to each other, whereas the center of gravity can move. The molecules are oriented in one dimension (orientational order) but do not have positional order. Due to its wide use, nematic LCs make up the most studied mesophase. For a complete physical study several formalisms are necessary. The study of the hydrodynamic theory, the theoretical formalisms of solids and crystals, and even the deepening of the knowledge of its molecular and electronic structure is necessary in order to understand its electro-optical properties. As in other types of molecules, nematic LCs have a non-symmetric charge distribution. The atomic or molecular forces differ according to the direction inside the molecule. A classic LC molecule, such as 5CB with rod-shape [Figure 15 (a)], is more easily polarized along the longitudinal axis than the transversal one. The strong generated dipoles result in an ordered position along a common direction whose name is molecular director ($\vec{n}$). The molecular director has a non-local influence in the molecular orientation. This orientation provides the solid characteristic of the LC. It also maintains a translation mobility as liquids. The main parameter to measure the local orientational order is the tensor order parameter, S. It is defined as an average deviation angle of each molecule with respect to the molecular director (Eq. 1).

$$S = \frac{\left\langle 3\cos^2\theta - 1 \right\rangle}{2} \tag{1}$$

As an example, if all the molecules are completely aligned to the mean director $S = 1$. In the other case, with random molecular position, $S = 0$. All crystals have a certain orientational order but differ in the positional order of their molecules [100].

The refractive index (n) and dielectric constants (ε), as well as the electrical conductivity (σ), are physical parameters that characterize the nematic LC response in the face of electrical, magnetic or optical fields. Due to its molecular structure and energy bands the response of a LC is dependent on the direction (anisotropy) and frequency (dispersion) of the applied fields. These two characteristics are detailed in the next sections. Finally, the theory modelling the molecular direction is explained.

2.1.1. Optical anisotropy (Birefringence)

The dielectric constants as well as the refractive index are physical parameters characterizing the nematic LC response in the face of electric, magnetic or optical fields. These two parameters are related by the permeability (μ). The response is very dependent on the direction and frequency of the applied external field due to the molecular structure and the energy bands. For this reason, the physical parameters mentioned before are considered in relation to the molecular direction (anisotropy) and frequency (dispersion).

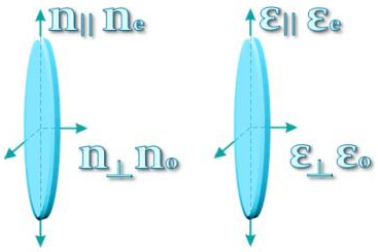

Figure 17. Anisotropic parameters of uniaxial LC molecules.

The elongated shape of the nematic LC molecules gives them anisotropy characteristics. Therefore, nematic LCs are optically anisotropic, behaving like uniaxial

birefringent materials in which the optical axes matches the molecular director direction. Moreover, the molecules are symmetrical so the physical parameters are also uniaxial [129] (Figure 17). Furthermore, the physical parameters (refractive index and permittivity) are described in two axis due to the anisotropy; the perpendicular axis is denominated ordinary and the parallel extraordinary. The maximum difference between refractive indices exhibited by the LC molecules is known as optical anisotropy or birefringence (Eq. 2).

$$\Delta n = n_e - n_o \tag{2}$$

In most LC, the value of the ordinary refractive index (n_o) is around 1.5 and the birefringence is positive ($\Delta n = n_{||} - n_{\perp} = n_e - n_o$) taking values ranging from 0.05 to 0.45 [35]. Some minerals have the intrinsic quality of birefringence. Despite this, it is not likely to find such high values as LC. This characteristic of the LC compounds is one of the most useful in optical applications.

In such a way, the light that impinges on a birefringent material with a polarization angle parallel to the optical axis experiences an effective refractive index that depends on the molecular angle (θ) with respect to the substrates (Eq. 3). This configuration is used for phase only spatial light modulation.

$$\frac{1}{n_{eff}^2(\theta)} = \frac{\sin^2(\theta)}{n_e} + \frac{\cos^2(\theta)}{n_o} \tag{3}$$

In fact, the LC sample may be employed as either Spatial Light Modulator (SLM) or a State of Polarization (SOP) corrector, simply by changing the polarization orientation of the incoming light. In the first case (SLM), only one polarizer parallel to the molecular alignment of the LC molecules is used. In the second case (SOP), the cell is placed between crossed polarizers aligned at 45º to the molecular alignment of the LC. In an SOP corrector light is split up into two orthogonal linear polarizations. These polarizations travel with a unique speed, also known as fast and slow rays or ordinary and extraordinary waves, respectively. When linearly polarized light passes through the LC device, ordinary and extraordinary waves experience spatially uniform phase retardation caused by the LC birefringence, giving rise to a SOP change. If no phase difference is introduced between the ordinary and the extraordinary beam, no change in the SOP occurs; the second polarizer (analyzer) at the output absorbs the light (Figure 18). If the extraordinary wave is retarded half a wavelength, the SOP changes producing a full transmission. The result is a fringe pattern or interference pattern which is very useful in order to know the spatial distribution of the birefringence.

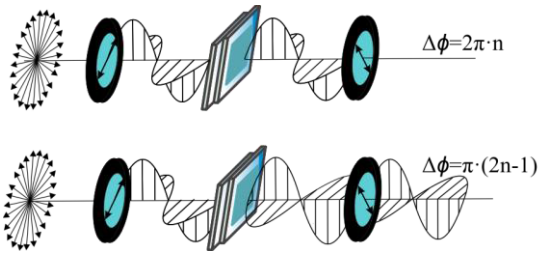

Figure 18. Typical transmissive configurations of birefringent materials for 2π phase shift (up) and π phase shift (down).

Thus in a uniaxial birefringent media, one polarization will behave as if it is travelling in an ordinary isotropic material, with one refractive index, while for the other polarization the refractive index varies in an extraordinary way with the angle of the impinging light. In this thesis, only zero twist nematic LCs are used (planar alignment).

Jones calculus

As commented above, light propagation through a LC consists of the linear superposition of two orthogonal waves, which travels over a fast and a slow axis. In order to model the LC it is convenient to introduce a matrix representation of the system. The most simple of these is the Jones Matrix. It was proposed by R. C. Jones in 1941. Polarized light is represented by a Jones vector, and linear optical elements are represented by Jones matrices. When light crosses an optical element the resulting polarization of the emerging light is found by taking the product of the Jones matrix of the optical element and the Jones vector of the incident light. Jones matrix based models generally provides a good compromise between physical adequacy and accuracy with computational efficiency and optimization facilities in the theoretical model. Moreover, the characterization methods that use Jones matrix models are less complex and require fewer measurements (less input polarization states) than other methods.

In the Jones Matrix modeling of a retarder plate it is assumed uniaxial birefringence of the material, an optical axis (c−axis) of the retarder plate is parallel to the surface and no dispersion of the material. Moreover, it is assumed that there is no reflection in the material surface and that the incident beam is entirety transmitted through the birefringent medium. Then, the light transformation due to its passing through a retarder plate is modeled as:

$$\begin{pmatrix} E'_x \\ E'_y \end{pmatrix} = R(-\alpha) W_o R(\alpha) \begin{pmatrix} E_x \\ E_y \end{pmatrix} \quad with\ E_x = E_y = \frac{I}{\sqrt{2}} \tag{4}$$

where E_x and E_y are the polarization components of the input beam in the *xy* plane, I is the light intensity, $R(\alpha)$ is the rotation matrix of the *sf*−plane (slow and fast axes) respect the *xy*−plane (Cartesian axes) given by Eq. 5, α represents the azimuth angle of the retarder plate, W_o is the Jones matrix of the retarder plate given by Eq. 6, and *Ex'* and *Ey'* are the polarization components of the transmitted beam in the *xy* plane. The detailed deduction of this expression can be found in ref. [130].

$$R(\alpha) = \begin{pmatrix} \cos\alpha & \sin\alpha \\ -\sin\alpha & \cos\alpha \end{pmatrix} \tag{5}$$

$$W_o = \begin{pmatrix} e^{-i\frac{2\pi}{\lambda}n_s d} & 0 \\ 0 & e^{-i\frac{2\pi}{\lambda}n_f d} \end{pmatrix} = \begin{pmatrix} e^{-i\frac{2\pi}{\lambda}n_{eff} d} & 0 \\ 0 & e^{-i\frac{2\pi}{\lambda}n_o d} \end{pmatrix} \tag{6}$$

The relative (ϕ) and absolute phase (Φ) can be considered as:

$$\phi = \frac{2\pi}{\lambda}(\mathrm{n_{eff}} - \mathrm{n_o})\mathrm{d}; \quad \Phi = \frac{2\pi}{\lambda}\frac{(\mathrm{n_{eff}} + \mathrm{n_o})\mathrm{d}}{2} \tag{7}$$

Considering these two parameters Eq. 6 can be transformed to:

$$W_o = e^{-i\Phi}\begin{pmatrix} e^{-i\frac{\phi}{2}} & 0 \\ 0 & e^{i\frac{\phi}{2}} \end{pmatrix} \tag{8}$$

The phase factor $e^{(-i\Phi)}$ of Eq. 8 can be neglected if the interference effects are not important or are not observable. Retarder plates are characterized by their phase delay, ϕ, their azimuth angle, α, and its transfer function matrix, W, which is represented by the product of the three matrices, obtaining:

$$W_o = R(-\alpha)W_o R(\alpha) \tag{9}$$

The passing of a light beam through a retarder plate can be described mathematically as a unitary transformation. Therefore many of the properties of the incident vector remain invariable; one of those properties is the orthogonality. If the polarization states of two beams are mutually orthogonal, they will remain orthogonal after passing through any retarder plate.

If the absolute phase delay is neglected, the representations of linear polarizers with the transmission axis parallel to the x− and y−axis, respectively, are given by:

$$P_x = \begin{pmatrix} 1 \\ 0 \end{pmatrix} \quad and \quad P_y = \begin{pmatrix} 0 \\ 1 \end{pmatrix} \tag{10}$$

Jones Matrix of LC using one polarizer

The characteristic transfer matrix of a homogenous LC cell with zero azimuth angle can be expressed as 2.13:

$$W_{LC} = e^{-i\frac{\phi}{2}}\begin{pmatrix} 1 & 0 \\ 0 & e^{i\phi} \end{pmatrix} \tag{11}$$

Since multiplying a Jones matrix by a constant phase factor does not affect the state of polarization, the $e^{(-i\phi/2)}$ term is omitted. In the case of a phase device, it is of interest that only the tunable eigenmode (in the above "y") is excited by the incoming light beam, since the orthogonal eigenmode ("x") will not get modulated by any variation in LC orientation. Finally, by multiplying

inversely the matrices of the optical components (output polarizer, Jones matrix of the LC, input polarizer and light in):

$$\begin{pmatrix} E'_x \\ E'_y \end{pmatrix} = \begin{pmatrix} 1 & 0 \\ 0 & e^{i\phi} \end{pmatrix} \begin{pmatrix} 0 \\ 1 \end{pmatrix} \begin{pmatrix} \frac{1}{\sqrt{2}} \\ \frac{1}{\sqrt{2}} \end{pmatrix} = \frac{1}{\sqrt{2}} \begin{pmatrix} 0 \\ e^{i\phi} \end{pmatrix} \tag{12}$$

From Eq. 3, Eq. 7 and Eq. 12, it can be deduced that a relative phase difference can be introduced in a structure by applying a specific voltage distribution (n_{eff} depends on θ). This is the main principle of the adaptive micro-optical phase modulators.

Jones Matrix of LC using two polarizers

Considering the LC with the fast and slow axes oriented at 45º with respect to the optical axes of the polarizers and Eq. 9, the Jones matrix of the LC is [130],

$$W_{LC} = \begin{pmatrix} \cos\alpha & \sin\alpha \\ -\sin\alpha & \cos\alpha \end{pmatrix} \begin{pmatrix} 1 & 0 \\ 0 & e^{i\phi} \end{pmatrix} \begin{pmatrix} \cos\alpha & -\sin\alpha \\ \sin\alpha & \cos\alpha \end{pmatrix} =$$
$$\begin{pmatrix} \cos^2\alpha + e^{i\phi}\sin^2\alpha & -i\sin(\frac{\phi}{2})\sin(2\alpha) \\ -i\sin(\frac{\phi}{2})\sin(2\alpha) & \sin^2\alpha + e^{i\phi}\cos^2\alpha \end{pmatrix} = \begin{pmatrix} \frac{1}{2}(1+e^{i\phi}) & -i\sin(\phi/2) \\ -i\sin(\phi/2) & \frac{1}{2}(1+e^{i\phi}) \end{pmatrix} \tag{13}$$

In Eq. 14 the total light output is obtained by multiplying inversely the jones matrix of each optical element (output polarizer, Jones matrix of the LC, input polarizer and light in):

$$\begin{pmatrix} E'_x \\ E'_y \end{pmatrix} = \begin{pmatrix} 0 & 0 \\ 0 & 1 \end{pmatrix} \begin{pmatrix} \frac{1}{2}(1+e^{i\phi}) & -i\sin(\phi/2) \\ -i\sin(\phi/2) & \frac{1}{2}(1+e^{i\phi}) \end{pmatrix} \begin{pmatrix} 0 & 0 \\ 0 & 1 \end{pmatrix} \begin{pmatrix} \frac{1}{\sqrt{2}} \\ \frac{1}{\sqrt{2}} \end{pmatrix} = \begin{pmatrix} 0 \\ \frac{1}{\sqrt{2}}\cos^2\frac{\phi}{2} \end{pmatrix} \tag{14}$$
$$T_{\parallel} = \frac{1}{\sqrt{2}}\cos^2\frac{\phi}{2}$$

Following the same procedure, the transmission for crossed polarizers is:

$$T_{\perp} = \frac{1}{\sqrt{2}}\sin^2\frac{\phi}{2} \tag{15}$$

The transmission varies between 0 and 1 depending on the value of ϕ. This equation is very important in order to simulate the interference patterns produced by a LC sample between crossed polarizers.

2.1.2. Dielectric anisotropy

The parameter used to determine the LC interaction with electrical signals is often expressed by permittivity, ε, (related in a quadratic proportion to refractive index). The absolute permittivity means the resistance encountered by an electrical field in a determined medium, that is, the material ability to transmit an electrical field. The relative permittivity is the permittivity expressed as a ratio relative to the permittivity of vacuum. This parameter is commonly known as dielectric constant and is also affected by the elongated shape of the LC molecules. As with birefringence, the maximum difference between dielectric constants in each molecular axis is known as dielectric anisotropy,

$$\Delta\varepsilon = \varepsilon_e - \varepsilon_o \tag{16}$$

This parameter is related to the refractive index by the permeability. Depending on the frequency range, one or another parameter is characterized. At optical frequencies (<100THz), optical anisotropy is used. On the other hand, the dielectric anisotropy is used at electrical frequencies (<100MHz). Recently, the study of dielectric constants in the microwave range (300MHz-300GHz) [131] and the terahertz range (THz) [132] are topical issues.

The dielectric anisotropy value can be either positive or negative depending on the electric dipole moment and its position with respect to the long molecular axis [130]. Over the years, this parameter has been studied giving rise to several formulations. One of the most accepted was proposed by Maier and Meier [133]. The dielectric anisotropy is determinant in the electrical energy, F_e. This energy appears in the LC when an external electric field is applied. Taking into account that,

$$F_e = -\frac{1}{2}\vec{D}\bullet\vec{E} \tag{17}$$

and following the Maxwell equations:

$$\begin{aligned} \vec{E} &= -\nabla V \\ D &= \overline{\overline{\varepsilon}} \cdot \vec{E} \end{aligned} \tag{18}$$

where the dielectric tensor for a nematic LC is:

$$\overline{\overline{\varepsilon}} = \begin{bmatrix} \varepsilon_o + \Delta\varepsilon n_x^2 & \Delta\varepsilon n_x n_y & \Delta\varepsilon n_x n_z \\ \Delta\varepsilon n_y n_x & \varepsilon_o + \Delta\varepsilon n_y^2 & \Delta\varepsilon n_y n_z \\ \Delta\varepsilon n_z n_x & \Delta\varepsilon n_z n_y & \varepsilon_o + \Delta\varepsilon n_z^2 \end{bmatrix} \quad (19)$$

$\Delta\varepsilon$ is the dielectric anisotropy and ε_o the ordinary permittivity. The following relation is obtained,

$$F_e = -\left(\frac{1}{2}\right)\varepsilon_0\varepsilon_o\overline{\overline{E}}^2 - \left(\frac{1}{2}\right)\varepsilon_0\Delta\varepsilon(\vec{n}\cdot\overline{\overline{E}})^2 \quad (20)$$

Equation 20 is used as theoretical formulation to implement the modelling of the unidirectional translation of LC molecules. This is detailed in the next section. As can be observed from Eq. 20, both summands are dependent on the electric field. However, the first one is independent of the molecular director $\vec{n}$ while the second one changes its value as a function of the direction of $\vec{n}$. This produces two representative cases:

i) With $\Delta\varepsilon > 0$ (positive anisotropy) the longitudinal axis of the molecules aligns parallel to the applied electric field when is higher than a critical value ($E > E_c$). That is because the electric energy is minimized when the director $\vec{n}$ is parallel to the electric field $\bar{E}$.

ii) With $\Delta\varepsilon < 0$ (negative anisotropy), the longitudinal axis of the molecules aligns perpendicular to the applied electric field. That is because the electric energy is minimized when the director $\vec{n}$ and the electric field $\bar{E}$ are orthogonal with respect to each other.

When all the factors affecting the LC physics are added the total energy can be estimated. The minimum state energy determines the static molecular position as a function of the applied electric field. This is detailed in the next section.

Finally, it is important to point out that dielectric anisotropy also affects the threshold voltage (V_{th}) of the nematic LC. Normally, the LC is sandwiched between two parallel substrates. The electric field is perpendicular to the substrates. In this case, the critical electric field (E_C) causing the molecular switching is:

$$E_c = \left(\frac{\pi}{d}\right)\left(\frac{k_{ii}}{\Delta\varepsilon\varepsilon_0}\right)^{1/2} \quad (21)$$

Where d is the distance between substrates.

- ✓ For parallel alignment (homogeneous): $k_{ii} = k_{11}$
- ✓ For twisted alignment, $k_{ii} = k_{11} + (k_{33}-2k_{22})/4$. In this case and for positive anisotropy, the critical voltage (V_C) is:

$$V_C = \pi \left[\frac{k_{11} + \frac{k_{33} - 2k_{22}}{4}}{|\Delta\varepsilon\varepsilon_0|} \right]^{1/2} \tag{22}$$

The Freedericksz transition begins from this value. The molecular director reorients by application of a magnetic or electric field.

Dielectric dispersion

The dependence of permittivity on the applied electric field frequency is known as dispersion. This physical effect is caused by the delay in molecular polarization with respect to an alternating electric field. The two different permittivities in a LC material usually have a different frequency-dependent response. The alternating electric field leads to a time lag between the average orientation of the dipole moment and the field. In general, the dipole moment is not along with the inertial axis of the molecule and there is a complicated relationship between the motion of the dipole, which determines the frequency of the permittivity, and the rotational motion of the molecule. The ordinary parameter (ε_o) has a Debye type dispersion typical of fluids. This one usually occurs at microwave frequencies (>10^9Hz). The extraordinary parameter (ε_e) usually shows a lower frequency dispersion, in the radio frequency range. Some researchers as Meier [134] suggest that this dispersion could be caused by the dipolar moment relaxation; specifically, of the longitudinal axis of the molecule. The reorientation of this parameter by application of an electric field is hindered by a potential barrier owing to intermolecular forces. Most of the experimental observations, are explained by the three rotational movements (Figure 19). The dipole moment (P) is split into two components parallel and perpendicular to the long molecular axis. This produces a typical frequency-dependent response (Figure 20):

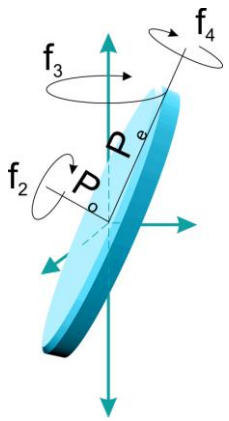

Figure 19. Three relaxation modes for the rotational movement of the LC molecule.

- For frequencies lower than $f_1 \approx 100$ Hz the ions present in the LC contribute to the electric current, and so to the detected impedance.
- The rotation around the short axes determines the permittivity response for frequencies lower than $f_2 \approx 10^5$ Hz. As can be observed, this rotation only affects the behavior of the extraordinary component. The ordinary component is not hindered by the intermolecular forces.
- The precession of long molecular axes are produced for a frequency of $f_3 \approx 10^8$ Hz. Once this frequency is exceeded, the P_e contribution is reduced to a certain level. At the same time a Debye type dispersion is produced by the dipole moment P_o.
- Finally, for frequencies higher than $f_4 \approx 10^9$ Hz [135], only the fast rotation of molecules about long axes can follow the electric fields. From this frequency, the ordinary component, P_o, cannot follow this rotational movement while P_e contributes in the same way to ε_e.

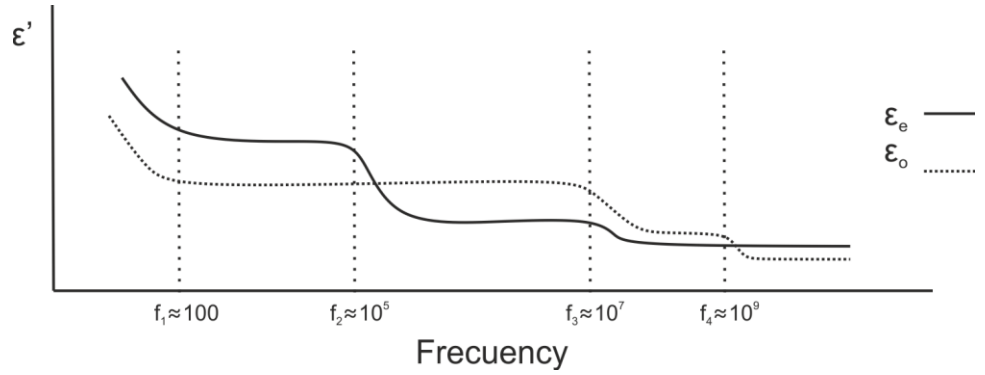

Figure 20. Spectra of permittivity (ordinary and extraordinary components) in a frequency range from 10Hz to 1GHz. Characteristic dispersion ranges.

Dielectric characterization. Impedance spectroscopy.

In order to characterize the electric properties of electrochemical systems, one of the most used techniques is the electrochemical impedance spectroscopy (EIS). It can be used to characterize the dynamics of bound or mobile charges in the bulk or interfacial regions of any solid or liquid material (ionic, semiconductor and dielectrics). In recent years, this technique has grown tremendously and is now being widely employed in a wide variety of scientific fields [136]. The medical field is one of the most demanding sectors for this technique: clinical scales to measure corporal parameters, efficacy of medicinal products [137], lung problems [138], nutritional control, cancer detection [139], etc. Another important sector is material engineering: study of new materials, batteries, metals (process of corrosion) [140], etc. In addition, there is a growing interest in the use of this technique in Bioengineering. This technique gives useful information about tissue or cells. Nematic LCs behave like a weak electrolyte [141] and the frequency response is complex. For these reasons, EIS technique is appropriate for characterizing their electrical response.

In order to use this technique, the Fourier transform is used to simplify the results. Thus, the differential equations are converted to parameters that use the Ohm law in the complex domain (Eq. 23).

$$V(i\omega) = \frac{I(i\omega)}{Ci\omega}; \quad V(i\omega) = I(i\omega) \cdot Li\omega \tag{23}$$

This technique is valid only for linear, causal and stationary systems, where the Fourier transform is also valid. That is one reason why the samples have to be characterized with low voltages [142]. The main parameter given by EIS is impedance. This concept, proposed by Oliver Heaviside in 1880, is the complex ratio of the voltage to the current for an alternating current (AC). Impedance enhances the concept of resistance to AC systems, and possesses both magnitude and phase. In a system of orthogonal axes, complex impedance is represented as $Z^* = Z' + iZ''$, where Z' is the real part and Z'' the imaginary part. Furthermore, in polar coordinates it is expressed with terms of Eq. 24,

$$\mathrm{Re}(Z) \equiv Z' = |Z|\cos(\theta); \quad \mathrm{Im}(Z) \equiv Z'' = |Z|\sin(\theta) \tag{24}$$

These parameters are usually displayed in Argand diagrams or complex plane, commonly known as Nyquist diagram (with *Z''* as a function of *Z'*). Also, there are other related magnitudes: complex admittance ($Y^* = 1/Z^*$), complex modulus ($M^* = i\omega C_0 Z^*$), and complex permittivity ($\varepsilon = M^{-1}$). The latter equation, can be used to relate permittivity with impedance (Eq. 25). This is a very useful equation to transform the impedance results of the EIS.

$$\varepsilon^* = \frac{1}{i\omega C_0 Z^*} = \frac{1}{i\omega C_0 (Z' + iZ'')} = \frac{1}{i\omega C_0 Z' - \omega C_0 Z''} = \frac{\omega C_0 (iZ' + Z'')}{-\left(\omega C_0 Z'\right)^2 - \left(\omega C_0 Z''\right)^2}$$
$$\varepsilon^* = \varepsilon' + i\varepsilon'' = \frac{Z''}{(Z'^2 + Z''^2)\omega C_0} + \frac{iZ'}{(Z'^2 + Z''^2)\omega C_0} \quad (25)$$

This parameter is usually depicted in complex plane (*ε''* as a function of *ε'*). The first researchers to use this type of representation were K. S. Cole y R. H. Cole in 1941; now it is known as Cole-Cole diagram. Different relaxation modes produce particular semicircles. By studying these graphs, different processes can be identified. The only drawback is that sometimes a process can be hidden in one semicircle [136]. In Figure 21 (a) a Nyquist diagram is depicted. As an example in this figure the polarization resistance (R_p) can be deduced from the upper frequency limit of *Z'*. Also the capacitance can be approximated from the upper part of the semicircle and R_p. On the other hand, Cole-Cole diagrams are most useful in analyzing relaxation processes. For example in Figure 21 (b), a relaxation process in a dielectric is represented by C_2 in parallel with C_1 and R_1.

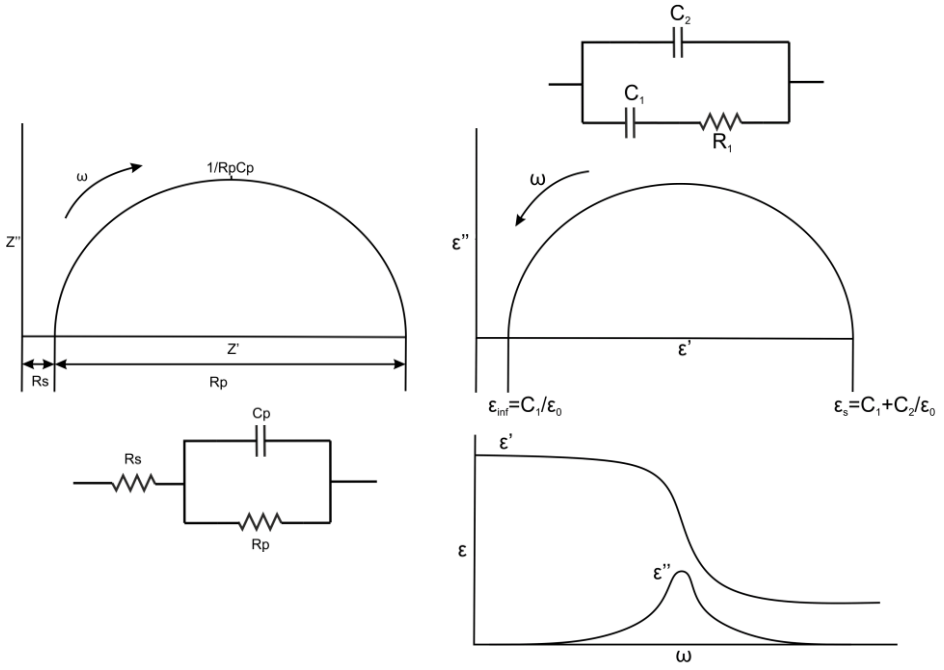

(a) Nyquist diagram. **(b) Cole-Cole diagram.**

Figure 21. Different diagrams to depict complex parameters.

These kinds of diagrams are useful to observe permittivity changes. Sometimes, the EEC are better at addressing the electrical responses of a specific material. The components values are estimated from the impedance measurements. An iterative fitting algorithm, such as Levenberg–Marquardt, is used to adjust the values of the components of the proposed equivalent circuit in a broad frequency range. A tedious work of trial-error is usually carried out until the proper EEC is found. Every component is required to have a physical meaning. The electrical response can be affected by the electrolyte (charges, free ions, microstructures, etc.) or the device characteristics (texture, geometry and material of the electrodes, dimensions, etc.). In this thesis, the EEC of the nematic LC is studied. This is important to model the response of the proposed devices.

In summary, in order to characterize LC by EIS some important issues have to be taken into account. The most important consideration is the use of low voltage electrical signals. In order to maintain linearity, it is recommended not to exceed 50mV. Another requirement is the low resistance of the electrodes. Even, for high frequencies Au electrodes are recommended. The main reason is to avoid masking other effects by the own relaxation mode of the cell itself. The thickness can also affect the impedance. The analyzer Solartron 1260 has the frequency-impedance limit equal to $f \cdot Z < 10^9\ \Omega Hz$ [143]. Some capacitances can be masked by parasitic capacitances around the sample. For these reasons, the sample used in Chapter 4 has a thin LC layer and a large electrode surface.

2.1.3. Theory of the molecular director: The Continuum Theory

Knowledge of the nematic LC molecular directions inside a device is essential for predicting the electro-optic response as a function of external stimulus. Some recent applications such as optical filters, microwave phase shifters and filters, active zoom, and tunable lenses, among others, have been areas of interest for nematic LC simulations. Recently, some studies have tried to solve this problem analytically [144]. However, in order to obtain accurate results, numerical methods are required. Recent numerical simulations have focused on nematic LC in tumbling flows, nematic dynamics [145], and new algorithms [146]. The objective of these works is to find the position of the nematic LC director inside the cell. In our study an original algorithm is used in order to solve the director equations under applied electric fields.

In the nematic LC physics understanding, the most accepted theory is the continuum theory. In this theory, the average local orientation of molecules is mathematically represented by a vector called director $\vec{n}$. All directors that form a LC cell determine the anisotropy inside it. This vector can be represented in Cartesian (n_x, n_y, n_z) or spherical coordinates with $r = 1$ (θ, φ), see Figure 22. The equilibrium state is such that all the molecules are aligned parallel to each other in the direction of $\vec{n}$. However, as a result of the external fields, this director is deformed. The continuum theory does not consider the nematic LC behavior at a structural level because the lengths of these deformations (about 1 μm) are considerably shorter than the molecular length (Armstrong). The basis for the continuum theory model was proposed at the end of the 1920s by C. W. Oseen [147] and H. Zöcher [148]. The first one developed a nematic LC static theory; the second one successfully applied this theory to the Freedericksz transition.

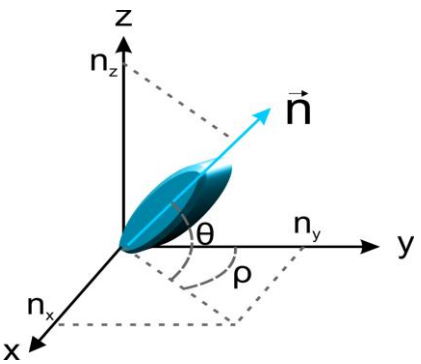

Figure 22. Molecular director of a LC molecule, Cartesian and Spherical coordinates.

However, it was not completed until over thirty years later when F. C. Frank studied this theory and presented it as elasticity deformation theory [149], offering a direct formulation of the energy. These equations are usually employed in the static director simulations. The dynamic theory is attributed to Oseen [150], the formulation of general conservative laws to Erickseen [151] and the constitutive equations describing the mechanical behavior to Leslie [152]; in fact, these equations are easily applicable to numerical simulations of the LC director dynamics. These theories are based on the study of two parameters: the Q tensor, which is related with *S* parameter (Eq. 1) [153] or director $\vec{n}$. The molecular director $\vec{n}$ is more frequently used due to its mathematical simplicity, low computational cost and more accurate results [154].

Until now different approaches have been proposed to minimizing the free Gibbs energy, which is composed by the electric energy plus free energy deformation (Frank-Oseen equations). These methods are based on Euler-Lagrange equations. To solve these equations, one of the most employed techniques is the Finite Element Method [155], this method is usually employed in complex structures; its programming involves a variational approach to the Frank-Oseen free energy formulation. The method also needs mesh grids that usually requires many lines of code. Another method is to solve the equations directly, employing numerical methods to solve the resulting differential equations. Several numerical methods have been proposed to solve this problem, finite difference [156], Bvp4c [157], etc. The finite difference method is a simple method but has to be precisely configured in order to work properly, the step constant is usually a difficult value to find (small values causes high computational costs and big values big errors). The Bvp4c is a MATLAB function; it is time-consuming but the less erroneous, actually there have been advances on the algorithm through reduction in errors but has more difficulties to converge. The main differences between them are the error and the computational cost. The aim of this work is to provide an easy tool to solve the molecular distribution. A simple, fast and reliable algorithm is proposed to solve these equations. This algorithm has been compared with previous methods in Appendix 1.

Molecular alignment of a LC is deformed under mechanical stress. In nematic LC, three deformations can be considered: splay, twist and bend (Figure 23).

(a) Splay (K_{11}). (b) Twist (K_{22}). (c) Bend (K_{33}).

Figure 23. Deformations in nematic LC.

The relation between deformation and stress, for each kind of deformation, is expressed as splay elasticity, K_{11}, twist elasticity, K_{22} and bend elasticity, K_{33} (see Figure 23). The elastic constants for a LC are around 10^{-6}, 10^{-7} dynes and therefore, much smaller than common solids. This fact makes modifications of molecules positions easy, due to electric or magnetic external fields. Mathematically, if an external perturbation, such as an electric field, is introduced in the system, the deformation of the molecular director can be estimated minimizing the Gibbs free energy density, F_G.

$$\int_{\Omega}\{F_G\} \tag{26}$$

This energy is composed of the contribution of two energies: the deformation free energy, F_d, and the electrostatic free energy, F_e (Eq. 20); $F_G = F_d - F_e$. F_d is the energy of the different deformation modes, as a function of the gradient of $\vec{n}$, and is determined by the free energy formulation of Frank-Oseen,

$$F_d = \frac{1}{2}\left(K_{11}\left(\nabla\vec{n}\right)^2 + K_{22}\left(\vec{n}\cdot\nabla\times\vec{n} + \frac{2\pi}{\xi}\right)^2 + K_{33}\left|\vec{n}\times\nabla\times\vec{n}\right|^2 \right) \tag{27}$$

where $\vec{n}$ is the molecular director, $\vec{n}$ = (n_x, n_y, n_z), K_{ii} are the elastic deformation constants and ξ is the pitch of a quiral helicoidal dopant (for twist purposes); in the simulation program this variable is called *P*.

The Gibbs free energy (W_G), given by the integral of the free energy density (F_G) over the thickness, has a minimum in the equilibrium state. However, due to the high nonlinearity of the free energy and the coupling between deformation and electric energies, a direct solution of the LC director deformation from the free energy equation is very difficult to obtain. Therefore, the modelling usually involves an iterative process, minimizing the Gibbs free energy to update the LC director profile. Also, the electric energy is minimized by solving Gauss's Law to up-date the potential profile interactively.

In order to simplify the problem, the molecular director orientation is described with two angles: θ, defined as the director tilt angle measured from the device surface, and φ, defined as the twist angle measured from the alignment direction (see Eq. 28):

$$\vec{n} = (\cos\theta\cos\varphi, \cos\theta\sin\varphi, \sin\theta) \tag{28}$$

With this simplification, considering Eq. 17 and one dimension, the electrostatic free energy results:

$$F_e = -\frac{1}{2}(\varepsilon_o - \Delta\varepsilon\sin^2(\theta(z)))\left(\frac{\partial V}{\partial z}\right)^2 \tag{29}$$

At this point, and considering the Gibbs free energy as:

$$W_G = \frac{1}{2}\int_0^d (F_d - F_e)dz \tag{30}$$

where d is the LC thickness, the minimum energy solution (subject to boundary conditions), produced in the nematic equilibrium state, is equivalent to solve the Euler-Lagrange equations. Those equations, which are in one dimension and spherical coordinates, are:

$$\begin{aligned}\frac{\partial F_G}{\partial \theta}-\frac{d}{dz}\left(\frac{\partial F_G}{\partial \theta'}\right)=0\\ \frac{\partial F_G}{\partial \varphi}-\frac{d}{dz}\left(\frac{\partial F_G}{\partial \varphi'}\right)=0\end{aligned} \tag{31}$$

This tedious task can be easily solved with symbolic software, e.g. MUpad (MATLAB) or MAPLE. In the MAPLE case, the software has implicit functions that solve the Euler-Lagrange equations with only two lines of code:

>>EL:=remove(has, EulerLagrange(Wg,z,[θ(z),φ(z)]),K)

>>(Thetadif,Phidif):=selectremove(has,EL,diff(diff(theta(z),z),z))

The result is Eq. 31 expanded. Moreover, these equations remove some unnecessary terms and isolate the second order differential parameter.

$$\begin{aligned}\theta''(z) &= \mathrm{f}(\theta(z),\varphi(z),\theta'(z),\varphi'(z))\\ \varphi'' (z) &= \mathrm{f}(\theta(z),\varphi(z),\theta'(z),\varphi'(z))\end{aligned} \tag{32}$$

These equations relate the tilt and twist angles and the applied voltage with the position, being the key to solve the nematic LC director orientation by numerical methods. In order to obtain Eq. 32, a simple instruction is used, solve:

>>solve(Thetadif, diff(diff(θ(z), z), z)))

$$\begin{aligned}&\frac{d^2\theta(z)}{dz^2}=cos(\theta(z))sin(\theta(z))\cdot\\ &\left(\begin{array}{l}K_{11}\left(\frac{d\theta(z)}{dz}\right)^2+2K_{22}\frac{d\varphi(z)}{dz}P-2K_{22}cos(\theta(z))^2\left(\frac{d\varphi(z)}{dz}\right)^2\\ -K_{33}\left(\left(\frac{d\varphi(z)}{dz}\right)^2+\left(\frac{d\theta(z)}{dz}\right)^2-2cos(\theta(z))^2\left(\frac{d\varphi(z)}{dz}\right)^2\right)-\left(\frac{dV(z)}{dz}\right)^2 ince\end{array}\right)\\ &/(K_{33}+K_{11}cos(\theta(z))^2-K_{33}cos(\theta(z))^2)\end{aligned} \tag{33}$$

>>solve(Phidif, diff(diff(φ(z), z), z)))

$$\frac{d^2\varphi(z)}{dz^2} = \frac{2sin(\theta(z))\frac{d\theta(z)}{dz}\frac{d\varphi(z)}{dz}\left(-2\cdot K_{33}\cdot cos(\theta(z))^2 - K_{22}P + K_{33} + 2K_{22}cos(\theta(z))^2\right)}{cos(\theta(z))(K_{33} + K_{22}\cdot cos(\theta(z))^2 - K_{33}\cdot cos(\theta(z))^2)} \quad (34)$$

In parallel, the electric field change across the cell, as a function of the anisotropy, must be taken into account. For potential profile estimation, Gauss's law is solved:

$$\nabla \cdot \vec{D} = 0 \quad (35)$$

Electric displacement can be expressed by the applied potential (V), see Eq. 18. Then, considering the permittivity tensor in z direction (Eq. 19) and isolating the second order differential equation of electric field V, the code is as follow

```
>>ez:=eo+ince·(n[3])
>>solve(diverge(e0·ez·E,[z]), diff(diff(V(z), z), z)))
```

$$\frac{d^2V(z)}{dz^2} = -\frac{2\cdot ince\cdot sin(\theta(z))\cos(\theta(z))\frac{d\theta(z)}{dz}\frac{dV(z)}{dz}}{eo + ince\cdot sin(\theta(z))^2} \quad (36)$$

Finally, a system of three second order differential equations (θ'', φ'', V''), Eq. 33, 34 and 36 is obtained. This system has two boundary conditions, corresponding to the two glass plate voltages, then, it can be expressed as:

$$Y'' = f(z, Y, Y'), \quad Y(0) = \alpha, \quad Y(d) = \beta \quad (37)$$

where α and β are vectors (3x1) with Y solutions at the extreme points 0 and d, respectively. The analytical resolution is very complex, but numerical methods can define approximations to the solution. The latter equation, as well as being a Boundary Value Problem (BVP), is non-linear reducing the possible methods to solve it. In this thesis, four different methods have been used:

- The classic FDM, with central approximation.
- The proprietary algorithm of MATLAB, Bvp4c.
- A novel algorithm based on shooting method proposed by the author [158].
- Finite element method (FEM)

As noted above, the Bvp4c is known for its minimal error in BVP solutions. So, the comparison between the three methods has been done in terms of computational cost and errors, taking as

reference the Bvp4c results. The best performance is demonstrated to be for the proposed algorithm (based on shooting method). In order to work with this algorithm, the differential equations are transformed to first order equations. Then, the differential equations are solved by Runge-Kutta and Newton-Raphson algorithms. This algorithm is used in the simulations of next section and chapter 4. The development and programming detail as well as the comparison with previous methods is detailed in Appendix 1. For more complex structures, Finite Element Method (FEM) will be necessary. The same approach explained before is used to extract the equations in two and three dimensions.

2.2. Theory of modal and hole patterned devices

The design of new LC micro-optical devices is involving currently important research resources. Prototypes based on this technology take advantage of the tunable electro-optical properties of these materials mainly for the phase shift tunability. As commented in section 1.2, in order to simplify the structures and to decrease the device control voltage, many topologies have been researched. Furthermore, the capacity of manufacturing LC microlenses is limited at the micrometric scale with the constraint of lithographic resolution. Some approaches, such as Fresnel zone method, with arrangements of multiple electrodes, complicate the final design. Other strategies consist of creating a lens effect by shaping the electric field generated with a hole-patterned electrode structure. However, those last approaches do not work properly for large hole sizes, because of the electric field vanishes gradually without reaching the entire area of the hole. In hole-patterned electrode structures, the phase gradient is generated by the fringe field effect as the size of the hole is sufficiently small, that is, the diameter/thickness ratio less than 2-3 [159]. The spreading of the electric field lines, yielded from the electrode, causes an elastic distortion of the LC that creates the lens response. Nevertheless, as hole dimensions increases in size, the fringe field effect is disregarded.

An option to mitigate this problem is to exploit the modal control technique. In this arrangement, an electric field gradient is generated across a layer of high sheet resistance in areas which are free of the contact electrode. That inclusion can be a possible solution to avoid the use of several electrodes. On the contrary, modal design becomes a handicap as size gets smaller [92] and involves a very careful design of the control layer resistivity. The smaller the lens size the higher the sheet resistance of the layer to keep an equivalent field distribution on the lens surface for lenses with different sizes.

There has been reported in the literature only one model describing the effective voltage distribution on the control electrode for modal lenses. It was proposed by G. V. Vdovin et al. in 1999 [160]. This model consider the field outside the device equal to zero. The LC is modelled as a lossy capacitor. The mathematical development is defined by Eq. 38.

$$\begin{aligned} \frac{\partial \delta}{\partial t} &= -\nabla_s i + j(d/2) \\ i &= R_{sq}^{-1} E = -R_{sq}^{-1} \nabla_s V \end{aligned} \tag{38}$$

where δ is the superficial charge, ∇_s is divergence operator, i the superficial current density, j the volumetric current density, R_{sq} the sheet resistance of the control electrode, E the electric field in the control electrode and V the supplied voltage.

Despite this model has been widely applied by some research groups [88], [161], it does not include distributed capacitances whose effect is negligible if not considered micrometric scale devices. As the lens sizes approaches the micrometer scale, the modal control layer becomes unnecessary. Then, the fringe field effect turns significant and the capacitive effects in the coplanar electrode structure of the resultant hole-patterned scheme must be taking into account. Depending on the transition between both schemes, the horizontal electric impedance can be predominantly capacitive, resistive or a combination of both.

As original contribution of this thesis, a novel EEC based on a transmission line is proposed. This one, models both modal and a hole-patterned electrode structures and establishes the hypothesis for implementing both topologies at the same time. It has been evidenced for the first time analytically, that at the micrometric scale, the modal control layer is needless as the fringe field effect is predominant in a coplanar electrode structure. The model establishes a powerful tool to predict both modal and hole-patterned electrical responses during the design process. It involves an analytic study simpler than the complex finite element analysis.

2.2.1. Electrical modelling for micro-optical devices

The model can be applied for any micro-optical device with two electrodes in the upper substrate and a continuous electrode in the other one. For example it can be applied to spherical and cylindrical LC lenses. In Figure 24 the case for a cylindrical lens is depicted. The new EEC is a transmission line that consists of two kinds of components in the direction of the wave propagation: resistors, R, and singular coplanar capacitors, C_1 (Figure 24). The LC is modeled with transverse components, perpendicular to the direction of the wave propagation: distributed capacitors, C_2, in parallel with distributed conductance, G, per unit area, respectively. The last two components make the model only valid in a certain range of frequencies (100 Hz – 10 kHz), it is demonstrated experimentally in section 4.1.

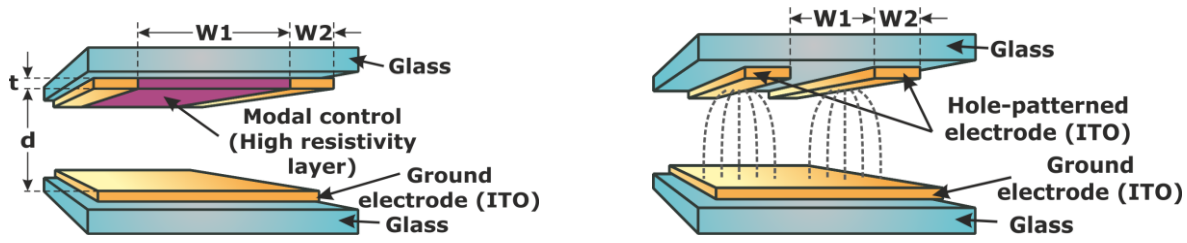

(a) Modal control technique. (b) Hole-patterned electrode structure.

Figure 24. LC cylindrical microlens. Note that, devices have not been drawn to scale and, for clarity of the graph, the LC and alignment layers have not been outlined.

In a modal topology, Figure 24(a), distributed resistors are $R = R_{sq}$, that is, the sheet resistance connected to model the control layer. Alternatively, in a hole-patterned structure, distributed resistors connected in the same place, $R = R_{CL}$, model the LC dielectric losses in the lens surface. For the complete model, R_{sq} is considered.

Distributed capacitors, C_1, describe the capacitive coupling between fingers of the comb geometry electrode of the cylindrical lens that is caused by the fringe field, shown in Figure 24(b). This capacitor results from the LC permittivity in the horizontal direction. The structure can be modelled by the following ECC:

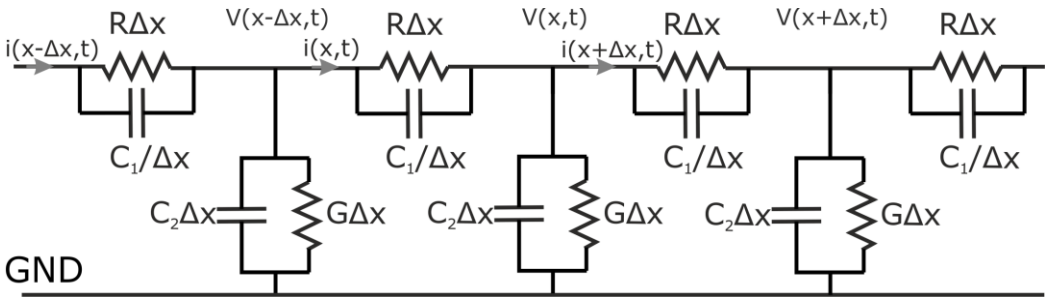

Figure 25. Equivalent electrical circuit for LC microlenses with coplanar capacitances C_1.

Research in the field of coplanar capacitances has given rise to a lot of works related to multiple applications: MOSFET transistors [162], microstrip lines [163], etc. One of the most accepted techniques for obtaining these capacitors is the theory of conformal transformations. Conformal mapping preserve the angles, transforming the structures to a complex plane. The result regions are simpler and easier to study [164]. For analytical purposes in these settings, an approximation to the problem has been taken from the coplanar capacitor theory [165]. The result is an equivalent parasitic capacitor, C_1, inversely proportional to a constant A described in Eq. 39. Constant A has been estimated using conformal mapping based on the Christoffel–Schwarz transformation,

$$A = \frac{2K(k)}{K(k')} \quad \text{with} \quad k = \frac{W_1}{W_1 + 2W_2}, \quad k' = \sqrt{1-k^2} \tag{39}$$

where W_1 is the space between electrodes (the cylindrical lens diameter), W_2 the electrode width, $K(k)$ the complete elliptic integral of the first kind and k the elliptic modulus. Finally the components of the model are determined by,

$$\begin{aligned} R = R_{sq} &= \frac{\rho}{t}\left(\frac{\Omega}{sq}\right); \quad C_1 = \frac{\varepsilon_0 \cdot \varepsilon'_1 \cdot d}{A}\left(F\right) \\ C_2 &= \frac{\varepsilon_0 \cdot \varepsilon'_2}{d}\left(\frac{F}{m^2}\right); \quad G = \frac{\sigma}{d}\left(\frac{S}{m^2}\right) \end{aligned} \tag{40}$$

where ρ and t are the resistivity and the thickness of the control layer (the high resistivity layer is considered), respectively, ε_0 the vacuum permittivity, d the LC thickness, σ the LC conductivity, and ε'_1 and ε'_2 the average real effective permittivities in the horizontal and vertical directions, respectively (for simplifying the analysis, average values have been considered). In addition, all of the EEC components are defined per unit length, Δx (x-axis is the direction of the transmission line), for a proper estimation of the analytical expressions,

$$R_{sq}\cdot\Delta x\left(\frac{\Omega}{m}\right);\quad \frac{C_1}{\Delta x}\left(\frac{F}{m}\right);\quad C_2\cdot\Delta x\left(\frac{F}{m}\right);\quad G\cdot\Delta x\left(\frac{S}{m}\right) \tag{41}$$

Following the Ohm and Kirchhoff's laws the current and voltage relations in the transmission line are set (equations 42 and 43).

$$i(x+\Delta x,t)=\frac{V(x,t)-V(x+\Delta x,t)}{R_{sq}\Delta x}+\frac{\partial V(x,t)-\partial V(x+\Delta x,t)}{\partial t\Delta x}C_1 \tag{42}$$

$$i(x,t)-i(x+\Delta x,t)=C_2\Delta x\frac{\partial V(x,t)}{\partial t}+G\Delta x\cdot V(x,t) \tag{43}$$

In order to estimate the infinitesimal variation of the voltage, equations 42 and 43 are divided by Δx and the limit when Δx tends to zero is estimated. The result are equations 44 and 45.

$$\lim_{\Delta x\to 0} i(x+\Delta x,t)=-\frac{\partial V(x,t)}{R_{sq}\partial x}-\frac{\partial V(x,t)}{\partial x\partial t}C_1\Rightarrow i(x,t)=-\frac{\partial V(x,t)}{\partial x}\left(\frac{1}{R_{sq}}+\frac{\partial}{\partial t}C_1\right) \tag{44}$$

$$\lim_{\Delta x\to 0}\frac{i(x+\Delta x,t)-i(x,t)}{\Delta x}=\frac{\partial i(x,t)}{\partial x}=-C_2\frac{\partial V(x,t)}{\partial t}-G\cdot V(x,t) \tag{45}$$

If the intensity value (Eq. 44) is included in Eq. 45 the result is Eq. 46.

$$-\frac{\partial V^2(x,t)}{\partial x^2}\cdot\left(\frac{1}{R_{sq}}+\frac{\partial}{\partial t}C_1\right)=-C_2\frac{\partial V(x,t)}{\partial t}-G\cdot V(x,t)\Rightarrow\frac{\partial V^2(x,t)}{\partial x^2}=\frac{C_2\dfrac{\partial}{\partial t}+G}{\dfrac{1}{R_{sq}}+\dfrac{\partial}{\partial t}C_1}\cdot V(x,t) \tag{46}$$

The result considering only one harmonic $V(x,t)=V(x)\cdot e^{j\omega t}$, is Eq. 47.

$$\frac{\partial V^2(x)}{\partial x^2}=\frac{G+j\omega C_2}{\dfrac{1}{R_{sq}}+j\omega C_1}\cdot V(x)=\Psi\cdot V(x) \tag{47}$$

The solution to this ordinary differential equation depends on the boundary conditions, that is, the voltages at the two lens edges, $V(x=-r)$ and $V(x=r)$, with x the position on the active area and r, the active area radius. By using MATLAB, Eq. 47 gives the solution to the voltage distribution for two sets of boundary conditions:

- $V(x = -r) = V_1$, voltage at the left side.
- $V(x = r) = V_2 e^{i\varphi}$, voltage at the other side (where φ is the electric phase shift).

Where V(x) is the voltage distribution as a function of the longitudinal position (x) of the transmission line.

$$V(x) = \frac{e^{\left(x\sqrt{\Psi}\right)}\left(V_1 e^{\left(-r\sqrt{\Psi}\right)} - V_2 e^{\left(r\sqrt{\Psi}\right)} e^{(\varphi i)}\right)}{e^{\left(-2r\sqrt{\Psi}\right)} - e^{\left(2r\sqrt{\Psi}\right)}} - \frac{\left(V_1 e^{\left(-r\sqrt{\Psi}\right)} - V_2 e^{(\varphi i)} e^{\left(r\sqrt{\Psi}\right)}\right)}{e^{\left(x\sqrt{\Psi}\right)} \cdot \left(e^{\left(-2r\sqrt{\Psi}\right)} - e^{\left(2r\sqrt{\Psi}\right)}\right)} \tag{48}$$

From a practical point of view there are two important specific cases: case 1, when the same voltage is applied at the sides of the active area, the electric phase shift is zero; case 2, when an inverted voltage is applied at the other electrode (electric phase shift of 180º), a prism like voltage profile is obtained. The mathematical development is shown for the case 1 but is similar for case 2. Taken into account the hyperbolic relations of Eq. 49,

$$\sinh(x) = \frac{e^{x} - e^{-x}}{2}; \quad \cosh(x) = \frac{e^{x} + e^{-x}}{2}; \quad \sinh(x) = 2\sinh(x)\cosh(x) \tag{49}$$

The solution of Eq. 48 is considerably simplified,

$$V(x) = \frac{e^{\left(x\sqrt{\Psi}\right)} V_1 \sinh(r\sqrt{\Psi})}{\sinh(2r\sqrt{\Psi})} + \frac{e^{\left(-x\sqrt{\Psi}\right)} V_1 \sinh(r\sqrt{\Psi})}{\sinh(2r\sqrt{\Psi})} = V_1 \frac{e^{\left(x\sqrt{\Psi}\right)} + e^{\left(-x\sqrt{\Psi}\right)}}{2\cosh(r\sqrt{\Psi})} = V_1 \frac{\cosh(x\sqrt{\Psi})}{\cosh(r\sqrt{\Psi})} \tag{50}$$

In summary,

$$\begin{aligned} &\text{Case 1: } V(-r) = V(r) = V_1 \cdot e^{j\omega t} \Rightarrow V(x) = V_1 \frac{\cosh(\sqrt{\Psi} \cdot x)}{\cosh(\sqrt{\Psi} \cdot r)} \\ &\text{Case 2: } \left\{ \begin{matrix} V(-r) = V_1 \cdot e^{j\omega t} \\ V(r) = V_1 \cdot e^{j\omega t + \pi} \end{matrix} \right\} \Rightarrow V(x) = V_1 \frac{\sinh(\sqrt{\Psi} \cdot x)}{\sinh(\sqrt{\Psi} \cdot r)} \end{aligned} \tag{51}$$

In addition to the previous calculations, voltage distribution has been necessarily obtained through an iterative process, for achieving an accurate result. Equation 52 connects the effective permittivities, ε'_1 and ε'_2, the dielectric anisotropy $\Delta\varepsilon$ (voltage dependent) and a new parameter p proportional to the average tilt angle of molecules,

$$\frac{\varepsilon'_1}{\varepsilon'_2} = \frac{\Delta\varepsilon \cdot p + \varepsilon_o}{\Delta\varepsilon \cdot (1 - p) + \varepsilon_o} \quad \text{with} \quad 0 < p < 1 \tag{52}$$

The iterative process for obtaining $V(x)$ follows the program steps:

i) Firstly, LC molecules are considered in a relaxed position (p = 1) for homogeneous alignment. Then, by Eq. 52, $\varepsilon'_1 = \varepsilon_e$ (extraordinary permittivity) and $\varepsilon'_2 = \varepsilon_o$ (ordinary permittivity).

iii) C_1 and C_2 are calculated via Eq. 40.

iv) $V(x)$ is obtained by Eq. 51 through the EEC model.

v) Voltage distribution, $V(x)$, determines angular position of the molecules (through Frank–Oseen equations, section 2.1.3).

vi) A new molecular distribution gives a new effective permittivity distribution in the x-axis, $\varepsilon(x)$. Next, it is averaged in that axis, about the lens diameter, to get a single value.

vii) Finally, the loop jumps again to the step i), deducing a new p value, etc.

This process converges to the final voltage distribution, as there are no changes in the p parameter and the error tolerance is fulfilled.

2.2.2. Using an analytical model to design liquid crystal microlenses

As commented above, a novel EEC has been developed to model LC microlenses; it is shown in Figure 24. This scheme is a transmission line involving distributed capacitances and models the effect of the typical parasitic capacitances between the teeth of the comb electrode for LC microlenses. The resulting equation of this model is Eq. (47). The denominator of this equation contains two key parameters, C_1 and R_{sq}. These two parameters determine the topology required to fabricate a LC microlens. The relationship between the components of the EEC (C_1, C_2, R_{sq} and G) and the structural dimensions is taken from Eq. 40. From impedance considerations, small-diameter lenses require very high resistivity layers; however, $|Z_{C1}|$ ($1/\omega C_1$) can be decreased up to a critical value at which a resistivity layer is no longer needed. In contrast, if the lens diameter is too large, the parameter $|Z_{C1}|$ becomes too high and can be neglected for a parallel topology. In the following sections, the structural requirements of a LC microlens are determined. The characteristics of the EEC depend on the $|Z_{C1}|$ and the resistance produced by R_{sq} (R).

- Modal microlens without a parasitic capacitive effect, $R << |Z_{C1}|$: the EEC developed for this case is the simplest to apply and is valid for large diameters (>1mm)
- Microlens with a complete EEC, $R < |Z_{C1}|$: in the most general case, the EEC exhibits both resistive (R) and capacitive (C_1) effects; however, the resistive effect predominates
- Modal limiting condition, $R = |Z_{C1}|$: the resistance and capacitance are comparable, resulting in a limiting condition
- Hole-patterned microlens, $R >> |Z_{C1}|$: a specific thickness-diameter relationship causes the electrical field to be distributed across the lens diameter

Modal Microlens without Parasitic Capacitive Effect

It is well known that the phase delay in a LC lens is nonlinearly related to the voltage distribution. To obtain a proper phase distribution for a symmetric microlens, i.e., to avoid

undesirable shrinkage effects at the sides of the lens or a plateau in the center of the optical phase, the voltage at the electrode and the microlens center must equal the saturation voltage and the threshold voltage, respectively. Thus, a new parameter is introduced as follows:

$$\alpha = \alpha' + j\alpha'' = V_1 / V_{x=0} \tag{53}$$

As previously mentioned, this relationship depends on the LC characteristics. The imaginary part corresponds to the electrical phase shift at the center of the lens. Two methods can be used to accurately estimate the modulus of this parameter. In the first and more accurate method, the LC birefringence is measured using spectroscopy. In the second method, the Frank-Oseen equations are simulated. If an external perturbation, such as an electric field, is formally introduced into the system, the deformation of the molecular director can be estimated by minimizing the Gibbs free energy. Subsequently, this parameter is considered to be a known variable. Solving Eq. 47 with the boundary conditions $V_{-x} = V_x = V_1$ (where x denotes the lens radius) for one harmonic yields

$$V_{x=0} = V_1 / cosh(\sqrt{\Psi} \cdot r) \Rightarrow \Psi = acosh^2(\alpha) / r^2 \tag{54}$$

In a nematic LC, the impedance, Z_{C2}, in the EEC is always smaller than the parallel conductance [166] G and can therefore be neglected (henceforth, the impedance in the EEC is suppressed). As parasitic capacitive effect (C_1) is not considered, the sheet resistance of the resistivity layer is given as follows:

$$R_{sq} = \frac{1}{\frac{r^2 j\omega C_2}{acosh^2(\alpha)}} = \frac{d \cdot acosh^2(\alpha' + j\alpha'')}{r^2 \left(\varepsilon_0 \varepsilon'_2 j\omega\right)} \approx \frac{d \cdot 2acosh^2(|\alpha|)}{r^2 \left(\varepsilon_0 \varepsilon'_2 \omega\right)} \tag{55}$$

where d denotes the LC thickness, and ε'_2 denotes the LC real permittivity perpendicular to the glasses. An analytical approximation is obtained using hyperbolic trigonometric relations (see Appendix 2). In the resulting equivalence solution, a sinusoidal function ([-1, 1]) is suppressed due to a hyperbolic cosine component (exponential behavior). This approximation only produces significant errors for low values of $|\alpha|$ (Figure 26).

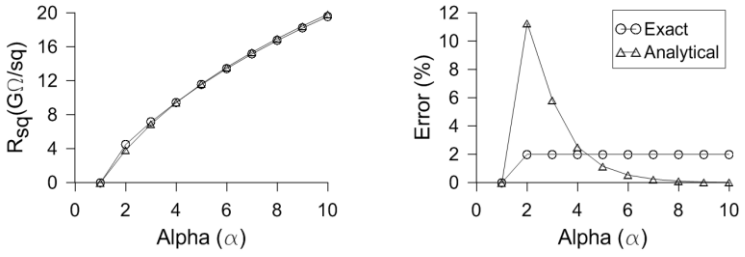

(a) r = 285µm, d = 50µm and f = 1 kHz. **(b) Comparison of errors for the two techniques.**

Figure 26. Square resistance as a function of Alpha (α).

The approximate solution is compared with the exact solution using a brute force algorithm. In this case, the error corresponds to the chosen tolerance. It is very important to estimate this resistance in the early stages of the design phase of LC lenses. Different materials and techniques have been developed to manufacture high resistivity layers for modal devices; however, only experimental studies have been conducted in the literature, thus far. Design at the micrometer scale is not a simple task and sometimes requires the use of very thin metallic layers with unusual physical properties (see section 3.2). Thus, Eq. 55 is an important design tool. The measured error is within the same range as those incurred in the manufacturing process and is not in itself a determining factor. In addition, the resistance is a frequency dependent parameter, such that the errors in the design estimates can be easily corrected. However, Eq. 55 shows that decreasing the diameter ($2r$) increases the sheet resistance quadratically. As previously mentioned, the critical value at which the impedance of the parasitic capacitor C_1 becomes smaller than the parallel resistance determines whether or not a high resistivity layer is required.

Microlens with Complete ECC

This general case is rarely encountered in practice, because an optimum design is only relevant for the modal or hole-patterned regime. For this reason, this case is not detailed in this thesis.

Modal Limit

As previously mentioned, there is an important consideration in the design of LC microlenses. The required resistance increases when the diameter decreases, resulting in a critical value at which the capacitor C_1 produces a distributed electric field, such that a high resistivity layer is not required. The modal limit corresponds to the resistance of the high resistivity layer being equal to the impedance modulus of the C_1 capacitor:

$$R = \frac{r}{l} R_{sq} = \frac{d \cdot 2 \cdot acosh^2(|\alpha|)}{r\varepsilon_0 \varepsilon'_2 \omega l} \tag{56}$$

$$|Z_{C1}| = \frac{1}{(l/r)\omega C_1} = \frac{r \cdot A}{\varepsilon_0 \varepsilon'_1 \omega l d} \tag{57}$$

where r denotes the radius, l denotes the lens depth, ε'_1 and ε'_2 denote the LC real permittivity parallel and perpendicular to the glasses, respectively, and A is a parameter that depends on fringe field effects and is related to the dimensions of the electrode and the lens diameter. In the modal limit, the resistance from the high resistivity layer is equal to the capacitor impedance. The radius that corresponds to this limit is given below.

$$R = |Z_{C1}| \Rightarrow \quad r_{CRIT} = d \cdot acosh(|\alpha|) \sqrt{\frac{2 \cdot \varepsilon'_1}{\varepsilon'_2 \cdot A}} \tag{58}$$

The exact solution of this formula requires that the molecular position be known. This position can be estimated using the Frank Oseen equations and an iterative algorithm. If the phase profile is a constant, the relation $\varepsilon_1/\varepsilon_2$ is also constant, and an approximated solution can be obtained. All of

the molecules in the quadratic range of the birefringence are at a certain angle to each electrode thus, the mean molecular position can be considered $\varepsilon'_1=0.7\Delta\varepsilon'+\varepsilon'_o$ and $\varepsilon'_2=0.3\Delta\varepsilon'+\varepsilon'_o$ [51]. A high resistivity layer is required when the lens radius is larger than r_{CRIT}. However, if the lens radius is smaller than r_{CRIT}, the LC impedance dominates the electric gradient, and a high resistivity layer is not required for manufacturing the devices. In this case, a suitable gradient can be achieved using the fringe field effect if the thickness follows the relationship given in Eq. 58. Thus far, this relationship has only been investigated experimentally. In this thesis, an analytical expression has been developed for the first time for the aforementioned relationship in terms of simple functions.

Hole-Patterned Microlens

As discussed above, Eq. 58 shows the limiting condition at which the resistance of the high resistivity layer equals the LC inherent impedance (Z_{C1}). Without a high resistivity layer, the voltage is distributed by the capacitor, C_1, thereby simplifying the ECC. Using Eq. 54, the thickness (d) can be related to the diameter ($2r$) as follows:

$$\Psi = \frac{C_2}{C_1} = \frac{\varepsilon'_2/d}{\varepsilon'_1 d/A} \Rightarrow \frac{r}{d} = acosh\left(|\alpha|\right)\sqrt{\frac{\varepsilon'_1}{\varepsilon'_2 \cdot A}} \tag{59}$$

This equation is essential for LC microlens manufacture, because it provides the key dimensions required to design generating phase gradients similar to those in conventional lenses (without shrinkage or plateau defects). The results from Eq. 59 are compared (Figure 27) with those obtained using the finite element method (FEM) to solve Poisson's equation:

$$\nabla \cdot (\varepsilon \nabla V) = \rho \tag{60}$$

where ε is the anisotropic dielectric coefficient, and ρ is the space charge density (which is zero in this case).

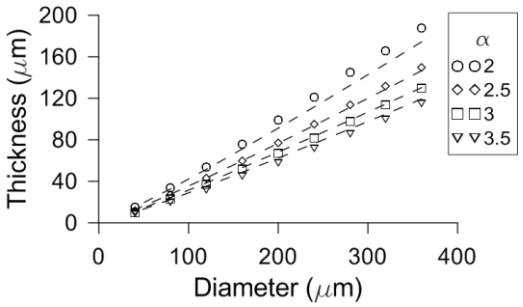

Figure 27. Relationship between the thickness and the diameter for different gains (α): the FEM simulations are shown as symbols and Eq. 59 results are shown as a dashed line.

The results of the developed equation are in fair agreement with the FEM estimates. This demonstrates that the component C_1 of the EEC is a good approximation to the fringe fields effects produced in this type of structures.

2.2.3. Results of the electrical model

Some simulation examples illustrate the voltage across the lens diameter for two LC lenses. The first one is designed to work with a hole-patterned electrode configuration and the second one to work with modal control. Both lenses have different constructive parameters that are designed following the theories proposed before. All of the theoretical results from the proposed model are experimentally demonstrated in section 5.2.2.

Firstly, for the hole patterned lens a specific application was chosen to validate the developed theory: a LC-based autostereoscopic display for a mobile application. Considering the MDA-98-1602 and following the theory proposed in section 2.1.3 the Kerr effect (which is also known as the quadratic electro-optic effect) was observed for the simulated birefringence result from approximately $1.3V_{RMS}$ to $3\ V_{RMS}$ (see section 4.1.1, Figure 48). Then the protocol requires that α = 2.3 to avoid undesirable effects. To satisfy the requirements of the autostereoscopic application, a cylindrical lens array for a 200 PPI display, W_1 = 254 μm. Other parameters are W_2 = 20 μm and A = 2.1494 (Eq. 39). For a 3D distance of 25 cm, an interpupilar distance of 65 mm and a pixel pitch of 127 μm, the necessary focal length is 0.48 mm (from geometrical optics, see section 5.1, Eq. 69). The value of the LC birefringence (in the quadratic range, Δn =0.1595) and the focal length determined a LC layer thickness of 105 μm (section 5.1, Eq. 68). Thus, following Eq. 58, a high resistivity layer would be necessary for a radius greater than r_{CRIT} = 189 μm (ε'_1 = 12.7 and ε'_2 = 7.9, Eq. 52); that is, lenses with radii of 127 μm do not require modal control. A high resistivity layer is not required for the specifications. Checking Eq. 59, the ratio between the hole diameter (D = 2r) and the thickness (d) yielded D/d = 2.55. A resulting thickness of 99.5 μm indicates that the phase profile will not have defects.

The graphs of Figure 28 (a) and (b) correspond to the voltage distribution of case 1 and case 2, respectively. The parameters are:

- Distance between electrodes (W_1): 254 μm; thickness d = 100 μm.
- No high resistivity layer.
- Real permittivity real (ε') = variable depending on voltage (see 2.2.1).
- Imaginary permittivity (ε'') = variable depending on voltage (see 2.2.1).
- Rest of components following Eq. 40 and datasheet of MDA-98-1602 from Merck, Δn = 0.2666@589.3nm (n_e = 1.7779; n_o = 1.5113) y $\Delta\varepsilon$ = 12@1kHz (ε_e = 16.2; ε_o = 4.3).

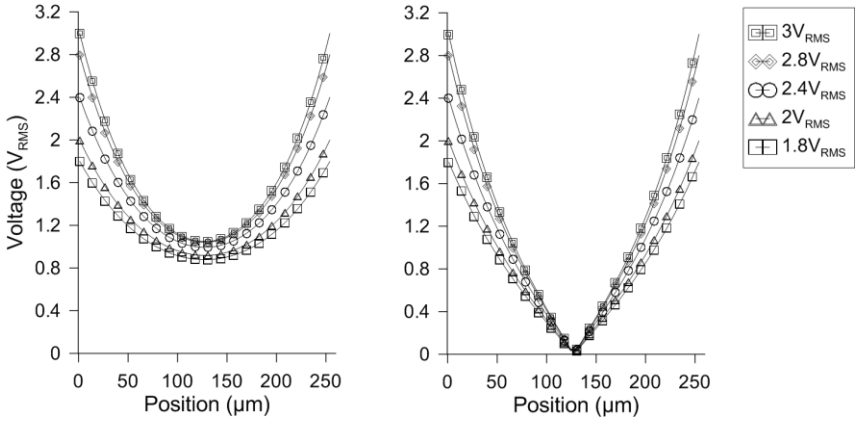

(a) Case 1, electrical phase shift: 0°. **(b) Case 2, electrical phase shift: 180°.**

Figure 28. Voltage distributions across a LC lens diameter for hole-patterned scheme.

Three relevant features are deduced from these results. Frequency dependence of the voltage distribution is barely relevant, over two decades (100 Hz – 10 kHz), for hole-patterned arrangements. This statement is more precisely expressed if it is detailed that the permittivity dispersion has little changes in this range. Another simulation outcome is how the voltage is maintained in case 1 at the center of the active area. This is observed because the permittivity change with voltage and anisotropy are considered by using the parameter p (Eq. 52). For example, the value of p is 0.88, 0.84, 0.78, 0.73 and 0.7 for 1.8, 2, 2.4, 2.8 and 3 V_{RMS} respectively. The third relevant feature is a zero crossing voltage that appears in case 2 at the center of the active area when an inverse driving voltage is applied between electrodes [case 2, Figure 28(b)] and frequency independent. This performance suggests the proposal of a configurable device for a feasible application that switches between lens- and prism-like voltage profiles.

For the modal case, the same application is chosen. In this case, the pixel pitch of the OLED display (285 μm) determines W_1 (570 μm). Other parameters are W_2 = 10 μm and A = 3.6751 (Eq. 39). For a 3D distance of 30 cm, an interpupilar distance of 65 mm and a pixel pitch of 285 μm, the necessary focal length is 1.3 mm (see section 5.1, Eq. 69). Considering the maximum value of the LC birefringence and the focal length determined, a LC layer thickness of 117 μm (section 5.1, Eq. 68) is necessary. Following Eq. 58, r_{CRIT} = 150 μm (ε'_1 = 12.7 and ε'_2 = 7.9, Eq. 52). For this reason, lenses with radii of 285 μm require modal control. The value of R_{sq} = 14 GΩ/sq (Eq. 55), this value could be reduce to 1.4 GΩ/sq if a 10 kHz signal is considered.

Two modal samples with the 570 μm pattern were fabricated. One with 90 μm of thickness, close to the designed values, and other with 50 μm of thickness in order to explore the possible defects and validate the simulation program. Unfortunately, the sample of 90 μm was defective and could not be studied. Despite this, the other sample gave important data and has also been used in the autostereoscopic application. For this reason, the theoretical model is done for this sample. Several voltages and frequencies are investigated for case 1 (Figure 29, left) and case 2 (Figure 29, right). The structural parameters are:

- Distance between electrodes (W_1): 570 μm; thickness d = 50 μm.
- R_{sq} = 3 GΩ/sq.
- Real permittivity real (ε') = variable depending on voltage (see 2.2.1). Imaginary permittivity (ε'') = variable depending on voltage (see 2.2.1).
- Rest of components following Eq. 40 and datasheet of MDA-98-1602 from Merck, Δn = 0.2666@589.3nm (n_e = 1.7779; n_o = 1.5113) y $\Delta\varepsilon$ = 12@1kHz (ε_e = 16.2; ε_o = 4.3).

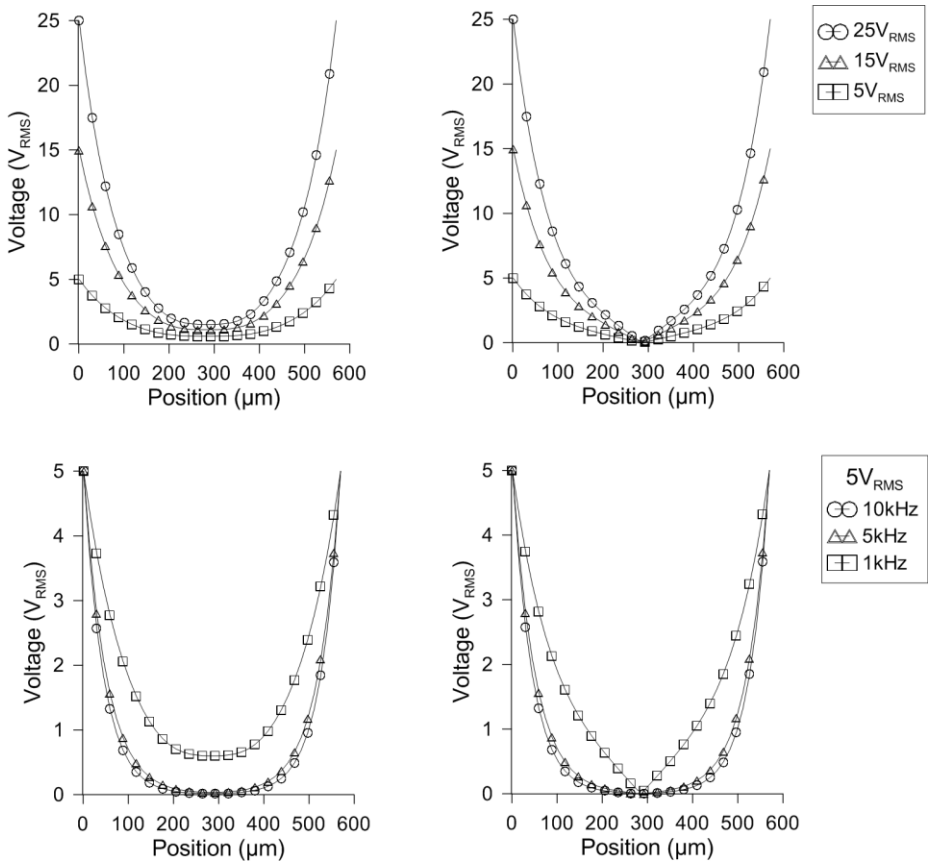

Figure 29. Voltage distributions across a LC lens diameter for modal scheme. Electrical phase shifts between electrodes are considered for electrical signals phase shifted (left) case 1, 0° and (right) case 2, 180°.

In this case, the frequency change a little the voltage profile. As can be observed, the necessary resistivity is too high. For this reason, the use of modal control at micrometric scale has not been reported in the literature. In this thesis, it is demonstrated for the first time modal lenses at micrometric scale by using nanometric metallic layers. The fabrication process is explained in detail in the next section. As commented above, all of the theoretical results from the proposed model are experimentally demonstrated in section 5.2.2.

3. Design and fabrication of micro-optical devices

In this chapter, different aspects of the design of micro-optical phase modulators will be addressed. As commented in previous sections, the design of the electrode pattern is mainly focused on an autostereoscopic application. Modal and hole patterned microlenses are proposed for this application. The fabrication of a modal lens imply a technological challenge at micrometric scale. For this reason, a brief discussion of different technologies to achieve the high resistivity layer is carried out. As original contribution a new manufacturing protocol is proposed to obtain the first modal microlens array. In the case of other proposed micro-optical phase modulators (rotary microlenses or microaxicons) the same electrode pattern is used but the arrangement of the electrodes is changed. The fabrication protocol will also be examined because precision, cleaning, and timing are critical. For this reason, a clean room specifically designed for the fabrication of liquid crystal devices is used (R&D Center CEMDATIC). At the end, a brief review of the fabricated devices is shown.

3.1. Design specifications of the electrode pattern

In this section, the design and fabrication parameters to be taken account of are described. As it was described in section 2.2.2, in order to have a proper phase profile (without shrinking at the sides or phase plateau at center), the microlens array dimensions are required to be in a very specific range. In the case of other proposed micro-optical phase modulators, the arrangement of the electrodes is key.

The design of the electrode pattern is determined by the main application of the lenticular arrays (an autostereoscopic device). Two electrode patterns are designed, one for an OLED autostereoscopic display (128 x 64 pixels) and other to work in a 200 pixels per inch (PPI) autostereoscopic display with 3D tunable distance (most of the mid-range smartphones have pixel densities in the range of 200-300 PPI.). Each lens of the array has been initially studied as an individual microlens. These studies have opened several lines of research:

i) A practical use in *flip* (Figure 30) or autostereoscopic applications.

ii) Comparison of the optical properties with commercial lenticular arrays.

iii) A study of the electro-optical properties of the array to control aberrations.

iv) A study of the electrical properties of the array to sense the temperature.

v) Developing of novel micro-optical phase modulators based on advanced electrode arrangements.

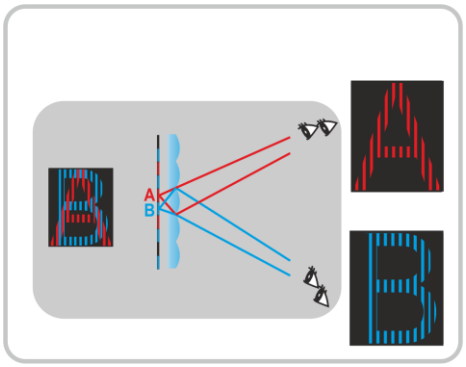

Figure 30. Basic operation scheme of a cylindrical lenticular array in a Flip device.

The main component of the proposed devices is the electrode pattern. In order to obtain this patterns on the ITO (Indium Tin Oxide) coated substrates, a special mask for the photolithographic process is required. For this, a design made with *Autocad* is etched in a Chrome mask of 980 Armstrong thickness, over a 5x5 inch glass sheets. This work is carried out by a Danish company (DELTAMASK). The company specializes in the manufacture of these types of masks and their etchings. Depending on the proposed topology, either one pattern or two in orthogonal position are used. If only one pattern is used, the other substrate is a continuous plane of ITO connected to ground.

Following the lines commented above, the first design pretends to obtain a microlens array to deviate the light in an autostereoscopic device. The prototype has two fundamentals parts: a 2D OLED display to reproduce the interlaced images and the microlens array, based on LC technology, placed precisely on top of each two-column set of pixels. This fact determines the distance between electrodes.

In this case, the proposed display is a commercial monochrome OLED of 1.6". The resolution is 128x64 pixels, the pixel pitch (pixel + interpixel) is 285µm (255 µm + 30 µm). Each microlens is required to have the diameter of two pixels (570 µm). Moreover, the electrode pattern is designed to obtain different configurations with only one device. For this, each pattern consists of a pair of comb-type finger electrodes (Figure 31). This configuration allows the application of different electrical signals as well as the measurement of the voltage at the center of each lens. The applications have been demonstrated to be numerous. For example, cylindrical microlenses are formed between two consecutive electrodes. In this case, the objective is to obtain an optical element capable of generating flip and 3D vision effect [42]. The central voltage can be measured in order to control the real phase profile. Also, a control over temperature changes in the autostereoscopic device can be estimated [33]. In addition, two different diameters are possible with only voltage control. If two voltages are applied ($V_1 = V_2$) the diameter is half of the initial design [49]. This versatile configuration has been used to compare the optical performance of the proposed device with commercial lenticular sheets [78]. The defects observed in these arrays leads to development of a novel electro-optical model for modal LC lenses at micrometric scale [50]. Moreover, the possibility of applying two different electrical signals in each electrode open up endless possibilities (by using different harmonics or complex electrical signals).

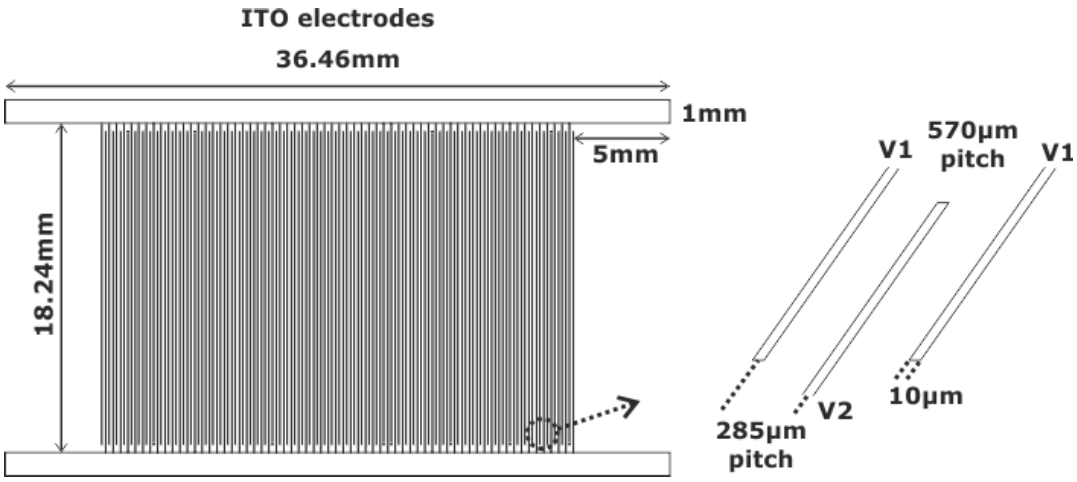

Figure 31. Electrode pattern consisting of a pair of comb-type finger electrodes for autostereoscopic device.

In addition, in a second line of action a design and fabrication of electrodes patterns with the size of 100 LPI lenticular sheets is carried out (Figure 32). In this case, the lens diameter is 254 µm for each lens (100 LPI) or 127 µm if both comb-type finger electrodes are used. In this second line of action two types of arrays are fabricated, with and without high resistivity layer. The arrays could work both in 200 PPI and 400 PPI displays. As commented in section 2.2, the voltage distribution is modeled [51] and new analytical expressions for designing LC microlenses are developed and experimentally demonstrated [52]. These equations determine for the first time a theoretical limit that stablishes whether a high resistivity layer might be necessary (based on the structural parameters). It also determines analytically the relation in hole patterned lenses to have perfect phase profiles (without shrinking at the sides or phase plateau at the center). One of the proposed applications has been a tunable LC cylindrical micro-optical array for aberration compensation [43]. When hole patterned arrays are used in an autostereoscopic application, the temperature can also be controlled [34]. As it is demonstrated in section 5.2.3, a complete tunability of the 3D distance could be achieved.

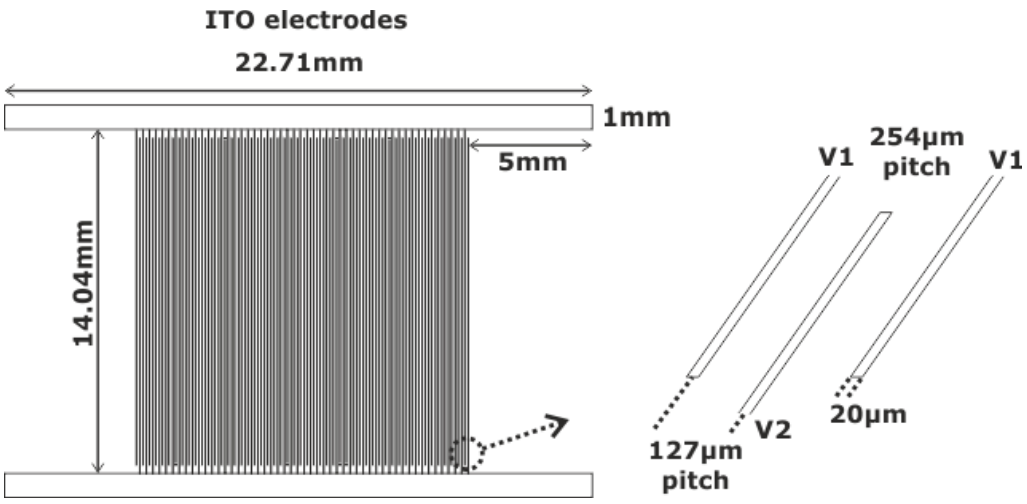

Figure 32. Electrode pattern consisting of a pair of comb-type finger electrodes for 100 LPI device.

Finally, the third line of action takes advantage of the designed electrode pattern in the second line. Following the results obtained in a research stay at Durham University [46], the ground substrate is replaced by another comb-type finger electrode. In this case, the two substrates are placed in orthogonal position with respect each other. As with previous lines of action, the devices are fabricated with and without high resistivity layers. In the first case, by using a specific phase shift between electrodes a micro-axicon array is obtained [44]. When no high resistivity layer is used, a cylindrical LC microlens array with rotary axis and tunable capability is demonstrated [45].

It is worth mentioning that the deep knowledge of the LC physic modelling has opened up other lines of research in the generation of optical phase modulators based on LC. For example, LC lensacons, logarithmic and linear axicons [48] or micro-optical phase modulators for low voltage and high transmittance blue-phase LCDs [167].

3.2. High resistivity layer in modal devices

The value of the resistivity can be obtained following the theories proposed in this thesis (see section 2.2.2). Specifically, the array dimensions determine whether or not a high resistivity layer might be necessary. As it was theoretically demonstrated, the required resistivity of the high resistivity layer at micrometric scale is very high (GΩ/sq). These values are not common and imply a considerable research effort. To date, different materials have been employed as control electrodes; for example, titanium oxide (TiO_2), PEDOT:PSS [Poly(3,4-ethylenedioxythiophene) poly(styrenesulfonate)], and thin layers of ITO have been reported. Problems arise due to the not high enough resistivity; these materials are limited to diameters larger than 1 mm. The resistivity in these materials is approximately 1–10 MΩ/sq, which is too small to achieve a proper voltage distribution in micrometric devices.

Some of the materials described in the literature have been used in the some devices proposed in this thesis (e.g. PEDOT:PSS or TiO_2). Despite this, their use have been demonstrated to be only valid when phase shifted electrical signals are used (see chapter 6). In order to generate microlenses, the search for a novel material, transparent and with high resistivity, is necessary. In this thesis, a new manufacturing protocol based on a set of two layers (a dielectric layer of SiO_2 and a metallic layer of nickel) for lenses with modal driving has been reported for the first time. This compound is made of a metallic material. Despite the fact that these kinds of materials are

conductive, there are several studies in the literature indicating a dramatic decrease of this parameter at nanometric scale. Specifically, the research of metallic layers at nanometric scale is a hot research topic [168], [169].

In this thesis, the material under study is Nickel (Ni). In order to compare with previous studies, [170], [171], an analysis of the resistivity in test samples has been made by using the very definition of sheet resistance (the resistance of a material when it has the same length and width). To measure "ohms per square", pieces of the sample with square surface have been prepared. A special design is patterned in the ITO coated substrates by low-resolution photolithography (Figure 33). Some square areas that are measured are colored red in Figure 33.

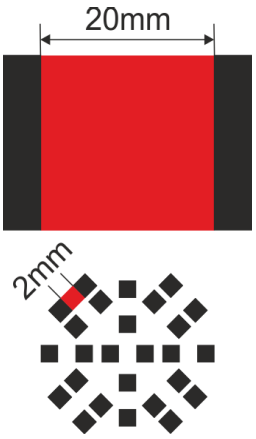

Figure 33. Designed masks to measure the sheet resistance. The side of the squares is (top) 20 mm and (bottom) 2 mm.

A high resistance meter Model HR2 (AlphaLab, Inc) is used to measure the samples. The Model HR2 meter measures resistance in nine ranges from 1 Ω to 1.9999 TΩ, and conductance in a single range of 0.00 to 199.99 pS (pico siemens, or pico mhos), all at low voltage of < 2 V across the sample. Basic accuracy is ± 2%.

The sheet resistance as a function of the deposited thickness is shown in Figure 34. This result is compared with two previous studies of Lienhard *et al.* [170], and Giurgola *et al.* [171]. As can be seen, in order to obtain high resistivity (~GΩ/sq) an approximated thickness of 65Å is necessary. In this scale, the errors are considerable so this value is a preliminary approximation.

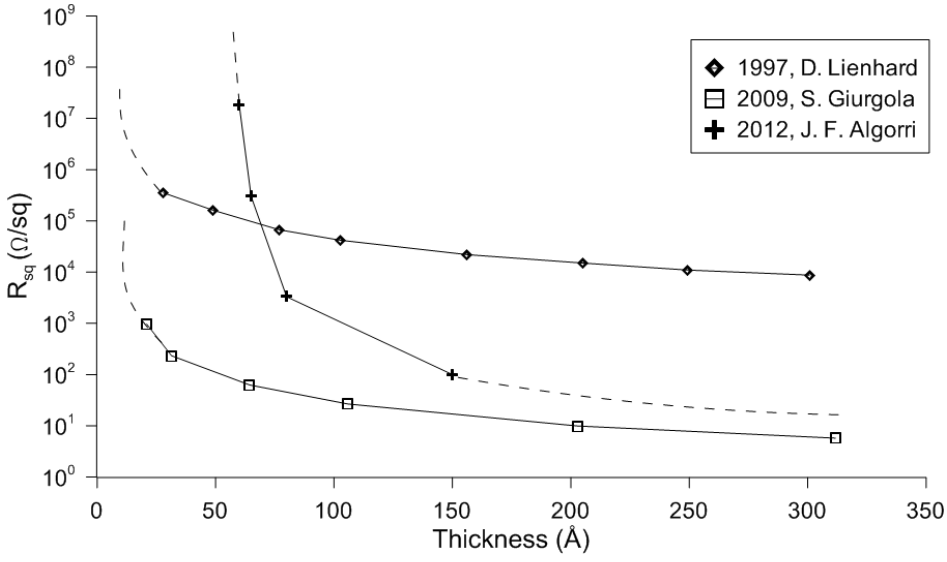

Figure 34. Comparative between measured sheet resistance and other studies.

Differences between graphs are due to the type of substrate used in each study. The measurements of these layers reveal three different stages. For thick films (> 1000 Å), essentially bulk electrical properties are measured (the resistivity value converge to $\rho \infty 6.4 \cdot 10^{-8}$ Ω·m). In the range of hundred Angstrom, an increased resistivity is observed. This can be interpreted in terms of

a shortened mean free path for the electrons arising from the small thickness dimension. The last stage, in the thickness range of a few to several tens of Angstroms, the resistivity is increased drastically. Bearing in mind that an atom of Nickel has a diameter of 1.25 Å, layers with an approximate thickness of 50 Å include only about 40 rows of atoms. There are in-homogeneities on the deposition creating a roughness surface (like islands). Some of this roughness are even higher than a few rows of atoms [172]. Several studies have demonstrated that these islands are caused by the metal's function of Nickel [173], [174]. Because of this, the first sputtered atoms tends to group in islands separated from each other. This physical phenomenon produces the drastic increasing in resistivity for a specific thickness, known as percolation limit. This concept has emerged as the result of research on fluids through porous mediums. In recent years, this concept has been used in electronics to model the electrical current through a random net of resistances (Figure 35). Some researchers model the percolation limit in metallic layers as a net of resistances and capacitors (where the islands are not connected) [175]. In summary, we conclude that Nickel can be high resistive. Despite this, the deposition of a specific thickness is very difficult to achieve.

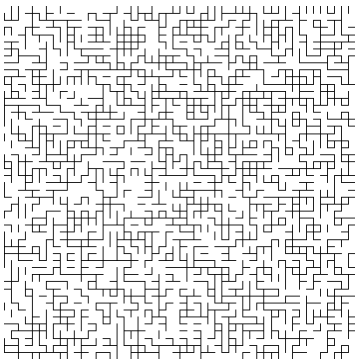

Figure 35. Percolation mesh.

As commented above, the necessary sheet resistance is too high. In order to achieve this value by using Nickel the percolation limit has to be reached. Another option is the use of amorphous Silicon (instead of SiO_2). As it is reported in ref. [176], when a layer of amorphous Silicon is sputtered with Nickel and then is crystallized (with high temperature), the sheet resistance reaches GΩ/sq [177].

Another material that could be used is graphene [178]. The use of this material is of topical importance. Layers of reduced graphene oxide with a sheet resistance of 19MΩ/sq have been reported. Alternatively, we propose the usage of materials with high permittivity to replace the high resistivity layer. These ideas have to be further investigated.

3.3. Fabrication of micro-optical devices

In this section, the fabrication protocol is explained in detail. Given the specific characteristics of the electrode pattern (micrometric size), the use of a clean room (class 100) is required (Figure 36). This denomination includes areas with no more than 100 particles higher than 0.5 μm per cubic feet of air (approximately 3600 particles per cubic feet). All devices performed in this work had been manufactured in a clean room which is property of "Centro de Materiales y Dispositivos Avanzados para TIC" (CEMDATIC) of "Universidad Politécnica de Madrid" (UPM). The fabrication protocols must be strictly followed in order to obtain repeatability in the experiments. Each process requires different cleanliness levels. For this reason, the clean room is divided into different working areas in terms of processes (clean or contaminants) to be undertaken. Thus, it has been divided into four zones, each with three dissimilar cleaning environments. The first area is used as a dressing area for special clothing (mask, latex gloves, head cap, bootees and UV light goggles, when necessary). The dressing area is kept at a lower pressure than the semi-clean room, which in turn is lower than in the clean area. The second area (semi-clean), is used for processes that need no clean environment or contaminant processes (e.g. wet etching, developing, etc.). Finally, the clean area is divided into two spaces. One small chamber, which is equipped with a

special plastic dust protection cloth, is used for the cleanest processes. The chamber also feature laminar vertical air flow modules Telstar 900 assembled with HEPA filters providing a nominal cleanliness class 100. The zone outside the chamber is used for clean processes that might generate particles, (e.g., rubbing).

Figure 36. Inside view of the clean room (class 100). New facilities of CEMDATIC (UPM). This is the most controlled area where high critical processes are carried out.

Briefly, the fabrication process begins with photolithography. Once this task has been achieved, the glass is cut as needed. The pieces of glass are then cleaned by an ultrasonic bath. After this, different layers are evaporated (SiO_2, Ni) or deposited (PEDOT, polyimide). The polyimide layer is rubbed to produce alignment in the LC molecules. With the two substrates the cell is mounted (separating them by using UV curable adhesive with spacers, or Mylar, and in some cases Gasket). Finally, the LC is filled by capillarity. In the next sections, these processes are explained in detail.

3.3.1. High resolution photolithography

To manufacture the proposed devices, a Glaston polished glass (supertwist quality) with thickness 0.7mm and a 125nm layer of Indium tin oxide (ITO) is used. The ITO layer is a transparent electrode (80-90%) whose surface resistivity is 20 Ω/sq. These sheets of glass come in sizes of 40x40 cm. Therefore, a cutting process is necessary.

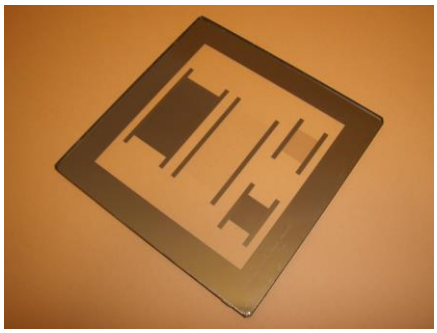

Figure 37. Chrome mask.

For the photolithographic process, UV light is used to transfer a designed pattern from a photomask (Figure 37) to a light-sensitive chemical photoresist on the substrate. Depending on whether the photoresist is positive or negative, the exposed material is degraded or stabilized, respectively. In this thesis, positive material is always used. In these

photoresists, exposure to the UV light changes the chemical structure (a de-polymerization) so that it becomes more soluble in the developer. Photoresist is distributed over substrate surface using a spinner (EC101D-R485 of Headway Research, Inc.). The spinner has rotation speeds of up to 10,000 rpm and a maximum diameter of 9.5cm (Figure 39 left).

The process begins with the photoresist deposition. The small size of the electrodes requires the inclusion of additional layers. A microposit adhesive (Microposit Primer, Shipley Far East Ltd.) is deposited over the whole substrate surface by a pipette. This layer is distributed by spinning (5'' speed ramp and 35'' at 4500 rpm). This layer prevents in-homogeneities in the photoresist distribution. Then, by using a syringe the photoresist (Microp. Photores. S1805 TMG2, Shipley Far East Ltd. Japan) is collected. The needle is replaced with a filter of 0.45μm (Millipore Millex filter 450) that filter out particles larger than 0.45μm. When the photoresist is deposited over 2/3 of the substrate the spinning starts (5'' speed ramp and 35'' at 4500 rpm). After spinning, the photoresist is prebaked in the hot stage at 90ºC for 30 minutes (Figure 39 right). In this step, the photoresist polymerizes. UV exposure process is performed in the mask aligner OAI Hybralign Series 400 (Figure 38).

Figure 38. Mask aligner (Hybralign 400 de OAI): positioning and UV insolation platform.

This device consists of a 500W UV lamp (high pressure mercury lamp). After this lamp has reached the optimum temperature the protocol to follow is:

- The ITO glass (with photoresist) is placed on the platform, where it is held by vacuum.
- The chrome mask (Figure 37), previously cleaned and dried, is placed over the frame, firmly attached to an additional piece.
- The ITO glass is aligned with the mask to print the patterns in the glass.
- With the frame down and fixed, it is allowed to move the ultraviolet exposure area.
- The insolation begins automatically and takes 30''. Special goggles are required.

In the developing stage, the insolated photoresist is removed. This stage is the most difficult step in the photolithographic process. The optimal developing time is obtained after several trial-error tests. This time is inversely proportional to the illumination of photoresist and directly proportional to its thickness. Insolated substrates are introduced in a bucket full of developer (Microposit Developer, Shipley Far East Ltd. Japan). The remaining developer is eliminated with distilled water. After this, the substrates are dried using a pressurized N_2 gun and placed in a hot stage 30' at 110º. Thus, the photoresist is hardened by protecting the electrode from the acid attack.

Figure 39. *Spinner* and hot stage.

In the last stage, a wet etching process is carried out. By using a chemical-corrosive attack the unprotected ITO areas are removed rendering the final electrode design. The bucket is filled with 50% of water (H_2O), 1% of nitric acid (HNO_3) and 49% of (HCl). In this case, the optimal time is also obtained after several tests. This time is dependent on the ITO thickness and the correct proportions of the chemical mixture. Temperature and soaking times are optimized to 65ºC and 35s respectively. After this time, the substrates have to be rinsed in water fast enough to prevent the acid mixture from undercutting the photoresist layer. Once the ITO has been attacked, the remaining photoresist is removed by using a solvent liquid (Microposit Remover). Special care is needed in this step to avoid the removal of ITO. Finally, the substrates are cleaned with water and dried using a pressurized N_2 gun. The substrates are ready for the next stage.

3.3.2. Deposition and evaporation of high resistivity layers

Three kinds of materials are used as high resistivity layers. One of them is developed at Durham University by coating glass substrates with TiO_2 films (11-14MΩ/sq). The other material is PEDOT:PSS. Several samples have been tested at CEMDATIC. It is difficult to obtain homogeneous layers with this material. The deposition process has been optimized. The mask of Figure 33 (bottom) has been used to test the resistivity and homogeneity. The measured square resistance ranges from 7 to 14 MΩ⁄sq for spinner speeds of 3,000 and 4,500 rpm, respectively (30''). The best homogeneity is observed for the higher speeds. The obtained resistivity are not high enough for some applications. For this reason, the research on a novel material is required.

Figure 40. Evaporation equipment and external display which shows the growing speed and thickness.

As an original contribution, in this thesis the use of metallic layers in modal devices has been proposed. Two kinds of samples have been developed. Some samples are previously coated with a 250Å layer of SiO_2. This one prevents ion leakage from the substrate glass and reduces the risks of short-cuts. Moreover, it increases the homogeneity of the deposited layer of Ni. The devices without SiO_2

have shown a reduced resistivity for the same thickness of Ni. As can be seen in (Figure 34) the percolation limit is higher than in other studies. The effective layer of Ni is possibly thinner than programmed in the evaporation equipment. This can be explained by a penetration of some atoms of Ni in the SiO_2 layer.

For these reasons, the protocol of choice is SiO_2 + Ni. The Ni layer is deposited on top of the SiO_2 layer. In section 3.2 high resistivity for layers thinner than 60Å has been demonstrated. All of these layers are deposited by Physical Vapor Deposition (PVD). For this, a Telstar Vacudel 300 equipped with a vacuum system consisting of a turbo molecular pump Alcatel TMP5400 supported by a rotary pump Telstar Torricelli RD-18 (Figure 40) is used. This equipment has been modified so that the distance between the source and the target is about 75 cm. In this way, the incidence angle of the evaporated material is almost constant along the sample and the deposition is more homogenous. By applying an electric current of 115 A an evaporation speed of 1 Å/s is achieved. This speed is low enough to assure a correct deposition. Some other factors have to be taken into account, time between depositions or caution in the storage of the evaporated samples. The resistivity could be increased as the Ni layers oxidize.

3.3.3. Alignment protocol

The alignment of the LC molecules inside the devices is a crucial issue. The molecular alignment avoids domains or discontinuities in the orientational order, which can cause dispersion in the light passing through the sample. To obtain the alignment a special treatment (either physical or chemical) is carried out.

Organic materials such as Silane (SiH_4) induce vertical alignment, known as homeotropic. Other methods include the use of inorganic materials such as SiO_x or SiO_2 [179]. The advantage of use inorganic materials over organic materials as alignment layers is their toughness towards external causes such as radiation, temperature variation, etc.

Parallel alignment, also known as homogenous, is easier to obtain. An organic material (polyimide or polyamide) is deposited in a substrate and subsequently rubbed. The rubbing process produces microgrooves on the substrate surface, inducing the LC molecules to align in a certain direction parallel to the substrate. Another aligning mechanism is based on shear stress induced on the alignment layer and intermolecular interactions between LC and polyimide. A built-in-house rubbing machine does rubbing process. This device consists of a rotating cylinder covered with a special microfibered cloth and a moving platform. Substrates are placed to be rubbed under the cylinder (Figure 41). Once the two substrates are rubbed, the device is assembled. When the rubbing direction has a certain angle with respect to the other substrate, normally 90º or 270º, molecules form helix type structures. This is known as helical twist and is commonly used in TN LCD. The molecules change its positional direction between layers, producing a similar order

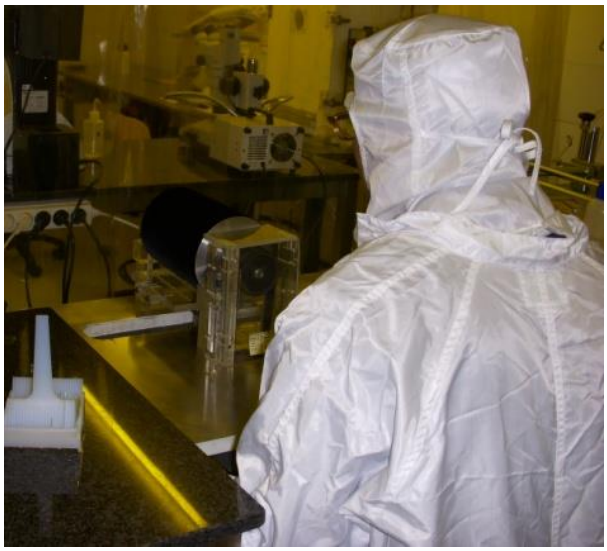

Figure 41. Built-in-house rubbing machine.

than cholesteric. Difference is that in cholesteric the total twist is given by the physical properties of the chiral dopant, whereas in twisted nematic is given by the position of the substrates.

In this thesis, the LC is used as an adaptive phase-only modulator so no twist of the molecules is necessary. For this reason, a planar alignment is used. A polyimide (PIA2000) is deposited over the two substrates. This layer is rubbed in the direction of the electrodes for the upper substrate and in antiparallel direction for the other one. The result is an antiparallel alignment in the electrode direction. With this configuration, the molecules are aligned in the same direction as the used in OLED displays.

The alignment layer deposition follow a similar protocol as photoresist (commented before). In this case, the polyimide is deposited in the spinner. By using the hot stage (Figure 39), additional solvents are eliminated. In order to avoid defects in the deposited layer, this process is done at medium temperature (80º) during 20''. After a curing at 150º (approx. 1h30') the rubbing process is carried out.

3.3.4. Assembling and filling

Depending on thickness, different methods have been used in the assembling process. There are two main techniques: with distributed spacers or without them. In the first case, the spacers are made of silica with cylindrical or spherical shape (0.8 µm, 1.5 µm, 4 µm, 20 µm, etc.).

Spacers are previously mixed with a solvent (ethanol, methanol, ethyl ether, etc.). After a sonication to avoid aggregates, they are deposited by using a spray. When the solvent is evaporated the spacers are homogenously distributed along the substrate. The main disadvantage is the possible defects in the active area. In this case, sealing can be made by using optical glue or gasket. Gasket is a kind of glue cured by heating. Mask designs are fabricated on serigraphic resin frames (15×20 cm^2 stainless steel 400 mesh from Sefar Maissa S.A., Spain) using a CO_2 laser (Epilog Legend Elite). The design consists on a rectangular motif with two apertures (for filling by capillarity). The cured occurs applying simultaneously heat and pressure (0.5 Kg/cm^2), uniformly over the whole cell surface. After assembling, the cell is cured with UV light for two minutes.

Figure 42. Curing by UV light.

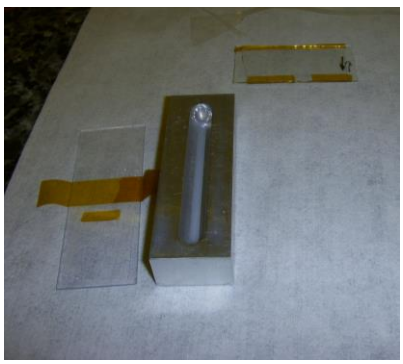

Figure 43. LC in a recipe and sample.

In the case of gasket-only spacers, the substrates are glued with an ultraviolet curing adhesive (Norland 65 or Norland 68) mixed with the spacers. This adhesive is mixed with spacers during 4 or 5 minutes. After this, is deposited around the active area leaving two apertures to fill by capillarity the assembled cell with the LC. Then the adhesive is cured with the UV light during 4 minutes (Figure 42).

For thicker cells (>20 µm), no spacers are available. In this case, transparent sheets of polyester, known as Mylar (Isovolta Group), are used. The available thicknesses are, 25 µm, 50 µm, 75 µm, 100 µm, 125 µm, 250 µm y 350 µm. For

50 µm cells, a polyimide film (Kapton) can also be used. For sealing the optical glue is deposited on top of the Mylar. The Mylar is placed around the active area leaving two apertures. The filling is realized by capillarity. Empty samples are placed in a recipe full of LC (Figure 43). The samples are completely filled in a few seconds (depending on thickness, surface and LC viscosity). Finally, the apertures are sealed with optical glue and cured by UV light.

3.4. Fabricated samples

Based on the same electrode pattern and by using different arrangements, several samples have been fabricated. All of the fabricated samples are filled with MDA-98-1602 from Merck, Δn = 0.2666@589.3nm (n_e = 1.7779; n_o = 1.5113) y $\Delta\varepsilon$ = 12@1kHz (ε_e = 16.2; ε_o = 4.3). It is important to note that other samples have been previously made in order to optimize the fabrication process. In Table 3 a brief summary of the fabricated devices is shown. The surface of the whole active area is indicated in square centimeters (cm^2). The diameter indicates the size of each micro-optical element in the array. The type of material and thickness used as high resistivity layer is indicated in "HR layer thickness". Finally, the reference in which the sample has been used is also shown.

SAMPLE	CODE	PARAMETER				USED IN REF.
		Surface (cm^2)	Diameter (µm)	LC Thick. (µm)	HR layer thickness (Å)	
MONOPIXEL	MONO	4.82	---	6.5	Ni 150	[158]
AUTOSTEREOCOPIC	OLED90NI0	4.82	570	90	0	---
AUTOSTEREOCOPIC	OLED50NI55	4.82	570	50	Ni 55	[180] [181] [50] [42]
HALF AUTOSTEREOCOPIC	OLED90NI0-2	4.82	285	90	0	---
HALF AUTOSTEREOCOPIC	OLED50NI55-2	4.82	285	50	Ni 55	[78]
100LPI	100LPI100NI0	1.78	254	100	0	[43] [51] [52]
100LPI	100LPI50NI0	1.78	254	50	0	---
100LPI	100LPI40NI0	1.78	254	40	0	[34]
100LPI	100LPI40NI60	1.78	254	40	Ni 60	[33]
100LPI	100LPI90NI60	1.78	254	90	Ni 60	---
HALF 100LPI (200LPI)	200LPI100NI0	1.78	127	100	0	---
HALF 100LPI (200LPI)	200LPI50NI0	1.78	127	50	0	[43]

HALF 100LPI (200LPI)	**200LPI40NI0**	**1.78**	**127**	**40**	**0**	**---**
HALF 100LPI (200LPI)	**200LPI40NI60**	**1.78**	**127**	**40**	**Ni 60**	**---**
HALF 100LPI (200LPI)	**200LPI90NI60**	**1.78**	**127**	**90**	**Ni 60**	**---**
OPTICAL ARRAY	**OPTARRAY**	**1**	**500**	**20**	**TiO_2**	[46]
MICROAXICON	**MICROAX**	**1.78**	**127**	**40**	**PEDOT 60-80**	[44]
ROTARY 200LPI	**200LPIROT**	**1.78**	**127**	**50**	**0**	[45]

Table 3. Fabricated samples with good performance.

Firstly, monopíxel (MONO) samples are manufactured; their purpose is the characterization of the electro-optic response of the LC itself. In this regard it has been measured, firstly, its electrical response as a function of the amplitude and frequency of the applied electrical signal. An EEC to model it is proposed. Moreover, its optical response by measuring the dispersion of birefringence is characterized. The remaining samples are used for different applications. For characterization of the microlenses, generation of autostereoscopic images, temperature sensing, control of aberrations, generation of microaxicons, cylindrical lenses with rotary capabilities, etc.

In Figure 44 two samples are shown. The device of Figure 44 (a) is a lenticular array with 100 or 200 LPI; this allows the study of a possible 200 or 400 PPI autostereoscopic display with 3D tunable distance. The electro-optic response will be studied in terms of phase shift profile, focal distance, 3D tunable distance, etc. The Figure 44 (b) is a lenticular device designed for a monochrome 2D OLED display. By using the second comb electrode, a comparison with commercial lenticular arrays similar in size will be carried out. This device will create flip effects on the screen. The autostereoscopic performance has also been studied. However, the requirements to generate flip effect are less demanding. A detailed study of the electro-optical characteristics of these devices is presented in next chapters.

(a) Lenticular array of 100 LPI (100LPI40NI60).

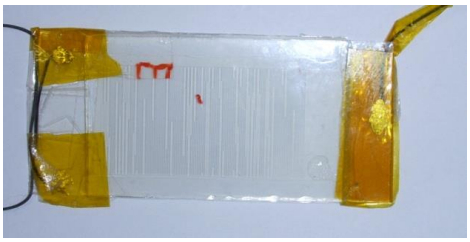

(b) Lenticular array for autostereoscopic device (OLED50NI55).

Figure 44. Some fabricated samples.

4. Electro-optic characterization of nematic liquid crystals

One of the most important things in order to design and manufacture liquid crystal devices is to have a deep knowledge of the liquid crystal electro-optical parameters. Among them, optical anisotropy is determinant. This feature, which can be tuned by an external AC voltage, has been characterized to validate the proposed theoretical modelling of the molecular position. Another important parameter is the dependence of the birefringence with wavelength (dispersion). This parameter determines important characteristics like differences between phase modulations when different wavelengths are considered. Last but not least, the impedance is characterized by electrical impedance spectroscopy. From the impedance measurements and knowing the structural parameters of the liquid crystal sample, the permittivity is estimated. By using these results an equivalent electrical circuit for a broadband frequency (1Hz - 10MHz) is proposed and demonstrated. The values of the dielectric constants when higher voltages are applied are measured by using a Wheatstone bridge. In this case, the solution of the proposed theoretical modelling of the molecular position is also demonstrated. The final result is a detailed electrical model of nematic liquid crystal as a function of voltage (dielectric and optical anisotropy) and frequencies (dispersion).

4.1. Optical anisotropy characterization

As commented in section 2.1.1, one of the most important LC characteristics is its optical anisotropy or birefringence. This feature, which can be tuned by an external AC voltage, has been characterized to validate the presented algorithm in section 2.1.3. Another important parameter is the dependence of the birefringence with wavelength (dispersion). This parameter determines important characteristics as the difference between the phase modulation when different wavelengths are considered. In the case of LC lenses, dispersion affects the focal length.

In this section the optical anisotropy of the nematic LC is studied. The experimental results are compared with the theoretical modelling. The experimental set-up is depicted in Figure 45. This set-up is based on the transmittance produced by the LC when is placed between crossed and parallel polarizers (see Figure 18). The components of the set-up are:

- An AvaSpec-128 Fiber Optic Spectrometer of Avantes. It is made of 128 photodiodes (128 pixels). The spectrometer works in a range of 360 to 890 nm (visible range); resolution is 4 nm.
- The LC sample is MONO (Table 3). The nematic LC used is MDA-98-1602 from Merck, Δn = 0.2666@589.3nm (n_e = 1.7779; n_o = 1.5113) y $\Delta\varepsilon$ = 12@1kHz (ε_e = 16.2; ε_o = 4.3).
- AC square signals of 1 kHz are applied. The amplitude range from 0.1 V_{RMS} to 6 V_{RMS}; the resolution is 5 mV_{RMS}.

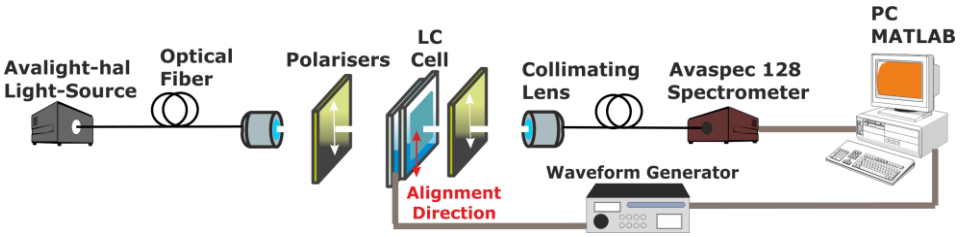

Figure 45. Experimental set up for transmittance measures. In this case, between parallel polarizers.

As it was demonstrated in section 2.1.1, optical transmittances between parallel ($I_{||}$) and crossed polarizer ($I_{\perp}$) are determined from Jones matrices (Eq. 14 and 15). From previous equations it can be deduced the phase retardation for a specific wavelength (Eq. 61).

$$\phi = \begin{cases} N_m\pi + ar\cos\left(\dfrac{I_{||} - I_{\perp}}{I_{||} + I_{\perp}}\right) & N_m = 0,2,4,6,... \\ (N_m + 1)\pi + ar\cos\left(\dfrac{I_{||} - I_{\perp}}{I_{||} + I_{\perp}}\right) & N_m = 1,3,5,7,... \end{cases} \quad (61)$$

where N_m is the number of maximums and minimums in the transmittance profile. The transmittance profiles are processed by MATLAB, particularly concerned with the calculus of the phase as a function of voltage following Eq. 61. The result is a set of birefringence values as a function of voltage (optical anisotropy) for various wavelengths (dispersion).

4.1.1. Birefringence as a function of voltage: Optical anisotropy

Given the proposed equations and the measured transmittance, the phase retardation is obtained. As an example, Figure 46 depicts the measured transmittance produced by the set-up of Figure 45. For the estimations, the following considerations are taken into account:

- ✓ The minimum value of phase retardation (ϕ) is produced at higher voltages.
- ✓ As the applied voltage is reduced the phase retardation increases.
- ✓ At the first crossing between $I_{//}$ and $I_{\perp}$ the argument of the arccosine is equal to zero and the phase retardation is $\pi/2$.
- ✓ If voltage continues decreasing, when $I_{\perp}$ reach the maximum value (which corresponds with the minimum of $I_{//}$) the argument of the arccosine is equal to 1 and the phase retardation is π.
- ✓ At this point N_m is 1. The phase retardation in the next crossing is $\pi + \pi/2$ and in the next maximum of $I_{\perp}$ is 2π.
- ✓ For further N_m the same process is done.

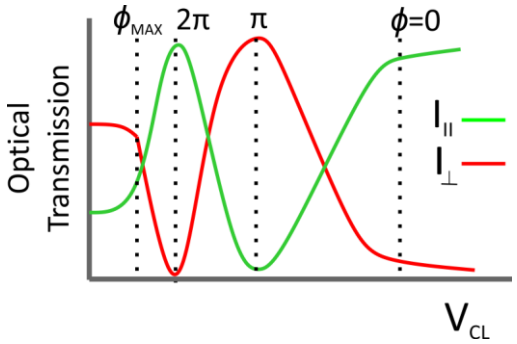

Figure 46. Depiction of the optical transmission of a LC simple between crossed polarizers, $I_{\perp}$ and parallel polarizers, $I_{||}$ as a function of voltage.

The automated process of the measurement and estimation of the birefringence is done by a specific software tool programed with MATLAB. From the phase retardation and considering Eq. 7 the value of the birefringence is obtained. The program apply the process commented above and interpolate the results to give a smooth curve.

When the voltage is increased the birefringence tends to zero. The reason is the perpendicular position of the molecules. The effective refractive index approach to the ordinary value. For voltages below the threshold, the molecules align parallel to the substrate, the effective refractive index tends to the extraordinary value making higher the birefringence. At this point, the dispersion is also higher.

For example, for three characteristic wavelengths of the visible spectrum (λ_R = 600 nm, λ_V = 550 nm y λ_B = 470 nm), the dispersion of the LC for the three RGB primary colors can be estimated (Figure 47). This result is very useful for future considerations of devices working with commercial displays (as 3D applications), depending on the wavelength different focal lengths are obtained. For this reason, dispersion is studied in next section.

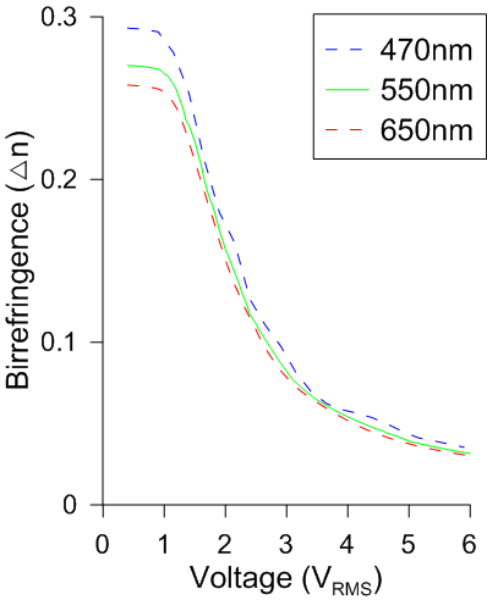

Figure 47. Birefringence as a function of voltage for three different wavelengths.

Simulations of birefringence as a function of voltage

As commented in section 2.1.3 an algorithm has been developed to know the direction of the LC molecules for a specific applied voltage. The theoretical estimations also use MDA-98-1602 enabling the comparison between experimental and theoretical results. By using this program and considering Eq. 3, the effective refractive index is known. Then the mean value of the effective refractive index of the molecules contained from one substrate to another (from 0 to *d*) is estimated by using Eq. 62.

$$\left\langle n_{eff} \right\rangle (V) = \frac{1}{d}\int_0^d n_{eff}(V,z)dz \tag{62}$$

Following this equation, the birefringence as a function of voltage is determined. The voltage dependence of the effective birefringence of a monopixel cell, with the same characteristics as the experimental set-up, is simulated following the proposed algorithm. Experimental birefringence profile is obtained, for the same wavelength as used in the datasheet (589.3 nm), using the procedure described in section 2.1.3. Figure 48 shows the comparison between the simulated and experimental results of the LC cell birefringence.

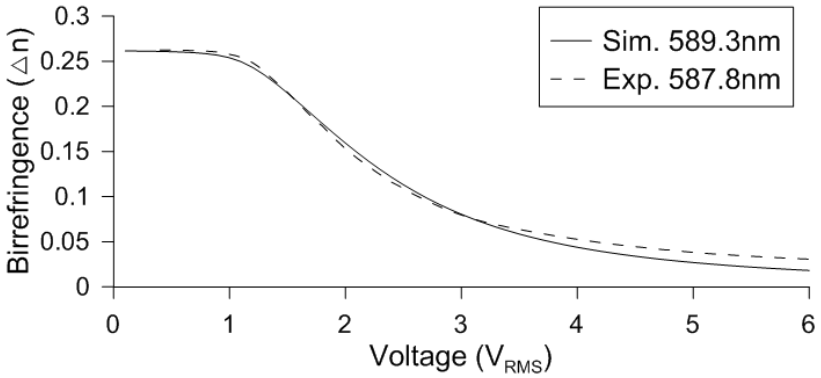

Figure 48. Simulated and experimental birefringence as a function of voltage.

Upon comparing experimental data to those obtained in simulation, extremely close results are found. For high voltages birefringence tend to zero due to the perpendicular position of the molecules with respect to the cell surface. When the voltage is lower than the threshold the molecules are aligned parallel to the surface and the birefringence is the highest. The model shows a small discrepancy for high voltages mainly caused by convergence problems when the angle tends to zero. Notwithstanding, these similar results validate the proper operation of the proposed algorithm. These simulations can be easily extended to other experimental devices where voltage distribution is known.

4.1.2. Birefringence as a function of wavelength: Dispersion

As commented above, dispersion is a critical parameter in LC display related applications. The dispersion is characterized at 0.35 V_{RMS} (when it has the maximum value). The wavelength ranges from 530 nm to 880 nm. The result is shown in Figure 49. As can be seen, the higher the

wavelength the lower the birefringence (it is also observed in Figure 47). This result is compared to the parameters obtained through datasheet from Merck Δn = 0.2666@589.3. The measured value is Δn = 0.2605@587.8, very close to those of datasheet. The lower value can be caused by the angle produced by the alignment layer (4º - 5º).

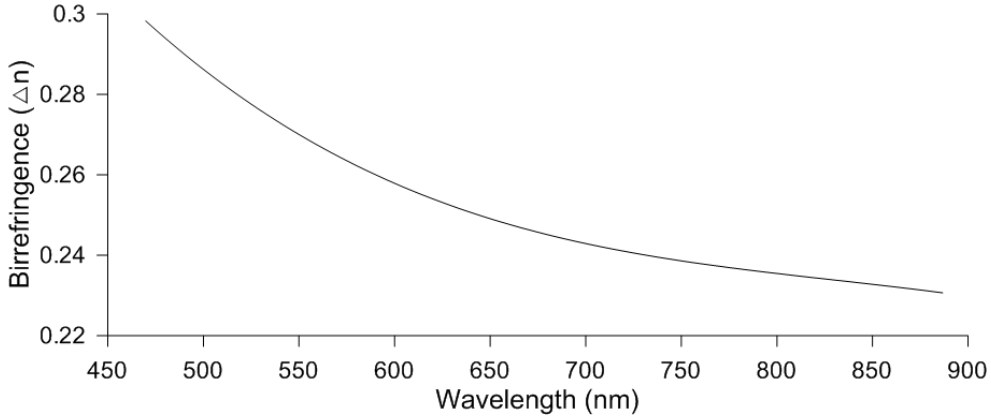

Figure 49. Birefringence dispersion at 0.35V.

This measured tendency is very common in nematic LC. From this parameter the value of the extraordinary refractive index can be estimated ($n_e = \Delta n + n_o$).

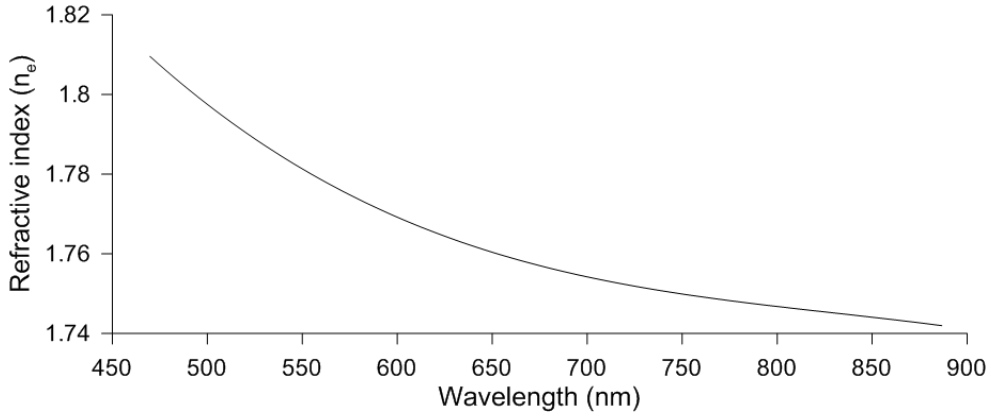

Figure 50. Extraordinary refractive index dispersion.

This tendency is usually modelled by different equations. One of the most accepted model use the Cauchy equations [182]. The dispersion is characterized by the following equation,

$$n_i(\lambda) \cong A_i + \frac{B_i}{\lambda^2} + \frac{C_i}{\lambda^4} \tag{63}$$

Following this model, the Cauchy coefficients for the extraordinary refractive index of MDA-98-1602 are obtained. The fitting gives A = 1.728 B = $1.036 \cdot 10^{-14}$ and C = $2.477 \cdot 10^{-27}$. This parameters are very useful in order to model the behavior of the LC in different simulations.

4.2. Permittivity characterization

As commented in section 2.1.2, another important parameter characterizing the LC properties is the permittivity. As any electrolyte nematic LC suffers different relaxation times in the dielectric constants. This fact complicates the modelling of nematic LC. In order to determine the complex permittivity as a function of the applied frequency, a previous analysis by using EIS is necessary. This effect has to be known in order to avoid undesired responses in the modelling.

As has already been stated, nematic LC behaves like an electrolyte: a capacitor in parallel with a conductance (dielectric losses caused by ionic impurities). This material is sensible to the module of the applied electric field. When an alternating electric field is applied, a polarization is generated; this one is dependent on the geometry, dielectric constant and electric field. This fact is key in order to modify the birefringence with voltage. The threshold voltage and the response curve depend strongly in the permittivity behavior. The solution of the molecular position is also necessary to know the dielectric constants as a function of voltage. The capacitance and conductance can be estimated from these values (Eq. 40).

Experimentally different methods have to be applied in order to measure the dielectric constants of nematic LC:

- For voltages lower than 100 mV EIS is used. This technique characterizes the impedance as a function of frequency.
- For voltages higher than 100 mV EIS cannot be used, because the device is limited to 3 V_{RMS}. A complex batch could be configured (using alternating bias voltage) but is beyond the scope of this thesis.
- A classical Wheatstone bridge allow the measurements for higher voltages and make possible the measure in a specific range (0.1 – 12 V_{RMS}).

First of all the impedance is characterized by EIS. From the impedance measurements and knowing the structural parameters of the LC sample, the permittivity is estimated. By using these results an EEC for a broadband frequency (1 Hz – 10 MHz) is proposed and demonstrated. The values of the dielectric constants when higher voltages are applied are measured by using a Wheatstone bridge. In this case, the solution of the proposed algorithm in section 2.1.3 is also demonstrated. The final result is a detailed electrical model of nematic LC as a function of voltage (dielectric and optical anisotropy) and frequency (dispersion).

4.2.1. Dielectric response as a function of frequency: Dispersion

As in the previous section, the LC sample is MONO (Table 3). The nematic LC used is MDA-98-1602 from Merck, Δn = 0.2666@589.3nm (n_e = 1.7779; n_o = 1.5113) y $\Delta\varepsilon$ = 12@1kHz (ε_e = 16.2; ε_o = 4.3). The measurement device is a Solarton 1260 connected to a personal computer (PC) through GPIB:

- This device operates at a frequency range of 10 μHz – 32 MHz.

- The impedance module ranges from 10 mΩ a 100 MΩ (5 digit resolution).
- For the experiments low voltage signals are applied (50 mV_{RMS}). Despite this, the maximum range varies from 0 to 3 V_{RMS} for frequencies lower than 10 MHz [183].
- The applied DC signal is zero in order to avoid electrolytic degeneration of the LC cell by ion generation and migration, and eventual adsorption of the charges onto the alignment layers. Despite this, a bias voltage can be applied ranging from -40.95 V to +40.95 V with a maximum current of ± 100 mA.

The data processing is done by a proprietary software of Solarton (ZPlot). This software makes possible automatized measurements by applying frequency or voltage sweeps. With ZView software, data can be explored in real time. A graphic interface provides different electrical circuits to adjust the response. Also custom models can be introduced. The fitting algorithms can be selected [184].

As commented above, the LC sample is MONO (Table 3). The results of the impedance measurement are given in module and phase, they are represented in the Bode diagrams of Figure 51.

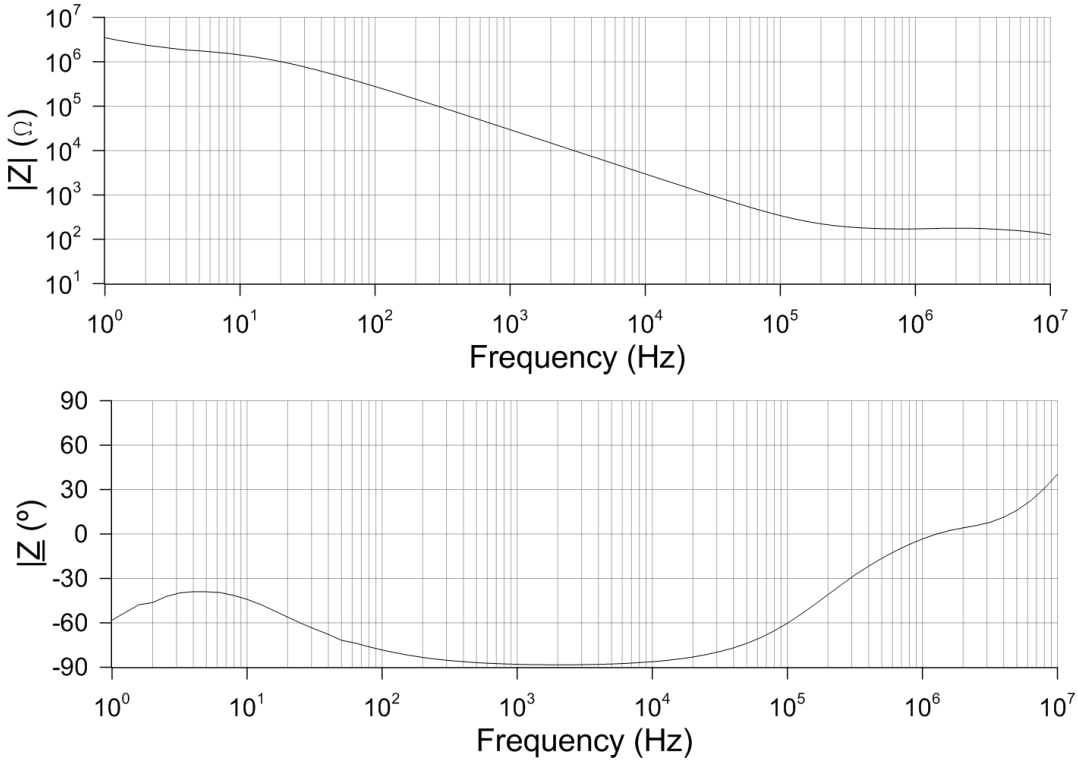

Figure 51. Frequency response of MDA 98-1602 nematic LC given as (upper) impedance module and (bottom) phase.

From these results it can be found certain frequency ranges with a clear tendency:

- ✓ For low frequencies (1 Hz – 100 Hz) the phase tend to -40º. This is caused by the ionic impurities. The sample behaves like a very lossy capacitor.

- ✓ From 500 Hz to 5 kHz the phase shift is almost -90º (min. -88º). This indicates a capacitive behavior with some losses. This is usually modeled as a capacitor in parallel with a resistance.
- ✓ Increasing the frequency ranges (100 kHz – 1 MHz) the pure capacitor effect decreases again. Now it is caused by a reduction of the dielectric constant (see section 2.1.2, Figure 20). In this case, the dominating resistive effect is produced by the electrodes.
- ✓ Finally, an inductive effect is observed (>1 MHz) probably caused by the long wires used in the experiment (10 cm).

Taken into account the capacitance of the empty cell C_0 = 1.18 nF, and Eq. 25, the real ordinary permittivity and the imaginary part, can be estimated. The results are compared to another commercial nematic LC, the E7 (Figure 52). Data of this LC is taken from the literature [166].

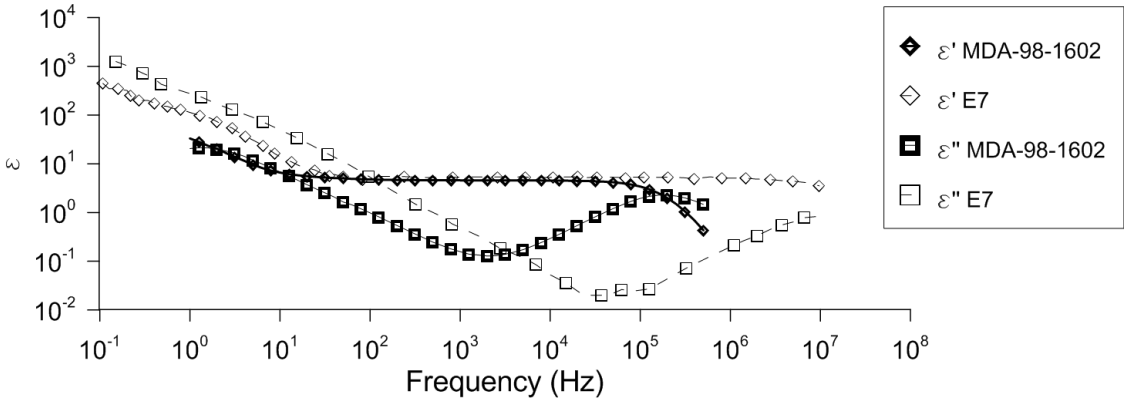

Figure 52. Complex permittivity response of MDA 98-1602 and E7 nematic LC.

Dispersion can be observed for both LC (100 kHz MDA and 10 MHz E7). Differences in frequencies can be explained through the constant time of the cell. Differences in the cell resistivity lead to changes in the dispersion frequency [185]. In order to avoid this effect very low resistive electrodes are necessary (e.g. Au). The value of the dielectric constants determines some important parameters of the electrical model as capacitance and parallel conductance (Eq. 40). This result is very important to determine the range where equivalent components can be considered constants.

4.2.2. Equivalent electrical circuit

Interpretations of graphs are complex and can lead to multiple explanations. For this reason, a complete EEC for a broadband frequency is proposed (Figure 53). The EEC components are obtained from the EEC model by fitting the experimental results and the parameters through a non-linear least-squares Levenberg-Marquardt algorithm. The software package ZView (Scribner) version 3.3f is used. Each component of this circuit is linked to different physical parameters of the sample.

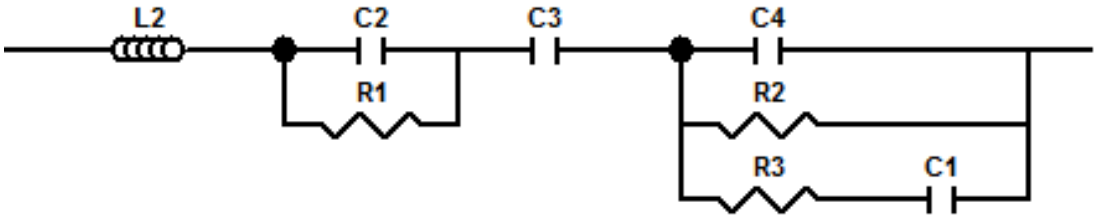

Element	Freedom	Value	Error	Error%
L2	Free(+)	3,0302E-6	6,7755E-08	2,236
C2	Free(+)	1,0898E-8	1,2303E-09	11,289
R1	Free(+)	1,3595E6	70507	5,1862
C3	Free(+)	5,6699E-8	1,1556E-09	2,0381
C4	Free(+)	6,289E-11	2,6915E-12	4,2795
R2	Free(+)	305760	78058	25,529
R3	Free(+)	174	1,5112	0,86851
C1	Free(+)	1,3253E-8	1,8293E-09	13,803

Figure 53. Complete equivalent electrical circuit for nematic MDA-98-1602.

The ECC is composed by 3 resistors (R_1, R_2, R_3), 4 capacitors (C_1, C_2, C_3 y C_4), and one inductor L_2. Each component has a physical significance that describes the different elements contributing to the sample response:

- ✓ L_2 is probably caused from wires length (10 cm).
- ✓ C_2 is a double layer capacitor formed in the interface of the alignment layers and LC. R_1 resistor is the resistance of the Faradaic reaction.
- ✓ C_3 can be caused by ionic impurities producing a charge accumulation at the electrodes.
- ✓ C_4, R_2, R_3 and C_1 form the circuit employed to describe the Debye dielectric relaxation (see section 2.1.2).
- ✓ C_4 results from electronic and atomic polarization. These processes are detected at high frequencies. C_1 describes the slow orientation of dipolar polarization which is detected at frequencies lower than C_4 processes. R_3 represents the dipolar displacement (heat dissipation). R_2 represents the conductivity of the LC.

The proposed EEC has been compared to the measured impedance. The module and phase is shown in Figure 54.

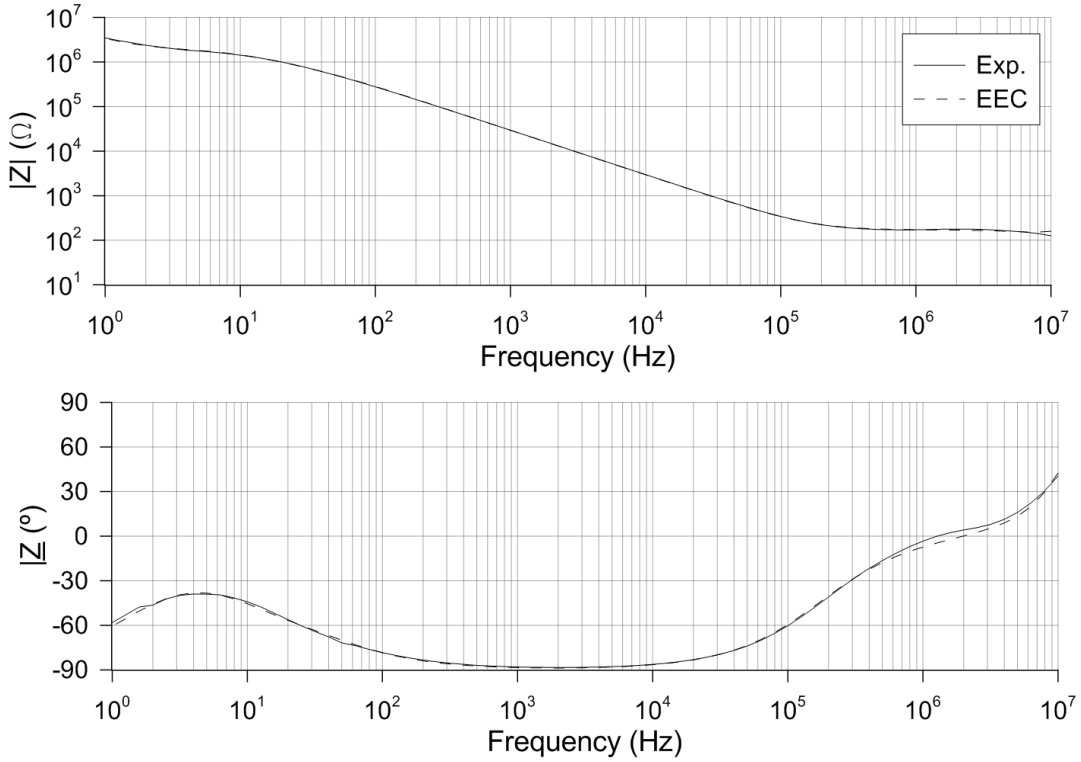

Figure 54. Comparative between experimental and EEC (upper) module and (bottom) phase.

It has been observed that certain components can be neglected in certain frequency ranges. In other words, the model can be simplified as a function of the application. Some relevant aspects are:

- ✓ For low frequencies (<10 Hz) the polarization process of the electrodes and the charge accumulation are dominating. For this reason, C_2, C_3 and R_1 can be considered, neglecting the rest of the electrical components.
- ✓ At medium frequencies (10 Hz – 10 kHz) the previous components decrease their impedance. The LC capacitance and the polarization resistance became predominating. The phase is close to -90º so the capacitor is even more relevant.
- ✓ For higher frequencies (10 kHz – 10 MHz) the Debye relaxation predominates. R_3 and C_1 have to be considered.

The previous analysis makes possible to characterize the nematic LC in a specific frequency range. The simplified EEC is determinant to model the LC electro-optic response. It is included in the electrical model proposed in section 2.2 and the simulations of the proposed devices. Another important parameter is the response of this EEC as a function of voltage. This is studied in the next section.

4.2.3. Dielectric response as a function of voltage: Dielectric anisotropy

In this section, the electrical response as a function of voltage is characterized by using a Wheatstone bridge. A Wheatstone bridge is an electrical circuit used to measure an unknown

electrical component by balancing two legs of a bridge circuit, one leg of which includes the unknown component. It was invented by Samuel Hunter Christie in 1833 and improved and popularized by Sir Charles Wheatstone in 1843. The main requirement is a knowledge of the type of electrical component that is measured. In this case and following the results of the previous section, a capacitor in parallel with a conductance (medium frequencies). Thanks to this method, the nematic LC can be characterized in a voltage range.

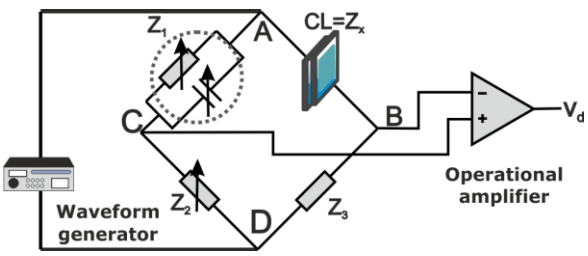

Figure 55. Wheatstone bridge for measuring the LC dielectric permittivity of MDA-98-1602 in a voltage range.

The set-up is depicted in Figure 55. It is composed of the same LC cell previously used (Z_x), placed in one leg. On the left side are the variable components (Z_1) for tune purposes. In order to simplify the measurements, two equivalent impedances are placed in the lower part of the legs (Eq 64). This is why Z_2 is a potentiometer. This bridge configuration produces null voltages between BC when the following equation is reached:

$$Z_x = \frac{Z_1 \cdot Z_3}{Z_2} \tag{64}$$

If the components of the lower part of the legs, are equal, $Z_2 = Z_3$. The bridge is in equilibrium when BC voltage is equal to zero ($V_d = 0$), in other words, when $Z_x = Z_1$. As commented above, this EEC is valid only for a certain range of frequencies (100 Hz - 10 kHz). In this case the EEC is simply a capacitor parallel to a resistance (dielectric losses). Due to the high value of the capacitor a custom variable capacitor is build. For better precision, an operational amplifier (AD620) with x100 factor gain is placed in BC points. Measurements of resistance and capacitance (Z_1) are taken when V_d = 0, for a range of voltages from 0 – 12 V_{RMS} (frequency = 0.1 – 100 kHz). The conductance ($G = 1/R$) and capacitance (C) profiles are shown in Figure 56.

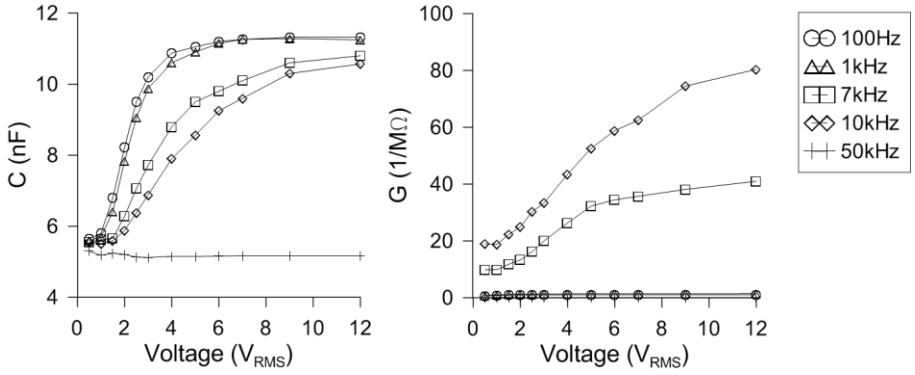

Figure 56. Capacitance (*C*) and conductance (*G*=1/*R*) of nematic LC MDA-98-1602 as a function of voltage and frequency.

The capacitance and conductance increase with voltage. This is caused by the homogeneous alignment of molecules. In this case, the considered permittivity in the relaxed position is the ordinary component (ε_o = 4.3). When the voltage increases, the molecules align parallel to the electrical field reaching a perpendicular position. In this case, the predominating permittivity is the extraordinary component (ε_e = 16.2). With cell dimensions and classic capacitor equation, permittivity is easy to calculate from this measure. To validate the set-up, the results are compared with the previous measurements taken by EIS (Figure 57).

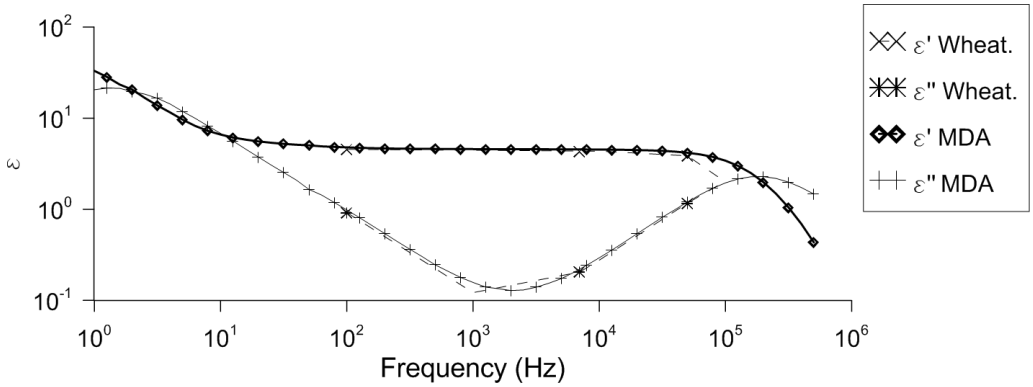

Figure 57. Complex permittivity response of MDA 98-1602 measured by EIS and Wheatstone bridge.

These results validate both experiments. The advantage of using the Wheatstone bridge setup is the possibility of measure the LC with an applied voltage up to 12 V_{RMS}. Thanks to this, the extraordinary permittivity can also be measured.

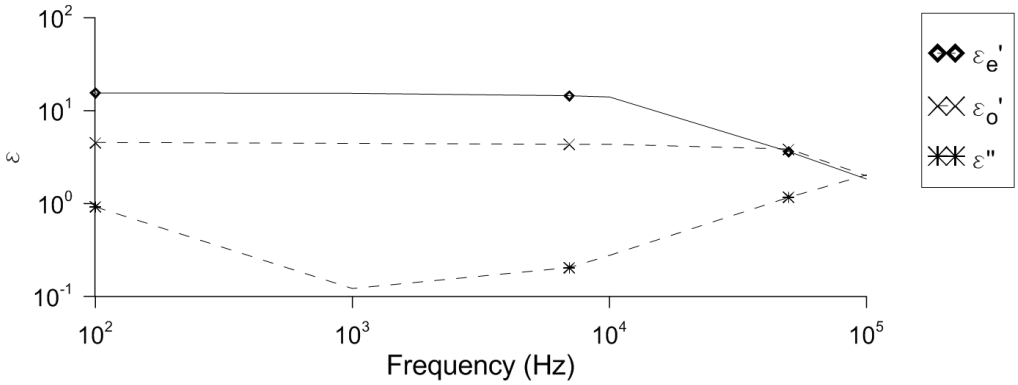

Figure 58. Dispersion of the ordinary and extraordinary dielectric constants.

As predicted in section 2.1.2, it is observed a higher constant time for the extraordinary component. For this reason, the dispersion frequency is lower. The variation of the components of the EEC with voltage and frequency is determinant to correctly model devices based on nematic LC. What is more important is to validate this results with the theoretical model. Once the permittivity is extracted, a simulation with the same cell parameters is carried out.

Simulations of permittivity as a function of voltage

As commented in section 2.1.3 a computer program has been developed to know the direction of the LC molecules for an applied voltage. The theoretical estimations also use MDA-98-1602 enabling the comparison between experimental and theoretical results. By using this program the molecular angles inside the sample are estimated. Considering Eq. 65, the effective permittivity is determined.

$$\varepsilon_{eff} = \varepsilon_o \cos^2\theta + \varepsilon_e \sin^2\theta \tag{65}$$

Then the mean value of the effective permittivity of the molecules contained from one substrate to another (from 0 to d) is estimated by using Eq. 66. This equation gives the permittivity estimation as a function of voltage.

$$\left\langle \varepsilon_{eff} \right\rangle (V) = \frac{1}{d}\int_0^d \varepsilon_{eff}(V,z)dz \tag{66}$$

Following the previous equations, the theoretical permittivity as well as capacitance can be estimated at 1 kHz (data from datasheet is provided at this frequency). The value of the imaginary component is not provided in the datasheet, making mandatory an experimental measurement to know it. The results of the simulations are compared with the previous experimental measurements.

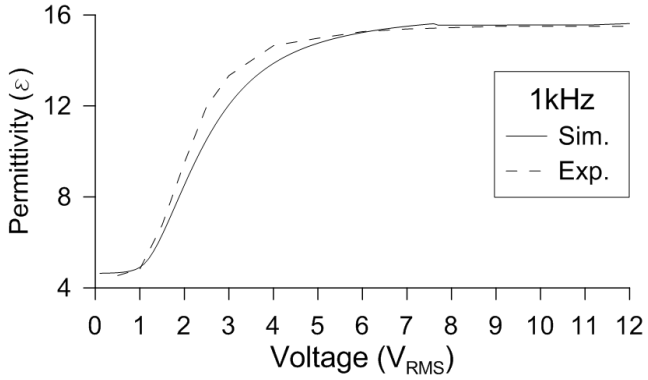

Figure 59. Theoretical and experimental permittivity as a function of voltage.

This example validates the behavior of the proposed algorithm again. Both the experimental measurements of optical and dielectric anisotropy have shown a good agreement with theoretical predictions. Slight differences between data could be caused by experimental measurement errors. In the case of imaginary permittivity extracted from conductance, the simulations cannot be carried out due to lack of this data in the LC data sheet.

5. Adaptive micro-optical lenticular arrays

In the near future most of the multimedia content will be displayed in mobiles or tablets. To apply spatial multiplexing in these devices, some aspects have to be taken into account. As the observer usually has the device in his own hands, the 3D distance is considerably lower than with big displays. This requires a higher optical power. As every observer has different physical characteristics a tunability of this distance is especially required for a useful device. To overcome these drawbacks, microlenses with tunable and high optical power are required. For this application, the key parameter for designing the lenticular array is the focal length of each individual optical element. For this reason, the equations governing this parameter are presented in this chapter. Due to the micrometric size of each microlens embedded in the lenticular array, special optical components are necessary in order to characterize them. For example, optical zoom or micropositioner. In this thesis, the control and characterization software and the micropositioner are custom fabricated. This software automatizes the characterization process giving important results as phase modulation, focal distance, thickness or aberrations. Those values have been found to be similar to that of commercial lenticular sheets of comparable diameter per lens. By comparison of the experimental results with the theoretical predictions, the proposed electrical model is experimentally validated. Finally, demonstration of the viability of this technology for an autostereoscopic application as well as some original solutions to temperature dependence and aberrations are proposed and experimentally demonstrated.

5.1. Designing a lenticular device

As commented above, the key parameter for designing a lenticular lens array is the focal length of each individual lens. In conventional lenses, an approximation of the focal length can be extracted from Fermat's Principle and contributions of Gauss to Gaussian optics. This focal length approximation has been the fundamental theory for designing lenses for many years and is given by

$$f_O = \frac{n_1}{n_2 - n_1} \cdot R \tag{67}$$

where n_1 is the refractive index of the surrounding medium, n_2 is the refractive index of the lens material and R is the radius of curvature of the lens. As commented in previous chapters, it should be possible to design a lens without curvature but with a material that has a gradient in the refractive index; this device is known as GRIN lens. Specifically, for GRIN lenses an estimation of the focal length, f_{GRIN}, becomes simple taking into account focusing of parallel rays,

$$f_{GRIN} = \frac{R^2}{2 \cdot d \cdot \left(n_{\max} - n(r)\right)} \tag{68}$$

where R is the lens radius (half lens pitch), d is the thickness of the lens (thickness of the LC layer) and n_{max}–$n(r)$ is the difference between the maximum refractive index, n_{max} (at the optical axis of each lens) and the refractive index at the position r (that is, at the edge of the lens). Thus, d can be derived for a particular value of f_{GRIN}, according to the application.

As it was commented in section 3.1, in order to have a proper phase profile (without shrinking at the sides or phase plateau at center), the microlens array dimensions are required to be in a very specific range. The design of the electrode pattern is determined by the main application of the lenticular arrays (an autostereoscopic device). Two electrode patterns are designed, one for an OLED based autostereoscopic display with 128 x 64 pixels (see section 3.1, Figure 31) and other to work in a 200 PPI autostereoscopic display (see section 3.1, Figure 32). Each lens of the array has been initially studied as an individual microlens.

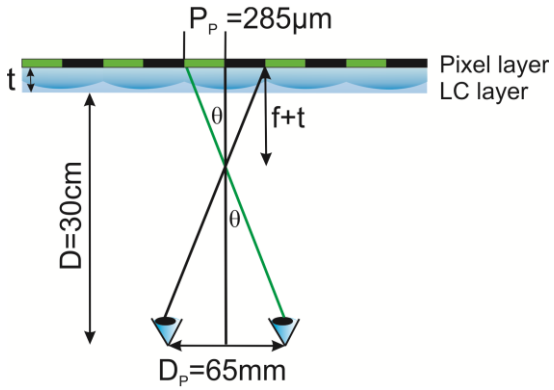

Figure 60. Scheme of the geometry of 3D imaging by lenticular method.

In order to avoid adverse effects on vision, observer should be positioned at the appropriate distance, D, from the screen (Figure 60). Also, the 3D effect may not be visible when the screen is viewed at an angle. So, designing the focal length of the lenticular array must be defined for a precise position of the observer in front of the device, thus size of the viewing zone is equal or greater than the interpupillary distance, D_p.

By considering the extreme case in which the rays from the two endpoint pixels reach different eyes and for a 3D distance of 30 cm, the focal distance can be extracted by trigonometry (Figure 60),

$$\left.\begin{aligned}\tan\theta &= \frac{Dp\ /\ 2}{D\ -\ f}\\ \tan\theta &= \frac{Pp\ /\ 2}{f\ +t}\end{aligned}\right\} f = \frac{D\cdot Pp\ -\ Dp\cdot t}{Dp+Pp} \approx \frac{D\cdot Pp}{Dp} \tag{69}$$

The last equation, which relates the 3D distance to the necessary focal distance for a microlens array placed in front of the display, is essential for the design of autostereoscopic devices based on microlenses. For these parameters the minimum focal length would be 1.3 mm for the OLED display (OLED) and 0.48 mm for the 200 PPI display. The focal length achieved with the maximum birefringence always increases with decrements in the applied voltage. The 3D distance obtained for the OLED display is 30-35 cm (see section 5.3.1, Figure 88). In the 200 PPI case, the 3D distance, estimated by using Eq. 69, could be controlled from 22 cm to a few meters (this is demonstrated experimentally in section 5.2.3). Without voltage, the LC lens behaves like a transparent glass.

The focal length (f_{GRIN}) and diameter ($2R$) are determined by the application, so only two adjustable variables, the thickness and birefringence, remain. The birefringence is a parameter determined by the material; the commercial nematic LC MDA-98-1602 from Merck is selected because of its high birefringence, Δn = 0.2666. Therefore, only one adjustable parameter, the thickness, remains. In order to have enough test samples to demonstrate the theories proposed in section 2.2 and to work in different applications proposed in next sections, different thicknesses are manufactured (100 μm, 90 μm, 50 μm and 40 μm).

All devices of this chapter are composed by two ITO coated substrates. The substrates are separated by a space with one of the thicknesses commented above. The ITO coating of one substrate is patterned with one of the electrode designs of section 3.1. The other one is a continuous electrode (to connect the ground). The resulting cavity is filled with a nematic LC MDA-98-1602. The LC is used as an adaptive phase-only modulator so no twist of the molecules is necessary. For this reason, a planar alignment is used (see section 3.3.3).

5.2. Electro-optic characterization

In this section, different parameters characterizing the electro-optic response of the individual microlenses are measured. Each parameter needs its own experimental setup. For this reason, the experimental set-up and results are described in each sub-section. These results validated the design and manufacture process as well as the theoretical models proposed in this thesis.

5.2.1. Phase shift diagrams

The wavefront surface, *W(x,y)*, has been approached through the optical path length (OPL) that light experiences upon transmission through the LC layer. Throughout the process, LC device works in dynamic regime (unidirectional translation perpendicularly to substrates) and it is addressed by an external driving voltage. In a first step, the phase fringe patterns are recorded by means of a CCD sensor and the image intensity is enhanced. Next, 3D phase maps are extracted from the device electro-optic response. A simple method to do this has been carried out. Figure 61 shows a simplified scheme. Next, an imaginary horizontal line (placed in the x-axis direction) is swept in the y-axis direction, that is, from the top to the bottom of the active area. This line superimposed on the interference pattern defines an intensity profile for each position. The corresponding phase profile, $\Delta\phi(x,y)$, is generated from every intensity profile; an algorithm has been specifically developed for this task. The values of the phase profiles range from 0 to 255 (each point stored in one byte, 255 levels). Next, the set of phase profiles forms a 3D phase map. In this map, the optical phase shift, $\Delta\phi(x,y)$, is measured in units of 2π radians and is referred to a position in Cartesian coordinates *(x,y)* measured in microns.

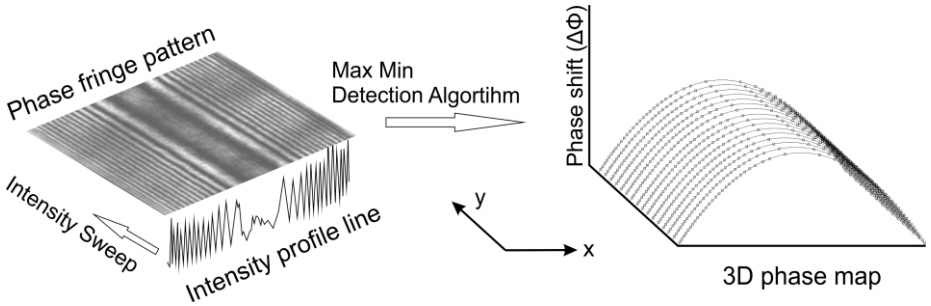

Figure 61. The simplified scheme of the method for a 3D phase map extraction.

The initial interference pattern is the result of placing the LC device between two crossed polarizers (see section 2.1.1). This device produces a gradient in the refractive index produced by a voltage variation across the surface. The result is a specific birefringence as a function of the position *(x,y)*. The birefringence causes phase differences between ordinary and extraordinary components of light, changing the polarization state of the incoming light. For each position in the active area there is a determined birefringence and thus a specific phase shift $\phi(x,y)$. In this way, an interference pattern ranging from bright to dark intensities is observed, corresponding to 180º and 0º of phase shift, respectively. Because of its many applications, the studies of this type of interference patterns are numerous.

Until now several techniques have been proposed for phase reconstruction, among them, some of the most important are Fringe Skeletonizing [186], Fourier transform [187], use of wavelets [188], Phase Trackers [189] and Genetic Algorithm [190]. In our experiment, due to the proposed setup between crossed polarizers, the scattering produced by the LC, and the fact than only one light source is used, some algorithms are unfeasible or erroneous. For example, Phase Trackers or Fourier use an additional reference source. On the other hand, the image quality for other algorithms gives some errors. Checking different types of algorithms for the generated images of this specific setup, the Fringe Skeletonizing is found to be the most fast and robust. Although it is one of the oldest techniques, it is one of the most used because it is faster and proven. This technique is based on the very definition of interference.

Finally, the experimental wavefront surface, *W(x,y)*, can be easily determined from the phase shift measurements, *Δϕ(x,y)*. For this, the phase shift measurements are converted to optical path length, *Δnd(x,y)*, using Fresnel approximation (Eq. 70). Finally, dimensions are normalized.

$$W(x,y) = \Delta n(x,y)d = \frac{\Delta\phi(x,y)\cdot\lambda}{2\pi} \tag{70}$$

Where $\Delta n(x,y)$ is the effective birefringence at some specific point *(x,y)* of the active area, *d* is the thickness of the LC layer, $\Delta\phi(x,y)$ is the phase shift measurement and λ is the wavelength of the incoming light.

Experimental set-up and characterization software

The system is placed in an optical table as shown in Figure 62. The experimental set-up consists of: a He-Ne laser source (632.8 nm), neutral density filters, a linear polarizer at 45º, a LC sample with the alignment direction at 90º and moved by a custom-made micropositioner (40 μm resolution), a ×10 microscope objective, another polarizer at -45º and a B/W CCD digital camera (effective no. of pixels 1344×1024). All the angles are referred to the horizontal direction of the table plane.

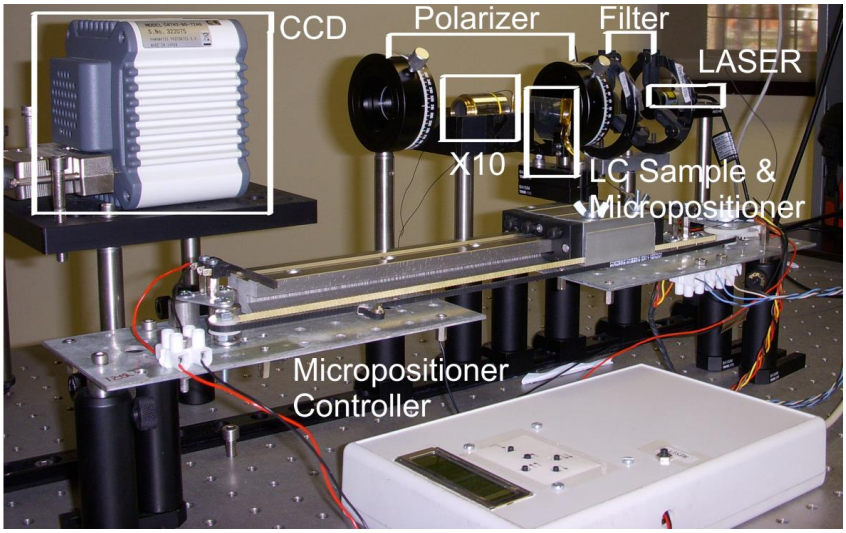

Figure 62. Experimental set-up for characterizing a tunable LC cylindrical micro-optical array for aberration compensation.

As commented above, interference fringes are captured placing test samples between two crossed polarizers with the rubbing direction of the lenticular lenses at 45º from the linear polarization at the input. A variable frequency and amplitude square signal is applied to the control electrode of the LC lenticular lenses. The first polarizer splits incident light wave into two orthogonal components, the extraordinary and ordinary waves. When light passes through the LC device, waves experience spatially uniform phase retardation caused by the birefringence of LC (see section 2.1.1). As a gradient voltage has been designed to be generated inside the LC device, a gradient birefringence is also generated. At this point, second polarizer recombines the two waves and causes them to interfere. The results is an interference pattern composed of darks and clear zones corresponding to constructive and destructive interferences. This means that two neighboring

interference fringes have a phase difference of 2π. Unlike other lens, where lens aperture is visible to the naked eye, these lenses have a micrometer pitch length. A ×10 objective properly focused is placed in the path of the beam to see correctly the interference pattern. Finally, interference fringes are recorded by a CCD camera as applying various voltages and frequencies square signals. Phase profiles are obtained from interference patterns developing an image recognition program that processes images and plots phase retardation versus horizontal position across the LC lens.

The characterization software is based on a Graphic User Interface (GUI) programmed with MATLAB. This one receives the fringe captures through the CCD. Some examples of the captured images are shown in Figure 63:

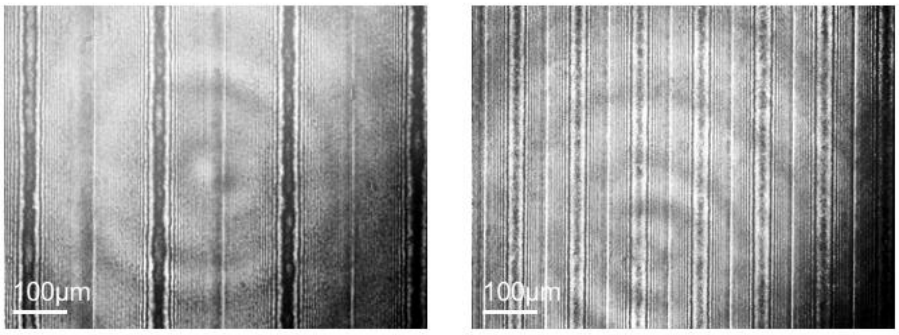

(a) 100 LPI device. **(b) 200 LPI devices.**

Figure 63. Interferograms obtained in the CCD (x10 objective).

Besides, it has several options for image processing, for example: contrast improvements on fringe images, automatic rotations (when the device is at a specific angle), electrodes detection, area of interest selection, etc. Once the images from the CCD are processed, the program is capable of unwrapping the phase in two or three axis by Fringe Skeletonizing technique.

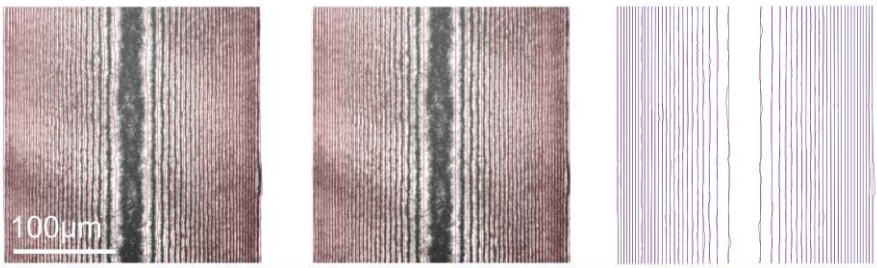

(a) **(b)** **(c)**

Figure 64. Fringe Skeletonizing technique (a) interference pattern and Skeletons (b) Skeletons taken the mean value of the peaks (c) comparison between captured skeletons and mean value.

There is certain ambiguity in the spatial position of the fringe position. After a fringe skeletonizing by peak detection [Figure 64(a)] the red lines show the result. The software takes an average across all peaks detected [Figure 64(b)], this mean value is drawn as a blue line. As can be seen in Figure 64(c), the differences between the mean lines (blues) and the measured lines (reds) are unappreciable. In the worst case (fringes in the center of the active area), the maximum deviation is 0.5µm. A snapshot of the program is shown in Figure 65.

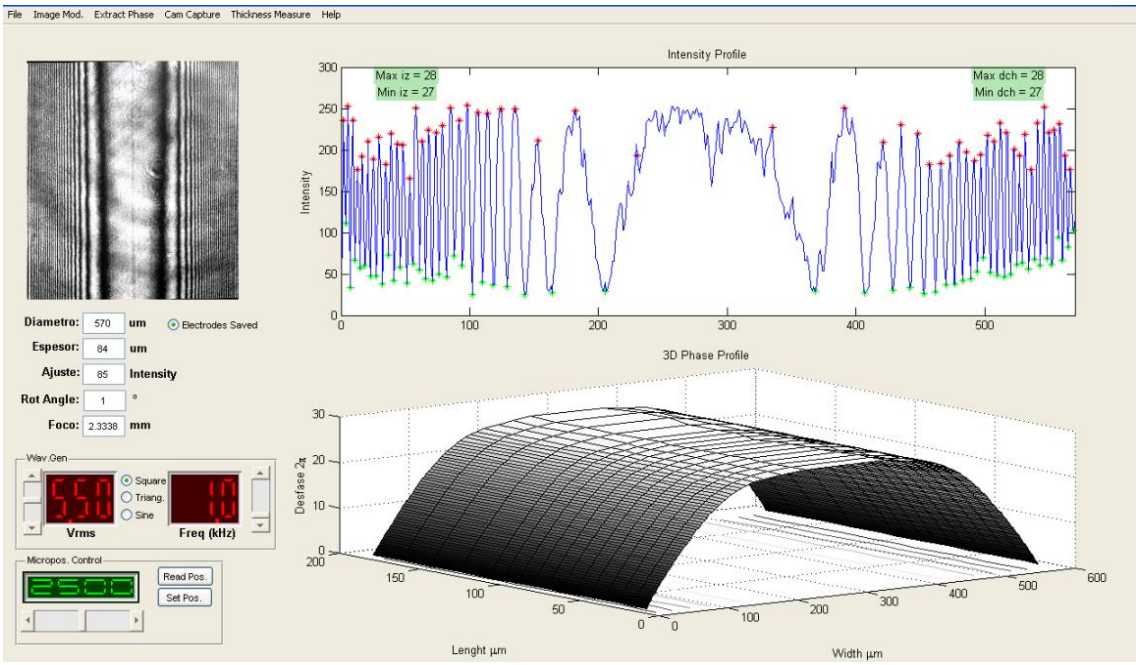

Figure 65. Snapshot of the program.

Experimental results

Firstly the modal sample is studied. Results of characterization for first addressing approach (for applied signals only to one of the comb electrodes, sample OLED50NI55) have allowed a thorough study of the manufacturing protocol together with the amplitude and frequency dependence on the phase behavior of the lenticular device.

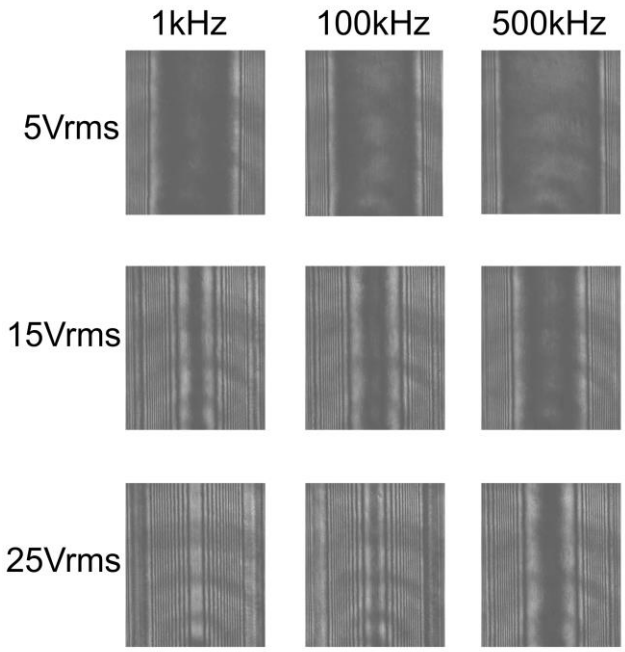

Figure 66. Frequency and voltage (RMS) dependence of interference patterns (before image processing) of cylindrical LC lens when only one of the comb electrodes is used as a control electrode.

Figure 66 includes interference fringes for some representative values of frequency and voltages (root mean square) of addressing waveform, so width of each image matches with a lens diameter. It is shown that, for a fixed frequency, as voltage increases, phase differences spread out over the lens surface. However, lens diameter designed for this approach turned out too long (570 μm), forcing high driving voltages and given rise to undesirable shrinking effect. It means that voltage distribution drops below threshold before reaching the center of the lens, thus suggesting a too large sheet resistance of the control electrode for these approach. Shrinking effect resulted in a significant decreasing aperture diameter of lenses, probably due to a saturation of the tilt angle of molecules near the edges. This result also restricts the maximum effective phase retardation (28π), as shown in Figure 67 (left graph, 1 kHz frequency AC square signal).

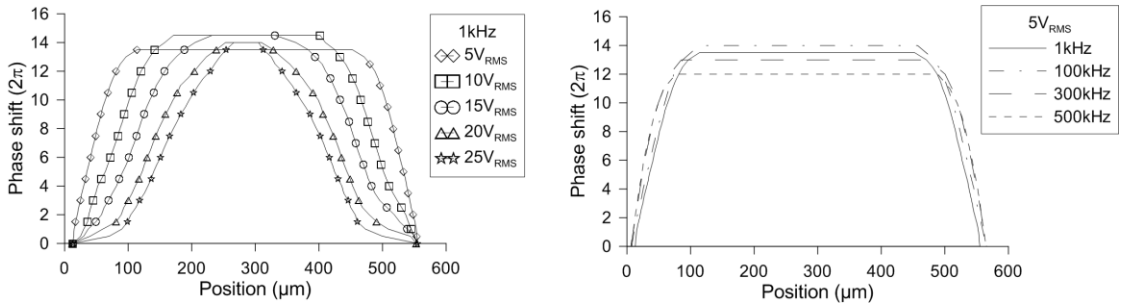

Figure 67. Frequency and voltage dependence of phase retardation of cylindrical LC lens when only one comb electrode is used as a control electrode.

On the other hand, another noticeable effect, for a fixed voltage, is the growing of the flat-like phase in the center of the lens, that is, without any change in retardation phase, as frequency increases. Figure 67 shows some examples of this behavior for 5 V_{RMS}, 15 V_{RMS} and 25 V_{RMS} and several frequencies. Such an effect is related to the frequency dependence of the electrical response of manufactured devices. LC impedance, from the control electrode to the counter electrode, experiences a drop as frequency increases. The EEC explains that LC capacitance tends to shorting at high frequencies, so dropping the electric field at the center of the cell.

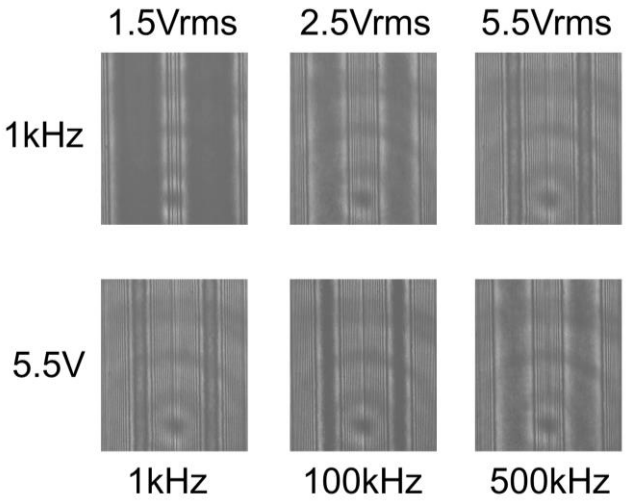

Figure 68. Frequency and voltage (RMS) dependence of interference patterns (before image processing) of cylindrical LC lens when two comb electrodes are used as a control electrodes.

Performance of first addressing approach (leading one comb electrodes) can be improved through the second addressing approach (sample OLED50NI55-2). By leading two comb electrodes allows us to design a lenticular array with optimum features. In this case, lens diameter is the half of the previous one (285 μm), so that it becomes a suitable arrangement of lens size and sheet resistance of the control electrode. Unlike first approach, AC square driving applied to the current device configuration gives rise homogeneous phase responses within a full range of voltages and frequencies. Figure 68 shows interference fringes recorded for some representative values of frequency and voltages of AC signals. Width of each image matches with two lens diameter (quantitatively it is the same width than in Figure 66.

As expected, for a fixed frequency, as voltage increases phase retardation profiles increases (focal length decreases). Maximum phase retardation is reached at the lens center (experimentally 28π) and minimum at the edges (Figure 69). Lower voltages than those of the previous approach are used, avoiding shrinking effect appears. Minimum focusing distance whereby the maximum phase retardation is achieved has been obtained with only 5 V_{RMS}. Again, for a fixed voltage, similar frequency dependence of interference patterns happens. To finish, by tuning voltage and frequency parameters, a good choice for the optimal operating point in the second approach may be consider the pair (5.5 V_{RMS}, 1 kHz).

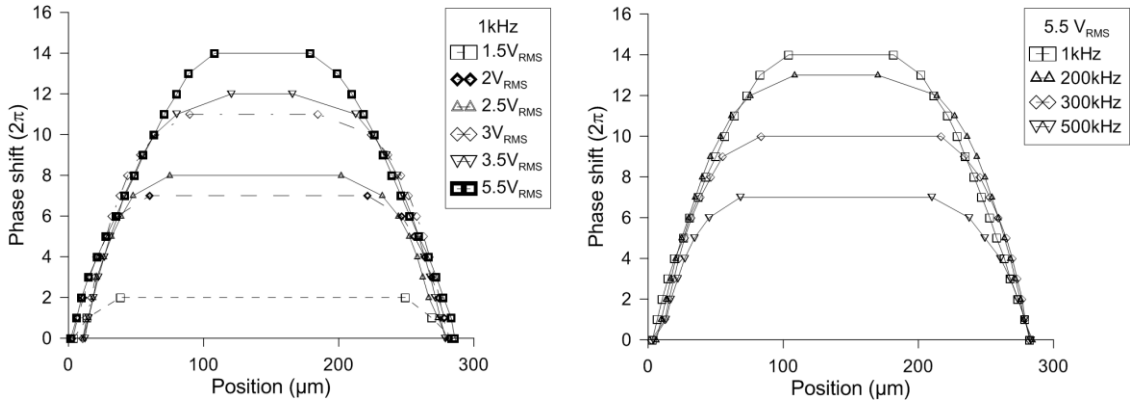

Figure 69. Frequency and voltage dependence of phase retardation of cylindrical LC lens when two comb electrodes are used as a control electrode.

After this, the hole patterned scheme is also studied. The results of hole patterned microlenses specifically designed following the proposed theory in section 2.2.2 (sample 100LPI100NI0) is shown in Figure 70.

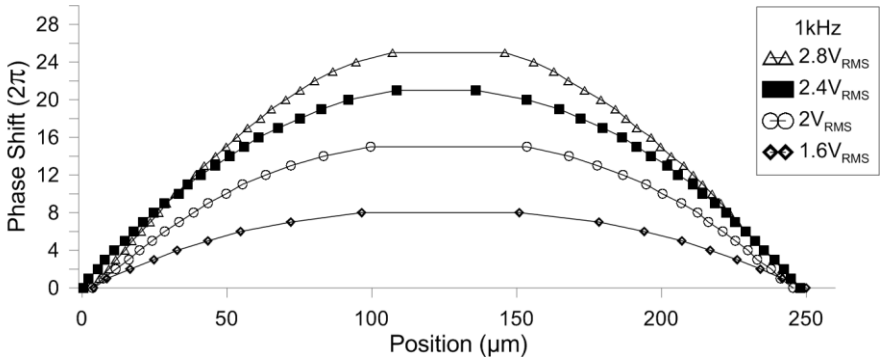

Figure 70. Voltage dependence of phase retardation of a hole-patterned cylindrical LC lens when one comb electrodes are used as a control electrode.

As expected, there are not phase defects (plateau at center or shrinking at the sides). There is no change with the applied frequency for a fixed voltage. As voltage increases phase retardation profiles increases (focal length decreases). Maximum phase retardation is reached at the lens center (experimentally 50π) and minimum at the edges. The voltage is even lower than those of the previous approach. For this reason, shrinking effect neither appear. Minimum focusing distance whereby the maximum phase retardation is achieved has been obtained with only 2.8 V_{RMS}. These results are determinant in order to validate the proposed electrical model in section 2.2. In next section it is demonstrated both for modal and hole patterned lenses.

5.2.2. Experimental demonstration of the electrical model

In this section, the electrical model is demonstrated. For this, the parameters previously used in the results of the electrical modelling (section 2.2.3) are used. This parameters are similar to that used in the fabricated devices.

Modal liquid crystal microlenses

With the voltage distribution, the molecular ordering is known. The developed program graphically depicts LC molecular distribution inside the cell in 2D images of transversal sections of the sandwich from the top to the bottom electrodes (Figure 71). Following Equations 3, 7, and 62 the phase profiles are estimated. The unwrapped phase defects of the LC cylindrical microlenses can be described and discussed from the diagrams.

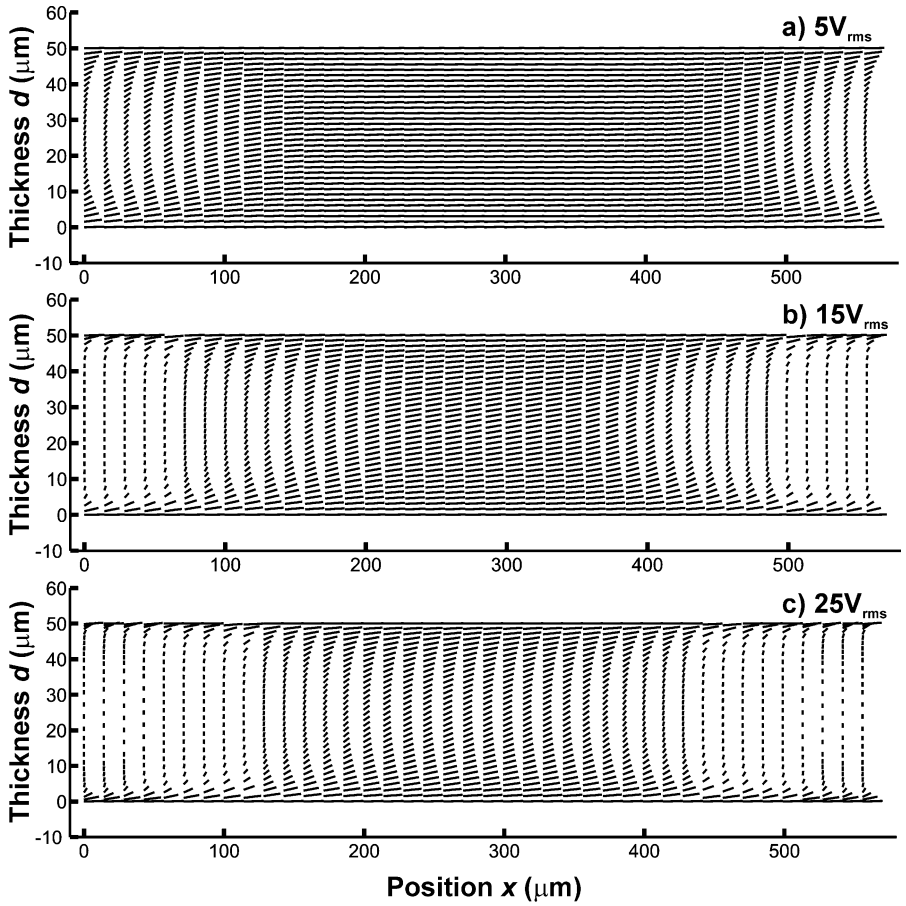

Figure 71. Simulation of molecular arrangement for some representative values of voltage. Glass plates are horizontal, in positions 0 and 50 µm. Electrodes are placed in positions 0 and 570 µm.

By inspection of Figure 71, molecular ordering can be described. Those diagrams include the solution of the director orientation for some representative values of voltage, 5 V_{RMS}, 15 V_{RMS} and 25 V_{RMS}, 1 kHz AC square signal. The voltage gradient was estimated in section 2.2.3. They represent 2D images of transversal sections of the sandwich from the top to the bottom electrodes. For 5 V_{RMS}, it is noticed that the voltage distribution drops below the threshold before reaching the center of the lens, since there are some molecules which position remains unswitched. It reveals a too large sheet resistance of the control electrode for this approach that can be foreseen in the phase of the lens design. On the other hand, a too long lens diameter forces high driving voltages for generating a phase gradient that spreads out over the lens surface. Such high voltages give rise to undesirable shrinking effect of the lens aperture, probably caused by saturation of the tilt angle of the molecules near the lens edges (Figure 71, 25 V_{RMS}). Besides, the shrinking effect resulted in a significant decrease of the aperture diameter of the lenses.

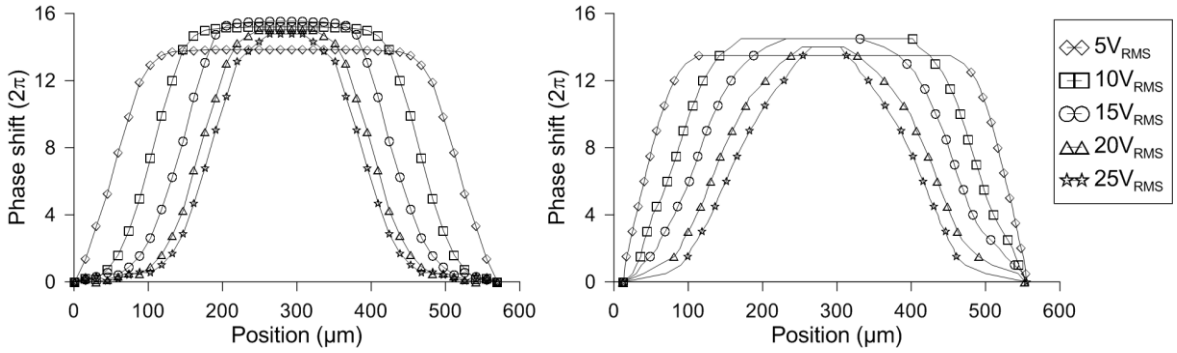

(a) Simulation results. **(b) Measurements of characterization.**

Figure 72. Phase shift profiles of a cylindrical LC lens as a function of control voltage.

Figure 72(a) and (b) graph some simulations and measurements, respectively, of the unwrapped phase defects in the modal LC cylindrical microlens, both as a function of the driving voltage amplitude (RMS). A set of only five voltage values has been chosen for clarity of the plot. The simulation of the unwrapped phase means a mathematical translation of the molecular arrangement to optical behavior. Thus, reasoning about the phase, for the smallest voltages the behavior involves the growing of a flat-like phase in the center of the lens, that is, without any change in the phase retardation. This fault is shown in Figure 72(a) and (b), for 5 V_{RMS}. Next, the flat-like phase is erasing in the voltage transition from 10 V_{RMS} to 15 V_{RMS}. But a decrease of the lens aperture arises, as stated with the description of the molecular orientation, for those values. The worst performance is obtained for the saturation voltage, 25 V_{RMS} and a shrinking effect is illustrated again with this measure. Both simulated and experimental unwrapped phase profiles are not parabolic due to a non-optimal design. This drawback could be prevented mainly caring for the design of the dimensions of the device.

Some viewpoints are argued to discuss the disparities between the simulations and the measurements of the unwrapped phase defects. Firstly, the results are subject to the experimental set-up. So, there are reasonable deviations of the current phase magnitude that can be attributed to the temperature and laser power fluctuations. The experiments have been carried out at room temperature while the LC datasheet parameters are specified to 20ºC. The wavelength dependence of the results is not relevant since the birefringence from the datasheet, $\Delta n = 0.2666$ at 589nm, and the one measured for 632.8nm, $\Delta n = 0.2642$ (and used in the simulation program), are very similar.

Besides, some tolerances of the manufacturing parameters are regarded as hypothesis thus leading to delimit an optimal margin of the device operation. In this point, the simulation algorithm has considered some cell gap values that lie within the interval 50 ± 5 μm, and also a slight 10% manufacturing tolerance of the sheet resistance (3 ± 1 GΩ/sq). In addition, some phase disparities between simulations and measurements can come from the difficulty of convergence of the algorithm for this boundary value problem as high voltages (more than 6 V_{RMS}) are applied to the device. The numerical methods usually cause instabilities that have been solved by using specific MATLAB functions.

From the experimental point of view, the results are strongly dependent on the width of the capture window for recording the interference patterns in the demodulation of the wrapped phase. The absolute phase magnitude and the threshold voltage are directly related to it. For this approach, a wide enough window has been used in practice. The discrepancies between the switching thresholds voltages also owe to only the simulations contemplate the strength of the alignment layer anchoring that forces an unchanged optical axis at a specific distance from the glass plates.

The discussion concludes that these results are indicative of the successful extension of the modeling of the unwrapped phase to defects in modal LC microlenses. The input program parameters are the key to design different kinds of microlenses without defects. The validation of the application has been proved and both results are fairly in agreement.

Hole patterned liquid crystal microlenses

There are no reports about the voltage distribution across a hole-patterned LC lens diameter, to the best of our knowledge. In this thesis, the simulated voltage distribution V(x) from the EEC (section 2.2.3, Figure 28) and the one obtained experimentally are compared. The comparison has been made with a cylindrical hole-patterned array lens (sample 100LPI100NI0). The main array characteristics are: A 254 μm microlens diameter, a 100 μm thickness and it is filled with a MDA 98-1602 nematic LC. The EEC model predicts the response of the manufactured lens (see section 2.2.3). The results of birefringence and voltage distribution are shown in Figure 73(a) and (c), respectively.

On the other hand, voltage distribution of the device has been estimated from the phase measurements of previous section. Next, there is a rough description of the protocol steps for extracting the experimental voltage distribution, V(x). The phase retardation of the lens, ϕ(x), has been reconstructed following the set-up detailed in section 5.2.1 (see Figure 70). In addition, the birefringence, Δn(x), can be determined by an inverse process,

$$\Delta n(x) = \frac{\Delta\phi(x) \cdot \lambda}{2\pi \cdot d} \tag{71}$$

Previously to the final step, the voltage dependence of the birefringence, Δn, shown in Figure 73(b), is extracted from Figure 48 (section 4.1.1). This measurement is a correspondence between birefringence and voltage, thus voltage distribution, V(x), can be achieved at each position, as shown in Figure 73(d). It is required to do an offset correction in the solution for a fitting result. This adjustment is set by adding each pixel voltage to each final voltage, which is equivalent to convert the relative phase into absolute phase retardation.

The comparison reveals that the profiles of the voltage distributions are fairly in agreement. The deviations can be attributed to the different data resolution from the simulated EEC and the measurements.

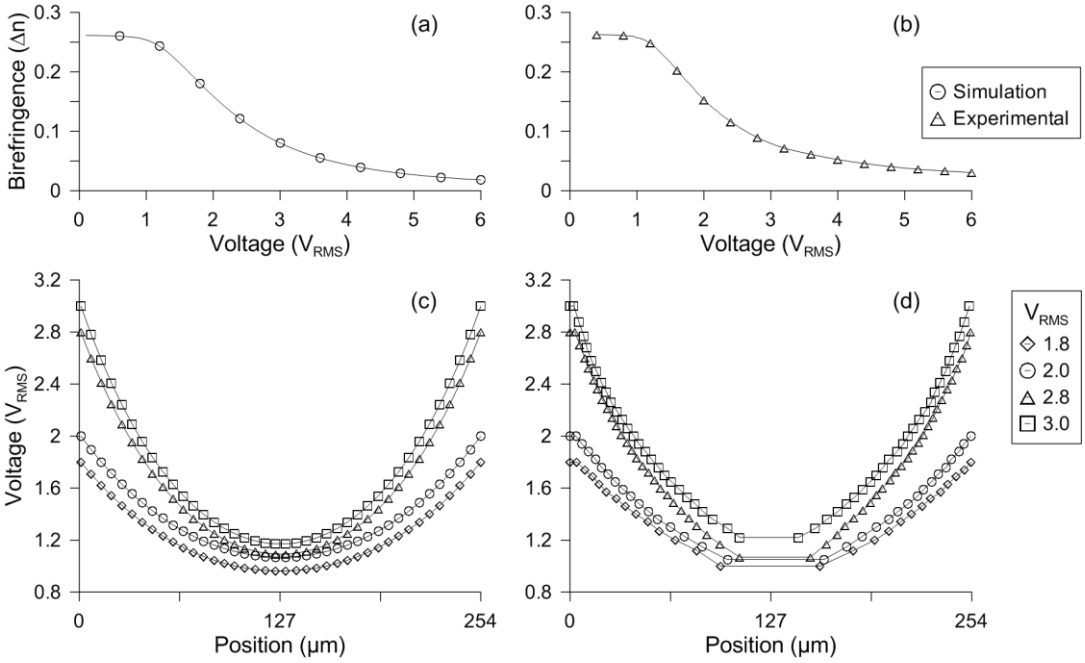

Figure 73. Simulated (a) and experimental (b) birefringences of a MDA 98-1602 nematic LC. Simulated (c) and experimental (d) voltage distributions when a 1 kHz square signal of V (V_{RMS}) is applied to the lens.

In conclusion, this novel EEC predicts the voltage distribution in LC microlenses for both modal and hole-patterned electrode schemes. In the last configuration the fringe field effect turns relevant as the lens aperture decreases. A coplanar capacitor has been chosen the electric component to model the electric response accurately. An accurate design of some constructive parameters, such as thickness or diameter, can be made previously to the device manufacture. In addition, it could lead to other key estimations of phase profiles, focal lengths, aberrations, etc. The model is also valid for spherical microlenses considering radial symmetry.

5.2.3. Focal distance

In the last years, microlenses of many applications are considerably growing in quality and decreasing in prices. However, new approaches and improvements must be necessarily accompanied by characterization systems of the focal length.

Experimental set-up and characterization software

Firstly, focal length definition for microlenses devices must be established. Microlens focus is standardized as the distance from the vertex of the microlens to the focus position [191]. This position is located by finding the maximum power density distribution as a collimated beam comes into the device surface from the backside. That is, the effective front focal length differs from the classical effective focal length since it is measured from the lens vertex. Also, by reducing the size of the lenses with array structures to a micrometric scale, focal length evaluation is not a simple task by means of mechanical measurements made to a surface of limited aperture lens, such as,

reciprocal magnification, focal collimation or auto-collimation. So, further research has been directed toward the study of the Gaussian shape of a laser beam [192], the lateral shearing interferometer in transmission [193] or the boundary-element method (BEM) [194]. Particularly in this thesis, standardized microlens focus definition has been used. Focal length measurements have been tested by the experimental setup shown in Figure 74. The results are no so critical due to plane surface of the LC device. The accuracy of the measurement depends on the micropositioner resolution (40 µm in this case).

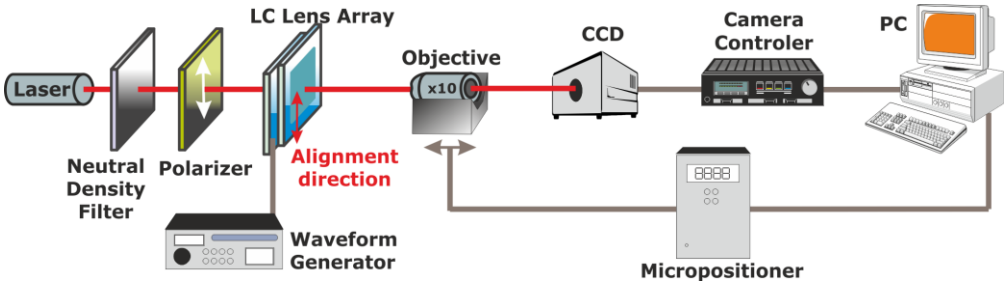

Figure 74. Experimental set-up for measuring focal lengths of lenticular devices.

Focusing properties are captured placing test devices behind a parallel polarizer with the rubbing direction of the lenticular lenses aligned to the main axis of the polarizer. The same laser as previous set-up is used. The studied samples are OLED50NI55-2, 100LPI100NI0 and 200LPI50NI0. A micropositioner has been built to measure the focal length sweeping the position of an x10 objective for finding the focal length. Finally, captured images are recorded by a CCD camera. Figure 75 shows a detail of the procedure for measuring the focal length.

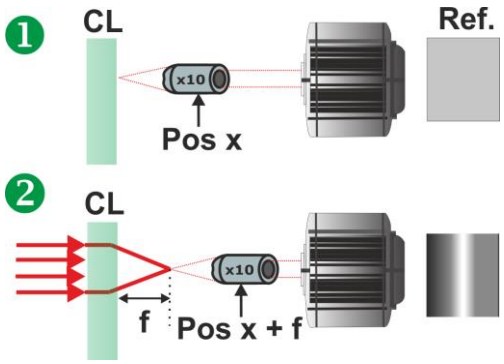

Figure 75. Detail of the procedure for measuring focal lengths.

The procedure involves two steps. The first step consisted of focusing the surface of LC lens, acting as the lens vertex, at an initial position *x*. Next, the micropositioner is remotely controlled for placing the objective a distance f from the initial position *x*, capturing the maximum of the power density distribution.

Experimental results

Firstly, the sample OLED50NI55-2 is characterized. Comparison between focusing properties of a cylindrical LC lens array and a commercial lenticular sheet is shown in Figure 76.

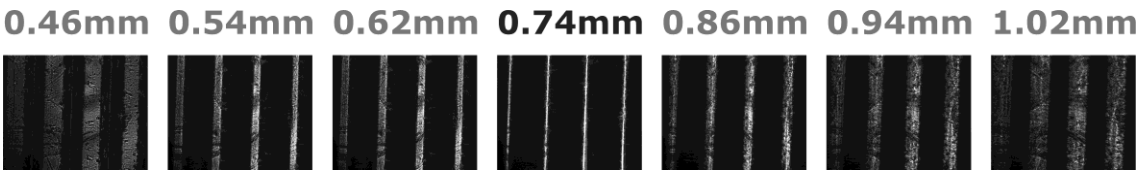

(a) Commercial lenticular sheet.

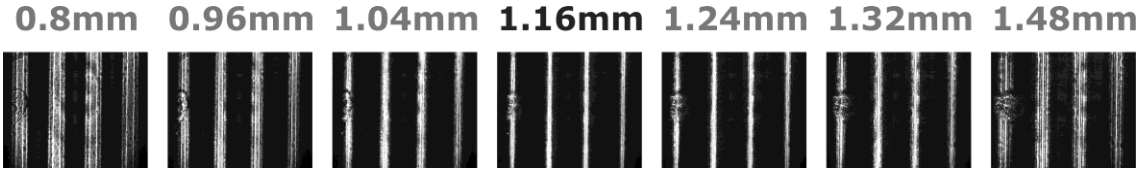

(b) Sample OLED50NI55-2, 1 kHz square signal of 5.5 V_{RMS} is applied.

Figure 76. Comparison between focusing properties of a cylindrical LC lens array and a commercial lenticular sheet.

Focal length of a 100 LPI commercial lenticular sheet is 0.74 mm [Figure 76 (a)]. LC lens array focused the laser beam at 1.16 mm [Figure 76(b)] as a 5.5 V_{RMS} square signal is applied to the control electrode. LC lenses and lenticular sheets were both found to be comparable when focusing a collimated laser beam.

On the other hand, viewing angle of both strategies, for getting 3D effect, has been evaluated. This parameter constitutes a typical feature of each lenticular scheme allowing us to classify the devices for developing suitable applications intended for them. From Figure 60, an estimation of the maximum deviation angle of a ray leaving the edge of an individual lens and reaching the corresponding observer's eye, θ_{max}, can be derived as,

$$\tan\theta_{\max} = \frac{P_P}{f} \tag{72}$$

where P_p is the pixel pitch and f the focal length. By doubling θ_{max}, viewing angle is calculated. After measuring focal lengths, the value of θ_{max} has been obtained from Eq.72. Viewing angle of the lenticular sheet is 19.5° and 14° for the same of the LC array. Both are values for achievable 3D vision applications with viewing angles typically narrower than 30°. However, viewing angle of the LC device is narrower than that of the lenticular sheet due to the designing condition of D is fixed. Certainly, that is a consequence derived from the rule: the narrower the viewing angle, the larger the viewing distance for 3D vision.

Comparing phase shift measurements against focal lengths

As commented above, because LC lenses are actually GRIN lenses, the estimation of the focal length, f_{GRIN}, of the LC lenses is simple, if the focusing of parallel rays is considered. Equation 73 allows us to relate phase shift measurements ($\Delta\phi$) (considering Fresnel approximation and Eq. 68), to focal lengths (f_{GRIN}), in order to confirm the validity of the experimental results for both magnitudes.

$$\left.\begin{aligned}\Delta\phi = \frac{2\pi}{\lambda}\cdot\int_{-r}^{r} n_{eff}(\theta)\,dz = \frac{2\pi}{\lambda}\Delta n d \\ f_{GRIN} = \frac{R^2}{2\cdot d\cdot\Delta n}\end{aligned}\right\} \quad f_{GRIN} = \frac{\pi\cdot R^2}{\lambda\cdot\Delta\phi} \tag{73}$$

Finally, in order to confirm the validity of the experimental focal length measured in the first experimental section, Eq. 73 allows us to obtain focal length (f_{GRIN}) by phase shift measurements ($\Delta\phi$). The same set-up conditions were established for comparing the results, that is, at 5.5 V_{RMS} and 1 kHz square signal. Maximum phase shift from the parabolic profile is $\Delta\phi = 14\cdot 2\pi$ (Figure 69). By Eq. 73 and considering that R is half the lens pitch (285/2 μm), f_{GRIN} = 1.15 mm. This result is similar to that previously measured by means of a focusing scheme (1.16 mm). These results allow us to conclude that both methods are fairly in agreement, proving the validity of the two experiments.

Tunable 3D distance

The tunability of the 3D distance is one of the fundamental objectives of this thesis. In this sub-section the standard 100 LPI and 200 LPI lenses are studied (sample 100LPI100NI0 and 200LPI50NI0).

The focal length is estimated from phase shift and Eq. 73. The 3D distance at which the user would perceive the stereoscopic effect is estimated following Eq. 69. The spot diameter refers to the width of the power density distribution. Only the best focus are considered (spot diameters lower than 10 μm). This only occurs when the phase profile do not have defects (see Figure 70). Finally the "measured focal length" is determined with the set-up explained before (Figure 74).

The results of the focal length, 3D distance, spot diameter and measured focal length are summarize in Table 4 and Table 5. All the measurements have an error caused by the resolution of the micropositioner step.

V_{RMS}	ϕ (2π)	Focal length (μm)	3D distance	Spot diameter(μm)	Measured focal length (μm)
2.6	25	512.03	2.63E-01	4	600
2.4	21	609.56	3.13E-01	4	640
2.2	20	640.03	3.28E-01	4	680
2	15	853.38	4.38E-01	6	840
1.8	12	1066.73	5.47E-01	6	1040
1.6	7	1828.68	9.38E-01	6	1440
1.4	4	3200.19	1.64E+00	4	2840
1.2	2	6400.39	3.28E+00	4	3400

Table 4. Different optical parameters of the sample 100LPI100NI0 (100 LPI and thickness 100 μm).

V_{RMS}	ϕ (2π)	Focal length (μm)	3D distance	Spot diameter(μm)	Measured focal length (μm)
2.6	8	400.02	2.05E-01	3.5	400
2.2	7	457.17	2.34E-01	4	440
1.8	6	533.36	2.74E-01	4	520
1.6	4	800.04	4.10E-01	5	760
1.4	3	1066.73	5.47E-01	7	920
1.2	2	1600.09	8.21E-01		

Table 5. Different optical parameters of the sample 200LPI50NI0 (200 LPI and thickness 50 μm).

The focal distance is plotted in Figure 77. It can be observed how this parameter can be tuned in a small voltage range. This result is the key to control the 3D distance, essential for a portable autostereoscopic device. As every observer has different physical characteristics a tunability of this distance is especially required for a useful device.

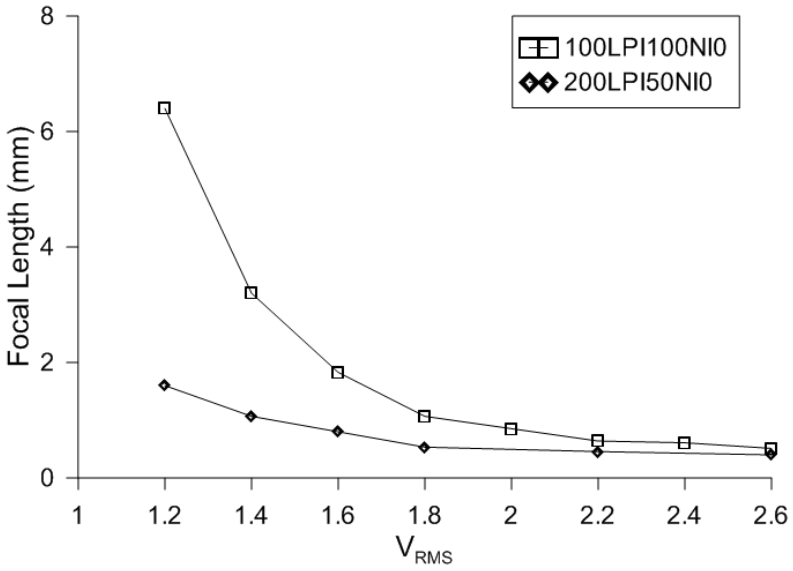

Figure 77. Tunable focal length (100LPI100NI0 and 200LPI50NI0).

Considering the sample 200LPI50NI0, the 3D distance produced by this microlens is plotted in Figure 78. In this example, the pixel pitch of the display is 63.5 μm (400 PPI). This could be used in a 12.19 cm x 6.8 cm with resolution of 1920 x 1080 pixels, very common in the current scenario of mobile telephone. It is observed, a huge tunability of the 3D distance. In conclusion, a good 3D experience could be perceived in a range of 60 cm, more than enough for an average anatomy.

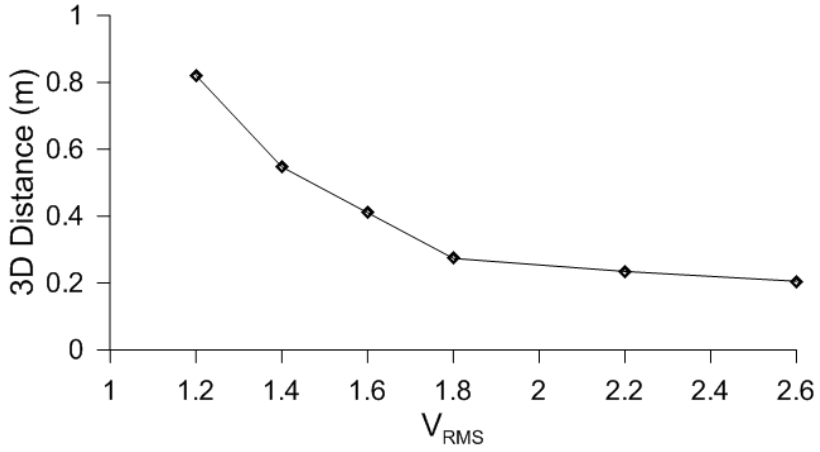

Figure 78. Tunable 3D distance for a possible 400 PPI autostereoscopic display (200LPI50NI0).

5.3. Applications of the micro-optical lenticular array

In recent years, many experimental and theoretical research groups worldwide have actively worked on demonstrating the use of LCs as adaptive lenses for image generation, waveform shaping, and non-mechanical focusing applications. In particular, important achievements have concerned the development of alternative solutions for 3D vision. In this thesis a LC-based 2D/3D autostereoscopic display prototype is proposed for the first time using a modal LC lens array (sample OLED50NI55) placed in front of a display; this array acts as a lenticular sheet with a tunable focal length by electrically controlling the birefringence. The performance of the 2D/3D device is evaluated in terms of the angular luminance, image deflection, crosstalk, and 3D contrast within a simulated environment. These measurements were performed with characterization equipment for autostereoscopic 3D displays (angular resolution of 0.03°).

Some problems as can be the temperature dependence of the LC (that can affect the 3D distance) is controlled by a novel temperature sensor. This sensor can be incorporated easily to the autostereoscopic device because has the same electrode pattern. Finally, other common problem as can be aberrations in this type of systems are also controlled by using complex electrical signals. These three original applications are described in detail in next sections.

5.3.1. Autostereoscopic device

An important advantage of OLED displays is their linear polarization, which is parallel to the columns of pixels. This polarization is used to cancel light reflection from internal electrodes. The LC arrays (sample OLED50NI55) have the alignment layers in the electrode direction (antiparallel configuration), so the molecules are aligned with the polarization of light and take advantage of the LC birefringence. This advantage saves the inclusion of a single polarizer in the prototype. Once the LC lenses are set at the correct dimensions, according to the pixel size, the most important step is to place each lens over two columns of pixels. For this process, a lenticular positioner is designed with OpenSCAD and is fabricated with a 3D printer (Figure 79). This device consists of a fixed base and two adjustable pieces that allow the horizontal and vertical positions to be precisely adjusted. The lenticular lens is controlled by an AC voltage (1 kHz) to preserve the LC characteristics (to avoid the concentration of ions). A simple driver, based on a PIC18F45k20 microcontroller and LM392 comparators, generates square waveforms with tunable frequencies and amplitudes. The entire system is portable if it is supplied with batteries.

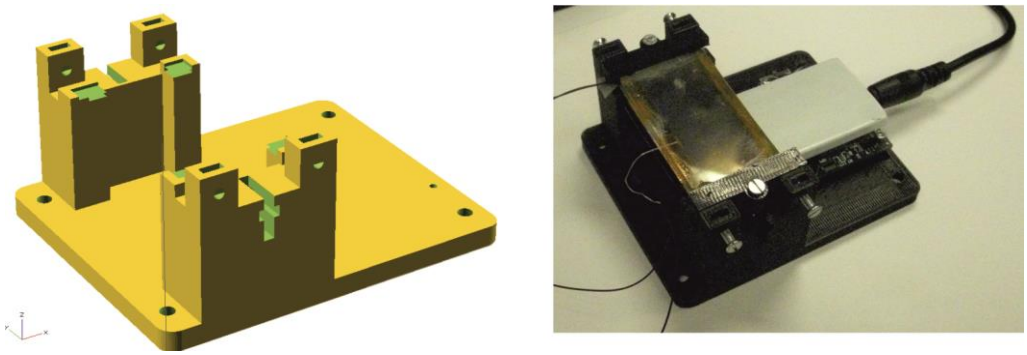

(a) OpenSCAD design. (b) Final prototype.

Figure 79. Lenticular positioner.

Electro-optic characterization

Electro-optic characterization related to 3D vision requires special equipment. This equipment must have the ability to measure light at different angles. To date, only simple characterizations of autostereoscopic systems have been described in the literature. These characterizations are based on photodetectors that are movable along one axis at the optimum 3D distance. Components such as goniometers (movable photometers), which are typically used for displays, have been used; however, such systems have limited angular resolution and position. It may be assumed that these limitations will render the measurements inaccurate in multiview autostereoscopic systems. The main problem in evaluating autostereoscopic displays is discerning which image reaches a particular eye. For this determination, it is very important to distinguish between two rays of incoming light (from a point on the 3D display) with similar directions. Moreover, the uncertainty of the position in the measurement must be smaller than the pupil size (1–4 mm) to make this measurement acceptable, otherwise, the exact information for one eye cannot be known. As shown in Figure 60, the corresponding angle of the pupil is atan(D_p/D), where D_p is the pupil size. Figure 80 presents the relation between this angle, which is equal to the minimum angular resolution, and the observer distance (D).

In a mobile application, an observer distance of 0.3–0.5 m can be considered (vertical dotted lines). If the more restrictive condition is used (pupil size of 1 mm), the minimum angular resolution is 0.19º to 0.11º. For such small resolutions, goniometers cannot be employed, and typical resolutions range from 0.25º (PM-FPMS) to 1º (GC 5000L). In contrast, measurement devices based on Fourier optics usually have a minimum resolution of 0.25º (Ezcontrast XL88MS). This situation requires the use of equipment with resolutions of less than 0.11º. The only equipment on the market that fits these characteristics is the VCMaster3D, which is specifically designed and manufactured by ELDIM for autostereoscopic applications. The setup is simple, as can be seen in Figure 81. For an angular resolution of 0.03º, the observer distance can be as high as 2 m for pupil sizes of 1 mm and 7.6 m for pupil sizes of 4 mm.

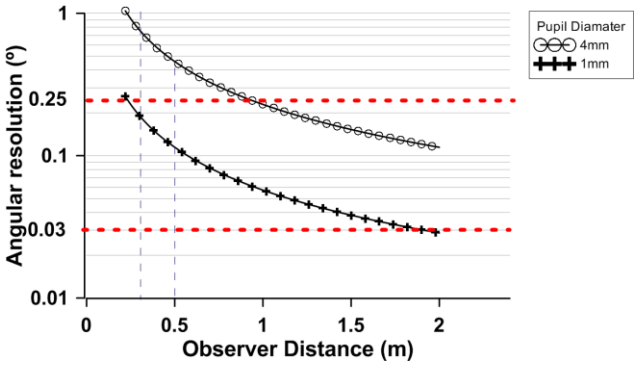

Figure 80. Angular resolution as a function of 3D distance.

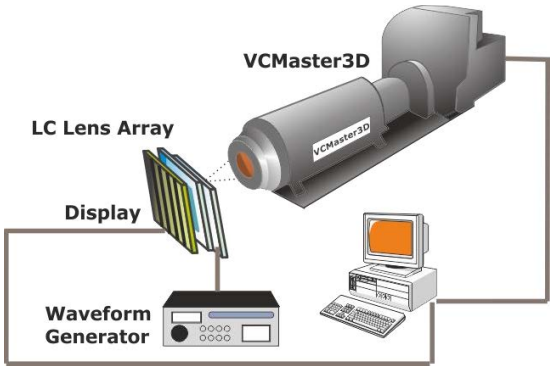

Figure 81. Set-up with VCMaster3D.

Based on the specifications, the autostereoscopic device is placed 1.5 cm in front of the equipment. With this equipment, the angular luminance from the lenticular LC lenses (sample OLED50NI55) is measured with an angular aperture of ± 50º (Figure 82).

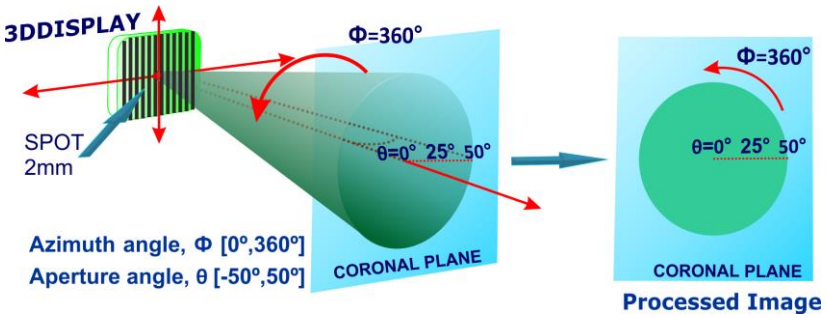

Figure 82. Capture mode of the VCMaster3D.

Light is uniformly distributed in the OLED display. To evaluate the quality of light deviation at different angles, a single special image has been employed. This image is composed of two interlaced images; one column of pixels is black, and the adjacent column is green. The objective is to illuminate only half of each lens and to determine the light deviation. In this approach, the two different views are a black image and a green image for the right and left eyes, respectively. The expected result is depicted in Figure 83.

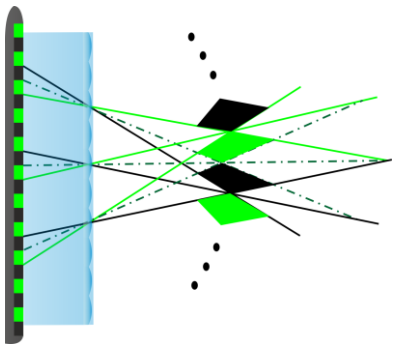

Figure 83. Diagram of the viewing zones caused by a black-white pattern.

The first experiment performed is an angular luminance measurement for different voltages applied to the sample OLED50NI55. In Figure 84, the light can be observed to deviate at different angles.

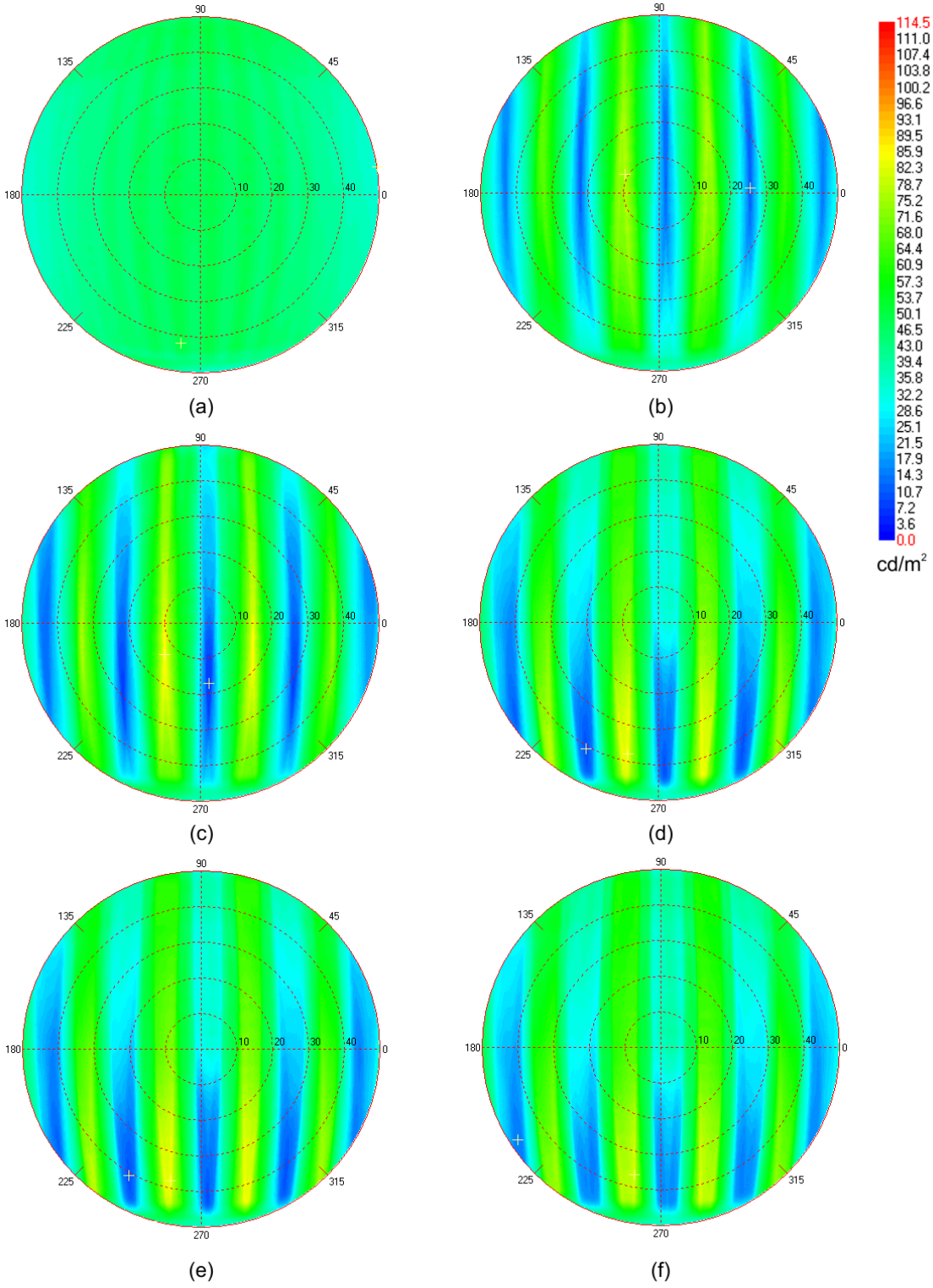

Figure 84. Viewing zones (cd/m²) caused by a black-white pattern for different voltages applied to the LC lenticular sheet. (a) 0 V, (b) 5 V, (c) 7.5 V, (d) 10 V, (e) 15 V, and (f) 20 V.

Different intensity patterns are obtained as a function of the voltage. If no voltage is applied, the light does not deviate. All of the molecules in the LC lenticular array are in the same position, so the array behaves like a common glass. When the threshold voltage is exceeded, a progressive variation in the tilt angle of the LC molecules appears. A response time of 0.5 seconds has been measured in this case (this time is determined by the thickness of the LC layer). This variation produces a gradient in the refractive index and concentrates the light at the focal point. These lenses still have high spherical aberration, so the concentration of light is not high. At 7.5 V, the optimum lens is obtained; in this case, the concentration of light is high (yellow areas), and there are clear separations between the views (blue areas). When this voltage is exceeded, the saturation of molecules at the ends of the lens causes a shrinking effect, allowing light to shine through and causing a decrease in the concentration of light. Additionally, the directivity of the light at different angles is loose.

Crosstalk

In autostereoscopic vision, the crosstalk parameter is used to measure the quality of the generated stereoscopic image. This parameter was first introduced by Montgomery in 2001 [195]. Each eye must see a different image. Nevertheless, when the right eye (or left eye) receives information intended for the left eye (or right eye), crosstalk (χ) is considered to occur. This parameter is defined as the relation between two luminance, corresponding to the incorrect image and the correct image (Figure 85). In an ideal case and with correct implementation, that is, at the correct focal distance for the specifications, there is a distance (Eq. 69) at which an observer will see white columns with one eye and black columns with the other eye. In this case, no unintended light reaches the eye. In contrast, if the lens has some type of defect, some light reaches the wrong eye.

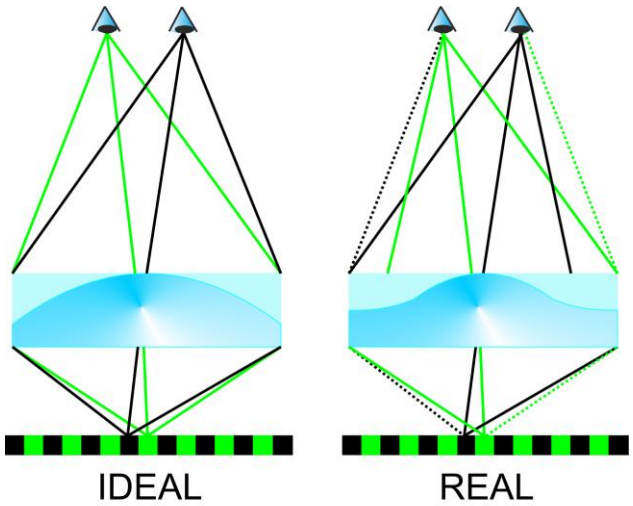

Figure 85. Diagram for the crosstalk produced in ideal and real cases.

To quantify this parameter, a second experiment is performed. In this case, two images (with two interlaced images each) are used. The first case is the same as in the previous experiment. The second case is the inverse of the first pattern in order to place the maximum intensity in the other view. The luminance of each one is defined as $Y_{B\text{-}W}$ (black-white) and $Y_{W\text{-}B}$ (white-black). The voltage applied to the sample OLED50NI55 in Figure 86 is 7.5 V_{RMS}.

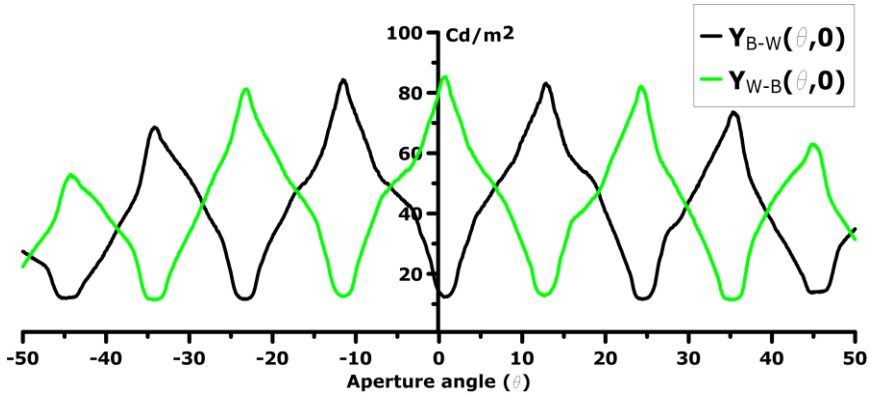

Figure 86. Diagram for the crosstalk produced in the ideal and real case.

In Figure 86, the angular luminance at the azimuth angle of 0º is represented for the two different images ($Y_{B\text{-}W}$ and $Y_{W\text{-}B}$). In this figure, it can be observed the deviation in each half lens of the lenticular sheet relative to the other half. Additionally, the crosstalk can be obtained as a function of the viewing angle. For example, for an angle of 2º, only the light of the white-black image should be observed. However, there is a small luminance from the black-white image at the same position that interferes with the previous image. In this case, the first pattern (white-black) has almost 90 cd/m^2, and the other pattern (black-white) is approximately 10 cd/m^2, so the experimental crosstalk is approximately 10% (Eq. 74).

The main cause of the measured crosstalk is light falling on the CCD from wrong pixels. This light deviation could be minimized by adjusting the resistivity of the layer in order to exploit the quadratic range of the LC birefringence. To this end, the deposition of the Nickel in the SiO_2 layer must be further investigated. A slight decrease in the resistivity is suggested for the reduction of the spherical aberration produced by a flatness effect in the lens center. Another cause of crosstalk is the deviated position of each lens of the array from the corresponding two columns of the 2D display. It can be corrected using a positioner system with micrometric movement resolution. Despite this, the crosstalk is small enough to clearly see two different images in the two eyes (Figure 89) and to experience the autostereoscopic effect.

Angular Crosstalk

For this experiment, four images with different patterns are used. One image is white-black and another is black-white to measure the right and left views. Additionally, black-black and white-white are used to determine the on-off transmission. Although the VCMaster3D is placed at 1.5 cm, these four measurements of the angular luminance allow the contrast associated with each eye to be estimated and allow the distribution of light to be calculated at a particular position for the left view, right view, and 3D contrast (the distribution of the 3D autostereoscopic effect). The angular contrast for each view is [196],

$$C_R(\theta,\varphi)=\frac{Y_{BW}(\theta,\varphi)-Y_{BB}(\theta,\varphi)}{Y_{WB}(\theta,\varphi)-Y_{BB}(\theta,\varphi)}=\frac{1}{\chi_R}$$
$$C_L(\theta,\varphi)=\frac{Y_{WB}(\theta,\varphi)-Y_{BB}(\theta,\varphi)}{Y_{BW}(\theta,\varphi)-Y_{BB}(\theta,\varphi)}=\frac{1}{\chi_L} \quad (74)$$

where Y_{BW} is the luminance of the black-white image in the polar coordinates determined by θ, φ, and so on. The employed equations are the inverse of the crosstalk equation; however, this measure is standard in display applications. The 3D quality is optimized when the C_R and C_L are maximized at the same point; therefore, the 3D contrast can be estimated by

$$C_{3D}(\theta,\varphi)=\sqrt{C_R(\theta_R,\varphi_R)\cdot C_L(\theta_L,\varphi_L)} \tag{75}$$

The product is used because good contrast is simultaneously required for each eye to obtain reasonable quality [197]. The square root maintains the dimensionality of the quantity for comparison with other display standards. Following these equations, the spaces for the angular contrast distributions are displayed in Figure 87.

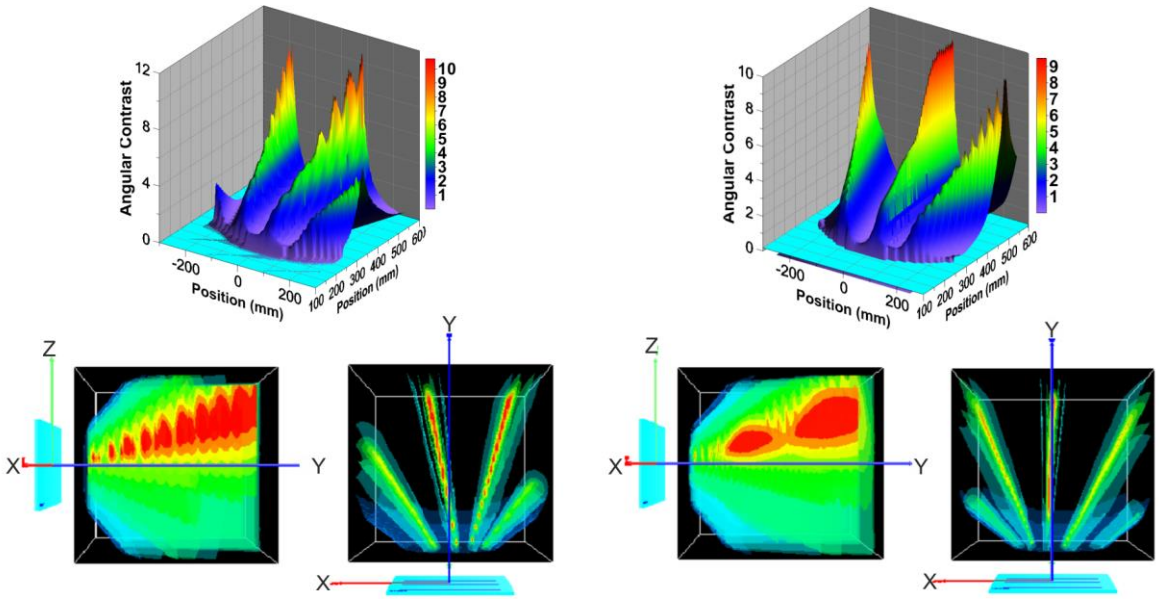

(a) Right view. (b) Left view.

Figure 87. Angular contrast.

In the first diagram, a 3D graphic presents the angular contrast (C_R, C_L) in the XY plane. Smoothing has been applied to improve the comprehensibility of the figure. In the other figures, the autostereoscopic display is represented by a small blue rectangle, and the angular contrast is represented in the x, y, and z coordinates in a simulated environment. The color scale ranges from blue to red for low and high contrast, respectively. This measure indicates the angles and positions at which the left view and the right view can be observed with better quality. In this case, the left view can be observed at three different angles. The best position is located in front of the display, slightly inclined from the XY plane. The right view can be observed at 15º relative to the YZ plane and at the same inclination from the XY plane as for the left view. From the previous data and Eq. 75, the 3D contrast (C_{3D}) is obtained.

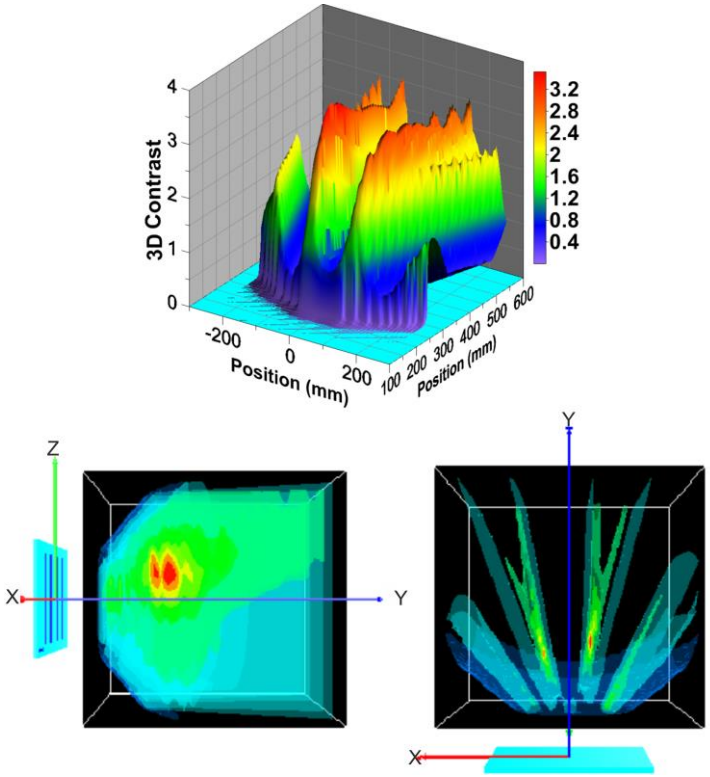

Figure 88. 3D angular contrast.

In Figure 88, the red areas also indicate the positions at which the autostereoscopic effect has the best quality. For the same voltage at the LC lenticular sheet (7.5 V_{RMS}), there are two clear viewing zones at -15º and 15º relative to the YZ plane and at a distance between 30 and 35 cm. This distance agrees well with the previous design. There are two other viewing zones at -45º and 45º; however, the 3D contrast is very low. This contrast ratio, which is inversely proportional to the crosstalk, can be improved in the manner described in the previous section.

Image Display

To illustrate the previous measurements, different captures are displayed. As shown in Figure 89, each view deviates at different angles. To measure this luminance, only columns of pixels switched on and off are required. In this final experiment, two images interlaced in one file are displayed in the autostereoscopic display. These images are not designed to create an autostereoscopic effect, but are sufficiently different to be clearly differentiable.

(a) Interlaced image. **(b) Two captures at different angles.**

Figure 89. Flip effect demonstration.

Two different images are observed when the viewing angle is changed. A digital camera placed at different angles is used to capture the images. If autostereoscopic images are required, this content must be generated with a special camera. The major requirement for this camera is the inclusion of two different objectives in the same transverse plane (like two eyes).

In summary, a 2D/3D switchable prototype based on an OLED display, LC microlenses, and a lenticular positioner has been designed and manufactured. The luminance measurements show 10% crosstalk between the views. The position between the display and the LC lenses is critical to the reduction of this parameter. The angular contrast measurements reveal an optimum distance of 30 cm to 35 cm for 3D vision. The obtained results are preliminary but demonstrate how this lenticular LC lens array could be applied in the next generation of autostereoscopic displays. By optimizing the structural parameters and improving the lenticular positioner, a tunable autostereoscopic display with low crosstalk could be manufactured.

5.3.2. Temperature sensor

One of the problems of LC technology is the temperature dependence of its electro-optical parameters. In the case of the proposed autostereoscopic device, the main problem of the refractive index change with temperature is the change of the 3D distance (by changes in the focal length). For this reason, a device sensing this parameter is essential in order to maintain the same focal distance at different temperatures. If the temperature changes but is known, the refractive index can be easily estimated. Then, the device can modify the voltage to adapt the focal distance to this new temperature. Moreover, temperature monitoring has been an indispensable tool for sensing changes in many different processes and systems, over time, in both research and industrial applications. Many diverse sectors, such as transport, control, automobile, industrial machinery, energy, medical, food, etc., are profiting from the incorporation of temperature sensor equipment. Currently, the temperature sensors range is broad enough to categorize them according to different criteria; the main one is contact and non-contact sensors (pyrometers). Nevertheless, the temperature dependent magnitude (sensing magnitude) and the inherent manufacturing technology are the rules mainly considered to classify them. In some way, this classification estimates the global extent of the conditioning and measurement circuits on the electrical design. The sensing magnitudes are usually connected to the output signals by a relationship derived from an interrogating circuit. Those signals often are in the electrical domain, such as a voltage, a current or a resistance; other times they are in the optical domain, for example, an optical transmittance or a reflectivity. Conventional contact temperature sensors can be either metallic (resistance temperature sensors, thermocouples, bimetallic structures) or semiconductor (thermistors, diodes, chip integrated circuits) based transducers. The highest sensitivities are typical of the semiconductor sensors with relative sensitivities ten times greater than that for metallic sensors. However, semiconductor thermistors are known to have a strong nonlinear relationship between temperature and resistance/voltage outputs, but they are used to more accurately measure the output signals. Particularly thermocouples exhibit a high linearity, in a wide temperature range. In the last years one of the most used temperature sensors is the chip integrated circuit. This sensor, based on integrated transistors, generates higher output than thermocouples, is more accurate than thermistors and is completely linear. As the circuitry is sealed it is not subject to oxidation. The main disadvantages are the self-heating and the slow response. On the other hand, the pyrometers use the radiation from the very hot objects as a sensing magnitude through non-contact measurements.

An alternative technology for temperature sensing is the use of LC. Despite cholesteric temperature sensors being the most common approach, in the last few years some attempts

employing nematic LC have been carried out. Most of these sensors are based on optical properties of a nematic LC and have the refractive index as the sensing magnitude. When the LC is introduced in some specific structures such as Fabry-Perot cavities, or photonic crystal fibers (PCF) [198] [28], lambda shifts result as the output signal. In the first case, sensitivities around 1 nm/ºC are obtained for maximum temperatures of 65 ºC [29]. For the case of PCF, some works have demonstrated sensitivities of 0.22 nm/ºC [199], -3.8 nm/ºC [200] and even 54 nm/ºC but for very small temperature ranges (34 ºC to 35.5 ºC) [30]. These systems are complex to build (filling the PCF is not an easy task) and require complex interrogating circuitries (a spectrum analyzer is usually required). Other approaches, based on the same sensing parameter, produce intensity variations on light passing through the sensor, as the output signal. For example, measuring the transmitted light in structures with plasmonic particles [201]. In summary, all of these systems have small temperature ranges and the sensitivities are usually low.

The parameter used to determine the LC interaction with electrical signals is often expressed by permittivity, ε, (see section 2.1.2). This parameter is also temperature dependent on as shown in Figure 90 [135].

Very few works can be found in the literature that exploits the permittivity as a sensing magnitude. A nematic LC sensor based on the LC electrical properties was first reported in 2012 [27]. This system generates a variable frequency as an output signal; the result is a temperature-frequency transducer. This kind of sensor has been demonstrated to have broad temperature range. Some disadvantages are that it also needs an interrogating circuit to measure the signal and the resulting sensitivity is directly proportional to the permittivity change with temperature, by a relationship derived from the interrogating circuit.

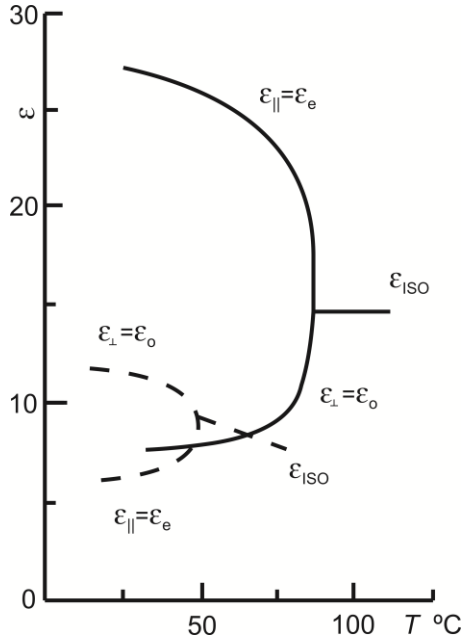

Figure 90. Typical behavior of the real permittivity temperature dependence for two nematic LC with positive (solid line) and negative (dashed line) permittivities.

In this thesis, a novel temperature sensor based on nematic LC permittivity as a sensing magnitude, is presented. This is one of the main reasons to include a second comb type array in the proposed design (Figure 31 and Figure 32). The used samples are 100LPI40NI0 and 100LPI40NI60. One of the comb electrode is supplied by an AC voltage source (V_1); the other electrode, comb 2, is used for measuring a voltage drop that senses the temperature dependence of the sensor. The experimental data has been obtained for ranges from -6 ºC to 100 ºC. Despite this, following the LC datasheet, theoretical ranges from -40 ºC to 109 ºC could be achieved. As it was predicted by the analytical study, the micrometric size of the proposed structure produces a high output voltage. The inclusion of a high resistivity layer increase more the sensitivity. Moreover the voltage's sensitivity to temperature response can be controlled by the applied voltage. This response allows temperature measurements to be carried out without any amplification or conditioning circuitry, with very low power consumption. Despite this sensor has been designed to work in LC-based autostereoscopic devices, it could be used in LCD displays, LCD projectors, portable equipment or any application where its properties procure an advantage with respect to current available sensors.

Experimental Set-up

The experimental set-up is based on a LTS350 heating and freezing stage, handled by a TP 94 system controller. For better accuracy, two additional precision centigrade temperature sensors have been added to the system. These redundant sensors avoid possible losses in calibration of the controller system and take into account possible temperature gradients caused by the lack of thickness homogeneity of the LC sensor. This gradient could be avoided with the use of thinner glasses (0.175 mm, for example). The complete set-up (Figure 91) is controlled by an automated MATLAB programmed for this purpose. This program processes the measured data and directly show some graphs of temperature dependence of voltage

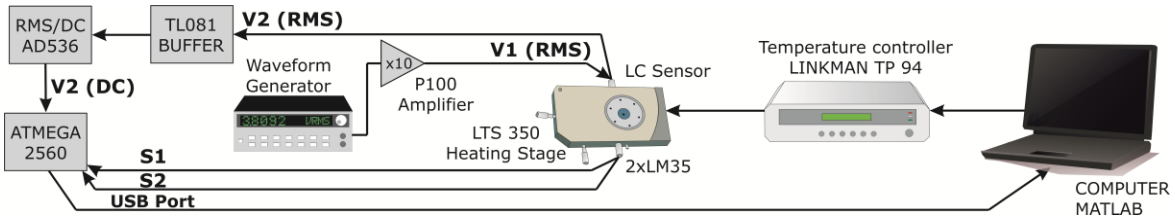

Figure 91. Experimental set-up for characterization of the LC temperature sensor.

The heating stage increases the temperature at a rate of 1 ºC per minute. The source of supply is an AC voltage controlled via a HP 33120A waveform generator and connected to V_1, through a high voltage broadband amplifier (P100). The output is 10 times the input voltage. AC square voltage signals have been chosen and no more than 50 V_{RMS} can be generated considering the limited voltage output (±50 V). As commented before, two LM35 temperature sensors measure the temperature, T, inside the stage. These silicon sensors are placed in each LC sensor surface and the outputs (S_1 and S_2) are connected to two analog inputs of ATMEGA 2560 microcontroller. This one sends data through USB port, and then data are processed by a MATLAB program. Three samples per minute are taken. The temperature changes the permittivity values, and consequently the voltage at V_2. This voltage is connected to a TL081 based buffer. The output of this buffer is converted to a DC signal by an AD536 RMS/DC converter. This chip converts the RMS (root mean square) value to the same absolute value in DC voltage (for example 1 V_{RMS} to 1 V_{DC}). The output of this chip is also connected to microcontroller's analog input and the measured data is stored by MATLAB.

Frequency study

Firstly, the sample 100LPI40NI0 is studied. In order to find the optimum operation frequency, a sweep frequency study has been performed. Three representative frequencies, for four different voltages, are displayed in Figure 92 in a temperature range between 20 ºC and 100 ºC (below the clearing temperature). Due to the large number of samples only some measurements are identified by symbols. All the measurements have been done by lowering and raising the temperature. No differences on the offset error have been observed between both experiments, concluding that the device has not hysteresis. The linearity of the response differs as a function of the supply voltage frequency. For example for $V_1 = 4$ V_{RMS} the linear regression coefficients (R^2) are 38%, 99.4% and 99.3% for frequencies of 100 Hz, 1 kHz and 10 kHz respectively. Furthermore, for $V_1 = 8$ V_{RMS}, R^2 is 86%, 98.8% and 99.6% for frequencies of 100 Hz, 1 kHz and 10 kHz respectively.

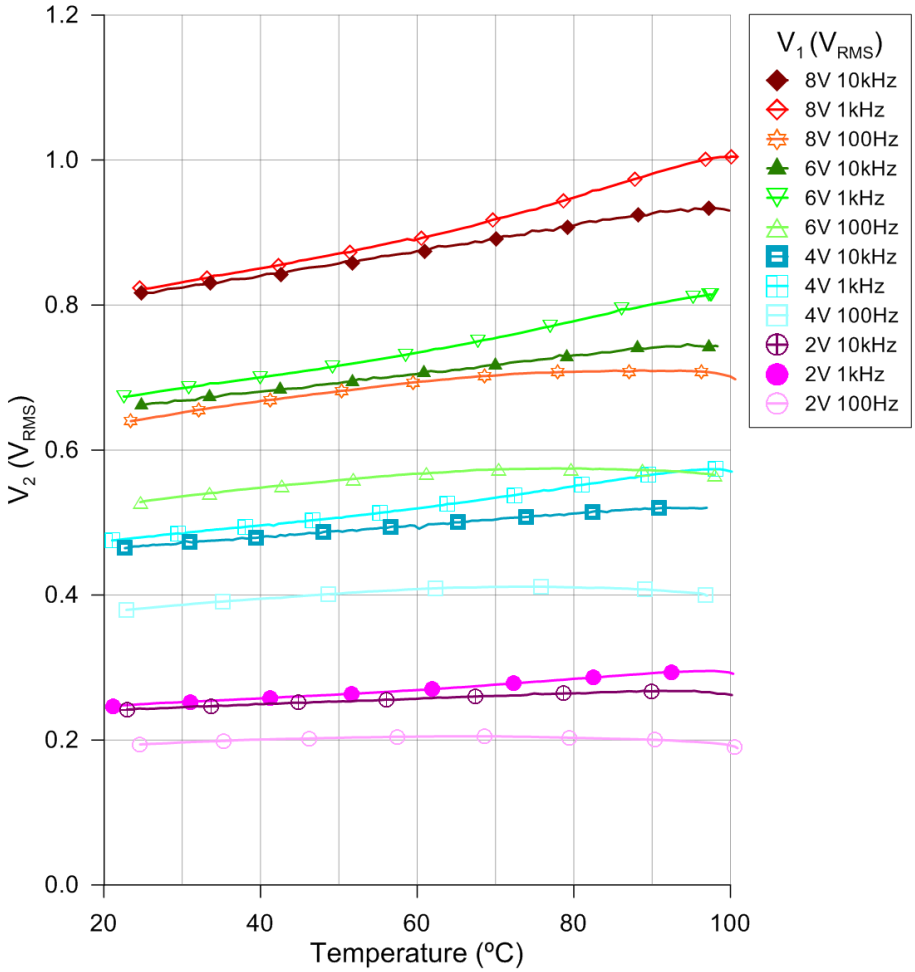

Figure 92. Temperature dependence of the LC sensor response for several voltages and frequencies at V_1.

The best linearity is observed for 1 kHz and 10 kHz. From the sensitivity point of view, these results have shown an optimum behavior at around 1 kHz. Looking at Figure 51, it can be observed the most capacitive behavior at this frequency. For 1 kHz the ε' is predominating so, one reason for this behavior could be different changes of the value of the ε' with temperature than the ε''. On the other hand, an increase in the voltage's sensitivity to temperature is observed for greater voltages. Following the reasoning of the previous argument, this is probably caused by greater changes with temperature of ε'_e than ε'_o (as it was observed in Figure 90). This study leads us to a broad range temperature measure at 1 kHz voltage frequency for different voltages.

Voltage study

As noted above, the higher the voltage the higher the sensor sensitivity. In Figure 93 the voltage, V_1, has been increased from 2 V_{RMS} to 50 V_{RMS}, in the temperature range from -6 ºC to 100 ºC, approximately. As with previous results, no hysteresis has been observed. There is an increase of the sensitivity with voltage but at the cost of losing linearity. For low voltages the linear regression coefficients are 99%. For higher voltages curves are fitted to a linear curve for comparison purposes (there is an almost linear relation between sensitivity and voltage). Despite this, the non-linear curves can be easily fitted to a three grade polynomial.

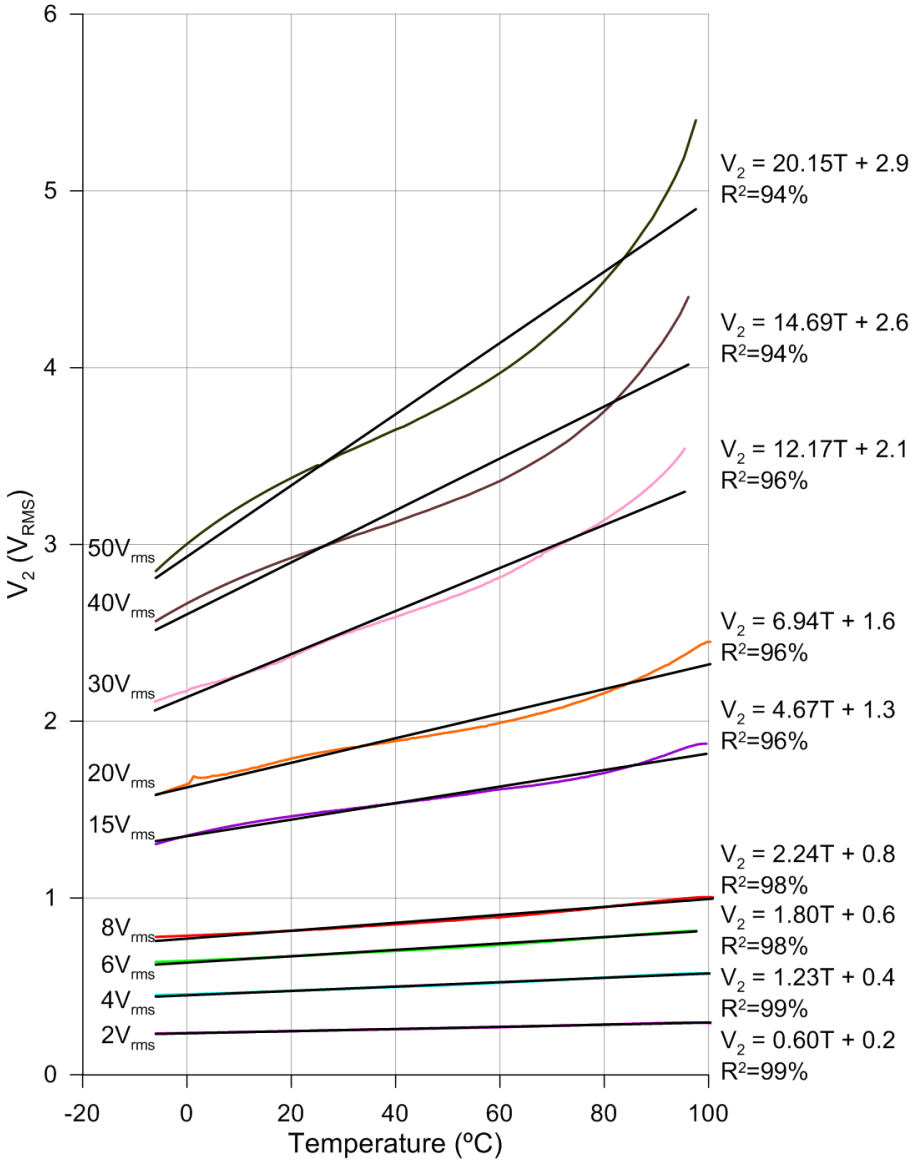

Figure 93. Temperature dependence of the LC sensor response for several voltages at V_1. Linear fits indicate the approximate sensitivity and R^2.

Modal temperature sensor

Another option is to include the high resistivity layer (sample 100LPI40NI60). As it can be deduced by the analytical model, the inclusion of a high resistivity layer suppress the effect of C_1 so the permittivity is only in one operand of the division (Eq. 47). For this reason, the sensitivity is increased. The results are compared to that obtained with sample 100LPI40NI0. These results confirm the theoretical prediction.

The first experiment consists of variations of the applied voltage frequency with a fixed amplitude (Figure 94). All the measurements have been done in an increasing and decreasing direction and no hysteresis has been observed. The resolution is limited by the LM35 sensors (0.5 ºC). For 1 kHz the sensitivity is highest. At this frequency the real permittivity (ε_{LC2}') is predominant, so one reason for this behavior could be greater changes of the real permittivity with temperature than the imaginary permittivity (ε_{LC2}'').

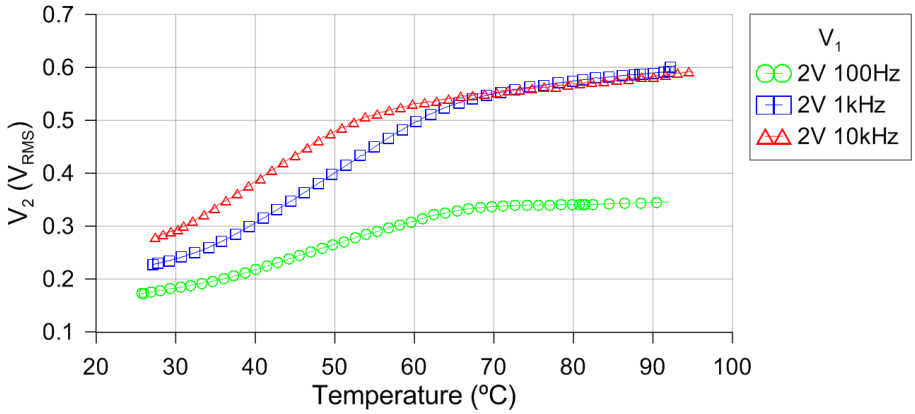

Figure 94. Frequency dependence of LC sensor response.

In order to demonstrate the Ni nanometric layer effect, the results of sample 100LPI40NI0 are compared in Figure 95.

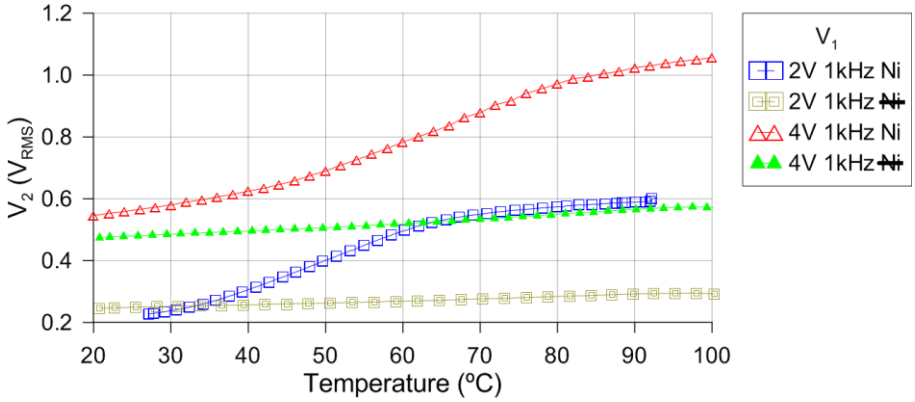

Figure 95. Voltage (RMS) dependence of LC sensor response for cells fabricated with Ni layer and without it.

For the case of the sensor without Ni, high voltages have been tested. Maximum sensitivities of 33 mV/ºC, for certain temperature ranges (60 ºC - 95 ºC), have been obtained. Further experiments have to be made in order to study the operating limit of the Ni sensor. The maximum current allowed by this layer will be a key parameter in order to apply more voltage. Higher sensitivities than the sensor without Ni are expected. The applied voltage (V_1) affects the sensitivity because the extraordinary component is more temperature dependent, $d\varepsilon'_e(T)/dT$ greater than $d\varepsilon'_o(T)/dT$ (Figure 90). This fact indicates that a homogeneous alignment, where all the molecules are perpendicular without any applied voltage, could lead to higher sensitivities for very low voltages.

As can be observed in Figure 96, the use of a Ni nanometric layer resulted in significant differences in the sensitivity. The difference between these two types of sensors and a linear fit are shown. The temperature sensitivity of the device with the Ni nanometric layer is almost six times greater, demonstrating a significant increase of this one with regard to the other structure. Possibly the introduction of R_{sqNi} parameter in Eq. 47 (resulting in the suppression of C_{LC1}) makes the sensitivity increase. As C_{LC1} is also temperature dependent and is dividing C_{LC2}, if it had been considered, it would have reduced the sensitivity considerably.

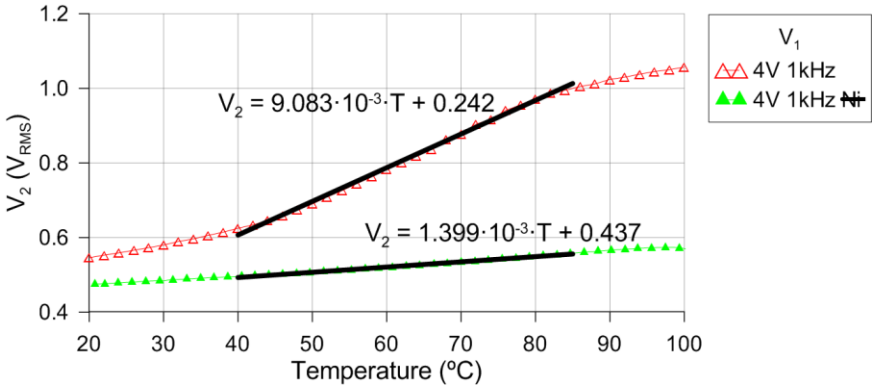

Figure 96. Linear fittings to sensor responses.

In summary, a novel idea in the research field of temperature sensors has been presented. The sensor response has been completely characterized. This new LC temperature sensor has several advantages with respect to other previous related LC sensors. In some aspects, this sensor is an improvement on the characteristics of some commercial temperature sensors. For example, it has higher sensitivities than silicon sensors (for certain supply voltages). In addition, it has more linearity than thermocouple sensors. The problem of thermo-couples or RTD with self-heating is avoided due to its low consumption. There is no need for any amplification due to its high output voltage. The structure is simple and has an active area easy to scale. Coplanar electrodes can be easily patterned at very small dimensions yielding miniaturized, reproducible, and ultimately low cost devices. An increase in sensitivity has been observed with the alignment process.

The incorporation of a resistive layer to this structure improves the sensor characteristics. The inclusion of a special alignment layer that results in a perpendicular alignment of the LC molecules could result in high sensitivities for low voltages. This idea have to be further investigated. This sensor can be used in autostereoscopic displays based on LC lenses, LCD displays, LCD projectors, portable equipment or any application where its properties procure an advantage with respect to current available sensors. This work has presented and characterized a novel idea, and opened new avenues for research.

5.3.3. Aberration compensation

One of the main drawbacks of systems using lenticular arrays is the generation of aberrations. In this thesis, it is demonstrated how the suitable choice of the applied voltage (complex electrical signals) can modify phase aberrations caused by both, the non-ideal distribution of the electric field and the nonlinear electro-optic response of the LC with voltage. The samples used are 100LPI100NI0 and 200LPI50NI0.

Monochromatic aberrations are caused by the geometry of the lens. Since P. L. Seidel defined the five main aberrations (Spherical Aberration, Coma, Astigmatism, Curvature of Field and Distortion), this classification has formed the basis of reference to the categorization of lens quality as defined by optical designers. Interferometrists often like to represent wavefronts as Zernike polynomials. This mathematical tool has been widely used because, unlike other polynomial set, they are orthogonal over a unit circle and represents balanced classical optical aberrations, yielding minimum variance over a circular pupil. These characteristics are lost when non circular pupils are employed. Some schemes for square pupils have obtained square polynomials from the orthogonalization of circle polynomials [202], using a circle inside the square. This procedure has the disadvantage of losing the part of the wavefront that falls outside the circle. Some other studies

overcome this problem by defining a unit square inside the circle [203]. In those studies, closed-form expressions for the low-order polynomials are used. These expressions are orthonormal over a determined pupil by using the recursive Gran-Smidt orthogonalization process [204]. Among the advantages of the last technique, it is the correspondence between polynomials' coefficients and the peak value of each aberration. Besides, it can also be employed for different types of pupils [205]. Despite this, there are some drawbacks in order to evaluate optical systems with rectangular or square pupil. Zernike coefficients can be obtained from the orthonormal coefficients but these ones are really designed to use it on rotational symmetric optics. They do not represent balanced classical aberrations and do not have the physical significance as those in the aberrations of rectangular optics. To overcome the last drawback, Liu *et al.* have developed a complete study by introducing 2D Chebyshev polynomials (related to some Seidel aberrations), instead of Zernike polynomials to characterize optical rectangular apertures [206]. In the referred work, a Schmidt corrector plate is characterized. Another interesting applications could be other types of lenses with non-rotational symmetry, the cylindrical ones. Chebyshev polynomials constitute a useful orthogonal basis for optics of rectangular apertures, making them an attractive option for characterizing the proposed device. The main reason for employ this type of polynomial, is the rectangular correspondence between polar conformal mapping of Zernike and Chebyshev forms.

Theoretical fundamentals of aberrations in rectangular optical systems

As mentioned above, the wave aberration is typically represented by using a decomposition in Zernike polynomials for square pupils in the analysis of aberrated systems. Particularly, the wave aberration *W(x,y)* for noncircular pupils (optical rectangular apertures) can be expanded in terms of Chebyshev polynomials that are orthonormal over the pupil [206],

$$W(x,y) = \sum_j A_j \cdot F_j(x,y) \tag{76}$$

where F_j are the 2D Chebyshev polynomials and A_j, are the aberration coefficients related each to a classical aberration of the wavefront. This expression is also named Chebyshev polynomial fit. Here x and y are the coordinates in the surface of the pupil.

The aberration coefficients, A_j, following the property of orthogonality, are estimated by a double integral of the wave aberration multiplied by the Chebyshev functions and divided by a weighting function (Eq. 77). The coefficients, A_j, can be determined directly when the wave aberration is a continuous function or, numerically, when the wave aberration is a data set. In this latter case, the most common approach is to use a numerical quadrature routine.

$$A_j = \int_{-1}^{1}\int_{-1}^{1} \frac{W(x,y)F_i(x,y)}{K\sqrt{1-x^2}\sqrt{1-y^2}}\,dxdy \tag{77}$$

The 2D Chebyshev polynomial set, F_j, is obtained by multiplying 1D classical Chebyshev polynomials by one another; the complete set of 2D polynomials is defined in ref. [206]. The polynomials that have a physical meaning similar to those used by Zernike polynomials, in classic optical systems, are listed in Table 1, in Cartesian representation up to 6th order. Like the Zernike

polynomials, they range from -1 to +1 over a defined interval and have a sinusoidal behavior as interferometric fringe maps. The normalized pupil, on the xy plane covers an area with square shape. For rectangular apertures the series have to be scaled. A normalization constant *K*, to maintain the orthogonality of the polynomials is also considered. The graphical representation of the polynomial terms F_j are shown in Figure 97.

Order	Chebyshev coefficients (A_j)	Polynomial un-normalized form (F_j)	Aberration	Normalization constant (K)
0	A_0	1	Piston	π^2
1	A_1	x	Tilt X	$\pi^2/2$
	A_2	y	Tilt Y	$\pi^2/2$
2	A_3	$2x^2-1$	X astigmatism	$\pi^2/2$
	A_4	xy	45º astigmatism	$\pi^2/4$
	A_5	$2y^2-1$	Y astigmatism	$\pi^2/2$
3	A_6	$4x^3-3x$	Primary coma X	$\pi^2/2$
	A_9	$4y^3-3y$	Primary coma Y	$\pi^2/2$
4	A_{10}	$8x^4-8x^2+1$	Primary spherical X	$\pi^2/2$
	A_{14}	$8y^4-8y^2+1$	Primary spherical Y	$\pi^2/2$
5	A_{15}	$16x^5-20x^3+5x$	Secondary coma X	$\pi^2/2$
	A_{20}	$16y^5-20y^3+5y$	Secondary coma Y	$\pi^2/2$
6	A_{21}	$32x^6-48x^4+18x^2-1$	Secondary spherical X	$\pi^2/2$
	A_{27}	$32y^6-48y^4+18y^2-1$	Secondary spherical Y	$\pi^2/2$

Table 6. 2D Chebyshev polynomials set related to classical aberrations [206].

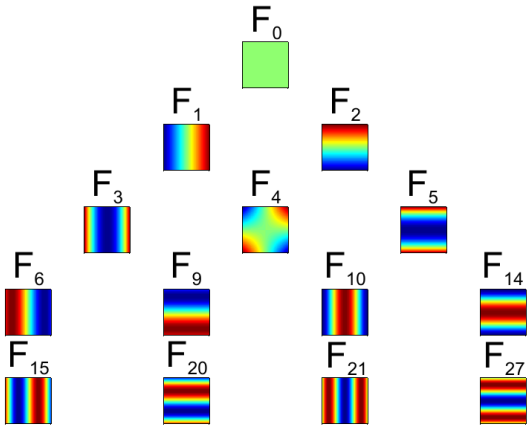

Figure 97. 2D Chebyshev polynomial set, F_j, related to classical aberrations.

In order to characterize the coefficients of the aberrated optical system, the measured wavefront is fitted to the Chebyshev polynomial set to subsequently derivate the coefficients A_j. The method to relate the measured wave aberration and the Chebyshev polynomial set is described below. Specific software has been programed to solve the problem. Finally, in order to check the measured wave aberration, a particular experimental arrangement has been implemented. It measures the optical wavefront and the aberrations coefficients, A_j, are extracted. In the following section the procedure is explained in detail. The aberration effects on the image can be estimated by studying the optical path length of the LC device.

Software development

To determine the solution of the system of linear equations, Eq. 76, where the unknown coefficients are A_j, a simple and fast method has been used. The proposed problem is solved using MATLAB software. The algorithm formulates a matrix equation and uses the *matrix left division* (*mldivide*) instruction. This operator employs different procedures depending on the coefficient matrix and computes the numerical solution in the least squares sense. The use of digitized interferograms could cause some errors in the final solution, but considering the number of sampling points produced by the CCD, these ones are negligible in comparison with the fitting error. The estimation of this error is described in subsequent sections. In order to evaluate the proposed algorithm and demonstrate the use of a LC device as an aberration compensation device, in rectangular micro-optical systems, the samples 100LPI100NI0 and 200LPI50NI0 are characterized by using the set-up described in section 5.2.1.

Experimental arrangement

Based on the proposed software (section 5.2.1), the lenticular array is analyzed in terms of the individual elements. For this purpose, a couple of electrodes for each micro-optical element is located and the area of interest is selected (254 μm × 254 μm). The image of this area is processed and the phase is unwrapped. With the 3D phase maps, aberration coefficients, A_j, are extracted by using Chebyshev polynomials. Also, some of the classical Seidel aberrations are evaluated by changing the applied voltage. Finally, the fit error is also estimated.

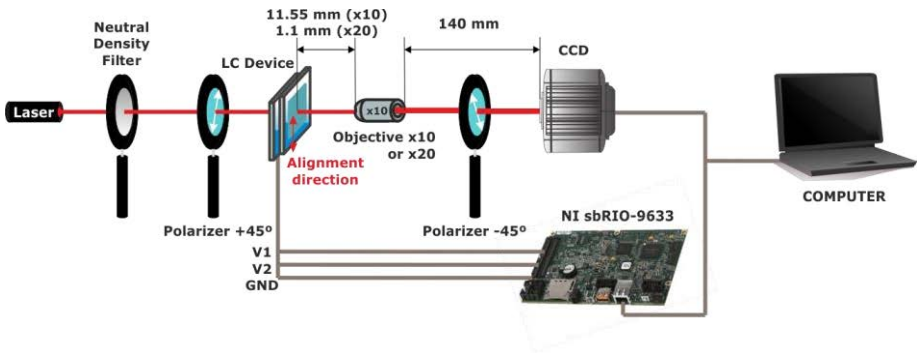

Figure 98. Experimental set-up for characterizing a tunable LC cylindrical micro-optical array for aberration compensation.

The system is placed in an optical table as shown in Figure 98. The experimental set-up is similar to that used in section 5.2.1 but changing the waveform generator and distances. It consists of: a He-Ne laser source (632.8 nm), neutral density filters, a linear polarizer at 45º, a LC sample with the alignment direction at 90º, a ×10 microscope objective, another polarizer at -45º and a

B/W CCD digital camera (effective no. of pixels 1344×1024). All the angles are referred to the horizontal direction of the table plane. Given the micrometric size of each optical element, LC arrays are placed onto a special micropositioner with micrometer control of the step via computer. Furthermore, function of the microscope objective is to be used like an optical zoom that allows visualizing each element in the CCD (x10 and x20, in the case of 100 LPI and 200 LPI respectively). In order to generate three complex electrical signals, a driving module has been designed and built. It consists of a custom electrical phase shift waveform generator that uses an NI sbRIO-9633 module. This module is an embedded control and acquisition device that integrates a real-time processor and a Xilinx Spartan-6 LX25 FPGA with four 12-bit analog output channels (±10 V). The LC arrays are connected to the FPGA and are switched by 1 kHz square signals. The characterization software for the phase extraction was described in section 5.2.1.

Estimation of aberration coefficients

In this section the process of the aberration estimation is shown. In this case, the 100LPI100NI0 sample is studied. The first step executed by the program is the 3D phase map extraction. Phase maps connect the phase shifts in radians with the position *(x,y)* on the active area. The area between two electrodes is first located by means of the computer program. The x and y axis, which range from 0 to 254 μm, are converted to normalized units (-1 to 1). Resulting phase shift diagrams are extracted from interference patterns of Figure 99(a); 3D (x, y, z) and 2D (x, y) maps are shown in Figure 99 (b) and (c) respectively. These graphs indicate the maximum phase shift as well as the different shapes of the phase profiles for different voltages.

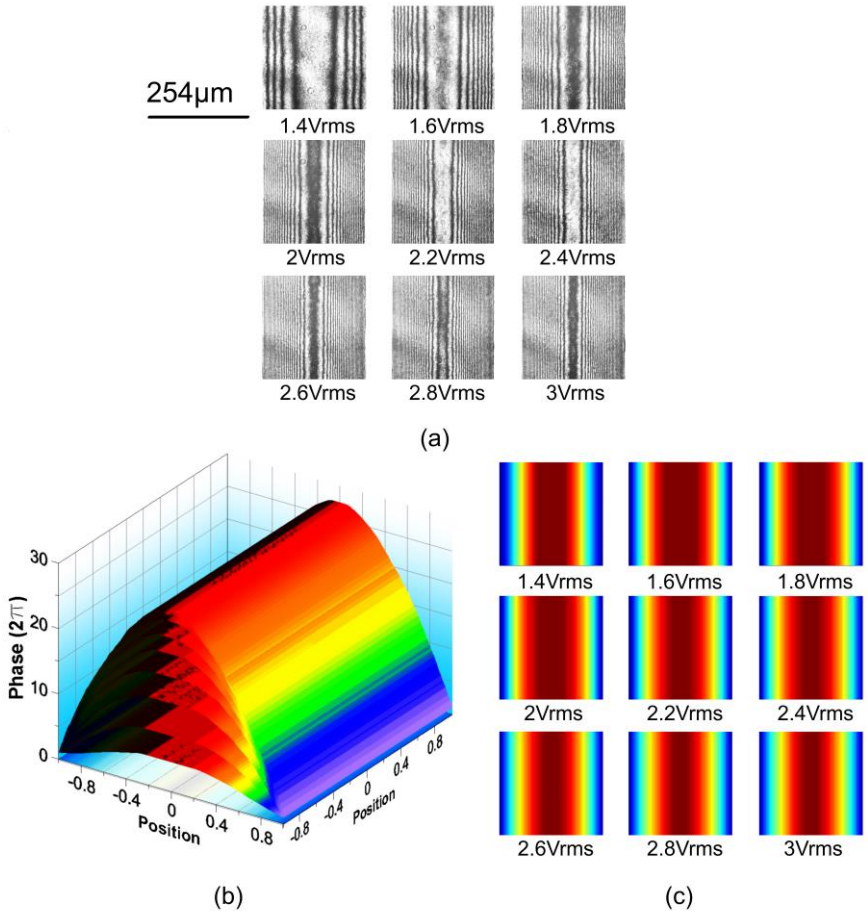

Figure 99. Experimental wavefront for 100LPI100NI0 (normalized), *W(x,y)*. (a) Interference fringes (b) 3D phase maps. (c) 2D *(x,y)* phase maps.

In the phase maps a complete tunability of the wavefront is observed. As stated previously, there are no shrinking or plateau defects both at the sides and center of the active area, respectively, due to the application of the theory to avoid phase defects proposed in section 2.2.2. On the next step, the experimental wavefront surfaces, *W(x,y)*, are estimated from the 3D phase maps (Eq. 70). For this, the process commented on section 4 is used. The result is the different experimental wavefront surfaces as a function of voltage. After that, these wavefronts are related to the Chebyshev polynomials by Eq. 77. The resultant Chebyshev aberration coefficients, A_j, have been displayed in Figure 100. Astigmatism coefficient has been suppressed in this figure (because it is very high compared to the others) and is studied individually in the next section.

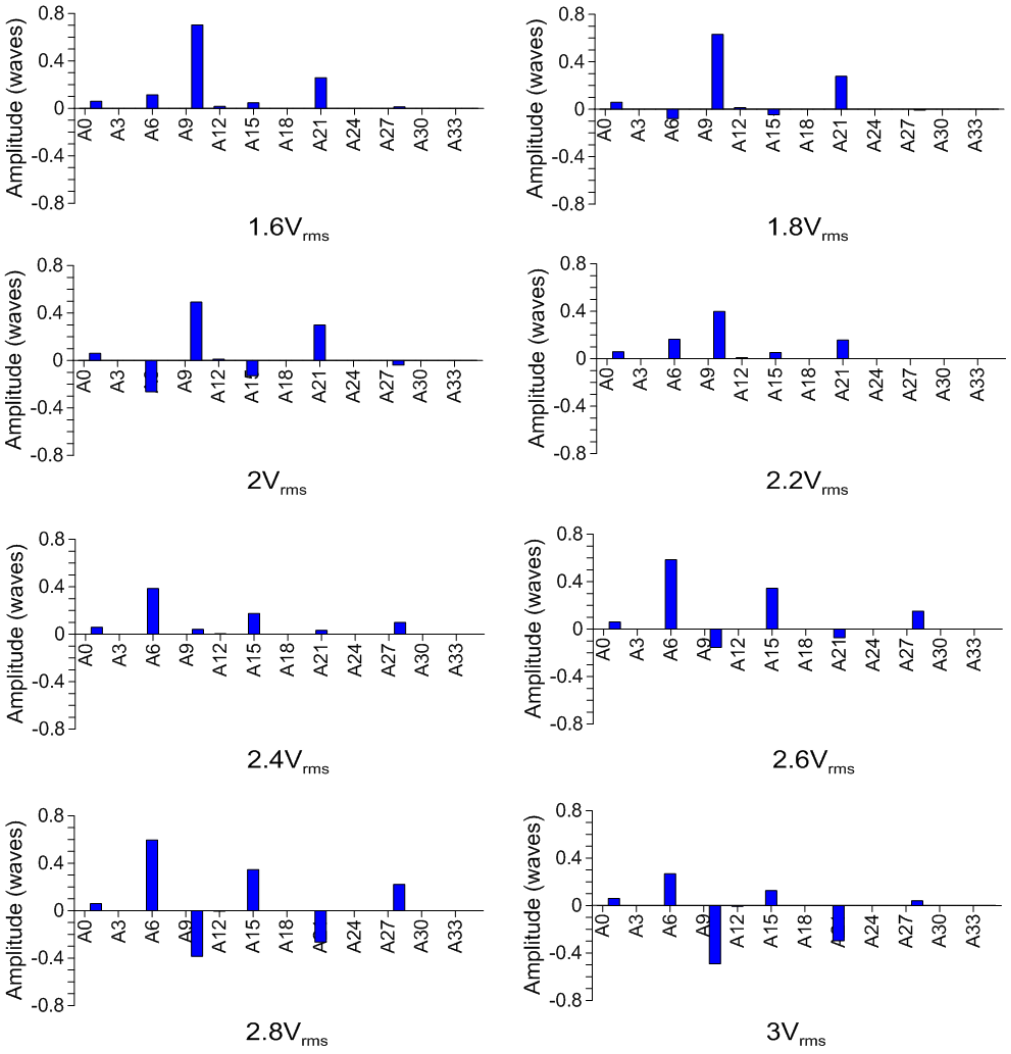

Figure 100. Amplitude of 36 Chebyshev aberration coefficients, A_j, for different voltages applied to the LC tunable micro-optical array (100LPI100NI0).

Chebysev coefficient can be both positive and negative, depending on the orientation of the deformation. As can be seen, there are some coefficients whose amplitude stands out from the others. These are the ones corresponding to spherical (A_{10}, A_{21}) and coma (A_6, A_{15}) aberrations in the *x* axis for the primary and secondary terms. Also, the aberrations can be controlled by means of the voltage applied to the LC array. For a better comprehension, each coefficient is shown as a function of voltage on independent graphs (Figure 101 and Figure 102).

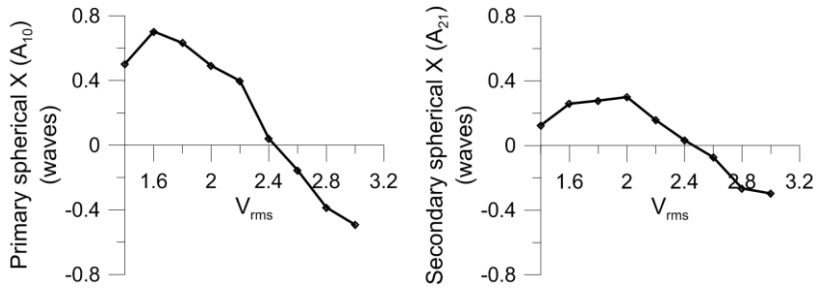

(a) Primary spherical X (A_{10}). **(b) Secondary spherical X (A_{21})**

Figure 101. Amplitude of spherical aberration coefficients as a function of voltage (100LPI100NI0).

The spherical aberration causes the rays of light coming from different apertures (of different microlenses in the LC array) to focus at different planes, resulting in resolution losses. Unlike spherical lenses, which are symmetric in both axis, cylindrical lenses are symmetric either in *x* plane or *y* plane. For this reason, this aberration receives a new type of denomination, spherical X or spherical Y. In this case, due to the position of the LC micro-optical element along Y direction (see Figure 61), spherical aberration X is considered. There is a tunable range from -0.6 to 0.8 waves. For some specific voltage, this aberration can even be suppressed, achieving an ideal lens.

The coma aberration coefficients, A_6 and A_{15}, are shown in Figure 102. These two coefficients are related to coma; it causes an effect of different focusing of raylights in off-axis directions in an extended lens, causing a wedge shape at the image of a point source. In this case, the coma aberration can be compensated in the amplitude range of -0.4 to 0.6 waves, for voltages from 2 to 2.6 V_{RMS} respectively.

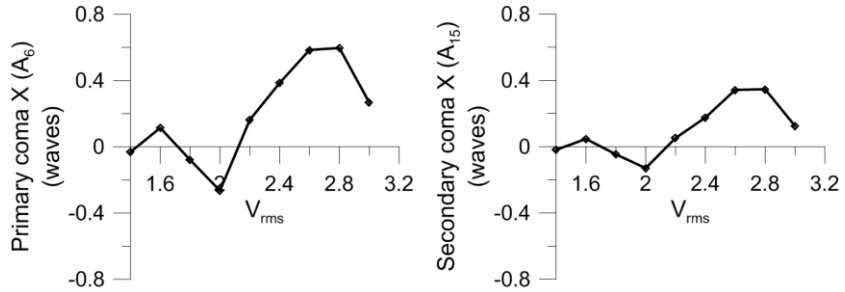

(a) Primary coma X (A_6). **(b) Secondary coma X (A15).**

Figure 102. Amplitude of coma aberration coefficients as a function of voltage (100LPI100NI0).

The resulting amplitudes of the different aberration coefficients, for the LC cylindrical micro-optical elements, extend from positive to negative values as a function of voltage applied to the LC device. This versatile tunability of the coefficients suggests, at least in principle, the very high potential of these devices to be used as aberration compensators particularly for cylindrical micrometric optical systems.

Particular attention has been paid in this study to the astigmatic aberration coefficient (A_3), due to its utility in correcting the astigmatic deviations, for example, for autostereoscopic applications for 3D vision. In fact, there is a direct proportionality between the astigmatic aberration coefficient [Figure 103(a)] and the focal length of each cylindrical micro-optical element of the array. In Figure 103(b) the focal length obtained by the Fresnel approximation ($2\pi \cdot |A_3|/\lambda$) [Figure 103(b)

"A_3"] is compared to the focal length obtained from the captured interference patterns [Figure 103(b) "FP"]. Also the associated RMS error is shown in Figure 103(c). As can be observed the higher the voltage the lower the difference. As the astigmatism is predominating for higher voltages the effect of the other aberration in the wave amplitude is depreciable. For this reason, by using only the astigmatism coefficient in the Fresnel approximation equation, the result is similar to the focal length obtained from the fringe patterns. The equations of the polynomial un-normalized form for X and Y astigmatic aberrations are proportional to a cylinder equation, as described in Table 6.

The results of the aberration characterization, in terms of this parameter, determine that the astigmatic aberration coefficient, A_3, can be tuned in a broad range from -0.5 to -6.5 waves, as shown in Figure 103(a). Therefore, this outcome indicates that the device could be used as a tunable astigmatic device for removing the astigmatism intrinsic to the lenticular sheets of the devices in the application for which it is intended. This is the reason for the normalized size of the lenticular array manufactured.

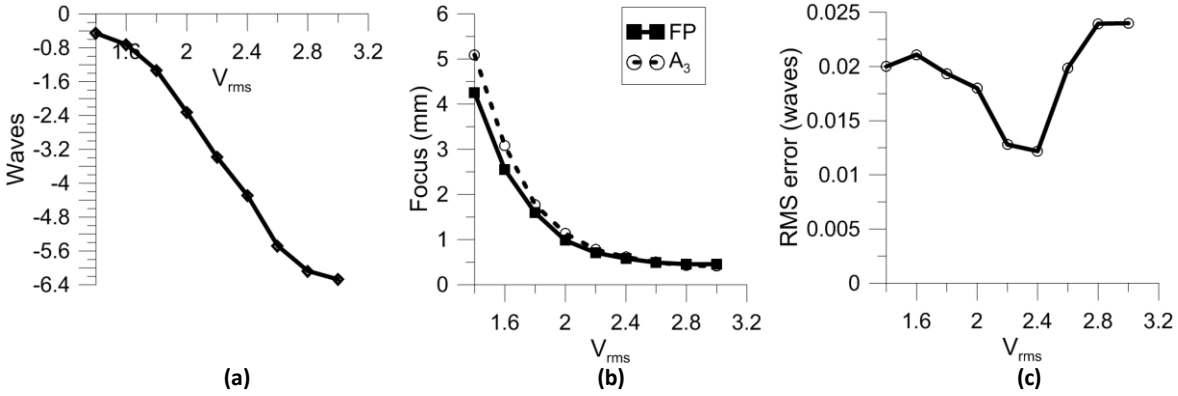

Figure 103. Different derived parameters of 100LPI100NI0: (a) Amplitude of astigmatism X aberration, A_3. (b) Focal distance as a function of voltage (FP from interference patterns and A_3 from astigmatism coefficient). (c) RMS error.

A very linear and high sensitivity is obtained. With a small range of voltage ($1.4V_{RMS}$-$3V_{RMS}$) a huge tunability is obtained (6 waves). The result is a sensitivity of 3.75 λ/V_{RMS}. This indicates that the individual elements of the array could be used in microscopy systems. This device can help to reduce the system aberration and the complexity of the set-up.

Independent control of aberrations

In the previous section, a broad control over astigmatism has been demonstrated. Other aberrations are maintained between -0.6 to 0.8 waves. Manipulation with any of the selected aberrations is accompanied by an appearance of other aberrations. In this section, selectivity in formation of aberrations is demonstrated. For this, four hypothesis are investigated. The use of different harmonics, complex electrical signals, over-voltage control and a combination of the previous two.

In this case, the 200LPI50NI0 sample is used. With this configuration, two different electrical signals can be applied at the sides of the active area. Firstly, the same experiment as in the previous section is carried out (in phase electrical signals, $V_1 = V_2$). The results are shown in Figure 104.

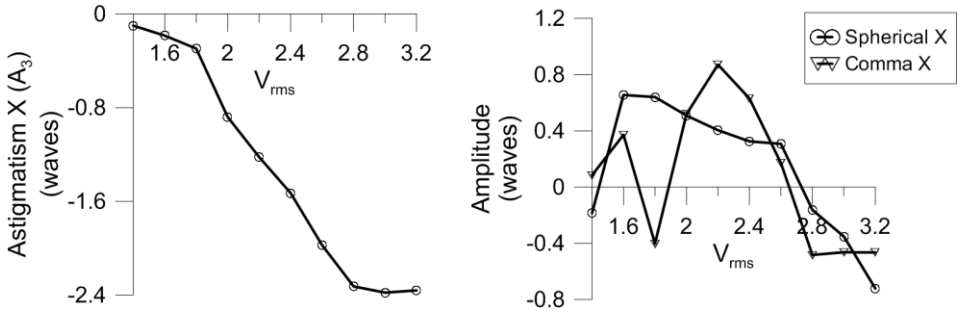

(a) Astigmatism X. **(b) Spherical X and coma X.**

Figure 104. Amplitude of aberrations as a function of voltage (200LPI50NI0).

As can be observed, the astigmatism behavior is very similar to the 100LPI100NI0 sample. The only difference is that in this case only half of the amplitude can be achieved (half of the phase retardation due to having half of the thickness). As in the previous section, the control over the astigmatism is accompanied by the appearance of a decreasing spherical aberration and an oscillation coma aberration.

Among the four hypothesis suggested below, the use of harmonics has not had satisfactory results. The LC permittivity has a small dispersion of the permittivity (at electrical frequencies) so very high frequencies (>100 kHz) have to be applied in order to observe changes in the optical phase profile.

The second experiment is based on the observation of a saturation regime for some specific coefficients (for voltages higher than 2.8 V_{RMS}). The phase shift reaches a maximum at the sides (related to the saturation voltage). Despite this, there is a curve before the birefringence is saturated (in a small voltage range, 0.6 V_{RMS} in this case). This curve affects the shape of the phase profile near to the electrode region while the amplitude is almost constant. For this reason, a saturation in some coefficients is observed (astigmatism and coma) while spherical aberration is modified. As can be seen in Figure 105, astigmatism is maintained in -2.4 waves while coma is -0.4 waves. These aberrations could be compensated by other optical elements while at the same time the spherical coefficient can be corrected in 1 wave by using only an increment of 0.6 V_{RMS}.

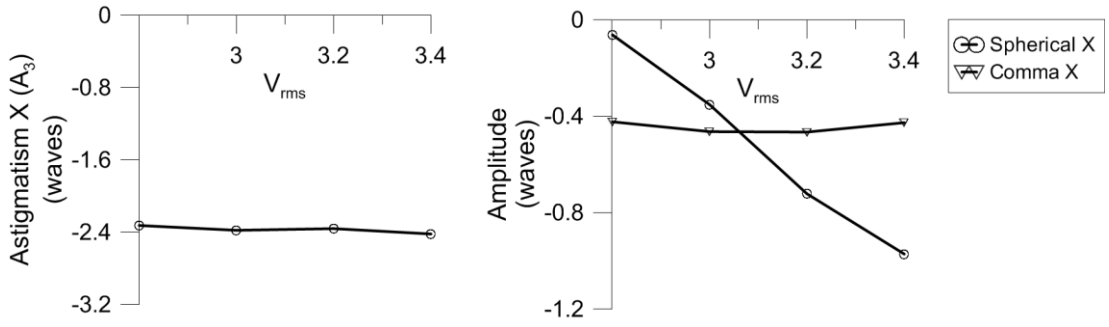

(a) Astigmatism X. **(b) Spherical X and coma X.**

Figure 105. Independent control of spherical aberration (200LPI50NI0).

The third experiment uses complex electrical signals to control the phase profile. When the upper comb-type finger electrodes (V_1 and V_2) have an electrical phase shift of 180º with respect to

each other, the signals are cancelled at the center of the electrodes. From 0º phase shift to 180º phase shift the voltage at the center is controlled while the voltage at the sides is the same. With this effect, the phase amplitude in the center of the active area is modified. When the electrical phase shift is increased the voltage gradient (between the center and the sides) is increased, as well as the phase amplitude. For this reason, the astigmatism is also increased (keeping the other aberrations in a reasonable margin). In this specific case, V_1 = 1.8 V_{RMS} and V_2 = 1.8 V_{RMS} but phase-shifted from 45º to 180º. As is demonstrated in Figure 106, the astigmatism can be controlled in more than 2 waves for an electrical phase shift between 45º and 180º. The other aberrations are maintained in a range of ± 0.2 waves.

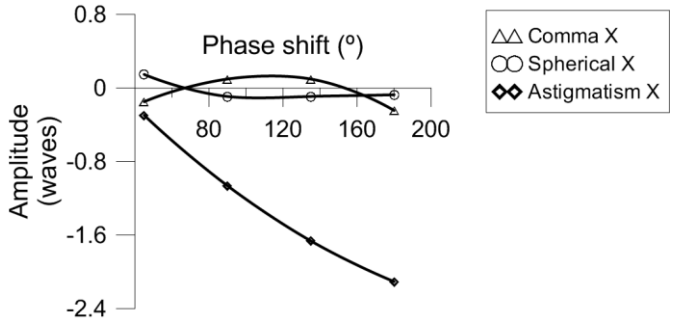

Figure 106. Independent control of astigmatism aberration (200LPI50NI0).

Finally, the combination of the two previous experiments has been studied. For this, a phase-shifted electrical signal (180º) is carried out at an over-voltage regime (from 1.8 to 4.5 V_{RMS}). The results are very interesting, the spherical aberration is almost suppressed while the aberration astigmatism is maintained at a constant value (Figure 107).

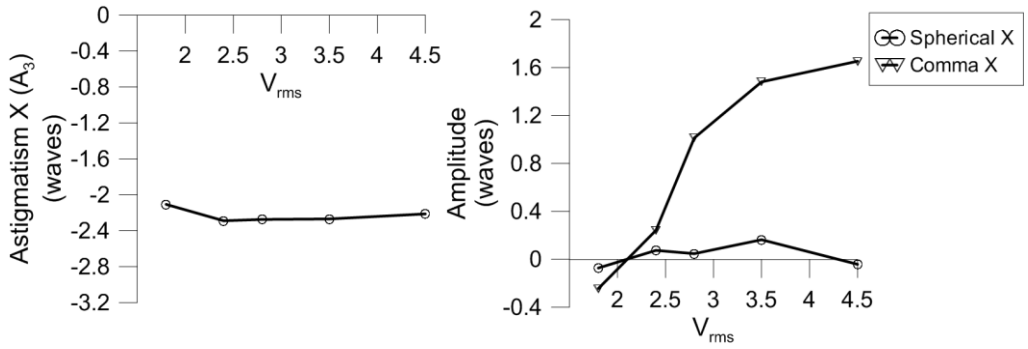

(a) Astigmatism X. **(b) Spherical X and coma X.**

Figure 107. Independent control of coma aberration (200LPI50NI0).

The physical explanation is in the voltage profile produced by the complex electrical signals. As in the previous experiment, the phase shifted electrical signals produce a zero voltage at the center of the active area. When the voltage is increased in the electrodes, the birefringence experiences the typical curve preceding the saturation region. In this case, the curve of the threshold voltage is maintained by the complex electrical signals while the electrode region suffers from the curve of the saturation region. For this reason, the shape of the phase profile is curved at the sides and the center, while the phase amplitude is almost constant. Some aberrations as spherical and

astigmatism are maintained constant while the amplitude of the coma is increased (because a phase profile with a coma type curve is produced).

The combination of both over-voltage and phase-shifted electrical signals open up endless possibilities. Unlike astigmatism coefficient, which always has a decreasing tendency, other aberrations have several zero crossings. This can be used to achieve an astigmatism with zero aberrations. The use of a simulation model (taking into account the Chebysev polynomials and the Frank-Oseen equations) could lead us to design the necessary electrical signals to obtain specific aberration coefficients. This idea has to be further investigated.

In summary, a novel method to extract aberrations in adaptive LC phase-only passive elements have been described. An aberration compensation device for rectangular micro-optical systems has been designed and fabricated. This could be very useful to control aberrations in autostereoscopic displays based on spatial multiplexing. Experimental results of its electro-optic behavior has been presented. A complete independent control over the spherical and coma aberration has been demonstrated. Also, an independent control over the astigmatism aberration has been demonstrated in a broad range. For some specific voltage the aberrations can be reduced to minimum values, achieving an ideal lens. The use of a simulation model (taking into account the Chebysev polynomials and the Frank-Oseen equations) to design the necessary electrical signals to obtain specific aberration coefficients has to be further investigated. Moreover, as with other related cases, the use of arrays could improve the image quality in some types of optical systems. The device could also be very useful for optical elements with micrometric size and rectangular aperture when each element of the array is used independently. The resulting fitting error has been measured, resulting in less than 0.013 λ.

6. Advanced micro-optical phase modulators

By using an advanced configuration of the patterned electrode proposed in previous chapters, other liquid crystal based devices working as micro-optical phase modulators have been developed. The first device is a solution for one typical problem of portable autostereoscopic devices. For these kind of devices, some aspects have to be taken into account. For example, the possibility of vertical and horizontal viewings and the need to change the 3D distance for different observers. As original contribution of this thesis a microlens array with rotary axis and tunable capability is proposed and experimentally demonstrated.

Although the main aim of this work was the manufacturing and characterization of liquid crystal lenses to work in autostereoscopic devices, the deep knowledge of the electro-optical properties of theses device have led to design novel devices to control the phase of light. Among these, adaptive axicons and optical vortices are relevant from both, the scientific and the technological point of view. Indeed, these devices may be used in many practical applications such as optical tweezers, particle trapping and optical communications.

6.1. Rotary micro-optical lenticular array

In the last year, the use of portable devices has grown rapidly. Everything indicates that in the near future most of the multimedia content will be displayed in mobiles or tablets. For these kind of devices, some aspects have to be taken into account. As the observer usually has the device in his own hands, the 3D distance is considerably lower than with big displays [42]. This requires a higher optical power. As every observer has different physical characteristics a tunability of this distance is especially required for a useful device. To solve the problem of optical power some solutions are thick LC devices [42], embedded polymer lens [207] or polymeric lenses [208]. Another common characteristic of this kind of device is the possibility of vertical and horizontal viewings. One proposal uses a modal LC lens to control this parameter [12]. This structure is based on a modal LC array, like the one proposed in this thesis [46] but for a micrometric size. Due to the micrometric size, the resistivity is not high enough to create a voltage gradient when all electrodes are at the same voltage. A ground voltage at the center of each lens is used to have a voltage gradient, reducing the advantage of tunability.

In this section, as original contribution of this thesis a microlens array with rotary axis and tunable capability is proposed and experimentally demonstrated [45]. The sample is 200LPIROT. This device is simple and reconfigurable by low voltage signals. No high resistivity layers or embedded materials are needed. The key of this invention is the use of phase shifted electrical signals. Thanks to these signals, a zero crossing voltage is produced in the center of each microlens without additional electrodes. This device can be used in the next generation of mobile displays with autostereoscopic capability. An interesting effect has been observed that could be of use in integral imaging displays. When the electrical signals are in phase, the generation of concentric fringes indicates a spherical lens with square aperture. This matches perfectly with the shape of conventional pixels. This idea has to be further investigated.

Structure and operating principle

The structure comprises two indium tin oxide (ITO) coated substrates. The ITO coating is patterned with the 100 LPI design (Figure 32). Unlike previous devices, the ground and upper electrode are patterned. As can be seen in Figure 108 (a), the substrates are arranged so that their electrodes are in orthogonal position with respect to each other. The substrates are separated by a 50 μm spacer made of Mylar sheets. The resulting cavity is filled with a nematic LC MDA-98-1602. The LC is used as an adaptive phase-only modulator so no twist of the molecules is necessary. For this reason, a planar alignment is used (see section 3.3.3). The active area of each microlens, red area in Figure 108 (a), is generated between two consecutive electrodes. This area has a width of 127 μm.

The operating principle is based on two physical requirements. The first one is a low enough impedance between electrodes in order to have a quasi-linear voltage gradient between the center of the active area and the electrode [see Figure 108(b), Voltage]. For this, a low distance between electrodes (micrometric size) is required. This impedance generates a quasi-linear voltage distribution from one electrode to another, for electrodes in the same substrate. Higher impedances cause the voltage to drop close to the electrode. The second requirement is phase shifted electrical signals. Specifically, the electrical signals in one substrate are required to have 180º of phase shift between electrodes. At the same time, the other two electrodes on the opposite substrate are connected to 0 V_{RMS}. If it is translated to complex notation, the resulting voltage distribution in the

upper side has a ramp shape, from V_1 to $-V_2$. If $V_1 = V_2$ the voltage has a zero crossing at the center of the active area.

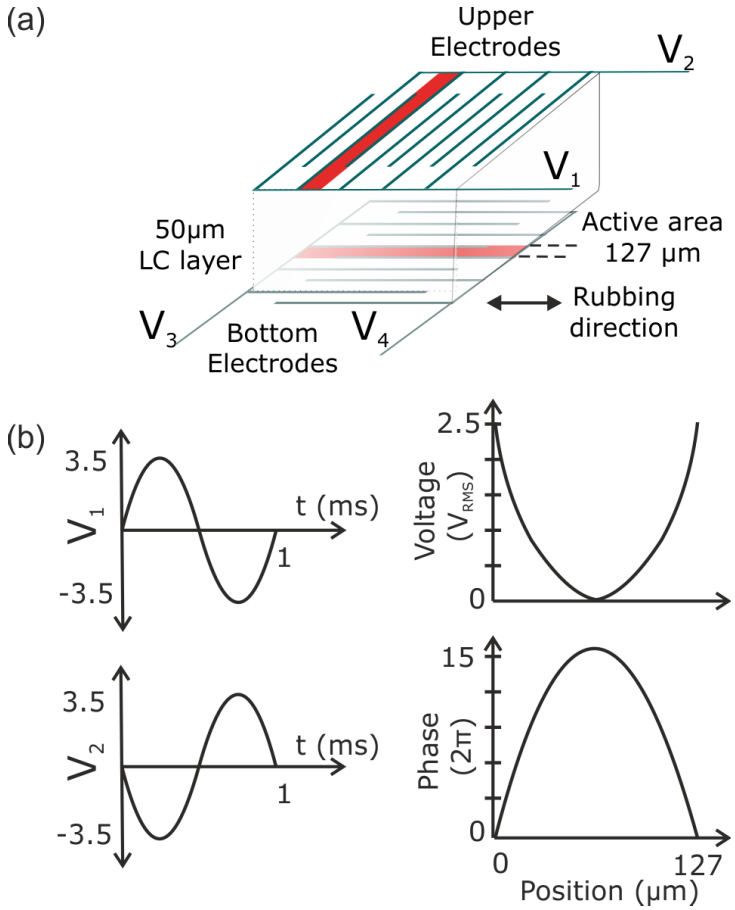

Figure 108. (a) Scheme of the electrodes arrangement Note drawings are not to scale. (b) On the left, an example of phase shifted electrical signals, (V_3 and V_4 connected to 0 V_{RMS}); on the right, a FEM simulation.

Another important physical effect making this device possible is the electrically controlled birefringence. As it was demonstrated in section 4.1.1, birefringence has a non-linear relation with the root mean square (RMS) value of the applied voltage. In the proposed device, this voltage has a quasi-linear shape. Finally, the molecules of the LC layer are aligned in a non-linear relation with the applied voltage producing an optical phase shift with parabolic profile [see Figure 108(b), Phase].

As an example, on the right of Figure 108 (b) a simulation of the electro-optical behavior of the proposed structure is shown. On the left, the employed phase shifted electrical signals are represented (V_3 and V_4 connected to 0 V_{RMS}). The Frank-Oseen equations are solved following the Euler-Lagrange equations (see section 2.1.3). The resulting system of partial differential equations are solved by using FEM. In Figure 108 (b) right, the voltage graph is the difference between the upper voltage distribution and the bottom one. The 2D profiles are considered between V_1 and V_2 electrodes placed over V_3. When the upper comb-type finger electrodes (V_1 and V_2) have an electrical phase shift of 180º with respect to each other, the signals are cancelled at the center of the electrodes. As the bottom electrodes (V_3 and V_4) are connected to 0 V_{RMS}, a ground plane is generated in the bottom substrate. Considering that the bottom electrodes do not form a continuous ground plane, little deviations have to be observed for high voltages (above saturation voltage).

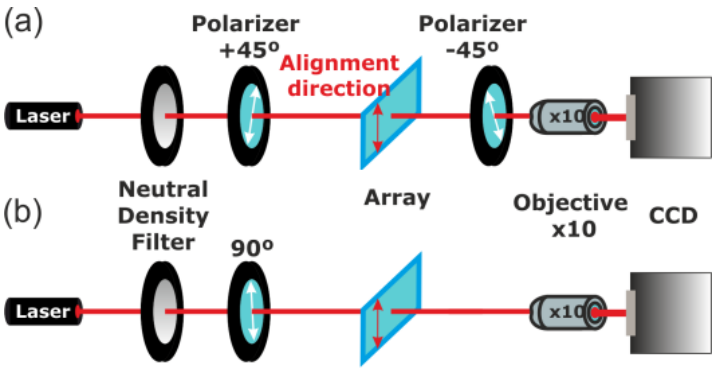

Figure 109. Experimental set-up for (a) interference pattern and (b) intensity measurements.

In order to generate phase shifted electrical signals, the same set-up of section 5.3.3 is used (Figure 98). In this set-up, a custom electrical phase shift waveform generator is used. The device is based on a FPGA Spartan-6 LX25. The same experimental setup is used (with variations in the used polarizers) to capture the different interference patterns as well as the focusing ability (Figure 109). The interference patterns are captured placing test samples between two crossed polarizers with the rubbing direction at 45º from them. For the focusing ability, only one polarizer is used. This one is placed parallel to the rubbing direction. In Figure 110, the need of phase shifted electrical signals is demonstrated.

Electro-optic characterization

When the applied voltages are in phase, the voltage distribution tends to create circular fringes. The main reason is that in this mode, there is no zero crossing between electrodes. Despite the fact that this mode is beyond the scope of this work, it could have very interesting applications in integral imaging displays. This idea has to be further investigated. In order to demonstrate the tunability of the proposed device a study of the cylindrical profile is shown in Figure 111. The profile is considered between two electrodes at different applied voltages. Two neighboring interference fringes have an optical phase difference of 2π. Both the fringe pattern and the profiles are included in Figure 111.

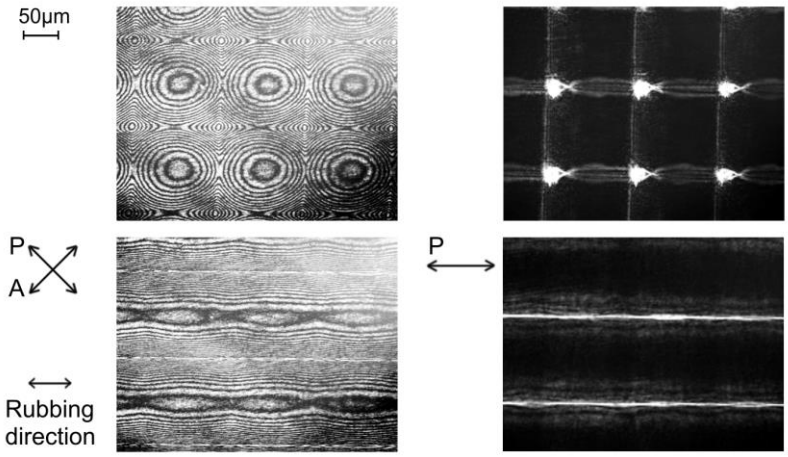

(a) Interference patterns **(b) Intensity measurements.**

Figure 110. Comparison between the use of electrical signals in phase (top) and phase shifted (bottom). A ×20 objective is used.

In Figure 111(c) the focal length distance of the measured phase profiles is shown. A maximum phase shift tunability from 4π to 34π radians is obtained for voltages from 1.3 V_{RMS} to 2.9 V_{RMS}, respectively. Where the maximum optical phase shift is defined as the difference between the optical phase shift at the center and the sides of the active area. The focal length is modified from 0.2 mm to 1.2 mm. As can be seen from Figure 111 there is a perfect match with a parabolic profile indicating that aberrations produced are minimal. Finally, the focusing ability is demonstrated in Figure 112. In this case an objective ×10 is used. The focusing power rotation by only voltage control is demonstrated.

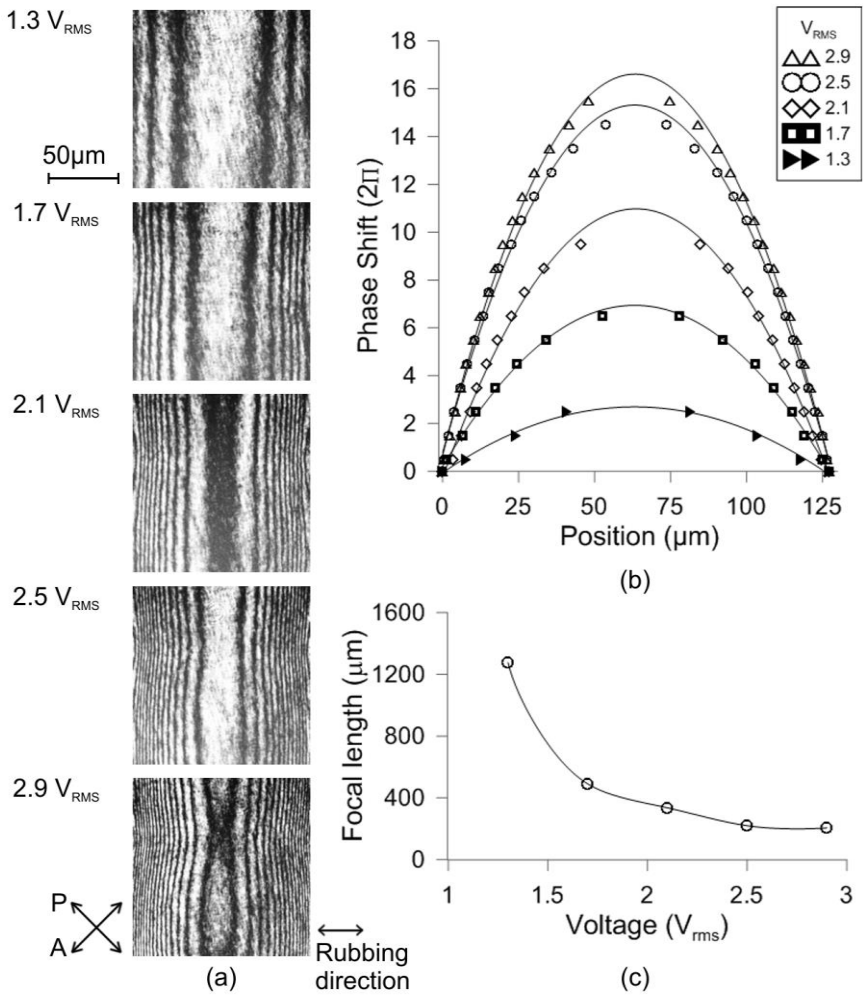

Figure 111. (a) Interference patterns for several voltages. $V_1 = V_2$ but phase shifted (180°), $V_3 = V_4 = 0$ V_{RMS} (b) Phase profiles extracted from (a). Points are experimental phase shifts. The continuous lines are the fitted phase profiles. (c) Focal length.

The switching time of the proposed device is directly related to the rising and decay time of the LC molecules. In this case, the decay time is 4 s (when the device is switched off). If the voltage is increased to 2.8 V_{RMS}, the necessary time for the molecules to reach the new position will be 1 s. This time can be considerably reduced by reducing thickness and using high birefringent materials. The operation speed in autostereoscopic devices, based on spatial multiplexing, does not need to be very fast [42]. At normal operation the LC lens always has the same voltage (no changes are required).

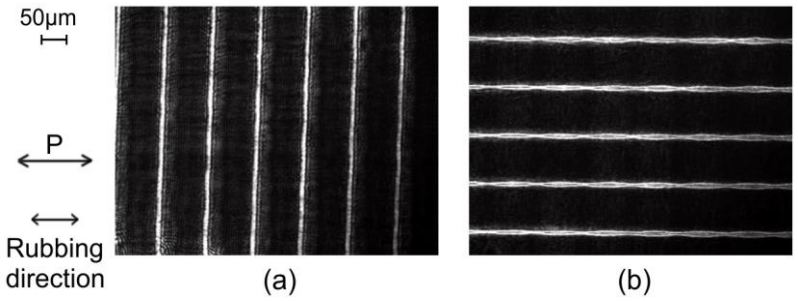

Figure 112. Focusing ability demonstrating the rotary axis capability. The applied voltage are (a) $V_1 = V_2 = 2.5\ V_{RMS}$ but phase shifted (180°), $V_3 = V_4 = 0\ V_{RMS}$, (b) $V_1 = V_2 = 0\ V_{RMS}$, $V_3 = V_4 = 2.5\ V_{RMS}$ but phase shifted (180°).

In summary, a novel micro-optical array is proposed and experimentally demonstrated. This device has rotary axis and tunable capability. Depending on the applied voltages a control over the maximum phase shift from 4π to 34π radians has been demonstrated. The wavefront deviation from the ideal parabolic profile is minimal. Owing to these properties this device is very promising for the next generation of autostereoscopic devices. The fabrication and control is simple leading to efficient and low cost devices with improved light efficiency, simplicity, and possibility of reconfiguration.

6.2. Modal micro-axicon array

In this section, a microaxicon array with high tunability and simple control is proposed. A control over the aperture and effective wedge angle is experimentally demonstrated. This device is simple and reconfigurable by low voltage signals. The proposed structure is capable of generate tunable axicons (thousands of elements) with micrometric size, simple control (four control voltages), low voltage and totally reconfigurable. The near field measurements demonstrate the generation of a non-diffracting Bessel beam array. Moreover this array is tunable both in phase amplitude and focus position. This device could contribute to developing new applications and to reducing the fabrication costs of the current devices.

Structure and operating principle

The used sample is MICROAX. The proposed device is very similar to the previous topology (Figure 108). The 100 LPI patterned is used in both substrates; these arranged so that their electrodes are in orthogonal position with respect to each other. The main difference is that in this case a high resistivity layer is used. Over the electrodes a low conductive and transparent polymer layer of PEDOT:PSS, is deposited. It is difficult to obtain homogeneous layers with this material. The deposition process is explained in section 3.3.2. The measured square resistance ranges from 7 to 14 MΩ/sq. A polyimide layer is deposited in order to obtain a molecular homogeneous alignment (see section 3.3.3). The substrates are separated by spacers of 40 µm. The resulting cavity is filled with MDA-98-1602. A top view of the electrode pattern is shown in Figure 113. When vertical electrodes are placed perpendicular to the horizontal ones, the confined volume is a cuboid. The top view of this volume is a square area (107x107 μm^2). Each comb-type electrode has 51 fingers, resulting in 100x100 optical elements. Every side of the active area is governed by one different voltage.

The operating principle is based on three physical effects. The first one, is produced by a low resistance between electrodes (in comparison with the LC impedance). This resistance generates a linear voltage distribution from one electrode to another for electrodes in the same side. The second effect is based on the combination of different electrical phase shifts. When the upper comb-type finger electrodes (V_1 and V_2) have an electrical phase shift of 180º, between them (e.g. V_2 = 180º), the signals are cancelled at the center of the electrodes. If it is translated to complex notation, the resulting voltage distribution in the upper side has the shape of a ramp, from V_1 to $-V_2$. The absolute value is a vertical prism array distribution. The same operating principle is required at the bottom electrodes (V_3 and V_4). In addition these electrodes have an electrical phase shift of 90º with respect to the upper electrodes. In complex notation, the resulting voltage distribution is also a ramp, but in the imaginary axis (from jV_1 to $-jV_2$).

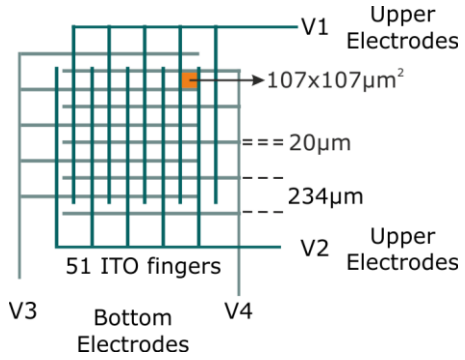

Figure 113. Tunable microaxicon array, top view of the patterned electrodes. Note drawings are not to scale.

The third physical effect is related to the nematic LC physics. The molecules of the nematic LC align parallel to the electrical field. This produces an electrically controlled birefringence. In nematic LC the birefringence has a non-linear relation with the root mean square (RMS) value of the applied voltage. In the proposed device, this voltage is the difference between the upper voltage distribution and the bottom one. Considering the complex notation, and $V_1 = V_2 = V_3 = V_4 = V$, it is easily observed how the corners of the active area has the same absolute value of $\sqrt{2}\cdot V$. However, the center of the active area has all the electrical signals cancelled. The result is a voltage distribution with a conical shape. Finally, the molecules of the LC layer are distributed in the same way, producing an optical phase shift with the shape of an axicon.

Electro-optic characterization

The same experimental set-up of the previous section is used. In order to capture the different interference patterns as well as the Bessel beams only the polarizers are changed (Figure 109). Interference patterns are captured by placing the sample MICROAX between crossed polarizers [Figure 109(a)]. Bessel beams are captured by placing test devices behind a parallel polarizer with the rubbing direction of the microaxicon array aligned to the main axis of the polarizer [Figure 109(b)]. As an example, in Figure 114, an interference pattern of two microaxicons and the resulting Bessel beams are shown. The electrical phase shift between electrodes is always maintained between experiments: V_1 = 0º, V_2 = 180º, V_3 = 90º, V_4 = 270º. The only modifiable parameter is the RMS amplitude, which is the same at each electrode, $V_1 = V_2 = V_3 = V_4 = V$.

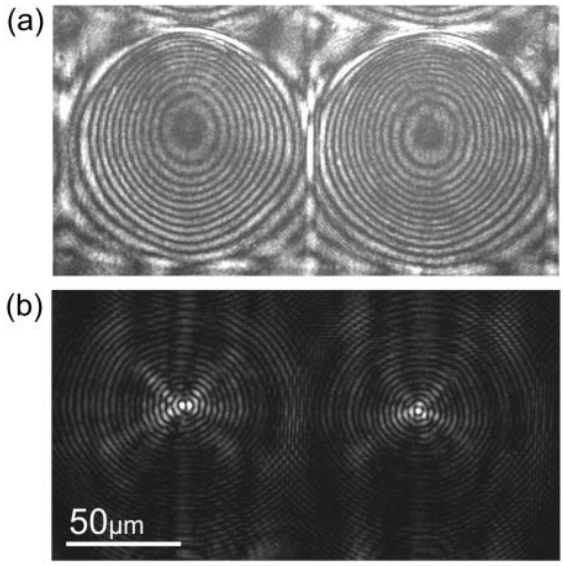

Figure 114. (a) Interference pattern and (b) intensity distribution of the Bessel beams, for V = 5 V_{RMS} and z = 2 mm.

An interesting effect has been observed when the voltage is increased over 4 V_{RMS}. As can be observed in Figure 115(a), the diameter is smaller than 107μm. A clear control over the microaxicon diameter (d), by means of the applied voltage, is demonstrated in Figure 115. As commented above this can be used to control the non-diffractive distance of a Bessel beam. Due to the waveform generator limitation the maximum applied voltage is 10 V_{RMS}. Above 4 V_{RMS}, the microaxicon diameter suffers an approximated reduction of 5 μm per V_{RMS} applied. The diameters range from 107 μm to 77 μm in the voltage range from 4 V_{RMS} to 10 V_{RMS}. Despite this, the diameter probably decreases linearly if more voltage is applied. The phase shift change is very small in comparison with the diameter reduction. Considering that z_{max} is modified, when the diameter of the microaxicon is changed, this effect produces a Bessel beam control in another way. One drawback could be an increasing of the background signal. The advantages of using this effect depends on the application and have to be further investigated.

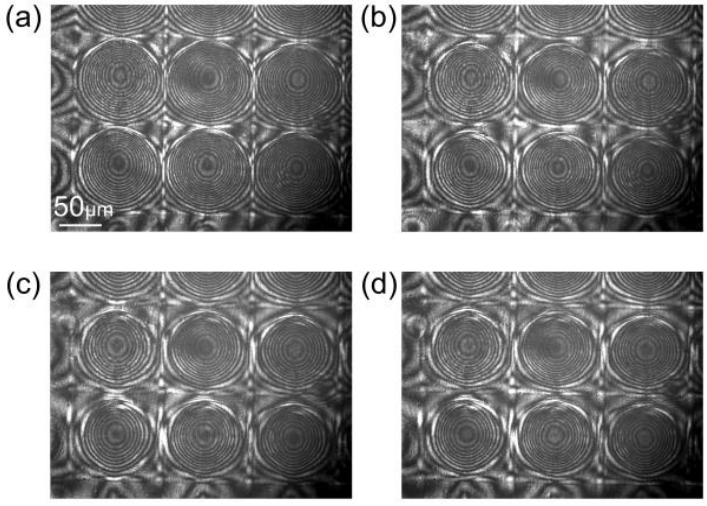

Figure 115. Tunable diameter for (a) V = 5 V_{RMS}, (b) V = 6 V_{RMS} (c) V = 7 V_{RMS} (d) V = 8 V_{RMS}.

Another interesting property of the proposed device is the tunable optical phase, of each individual microaxicon, for voltages lower than 4 V_{RMS}. This modifies the effective wedge angle (γ) of the microaxicon that also controls the resulting Bessel beam. The phase profiles are obtained from interference patterns developing an image recognition program that processes images and plots optical phase retardation versus horizontal position across the LC microaxicon. The results are shown in Figure 116. Phase tunability from 12π to 24π radians is obtained for voltages from 2 V_{RMS} to 4 V_{RMS}, respectively. As can be seen from Figure 116 there is a non-linear relation between the applied voltage and the maximal phase shift. The measured RMS wavefront error from the ideal axicon is approximately λ/3 for the three cases.

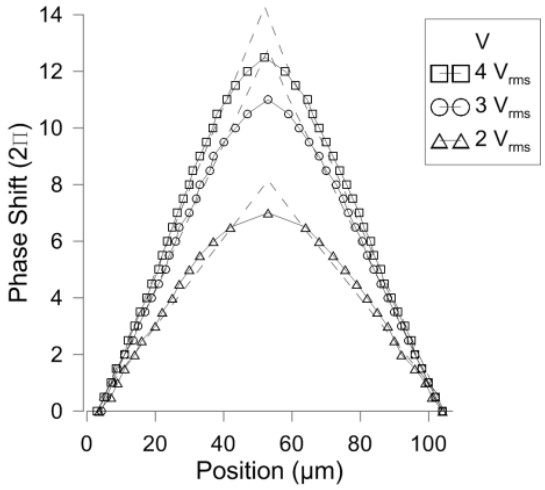

Figure 116. Tunable phase profile. The continuous lines are the experimental phase profiles. The dashed lines are the ideal axicon profiles.

In summary, a novel tunable LC microaxicon array has been presented. Experimental results of its electro-optic behavior demonstrate the validity. Depending on the applied voltages a control over the diameter as well as the effective wedge angle can be achieved. Controls over the diameter ranging from 107 μm to 77 μm have been demonstrated. These results are limited by the voltage source output but everything indicates that higher reductions on the diameter can be possible for higher voltages. In addition, a control over the phase profile, from 12π to 24π radians, has been also demonstrated. The RMS wavefront deviation from the ideal axicon is only λ/3. The realization of a voltage source, which can provide an offset voltage, could reduce the round tip of the microaxicon profile and the RMS wavefront error. Also the inclusion of other types of materials, as high resistivity layer, could improve the microaxicon homogeneity. The reduction of the LC layer could reduce distortions that limit their use in the generation of ultrashort optical needle beams. One solution is a thickness reduction in the LC layer. The same phase shift can be achieved for a higher birefringence LC. These ideas have to be further investigated. The proposed device has several advantages over the existing microaxicon arrays and is simple and low cost.

6.3. Modal array of micro-optical elements

In this section, a novel LC array based on modal control principle is proposed and demonstrated. The advanced device comprises a six striped electrode structure that forms a configurable 2D matrix of optical elements. A simulation program based on the Frank-Oseen

equations (section 2.1.3) and modal control theory (see Annex 3) has been developed to predict the device electro-optic response, that is, voltage distribution, interference pattern and unwrapped phase. A low-power electronics circuit, that generates complex waveforms, has been built for driving the device. A combined variation of the waveform amplitude and phase has provided a high tuning versatility to the device. Thus, the simulations have demonstrated the generation of a LC prism array with tunable slope. The proposed device has also been configured as an axicon array. Test measurements have allowed us to demonstrate that electro-optic responses, simulated and empirical, are fairly in agreement.

Structure and experimental set-up

The modal device proposed in this study is based on nematic LC technology. The sample is OPTARRAY. Figure 117(a) shows the structure comprising two high-resistivity layers. The high-resistivity layer consists of a very thin layer of titanium oxide with a sheet resistance of 11–14 MΩ/sq. The design of the electrode pattern consists of six striped ITO electrodes (three on the top and three on the bottom substrate); the spacers are 20 μm ±10%. The substrates are arranged so that their electrodes are oriented orthogonal to each other. The active area is 1 cm^2 and the electrodes are 1mm width (four square active areas of 500 μm).

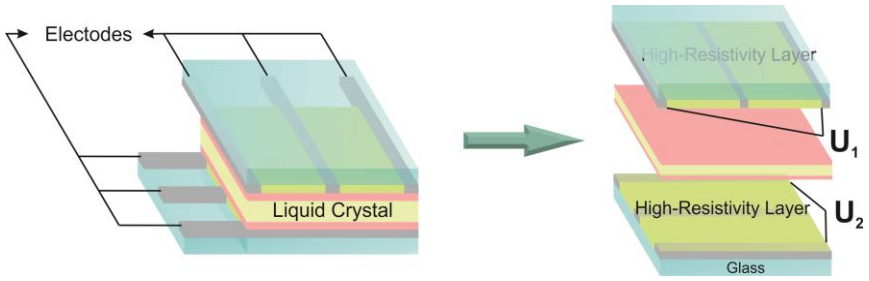

(a) Electrode layout. **(b) Device arrangement.**

Figure 117. Modal LC device proposed. Note drawings are not to scale.

The experimental setup, based on a commercial interferometer, is shown in Figure 118. The interference patterns are measured using a Zygo phase shifting interferometer in a double-pass configuration. LC device is placed, in a standard scheme, between a mirror and a linear polarizer. It has only four external contacts, since two couples of electrodes are connected with each other to the same signal in Figure 119(a). The top view of the active area is depicted in Figure 119(b). Unwrapped phase is directly obtained by the commercial interferometer in graphs in color by means of phase shifting technique.

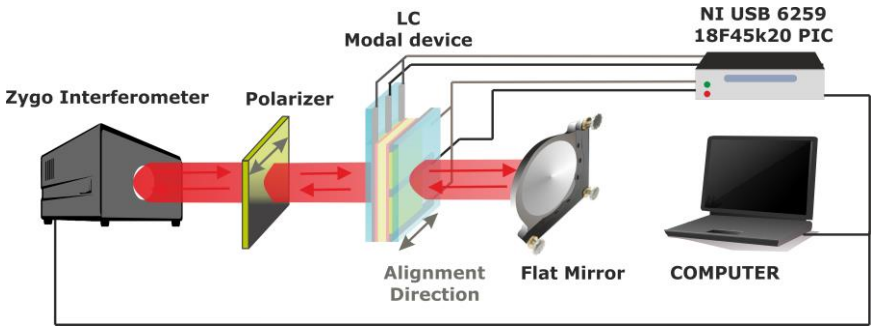

Figure 118. Experimental setup for characterizing the electro-optic response of the LC device.

As noted before, one of the most interesting operation regimes in modal devices is obtained using complex voltages, defined by amplitude and phase. The simulations confirm the need to use this type of voltage to completely exploit the device characteristics. For this purpose, a driving module has been designed and built with four external outputs. It consists of a custom phase shift waveform generator that uses an NI USB 6259 module to permit four analog outputs (±10 V) and a maximum speed of 1.25 MS/s in combination with a 18F45k20 PIC microcontroller as a master reference clock source to solve the problem of temporization and synchronization; the latter works as a tunable clock source to maintain a constant number of samples per waveform. The modal device is driven by the NI USB outputs and controlled using a computer.

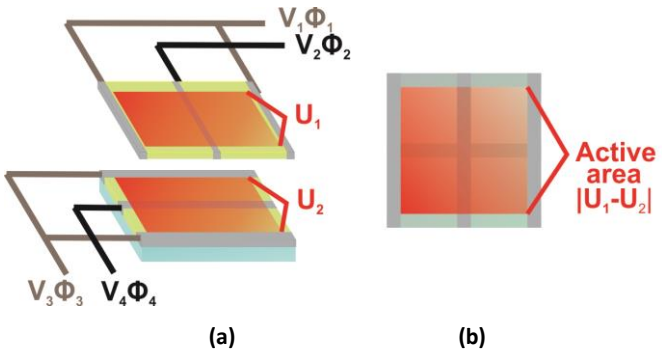

Figure 119. Electrode connections of the LC device. (a) Electrode connection and driving signal definitions and (b) top view of the active area.

A one-dimensional array of tunable liquid crystal prisms

An attractive optical unwrapped phase is produced via the use of opposite electrical phase shifts, that is, opposite signal polarity, in contiguous electrodes of the same substrate. This setting forces the voltage between the two electrodes to cross zero volts and to create a pyramidal voltage profile [see Figure 120(a)]. The result of applying this control is indeed a controllable one-dimensional LC prism array. Figure 120(b) and (c) illustrate the comparison of the experimental and simulated interferograms, for the horizontal and vertical distributed interference patterns. Driving signals set up are ($V_3 = V_4 = 6\ V_{pkpk}$, $\Phi_3 = 0^o$ and $\Phi_4 = 180^o$) and ($V_1 = V_2 = 6\ V_{pkpk}$, $\Phi_1 = 0^o$ and $\Phi_2 = 180^o$), respectively. The frequency remains constant, at 1 kHz, in all the experiments. Both examples confirm the simulation model; the comparison reveals that they are fairly in agreement. In this case, low frequency signals are preferable (lower than 1 kHz) in order to operate with a small modal parameter. Both examples confirm the validation of the simulation model; the comparison reveals that they are fairly in agreement.

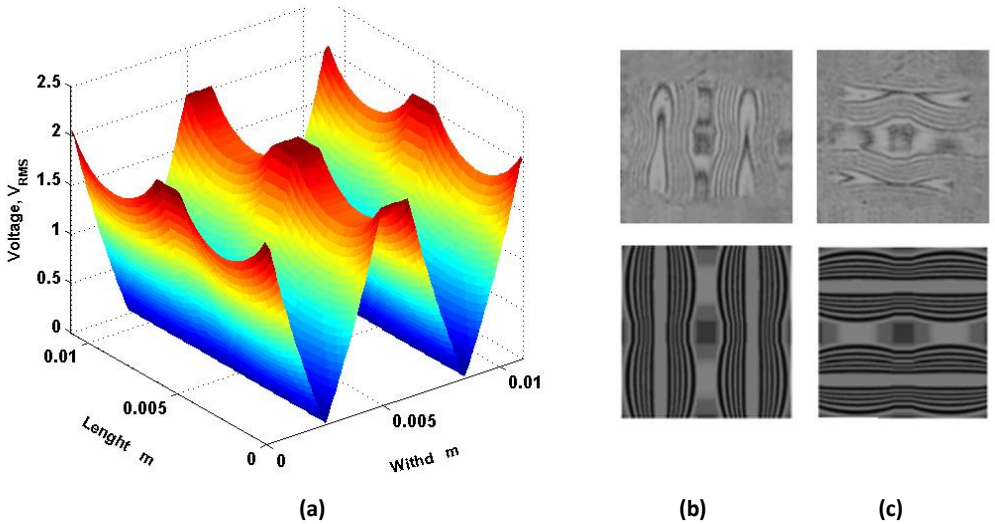

Figure 120. (a) Voltage distribution, $|U_1\text{-}U_2|$, for a one-dimensional array of LC prisms. Experimental (first row) and simulated (second row) for (b) the horizontal and (c) vertical distributed interference patterns.

The result of applying this control is indeed a controllable one-dimensional LC prism array. For controlling the optical phase profile of the optical elements of the whole array simultaneously, only the voltage amplitude is necessary. However, for advanced independent control of each individual stripped-element of the array, electrical signals with phase shifts between all the electrodes are employed. The result of this approach is simulated using the original structure with the six electrodes enabled [see Figure 121(a)]; experimental could not be performed by the current electrode setting. Signal frequency is 1 kHz.

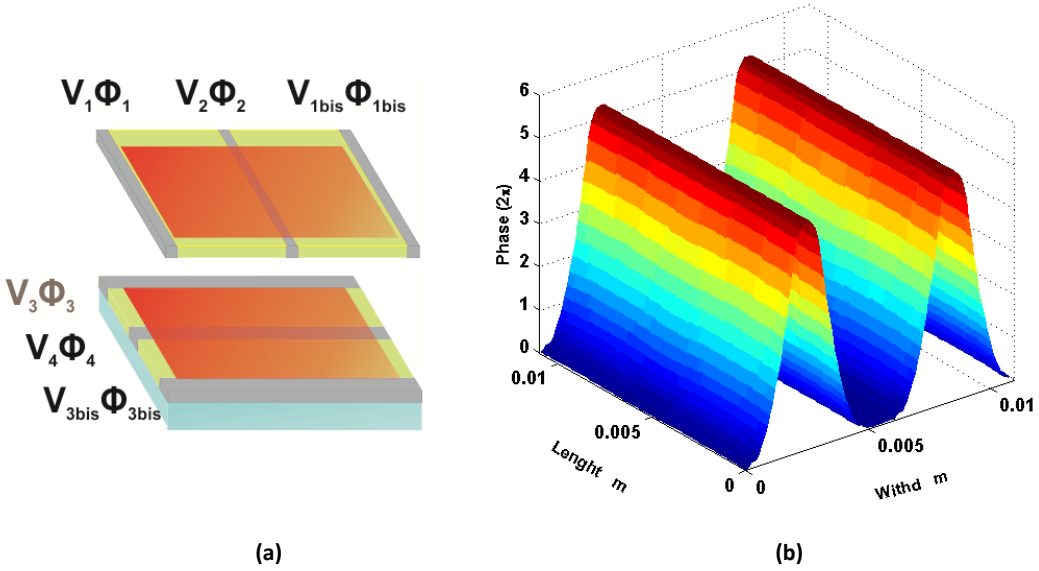

(a) (b)

Figure 121. Simulation of a LC tunable prism array with independent elements: (a) electrode layout and driving signal definitions and (b) 3D optical phase shift in the active area.

The prisms can be controlled independently applying different combinations of voltages. In a first case, with a constant electrical phase shift ($\Phi_1 = 180º$, $\Phi_2 = 180º$ and $\Phi_{1bis} = 0º$), the amplitudes of electrodes $V_1 = V_2 = V_{1bis}$ are increased from 0 to 6 V_{pkpk}, while $V_3 = V_4 = V_{3bis} = 0$ V_{pkpk}. During this interval, one of the prisms does not appear while the other shows a tunable profile. The second case is a customized design with a fixed active prism (the one placed on the right) and the second one varying its slope. All the parameters are constant ($V_1 = V_2 = V_{1bis} = 6$ V_{pkpk}, $\Phi_2 = 180º$, $\Phi_{1bis} = 0º$) instead Φ_1 that decreased from 180º to 0º. The last cases are the complementary, with symmetric parameters, to the previous ones. That is, in the third sequence only Φ_{1bis} controls; it is increased from 0º to 180º. And the last sequence has a constant electrical phase shift ($\Phi_1 = 0º$, $\Phi_2 = 180º$ and $\Phi_{1bis} = 180º$) and the amplitudes of electrodes $V_1 = V_2 = V_{1bis}$ are decreased from 6 to 0 V_{pkpk}. These situations demonstrates complete control over the prism array. This prism has a maximum optical phase shift of 10.6π.

The quality of one prism of the one-dimensional array is checked by evaluating the RMS wavefront deviation. An ideal prism has been taken as a reference prism. Figure 122 shows the comparison of both prism profiles for the higher voltage, 6 V_{pkpk}.

This voltage amplitude has been chosen because it leads to the higher RMS wavefront deviation from the ideal prism; a deviation of λ/10 has been measured. As with the previous device arrangement, a similar explanation can be argued; the effect of the non-linear LC birefringence is a key for voltages out of the linear dynamic range. Pursuing the same goal, a threshold voltage could be considered as the lower limit of the dynamic range instead 0 volts. This initial condition would lead to a perfect valley at the center of the lens with imperceptible plateau zones. Again, the small

defects that are noticed in the phase prolife also could be solved by new materials and manufacturing technologies of modal control taking into account for optimizing the response.

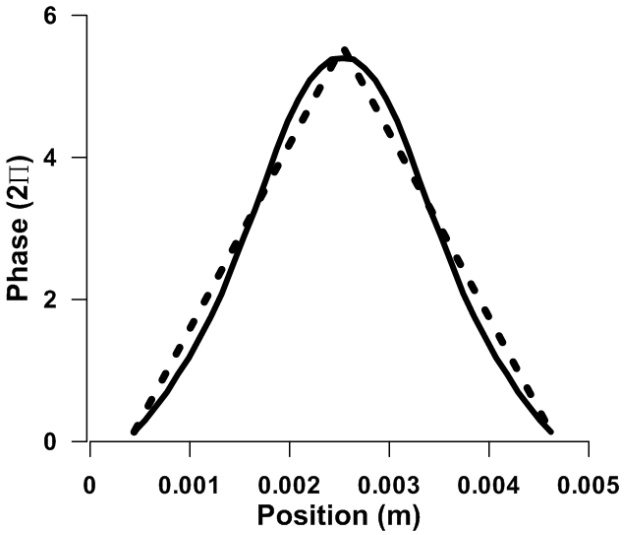

Figure 122. The phase profiles for both an ideal prism (dashed line) and the proposed prism (solid line) for 6 V_{pkpk}.

A two-dimensional matrix of tunable liquid crystal axicons

The previous setting exploits only the tuning features of the device in one dimension. By adding a new control dimension, the one-dimensional LC array described before, evolves into a new two-dimensional LC array. Table 7 summarizes the batch of measures carried out whose results are shown in Figure 123. It also lists the applied voltage amplitudes in V_{pkpk} for a set of constant electrical phases. The experiment is based on the use of opposite electrical phase shifts between electrodes in both substrates; being $\Phi_1 = 0º$ and $\Phi_2 = 180º$, in one substrate, and $\Phi_3 = 90º$ and $\Phi_4 = 270º$, in the other. Optical tunability is reached, for a constant phase shift, by varying the voltage amplitude of the signal. Figure 123(a), (b) and (c) show some interference patterns in XY plane for a fixed amplitude $V_1 = V_2 = V_3 = V_4$. The evolution of interference patterns, as amplitudes of some chosen electrodes increase, is shown in Figure 123(d), (e) and (f).

	(a)	(b)	(c)	(d)	(e)	(f)	All cases	
V_1	10	16	20	4	4	4	Φ_1	0º
V_2				10	14	16	Φ_2	180º
V_3				4	4	4	Φ_3	90º
V_4				10	14	16	Φ_4	270º

Table 7. Batch of measures carried out when an electrical signal is applied to the device with some constant electrical phases and voltage amplitudes in V_{pkpk}.

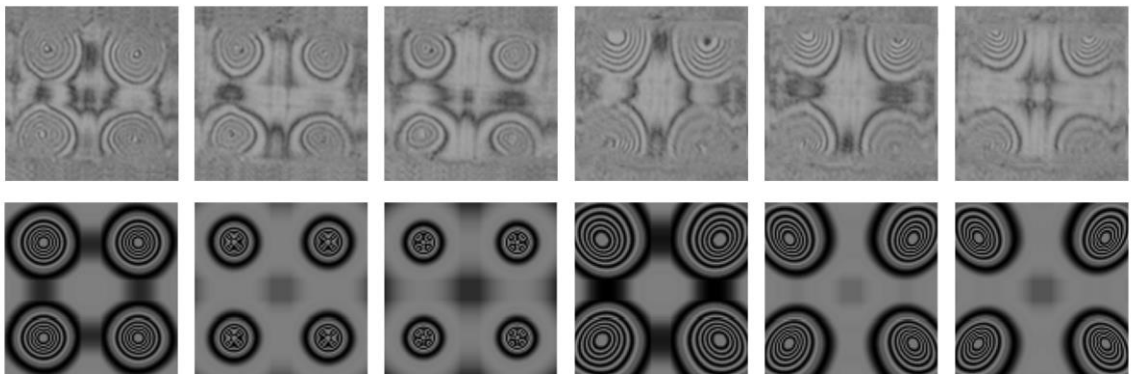

Figure 123. Experimental (first row) and simulated (second row) interference patterns for a two-dimensional matrix of tunable LC axicons.

The frequency remains constant, at 1 kHz, in all the experiments. This driving scheme generates the most interesting wavefronts identified in this work with respect to the tuning versatility and the potential application of the device. The device results in a 2×2 two-dimensional matrix of tunable rotationally symmetric prisms or axicons, that is, lenses featured by a conical surface. The simulations reveal a cone-type voltage that generates concentric fringes that can be controlled by V_{pkpk} at each electrode. Further, the focus point of each axicon can be tuned over the active area. The experimental interference patterns are shown Figure 124(a), the 2D and 3D simulated optical phase shifts in Figure 124(b) and (c). In this experiment, the electrical phase shifts (Φ_1, Φ_2, Φ_3 and Φ_4) and also the amplitudes in the external electrodes, V_1 and V_3, remain constant again, while the amplitudes in the central electrodes, $V_2 = V_4$, change. A possible sequence that V_2 follows could be: First, beginning with a voltage of 5 V_{pkpk} in each electrode and a maximum focus point (optical phase shift 12.9π) at the center of each sub-lens. Then, increasing V_2 until 7.4 V_{pkpk}, results in the focus moving toward the outside of the active area. And finally, decreasing V_2 until 1 V_{pkpk}, displaces the focus toward the center of the active area.

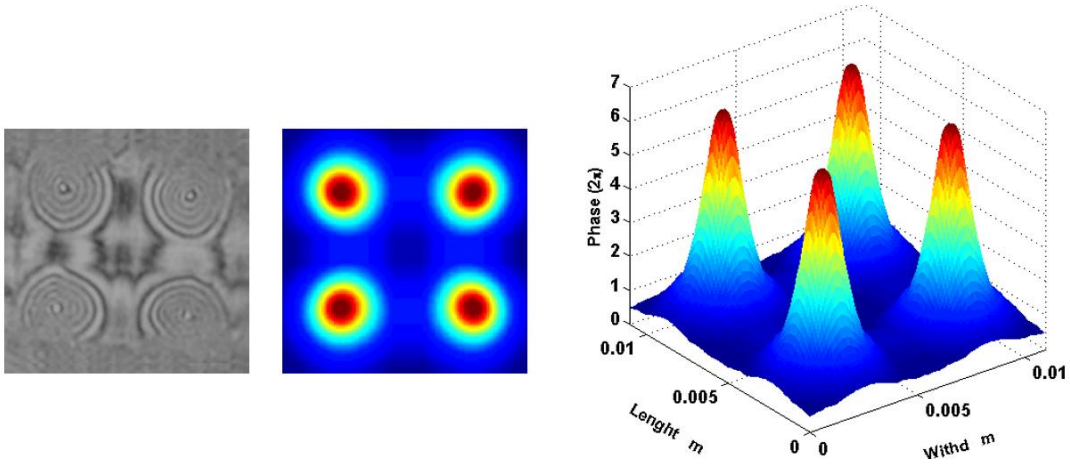

Figure 124. A two-dimensional matrix of tunable LC axicons: (a) Experimental interference patterns, (b) 2D simulated in XY plane and (c) 3D simulated unwrapped phase.

The prospective applications of the LC device proposed for adaptive optics can be performed for converting a parallel laser beam into four rings so as to create a set of four non-diffractive

Bessel beams or for focusing a parallel beam into four controllable long focus depths that can be electrically controlled.

The quantification of the optical quality of an axicon of the two-dimensional matrix could be analogously obtained as with the prism arrangement. Two planes, length and width, must be considered, instead of only the width plane. Once more, an ideal axicon could be achieved by optimizing the manufacturing techniques.

In summary, a novel configurable and tunable modal LC array of optical elements is presented. The wavefront generation using this device can be improved by using multiphase shift control voltages. The application of smart driving complex signals with opposite electrical phase shifts between electrodes in one substrate has allowed us to simulate a configuration that works as a one-dimensional array of tunable LC prisms. In an advanced approach with a similar strategy applied in both substrates, a two-dimensional matrix of tunable LC axicons, configured from the proposed device, has also been demonstrated experimentally. The simulation program, specially developed for achieving distinctive configurations of the device, predicts the voltage distribution inside the LC layer. Simulation results can be extrapolated to 1D and 2D matrices of higher size. Additionally, driving controls based on non-regular patterns of tunable voltages, in each electrode, has been attempted and have to be further investigated. By limiting the device operation to the linear range of the LC birefringence characteristic has been identified as key point to reduce aberrations.

6.4. Generation of optical vortices

In this section, an ideal spiral phase plate based on modal control is proposed and theoretically analyzed. The proposed structure generates a spiral-like voltage with simple voltage control. The LC layer produces an optical phase shift that depends on the voltage distribution. These two effects cause light passing through the device to be twisted like a corkscrew around its travel axis. Because of the continuous phase shift, the proposed device is expected to exhibit a conversion efficiency of approximately 100%. In addition, this device is more efficient and simpler than previously reported optical vortex generators. Moreover, the device is completely reconfigurable, i.e., the operating wavelengths and topological charges are tunable. The device can be used, to reduce the fabrication costs of current devices, and to generate different orbital angular momentum (OAM) modes with improved light efficiency, simplicity, and possibility of reconfiguration.

Structure and operating principle

The proposed device consists of two ITO coated substrates covered by a high resistivity layer. The substrates are separated by a spacer of thickness 20 μm. The resulting cavity is filled with MDA-98-1602. As this device is an adaptive phase-only modulator no twist of the molecules is necessary. For this reason, a homogenous alignment is required. One solution could be the same used throughout this thesis (PIA2000) rubbed in the direction of the electrodes for the upper glass and in the antiparallel direction for the other one. Figure 125(a) shows a schematic of the structure. The ground plane, shown in Figure 125(b), includes a circular area without ITO at the center, which is covered with a high resistivity layer to generate a specific voltage distribution (U_2). Figure 125(c) shows the upper plane composed of another circular area covered with a high resistivity layer. The voltage distribution in the upper plane is U_1. Additionally, this substrate includes two electrodes. The electrode pattern on the upper substrate consists of two striped ITO electrodes [Figure 125(d)].

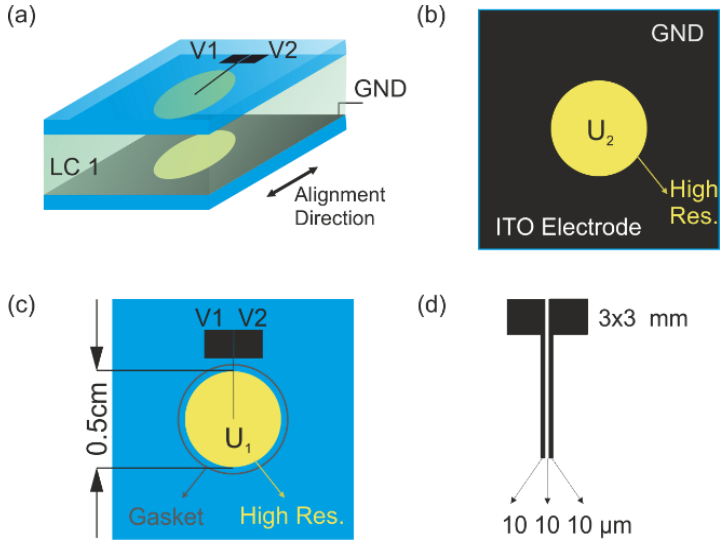

Figure 125. Optical vortex generator. (a) Schematic of the device, (b) bottom substrate, (c) top substrate, and (d) electrode layout of the top substrate. Note: drawings are not to scale.

The substrates are arranged in such a manner that their circular areas are aligned with each other. Several materials can be employed, depending on the required sheet resistance (R_{sq}). For example, thin films of ITO, Nickel, Titanium Oxide (TiO_2), or PEDOT may be employed. As commented in previous sections, the square resistance of these materials ranges from 0.1 to 10 MΩ/sq. In our structure, a resistance of 0.1 MΩ/sq, voltage frequency of 1 kHz (in this case only one sinusoidal harmonic is considered), and thickness of 20 µm are considered. In the following, V_1 and V_2 denote the applied voltage on the upper electrodes. The voltage distribution on the two high resistivity layers (U_1 and U_2) is described by a second-order two-dimensional coupled partial differential equation (PDE) system (see Annex 2). In section 6.3, the solution of this system is experimentally validated.

Electro-optic response

The simulation indicates the amplitude of voltage required to generate specific OAM modes. The proposed simulation tool will be advantageous in estimating the voltages to be applied. Figure 126 shows the results of the simulation. These results are obtained by estimating the voltage distribution and molecular orientation of LC molecules in the active area. As shown, the applied voltages V_1 and V_2 are 1.2 V_{RMS} and 2.5 V_{RMS}, respectively, in Figure 126(a), (c) and 2.5 V_{RMS} and 1.2 V_{RMS}, respectively, in Figure 126(b), (d). The LC layer can produce eight different OAM modes; $l = \pm1, \pm2, \pm3$, and ±4, where l is the topological charge determined by the number of phase changes per wavelength around the beam axis. Small changes in the applied voltage result in large changes in phase shift. It is important to note that multiples of 2π are needed to create optical vortices. Further, with slight changes of the applied voltage, the phase shift can be maintained at 2π (or its multiple), but the operation wavelength changes.

Another advantage of the device is the generation of several topological charges. The point spread function (PSF) of an optical vortex provides information about its topological charge. The PSF is the impulse response of a focused optical system, i.e., it shows the distribution of the light intensity of the focal spot. Figure 127 displays the PSF for several voltages for λ= 632.8 nm and

pupil radius = 2500 µm, evaluated by considering the optical path length and using Fourier transforms. Micro-optical vortices could be achieved by reducing the pupil radius.

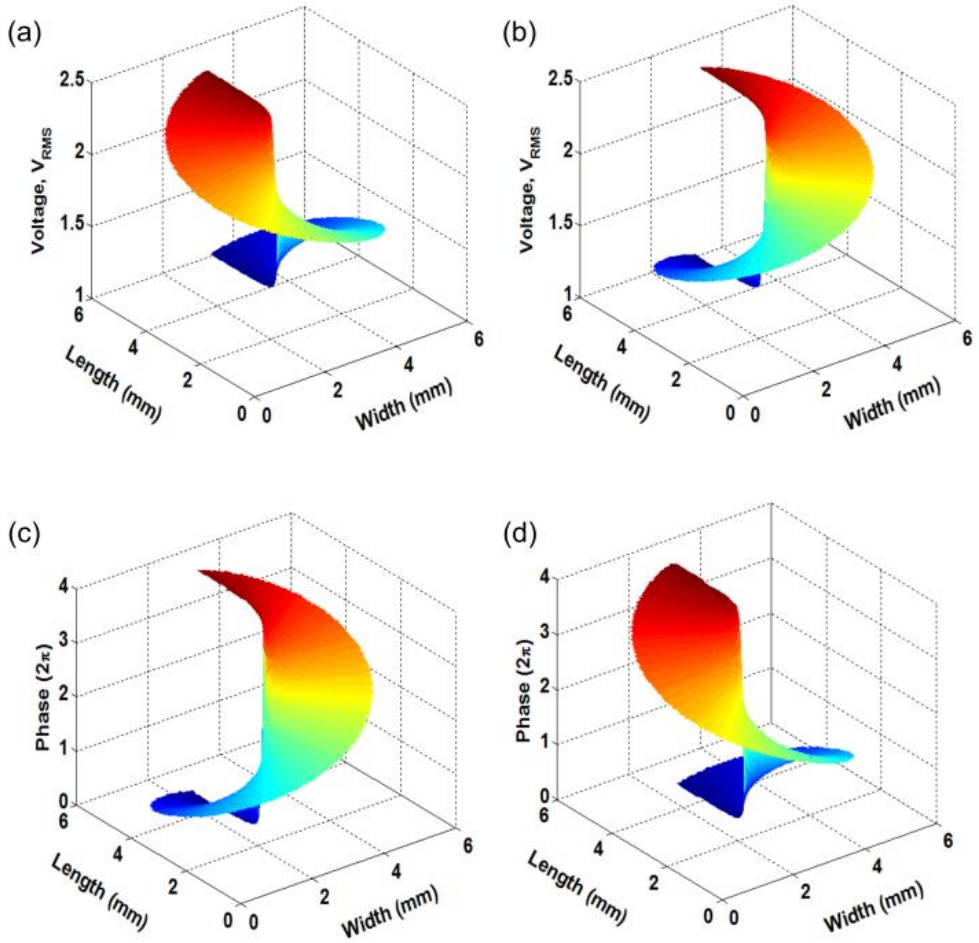

Figure 126. Simulated results of the voltages seen by the LC (upper part) and the 3D phase shift (bottom part) when the voltages applied to the ITO electrodes are V_1 = 1.2 V_{RMS} and V_2 = 2.5 V_{RMS} [(a) and (c)] 3D or V_1 = 2.5 V_{RMS} and V_2 = 1.2 V_{RMS} [(b) and (d)].

These results demonstrate that the topological charge can be controlled with precision. A slight variation of V_2 allows four different modes to be achieved. The negative topological charge can be easily determined by interchanging the voltages at V_1 and V_2, as shown in Figure 126. There are two characteristic curves in the LC birefringence response as a function of voltage that have to be avoided. The first one is produced when the electrical energy overcomes the elastic free energy and the molecules start to move. The other one is produced when the molecules start to reach the perpendicular position. In this case, the cuasi-linear range between this curves ranges from 1.2 V_{RMS} to 2.5 V_{RMS}. As an ideal SPP is characterized by a linear phase drop, this operating range has to be mantained. For example, above 2.5 V_{RMS}, the relation between voltage and phase shift is non-linear, resulting in a non-perfect, spiral-like phase. By increasing the device thickness, more topological charges can be easily generated. For instance, a thickness of 40 µm yields 8 positive and negative topological charges.

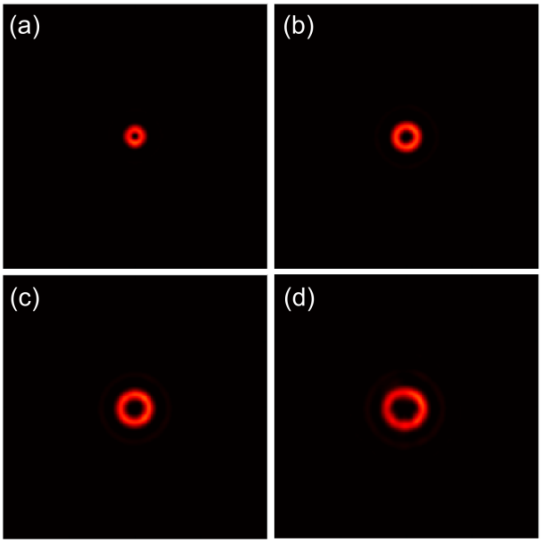

Figure 127. Tunable topological charge for (a) V_1 = 1.2 V_{RMS} and V_2 = 1.5 V_{RMS}, (b) V_1 = 1.2 V_{RMS} and V_2 = 1.8 V_{RMS}, (c) V_1 = 1.2 V_{RMS} and V_2 = 2.1 V_{RMS}, and (d) V_1 = 1.2 V_{RMS} and V_2 = 2.5 V_{RMS}.

In summary, a novel optical vortex generator has been proposed and theoretically analyzed. Simulations reveal that small changes in the applied voltage produce large changes in the phase shift. Simulations are essential for using this device because important design parameters, such as the thickness, square resistance of the deposited layer, and the frequency and amplitude of the voltage control, can be optimized prior to application. Owing to the continuous optical phase shift, this device is the best approximation to an ideal SPP proposed to date. Moreover, the device is completely reconfigurable (operating wavelengths and topological charges are tunable). Micro-optical vortices could be achieved by reducing the laser spot size. The device can be used in new applications (e.g. fiber optics communications or atom manipulation), to reduce the fabrication costs of existing devices, and to generate different OAM modes with improved light efficiency, simplicity, and possibility of reconfiguration.

7. Conclusions and future research lines

7.1. Fundamental results of this thesis

In this last chapter, the main conclusions, objectives completely fulfilled and the most relevant results of this thesis are summarized. They are classified into some groups according to the initial objectives planned.

The result about the **exploration and expansion** of the **theory** and **current fundamentals** are:

- A deep **study of different topologies** to obtain LC optical phase modulators has been carried out. To achieve autostereoscopic vision, it is proposed the use of adaptive micro-optical phase modulators based on liquid crystal technology (**tunable LC microlenses**).
- Another original contribution is a **novel EEC** for modeling LC microlenses. This novel EEC predicts the voltage distribution in LC microlenses for both modal and hole-patterned electrode schemes. In the last configuration, the fringe field effect turns relevant as the lens aperture decreases. A **coplanar capacitor** has been chosen as the electric component to model the electric response accurately. An accurate design of some constructive parameters, such as thickness or diameter, can be **previously made to the device manufacture.** In addition, it could lead to other key estimations of phase profiles, focal lengths, aberrations, etc. The model is **also valid for spherical microlenses** considering radial symmetry.
- An interesting feature of the model is that it provides an **analytical solution for microlenses** with modal and hole-patterned electrode schemes, by using a simple software tool. The resulting equations give accurate **information about the necessary resistivity** for manufacturing modal microlenses. Also, the capacitance provides key information for manufacturing hole patterned lenses. The respective equations are intended to be used as a tool for researchers to produce **optimal lenticular designs**. The model should result in time savings and maximize material resources, thereby avoiding the manufacture of test cells.

The results about the **study** in depth of the **liquid crystal** electro-optical characteristics are:

- Nematic MDA 98-1602 liquid crystal has been completely characterized. Birefringence and permittivity have been obtained for different voltages (**anisotropy**) and frequencies (**dispersion**).
- By using these results an **EEC for a broadband frequency** (1 Hz – 10 MHz) has been proposed and demonstrated.
- The previous analysis has made possible to characterize the nematic LC in a specific frequency range. The simplified EEC is determinant to **model the LC electro-optic response**.

The results about the development of an **own simulation tool** for the treatment the LC itself and the LC inside the modulators are:

- The **minimization of Gibbs free energy** has been solved for a LC molecular arrangement. With this, a **novel, accurate, fast and reliable algorithm** has been proposed and the theoretical prediction compared with experimental data has been presented.
- By using the characterization results, the solution of the proposed **theoretical modelling** of the molecular director **has been demonstrated**.
- It has been demonstrated how these simulations can be easily extended to **other experimental devices** where voltage distribution is known. For more complex devices, the equations has been solved by **Finite Element Method**.
- This algorithm in combination with the EEC for modeling LC microlenses has been validated for **designing lenses with specific parabolic phase profiles and without defects** such as shrinkage at the lens sides or a plateau at the lens center.

The results about the **design** and **fabrication** of microlenses are:

- The fabrication of a modal lens imply a technological challenge at micrometric scale. A **new manufacturing protocol** has been proposed in order to obtain the **first modal microlens array**.
- A **metal layer** acts as a high resistivity electrode and generates a distributed resistance across the surface of the lens pitch from the center to the edge.
- Metallic films **thicknesses** have been key parameter for designing a suitable voltage distribution through the inner surface of the control electrode.
- **Hole patterned arrays** fabricated following the proposed theories have been determinant in order to demonstrate the proposed EEC.

The results about full **characterization** of microlenses and **validation** of the electrical and simulation models are:

- Due to the micrometric size of each microlens embedded in the lenticular array, a **specific set-up** has been designed in order to characterize them.

- The **control and characterization** software and the micropositioner have been **custom fabricated**. This software automatizes the characterization process giving important results as **phase modulation, focal distance, thickness or aberrations**.
- Those values have been found to be **similar** to that of **commercial lenticular sheets** of comparable diameter per lens.
- By comparison of the experimental results with the theoretical predictions, **the proposed electrical and simulations models are experimentally validated**.
- The **high optical power and 3D distance tunability** have been experimentally demonstrated.

The results about the development of a **prototype for autostereoscopic vision** and the improvement of its features are:

- A **2D/3D switchable prototype** based on an OLED display, LC microlenses, and a lenticular positioner has been designed and manufactured. The electro-optic response is completely characterized in terms of **angular luminance, crosstalk and 3D contrast**. The luminance measurements show 10% crosstalk between the views. The angular contrast measurements reveal an optimum distance of 30 cm to 35 cm for 3D vision.
- The obtained results are preliminary but **experimentally demonstrate** how these lenticular LC lens arrays could be applied in the **next generation of autostereoscopic displays**.
- The temperature dependence of LC in this type of systems can be controlled by some **original temperature sensors** proposed for this application.
- A **novel hole patterned LC temperature sensor** has been completely characterized. This temperature sensor has several advantages with respect to other previous related LC sensors. In some aspects, this sensor is an **improvement on the characteristics** of some commercial temperature sensors. The structure is simple and has an active area easy to scale. Coplanar electrodes can be easily patterned at very small dimensions yielding miniaturized, reproducible, and ultimately low cost devices.
- The **incorporation of a resistive layer** to this structure improves the sensor characteristics. These sensors can be used in **autostereoscopic displays based on LC lenses**, LCD displays, LCD projectors, portable equipment or any application where its properties procure an advantage with respect to current available sensors.
- Aberrations are a typical problem in optical systems. A novel method to extract aberrations in adaptive LC phase-only passive elements have been described. An **original aberration compensation device** for rectangular micro-optical systems has been designed and fabricated. A complete independent **control over the spherical and coma aberration** has been demonstrated. Also, an independent **control over the astigmatism** aberration has been demonstrated in a broad range.
- A common characteristic of new portable devices is the switching between **vertical and horizontal views.** As **original contribution** a **microlens array with rotary axis and tunable capability** is proposed and experimentally demonstrated. This device has rotary axis and tunable capability. Depending on the applied voltages a control over the focal length from **0.2 to 1.2 mm** has been demonstrated. The wavefront deviation from the **ideal**

parabolic profile is minimal. Owing to these properties this device is very promising for the next generation of autostereoscopic devices.

The results about the **exploration of other devices** based on **similar topologies** to control and modify the phase of light are:

- Other LC based devices working as micro-optical phase modulators have been developed as a part of this thesis. Among these, **adaptive axicons and optical vortices** are relevant from both, the scientific and the technological point of view.
- A **novel tunable LC microaxicon array** has been presented. Depending on the applied voltages a control over the diameter as well as the effective wedge angle can be achieved. **Controls over the diameter** ranging from 107 μm to 77 μm have been demonstrated. In addition, a **control over the phase profile**, from 12π to 24π radians, has been also demonstrated. The use of microaxicons in arrays also has **important applications** such as, for example, ultrafast optical communications, generation of femtosecond Bessel beams, non-diffracting "flying images", high-resolution optical coherence tomography, etc. The proposed device has **several advantages over the existing microaxicon arrays** and is **simple and low cost**.
- **A novel configurable and tunable modal LC array of optical elements** has been demonstrated. The application of driving complex signals generates a one-dimensional array of **tunable LC prisms**. In an advanced approach with a similar strategy applied in both substrates, **a matrix of four tunable LC axicons**, has also been demonstrated. The simulation program, specially developed for achieving distinctive configurations of the device, predicts the voltage distribution inside the LC layer. Simulation results can be extrapolated to 1D and 2D matrices of higher size.
- A **novel optical vortex generator** was proposed and theoretically analyzed. Simulations reveal that small changes in the applied voltage produce large changes in the phase shift. Owing to the continuous optical phase shift, this device is the **best approximation to an ideal SPP** proposed to date. Moreover, the device is **completely reconfigurable** (operating wavelengths and topological charges are tunable). The device can be used in new applications (e.g. fiber optics communications or atom manipulation), to reduce the fabrication costs of existing devices, and to generate different OAM modes with improved light efficiency, simplicity, and possibility of reconfiguration.

7.2. Future lines

The development of this work has opened up numerous lines of research, among them are worth noting the following:

- Research in new high resistivity electrodes. For example, amorphous silicon layers with Ni nanoparticles or graphene. Find other kind of materials such as high permittivity materials to distribute the voltage. The inclusion of nanoparticles in the LC mixtures can change the electro-optical properties. Lenses with this kind of mixtures can be the solution to high diameters.

- Research in the use of different harmonics by using arbitrary waveforms in order to reduce aberrations and reduce switching times. The use of a simulation model (taking into account the Chebysev polynomials and the Frank-Oseen equations) to design the necessary electrical signals to obtain specific aberration coefficients has to be further investigated.
- Develop a RGB autostereoscopic display with better resolution. Some constructive problems has to be taken into account. The LC dispersion has to be compensated.
- Develop a simulation program of the angular luminance to predict the autostereoscopic response of a LC lens array.
- Study the possibility of a spatial-temporal multiplexing by using LC lenses and TN cells.
- Research the next step in autostereoscopic vision, integral imaging. The acquired knowledge in LC lenses can be used to design novel plenoptic systems based on LC technology. In this case spherical microlenses arrays could modify the plenoptic function by using different focal lengths.
- Continue the research in novel optical components based on advanced electrode configurations and LC technology.

7.3. Publications related to this work

7.3.1. International papers

1. V. Urruchi, J.F. Algorri, J.M. Sánchez-Pena, M.A. Geday, X. Quintana, N. Bennis, **"Lenticular Arrays Based on Liquid Crystals"**, Opto-electron. Rev., vol. 20, no. 3, pp. 38-44 (2012). DOI: 10.2478/s11772-012-0032-z
2. V. Urruchi, J.F. Algorri, J.M. Sánchez-Pena, N. Bennis, X. Quintana, J.M. Otón, **"Electro-optic Characterization of Tunable Cylindrical Liquid Crystal Lenses"**, Mol. Cryst. Liq. Cryst. , vol. 553, no.1, pp. 211-219 (2012). DOI: 10.1080/15421406.2011.609473
3. J. F. Algorri, V. Urruchi, J.M. Sánchez-Pena, N. Bennis, M.A. Geday, **"Liquid Crystal Microlenses with Gradient Refraction Index Control"**, Opt. Pura y Apl., vol. no. 45 (2) pp. 71-78 (2012). DOI: 10.7149/OPA.45.2.71
4. J. F. Algorri, G.D. Love, V. Urruchi, **"Modal liquid crystal array of optical elements"**, Opt. Express, vol. 21, no. 21, pp. 24809–24818 (2013). DOI: 10.1364/OE.21.024809
5. V. Urruchi, J.F. Algorri, C. Marcos, J.M. Sánchez-Pena, **"Electrical modeling and characterization of voltage gradient in liquid crystal microlenses"**, Rev. Sci. Instr., vol. 84, no. 11, pp. 116105 (2013). DOI: 10.1063/1.4832419
6. J. F. Algorri, V. Urruchi, P. J. Pinzón, and J. M. Sánchez-Pena, **"Modeling electro-optic response of nematic liquid crystals by numerical methods"**, Ópt. Pura y Apl., vol. 46, no. 4, pp. 327-336 (2013). DOI: 10.7149/OPA.46.4.327
7. V. Urruchi, J.F. Algorri, J.C. Torres, J.M. Sánchez-Pena, **"Modeling of Unwrapped Phase Defects in Modal Liquid Crystal Cylindrical Microlenses"**, IEEE Photon. Technol. Lett., vol.26, no.2, pp. 198-201 (2014). DOI: 10.1109/LPT.2013.2291863

8. J. F. Algorri, V. Urruchi, J. M. Sánchez-Pena, J. M Otón, **"An Autostereoscopic Device for Mobile Applications Based on a Liquid Crystal Microlens Array and an OLED Display"**, J. Disp. Technol., vol. 46, no. 4, pp. 327-336 (2014). DOI: 10.1109/JDT.2014.2313143

9. J. F. Algorri, V. Urruchi, N. Bennis, J.M. Sánchez-Pena, **"Using an Analytical Model to Design Liquid Crystal Microlenses"**, IEEE Photon. Technol. Lett., vol. 26, no. 8, pp. 793-796 (2014). DOI: 10.1109/LPT.2014.2306920

10. J. F. Algorri, V. Urruchi, B. Garcia-Camara, J.M. Sánchez-Pena, **"Liquid crystal lensacons, logarithmic and linear axicons"**, Materials, vol. 7, no. 4, pp. 2593-2604 (2014). DOI: 10.3390/ma7042593

11. J. F. Algorri, V. Urruchi, N. Bennis, J.M. Sánchez-Pena, **"A Novel High-Sensitivity, Low-Power, Liquid Crystal Temperature Sensor"**, Sensors, vol. 14, no. 4, pp. 6571-6583 (2014). DOI: 10.3390/s140406571

12. J. F. Algorri, V. Urruchi, N. Bennis, J.M. Sánchez-Pena, **"Liquid Crystal Temperature Sensor based on a Micrometric Structure and a Metallic Nanometric Layer"**, IEEE Elect. Dev. Lett., vol. 35, no. 6, pp. 666-668 (2014). DOI: 10.1109/LED.2014.2314682

13. J. F. Algorri, V. Urruchi, N. Bennis, J.M. Sánchez-Pena, **"Modal liquid crystal microaxicon array"**, Opt. Lett., vol. 39, no. 12, pp. 3476-3479 (2014). DOI: 10.1364/OL.39.003476.

14. J. F. Algorri, V. Urruchi, B. Garcia-Camara, J.M. Sánchez-Pena, **"Generation of optical vortices by an ideal liquid crystal spiral phase plate"**, IEEE Elect Dev. Lett., vol. 35, no. 8, pp. 856-858 (2014). DOI: 10.1109/LED.2014.2331339

15. J. F. Algorri, V. Urruchi, N. Bennis, J.M. Sánchez-Pena, **"Cylindrical Liquid Crystal Microlens Array with Rotary Optical Power and Tunable Focal Length"**, IEEE Elect. Dev. Lett., vol. 36, no. 6, pp. 582-584 (2015). DOI:10.1109/LED.2015.2419511

16. J. F. Algorri, V. Urruchi, J.M. Sánchez-Pena, J. M. Otón, **"Tunable liquid crystal cylindrical micro-optical array for aberration compensation"**, Opt. Express, vol. 23, no. 11, pp. 13899-13915 (2015). DOI:10.1364/OE.23.013899.

17. J. F. Algorri, P. C. Lallana, V. Urruchi, J. M. Sánchez-Pena, **"Liquid crystal temperature sensor based on three electrode and a high resistivity layer"**, IEEE Sensors J., vol. PP, no. 99 (2015). DOI: 10.1109/JSEN.2015.2439334

7.3.2. Congress contributions

1. V. Urruchi, J.F. Algorri, J.M. Sánchez-Pena, N. Bennis, X. Quintana, J.M. Otón, **"Electro-optic Characterization of Tunable Cylindrical Liquid Crystal Lenses"**, European Conference on Liquid Crystals, ECLC'11, ISBN: 978-961-6657-19-8, Maribor, Eslovenia, 2011.

2. J. F. Algorri, V. Urruchi, J.M. Sánchez-Pena, N. Bennis, M.A. Geday, **"Respuesta Electroóptica de Microlentes de Cristal Líquido Sintonizables"**, 7ª Reunión Española de Optoelectrónica, OPTOEL'11, ISBN 978-84-86116-31-6, Santander, España, 2011.

3. J. F. Algorri, V. Urruchi, J.M. Sánchez-Pena, N. Bennis, **"Caracterización Angular de la Luminancia en Microlentes de Cristal Líquido"**, Congreso Unión Científica Internacional de Radio, URSI 2011, ISBN 978-84-933934-4-1, Madrid, España, 2011.
4. V. Urruchi, J.F. Algorri, M.A. Geday, X. Quintana, N. Bennis, J.M. Sánchez-Pena, **"Lenticular Arrays Based on Liquid Crystals"**, XIX Conference on Liquid Crystals. Chemistry, Physics and Applications, CLC 2011, Proceedings P5-11, Międzyzdroje, Polonia, 2011.
5. J. F. Algorri, V. Urruchi, J.M. Sánchez-Pena, J.M. Otón, **"Simulations on distribution of phase retardation through liquid crystal lenses"**, 24th International Liquid Crystal Conference, ILCC 2012, Proceedings PIII-162, Mainz, Germany, 2012.
6. J. F. Algorri, V. Urruchi, J.M. Sánchez-Pena, J.M. Otón, **"Performance evaluation of a LC based 3D autostereoscopic display"**, Institute of Physics, IOP Photon'12, Proceedings P1-01, Durham, United Kingdom, 2012.
7. J. F. Algorri, V. Urruchi, J.M. Sánchez-Pena, **"An analytical approach to the design of liquid crystal microlenses"**, 40th Topical Meeting on Liquid Crystals, Proceedings P32, Paderborn, Germany, 2013.
8. J. F. Algorri, V. Urruchi, J. M. Sánchez-Pena, B. Romero, **"A novel algorithm based on shooting method to simulate the electro-optic response of a Nematic Liquid Crystal"**, 8ª Reunión Española de Optoelectrónica, OPTOEL'13, ISBN 978-84-88754-21-9, Madrid, Spain, 2013.
9. J. F. Algorri, V. Urruchi, B. Romero, J.M. Sánchez-Pena, N. Bennis, **"Assessment of optical aberrations of tunable liquid crystal cylindrical microlenses"**, XX Conference on Liquid Crystals. Chemistry, Physics and Applications, CLC 2013, Proceedings PC-24, Mikołajki, Poland, 2013.
10. C. Marcos, J. C. Torres, J. M. Sánchez Pena, I. Pérez, V. Urruchi, J.F. Algorri, N. Bennis, X. Quintana, **"New temperature sensor using a liquid crystal cell with homeotropic orientation as a sensing element"**, XX Conference on Liquid Crystals. Chemistry, Physics and Applications, CLC 2013, Proceedings PC-08, Mikołajki, Poland, 2013.
11. J. F. Algorri, V. Urruchi, J.M. Sánchez-Pena, N. Bennis, **"A novel liquid crystal temperature sensor based on modal control principle"**, European Conference on Liquid Crystals, ECLC'13, P2-27, Rhodas, Greece, 2013.
12. J. F. Algorri, V. Urruchi, G.D. Love, N. Bennis, J.M. Sánchez-Pena, J.M. Otón, **"Novel electro-optic components for focusing and guidance of light"**, Cost Action IC1208: Integrating devices and materials: a challenge for new instrumentation in ICT, Madrid, Spain, 2013.
13. J. F. Algorri, B. García-Cámara, A. García-García, V. Urruchi, J. M. Sánchez-Pena, **"Theoretical modeling of a Localized Surface Plasmon Resonance (LSPR) based fiber optic temperature sensor,"** Proc. of SPIE vol. 9157, 23rd International Conference on Optical Fibre Sensors, 915738 2014.
14. J. F. Algorri, B. Garcia-Camara, V. Urruchi, J.M. Sánchez-Pena, J.M. Otón, **"Analysis of Amplitude Modulation of Light through a Mixture of Metallic/Semiconductor Nanoparticles embedded in a Liquid Crystal for Temperature Sensing"**, Cost Action

IC1208: Integrating devices and materials: a challenge for new instrumentation in ICT, Praga, República Checa, 2014.

15. J. F. Algorri, B. Garcia-Camara, V. Urruchi, J.M. Sánchez-Pena, **"Temperature sensor based on a liquid crystal plasmonic wire grating"**, IEEE SENSORS 2014, pp. 390-393, 2-5 Nov. 2014.
16. J. F. Algorri, P. C. Lallana, V. Urruchi, J.M. Sánchez-Pena, **"Modal liquid crystal temperature sensor"**, IEEE SENSORS 2014, pp.1960-1963, 2-5 Nov. 2014.
17. A. García-García, R. Vergaz, J.F. Algorri, J.M. Otón, M. Geday, **"Espectroscopía de impedancia de células de cristal líquido dopadas con nanotubos de carbono"**, XII Reunión Nacional de Electrocerámica, Junio, Madrid, 2015.
18. J. F. Algorri, B. Garcia-Camara, V. Urruchi, J.M. Sánchez-Pena, R. Vergaz, **"All optical strain gauge based on plasmonic reflections of a wire grating"**, 9ª Reunión Española de Optoelectrónica, OPTOEL'15, Salamanca, España, 2015. Accepted.
19. J. F. Algorri, B. Garcia-Cámara, D. Podereux, R. Vergaz, V. Urruchi, J.M. Sánchez-Pena, **"Thermo-optical properties of polydimethylsiloxane (PDMS) doped with metallic nanoparticles"**, META'15, New York City, NY, USA 2015. Accepted.
20. B. Garcia-Camara, J. F. Algorri, V. Urruchi, J.M. Sánchez-Pena, R. Vergaz, **"Tuning and Enhancement of the Magneto-Dielectric Behavior of Semiconductor Nanoparticles"**, META'15, New York City, NY, USA 2015. Accepted.
21. J. F. Algorri, V. Urruchi, B. Garcia-Cámara, J.M. Sánchez-Pena, **"Polymer stabilized blue phase beam steering"**, Optics of liquid crystals (OLC) Sopot, Poland 2015. Accepted.
22. J. F. Algorri, J .C Torres, V. Urruchi, B. Garcia-Cámara, J.M. Sánchez-Pena, **"Optical vortices by a modal liquid crystal spiral phase plate"**, Optics of liquid crystals (OLC) Sopot, Poland 2015. Accepted.

7.3.3. Book chapters

1. J. F. Algorri, V. Urruchi, B. Garcia-Camara, J.M. Sánchez-Pena, Liquid crystal lensacons, logarithmic and linear axicons in: **Liquid Crystals: From Modified Phases to Applications**, Ed. MDPI, ISBN 978-3-906980-86-7, 2014.
2. B. Garcia-Cámara, J. F. Algorri, V. Urruchi, J.M. Sánchez-Pena, Directional Scattering of Semiconductor Nanoparticles embedded in a Liquid Crystal in: **Liquid Crystals: From Modified Phases to Applications**, Ed. MDPI, ISBN 978-3-906980-86-7, 2014.

7.3.4. Other related works

1. B. Garcia-Cámara, J.F. Algorri, V. Urruchi, J.M. Sánchez-Pena, **"Directional Scattering of Semiconductor Nanoparticles embedded in a Liquid Crystal"**, Materials, vol. 7, no. 4, pp. 2784-2794 (2014). DOI: 10.3390/ma7042784

2. J. F. Algorri, B. Garcia-Camara, V. Urruchi, J.M. Sánchez-Pena, **"High-Sensitivity Temperature Sensor based on a Fabry-Perot configuration with a Liquid Crystal doped with Plasmonic Nanoparticles"**, IEEE Photon. Technol. Lett., vol. 26, no. 8, pp. 793-796 (2015). DOI: 10.1109/LPT.2014.2369734
3. J. F. Algorri, B. García-Cámara, A. García-García, V. Urruchi, J. M. Sánchez-Pena, **"Fiber Optic Temperature Sensor Based On Amplitude Modulation of Metallic and Semiconductor Nanoparticles in a Liquid Crystal Mixture**", J. LightWave Tech., vol. PP, no. 99, (2015). DOI: 10.1109/JLT.2015.2396357
4. J. F. Algorri, V. Urruchi, J. M. Sánchez-Pena, **"Reflective sidewall electrodes for low voltage and high transmittance blue-phase liquid crystal displays"**, Liquid Crystals, (2015). DOI:10.1080/02678292.2015.1006152
5. A. García-García, R. Vergaz, J.F. Algorri, X. Quintana and J.M. Otón, **"Electrical response of liquid crystal cells doped with multi-walled carbon nanotubes"**, Belstein J. Nanotech., vol. 6, pp. 396–403. (2015). DOI:10.3762/bjnano.6.39
6. A. García-García, R. Vergaz, J.F. Algorri, and J.M. Otón, **"Multiwall carbon nanotube-liquid crystal systems as seen by impedance spectroscopy"**, J. App. Phys. D, under revision (2015).
7. B. García-Cámara, J. F. Algorri, A. Cuadrado, V. Urruchi, J. M. Sánchez-Pena, R. Vergaz, **"Size dependence of the directional scattering conditions on resonant semiconductor nanoparticles"**, Opt. Lett., under revision (2015).
8. J. F. Algorri, D. Podereux, B. García-Cámara, V. Urruchi, J. M. Sánchez-Pena, **"Polydimethylsiloxane (PDMS) doped with metallic nanoparticles as optical sensing element"**, IEEE Photon. Technol. Lett., under revision (2015).

REFERENCES

[1] O. Lehmann, “Über fliessende Krystalle (On flowing crystals),” *Zeitschrift für Phys. Chemie*, vol. 4, pp. 462–472, 1889.

[2] V. Freedericksz and V. Zolina, “Forces causing the orientation of an anisotropic liquid,” *Trans. Faraday Soc.*, vol. 29, pp. 919–930, 1933.

[3] M. G. Friedel, “The Mesomorphic states of matter,” *Ann. Phys. (Paris).*, vol. 18, pp. 162–174, 1922.

[4] G. H. Heilmeier, “Guest-host interactions in nematic liquid crystal. A new electro-optic effect,” *Appl. Phys. Lett.*, vol. 13, no. 3, p. 91, 1968.

[5] M. Schadt and W. Helfrich, “Voltage-dependent optical activity of a twisted nematic liquid crystal,” *Appl. Phys. Lett.*, vol. 18, no. 4, p. 127, Feb. 1971.

[6] H. Kawamoto, “The history of liquid-crystal displays,” *Proc. IEEE*, vol. 90, no. 4, pp. 460–500, Apr. 2002.

[7] F. R. Libsh and J. Kanichi, “TFT lifetime in LCD operation,” in *SID 93’ Dig. Tech.*, 1993.

[8] T. J. Scheffer and J. Nehring, “A new, highly multiplexable liquid crystal display,” *Appl. Phys. Lett.*, vol. 45, no. 10, pp. 1021–23, 1984.

[9] R. Soref, “Liquid crystal electric field sensing measurement and display device,” US3834794 A, 10-Sep-1974.

[10] E. Lueder, *Liquid Crystal Displays: Addressing Schemes and Electro-Optical Effects (Wiley Series in Display Technology)*. Wiley, 2001.

[11] E. S. Foundation, Ed., “Frontiers In European Research On Liquid Crystalline Soft Matter,” in *ESF Exploratory Workshop*, 2009.

[12] M. Koeberle, M. Hoefle, M. Chen, A. Penirschke, and R. Jakoby, “Electrically tunable Liquid Crystal phase shifter in antipodal finline technology for reconfigurable W-Band Vivaldi antenna array concepts,” *Antennas Propag.*, pp. 1536–39, 2011.

[13] M. A. Geday, X. Quintana, E. Otón, B. Cerrolaza, D. Lopez, F. G. de Quiro, I. G. Manolis, and A. Short, “Development of liquid crystal based adaptive optical elements for space applications,” in *Greece International Conference on Space Optics*, 2010.

[14] A. Gaebler, A. Moessinger, F. Goelden, A. Manabe, M. Goebel, R. Follmann, D. Koether, C. Modes, A. Kipka, M. Deckelmann, T. Rabe, B. Schulz, P. Kuchenbecker, A. Lapanik, S.

Mueller, W. Haase, and R. Jakoby, “Liquid Crystal-Reconfigurable Antenna Concepts for Space Applications at Microwave and Millimeter Waves,” *Int. J. Antennas Propag.*, vol. 2009, pp. 1–7, 2009.

[15] S. Muller, P. Scheele, C. Weil, M. Wittek, C. Hock, and R. Jakoby, “Tunable passive phase shifter for microwave applications using highly anisotropic liquid crystals,” in *IEEE MTT-S International Microwave Symposium Digest (IEEE Cat. No.04CH37535)*, 2004, vol. 2.

[16] V. Urruchi, C. Marcos, J. Torrecilla, J. M. Sánchez-Pena, and K. Garbat, “Note: tunable notch filter based on liquid crystal technology for microwave applications.,” *Rev. Sci. Instrum.*, vol. 84, no. 2, p. 026102, Feb. 2013.

[17] G. S. Lee, J. H. Lee, J. C. Kim, T.-H. Yoon, J.-H. Kim, J.-H. Yu, and H.-Y. Choi, “Nanoparticle Doped In-Cell Retarder for Low Operating Voltage in Transflective Liquid Crystal Displays,” *Jpn. J. Appl. Phys.*, vol. 48, no. 4, p. 042405, Apr. 2009.

[18] A. García-García, R. Vergaz, J. F. Algorri, X. Quintana, and J. M. Otón, “Electrical response of liquid crystal cells doped with multi-walled carbon nanotubes,” *Beilstein J. Nanotechnol.*, vol. 6, no. 1, pp. 396–403, Feb. 2015.

[19] R. Pratibha, S. Kumar, and K. K. Raina, “Effect of dispersion of gold nanoparticles on the optical and electrical properties of discotic liquid crystal,” *Liq. Cryst.*, vol. 41, no. 7, pp. 933–939, Mar. 2014.

[20] B. García-Cámara, J. Algorri, V. Urruchi, and J. Sánchez-Pena, “Directional Scattering of Semiconductor Nanoparticles Embedded in a Liquid Crystal,” *Materials (Basel).*, vol. 7, no. 4, pp. 2784–2794, Apr. 2014.

[21] B. García-Cámara, R. Gómez-Medina, J. J. Sáenz, and B. Sepúlveda, “Sensing with magnetic dipolar resonances in semiconductor nanospheres.,” *Opt. Express*, vol. 21, no. 20, pp. 23007–20, Oct. 2013.

[22] J. Bao-Guang, C. Zhao-Liang, and M. Quan-Quan, “Simulated human eye retina adaptive optics imaging system based on a liquid crystal on silicon device,” *Chinese Phys. B*, vol. 17, no. 12, pp. 4529–4532, 2008.

[23] S. Wang, L. Pan, R. Pindak, Z. Q. Liu, H. T. Nguyen, and C. C. Huang, “Discovery of a Novel Smectic-C^{*} Liquid-Crystal Phase with Six-Layer Periodicity,” *Phys. Rev. Lett.*, vol. 104, no. 2, p. 27801, Jan. 2010.

[24] S. He, W. Liang, K.-L. Cheng, J. Fang, and S.-T. Wu, “Bile acid-surfactant interactions at the liquid crystal/aqueous interface.,” *Soft Matter*, vol. 10, no. 26, pp. 4609–14, Jul. 2014.

[25] C. Carrasco-Vela, X. Quintana, E. Otón, M. A. Geday, and J. M. Otón, “Security devices based on liquid crystals doped with a colour dye,” *Opto-Electronics Rev.*, vol. 19, no. 4, pp. 496–500, Aug. 2011.

[26] A. Minovich, J. Farnell, D. N. Neshev, I. McKerracher, F. Karouta, J. Tian, D. A. Powell, I. V. Shadrivov, H. Hoe Tan, C. Jagadish, and Y. S. Kivshar, “Liquid crystal based nonlinear fishnet metamaterials,” *Appl. Phys. Lett.*, vol. 100, no. 12, pp. 12–13, Mar. 2012.

[27] C. Marcos, J. M. Sánchez-Pena, J. C. Torres, and J. I. Santos, "Temperature-Frequency Converter Using a Liquid Crystal Cell as a Sensing Element," *Sensors*, vol. 12, no. 3, pp. 3204–14, Mar. 2012.

[28] J. Li, S. Gauza, S.-T. Wu, T. T. Alkeskjold, J. Lægsgaard, and A. Bjarklev, "High dn o / dT Liquid Crystals and their Applications in a Thermally Tunable Liquid Crystal Photonic Crystal Fiber," *Mol. Cryst. Liq. Cryst.*, vol. 453, no. 1, pp. 355–370, Sep. 2006.

[29] E. Jang, "Electrooptic temperature sensor based on a Fabry-Pe/spl acute/rot resonator with a liquid crystal film," *IEEE Photonics Technol. Lett.*, vol. 18, no. 8, pp. 905–907, Apr. 2006.

[30] Y. Wang, M. Yang, D. N. Wang, and C. R. Liao, "Selectively Infiltrated Photonic Crystal Fiber With Ultrahigh Temperature Sensitivity," *IEEE Photonics Technol. Lett.*, vol. 23, no. 20, pp. 1520–1522, Oct. 2011.

[31] D. J. D. Davies, A. R. Vaccaro, S. M. Morris, N. Herzer, A. P. H. J. Schenning, and C. W. M. Bastiaansen, "A Printable Optical Time-Temperature Integrator Based on Shape Memory in a Chiral Nematic Polymer Network," *Adv. Funct. Mater.*, vol. 23, no. 21, pp. 2723–2727, Jun. 2013.

[32] J. F. Algorri, P. C. Lallana, V. Urruchi, and J. M. Sánchez-Pena, "Liquid crystal temperature sensor based on three electrodes and a high resistivity layer," *IEEE Sensors*, vol. In revisio, 2015.

[33] J. F. Algorri, V. Urruchi, N. Bennis, and J. M. Sánchez-Pena, "Liquid Crystal Temperature Sensor Based on a Micrometric Structure and a Metallic Nanometric Layer," *IEEE Electron Device Lett.*, vol. 35, no. 6, pp. 666–668, Jun. 2014.

[34] J. F. Algorri, V. Urruchi, N. Bennis, and J. M. Sánchez-Pena, "A novel high-sensitivity, low-power, liquid crystal temperature sensor.," *Sensors (Basel).*, vol. 14, no. 4, pp. 6571–83, Jan. 2014.

[35] J. F. Algorri, B. Garcia-Camara, V. Urruchi, and J. M. Sanchez-Pena, "High-Sensitivity Fabry-Pérot Temperature Sensor Based on Liquid Crystal Doped With Nanoparticles," *IEEE Photonics Technol. Lett.*, vol. 27, no. 3, pp. 292–295, Feb. 2015.

[36] J. F. Algorri, B. Garcia-Camara, A. Garcia-Garcia, V. Urruchi, and J. M. Sánchez-Pena, "Fiber Optic Temperature Sensor Based On Amplitude Modulation of Metallic and Semiconductor Nanoparticles in a Liquid Crystal Mixture," *J. Light. Technol.*, vol. PP, no. 99, pp. 1–1, 2015.

[37] P. Valley, M. Reza Dodge, J. Schwiegerling, G. Peyman, and N. Peyghambarian, "Nonmechanical bifocal zoom telescope," *Opt. Lett.*, vol. 35, no. 15, pp. 2582–2584, Jul. 2010.

[38] E. Otón, A. Carrasco, R. Vergaz, J. M. Otón, J. M. Sánchez-Pena, X. Quintana, and M. Geday, "2D tunable beam steering - lens device based on high birefringence liquid crystals," in *2011 International Conference on Space Optical Systems and Applications (ICSOS)*, 2011.

[39] S. P. Kotova, V. V. Patlan, S. A. Samagin, and O. A. Zayakin, "Wavefront formation using modal liquid-crystal correctors," *Phys. Wave Phenom.*, vol. 18, no. 2, pp. 96–104, May 2010.

[40] R. Davies and M. Kasper, "Adaptive Optics for Astronomy," *Annu. Rev. Astron. Astrophys.*, vol. 50, Sep. 2012.

[41] Y.-Y. Kao, Y.-P. Huang, K.-X. Yang, P. C.-P. Chao, C.-C. Tsai, and C.-N. Mo, "An Auto-Stereoscopic 3D Display Using Tunable Liquid Crystal Lens Array That Mimics Effects of GRIN Lenticular Lens Array," *SID Symp. Dig. Tech. Pap.*, vol. 40, no. 1, pp. 111–115, 2009.

[42] J. F. Algorri, V. Urruchi del Pozo, J. M. Sanchez-Pena, and J. M. Oton, "An Autostereoscopic Device for Mobile Applications Based on a Liquid Crystal Microlens Array and an OLED Display," *J. Disp. Technol.*, vol. 10, no. 9, pp. 713–720, Sep. 2014.

[43] J. F. Algorri, V. Urruchi, N. Bennis, J. M. Sánchez-Pena, and J. M. Otón, "Tunable liquid crystal cylindrical micro-optical array for aberration compensation," *Opt. Express*, vol. 23, no. 11, pp. 13899–13915, 2015.

[44] J. F. Algorri, V. Urruchi, N. Bennis, and J. M. Sánchez-Pena, "Modal liquid crystal microaxicon array.," *Opt. Lett.*, vol. 39, no. 12, pp. 3476–9, Jun. 2014.

[45] J. F. Algorri, V. Urruchi, N. Bennis, and J. M. Sánchez-Pena, "Cylindrical liquid crystal microlens array with rotary axis and tunable capability," *IEEE Electron Device Lett.*, vol. PP, no. 99, 2015.

[46] J. F. Algorri, G. D. Love, and V. Urruchi, "Modal liquid crystal array of optical elements.," *Opt. Express*, vol. 21, no. 21, pp. 24809–18, Oct. 2013.

[47] J. F. Algorri, V. Urruchi, B. Garcia-Camara, and J. M. Sanchez-Pena, "Generation of Optical Vortices by an Ideal Liquid Crystal Spiral Phase Plate," *IEEE Electron Device Lett.*, vol. 35, no. 8, pp. 856–858, Aug. 2014.

[48] J. Algorri, V. Urruchi, B. García-Cámara, and J. Sánchez-Pena, "Liquid Crystal Lensacons, Logarithmic and Linear Axicons," *Materials (Basel).*, vol. 7, no. 4, pp. 2593–2604, Mar. 2014.

[49] V. Urruchi, J. F. Algorri, J. M. Sánchez-Pena, N. Bennis, X. Quintana, and J. M. Otón, "Electrooptic characterization of tunable cylindrical liquid crystal lenses," *Mol. Cryst. Liq. Cryst.*, vol. 553, no. 1, pp. 211–219, 2012.

[50] V. Urruchi, J. F. Algorri, J. C. Torres, and J. M. Sanchez-Pena, "Modeling of Unwrapped Phase Defects in Modal Liquid Crystal Cylindrical Microlenses," *IEEE Photonics Technol. Lett.*, vol. 26, no. 2, pp. 198–201, Jan. 2014.

[51] V. Urruchi, J. F. Algorri, C. Marcos, and J. M. Sánchez-Pena, "Note: Electrical modeling and characterization of voltage gradient in liquid crystal microlenses.," *Rev. Sci. Instrum.*, vol. 84, no. 11, p. 116105, Nov. 2013.

[52] J. F. Algorri, V. Urruchi, N. Bennis, and J. M. Sánchez-Pena, "Using an Analytical Model to Design Liquid Crystal Microlenses," *IEEE Photonics Technol. Lett.*, vol. 26, no. 8, pp. 793–796, Apr. 2014.

[53] Charles Wheatstone, "Contributions to the Physiology of Vision," *R. Soc. London*, vol. 6, pp. 138–141, 1854.

[54] T. De Zwart, Siebe and G. H. Hiddink Martin, "Autostereoscopic image output device," WO/2009/101558, 2009.

[55] J. L. Pezzaniti, "Autostereoscopic 3-D display," 7070278, 2006.

[56] D. W. Berreman, "Variable-focus LC-lens system," 4 190 330, 1980.

[57] Susumu Sato, "LC lens-cell with variable focal length," *Jpn. J. Appl. Phys.*, vol. 18, pp. 1679 –1684, 1979.

[58] S. T. Kowe and D. S. Cleverly, "A Liquid Crystal Adaptive Lens," in *NASA Conference on Optical Information Processing for Aerospace Applications*, 1981.

[59] D. Cleverly, "Creation of a Lens by Field Controlled Variation of the Index Of Refraction in a Liquid Crystal," Syracuse University, 1982.

[60] N. A. Riza and M. C. Dejule, "Three-terminal adaptive nematic liquid-crystal lens device," *Opt. Lett.*, vol. 19, no. 14, pp. 1013–1015, Jul. 1994.

[61] T. Nose and S. Sato, "A liquid crystal microlens obtained with a non-uniform electric field," *Liq. Cryst.*, vol. 5, no. 5, pp. 1425–1433, Jan. 1989.

[62] T. Nose and S. Sato, "Optical properties of a liquid crystal microlens," in *Intl Conf on Optoelectronic Science and Engineering*, 1990, vol. 1230.

[63] G. Williams, N. Powell, A. Purvis, and M. G. Clark, "Electrically controllable liquid crystal fresnel lens," in *Opto-electronics Symposium SPIE 1168*, 1989.

[64] M. Ye, B. Wang, M. Uchida, S. Yanase, S. Takahashi, and S. Sato, "Focus tuning by liquid crystal lens in imaging system.," *Appl. Opt.*, vol. 51, no. 31, pp. 7630–5, Nov. 2012.

[65] Y.-H. Lin and M.-S. Chen, "A Pico Projection System With Electrically Tunable Optical Zoom Ratio Adopting Two Liquid Crystal Lenses," *J. Disp. Technol.*, vol. 8, no. 7, pp. 401–404, Jul. 2012.

[66] H.-C. Lin, N. Collings, M.-S. Chen, and Y.-H. Lin, "A holographic projection system with an electrically tuning and continuously adjustable optical zoom.," *Opt. Express*, vol. 20, no. 25, pp. 27222–9, Dec. 2012.

[67] Y.-S. Tsou, K.-H. Chang, and Y.-H. Lin, "A droplet manipulation on a liquid crystal and polymer composite film as a concentrator and a sun tracker for a concentrating photovoltaic system," *J. Appl. Phys.*, vol. 113, no. 24, p. 244504, Jun. 2013.

[68] A. Hassanfiroozi, Y.-P. Huang, B. Javidi, and H.-P. D. Shieh, "Hexagonal liquid crystal lens array for 3D endoscopy.," *Opt. Express*, vol. 23, no. 2, pp. 971–81, Jan. 2015.

[69] P. Optics, "Electronic Eyewear." [Online]. Available: www.pixeloptics.com/pages/electronic_eyewear.

[70] Y.-H. Lin and H.-S. Chen, "Electrically tunable-focusing and polarizer-free liquid crystal lenses for ophthalmic applications.," *Opt. Express*, vol. 21, no. 8, pp. 9428–36, Apr. 2013.

[71] Y.-H. Lin, H. Ren, K.-H. Fan-Chiang, W.-K. Choi, S. Gauza, X. Zhu, and S.-T. Wu, "Tunable-Focus Cylindrical Liquid Crystal Lenses," *Jpn. J. Appl. Phys.*, vol. 44, no. 1A, pp. 243–244, Jan. 2005.

[72] M. Ye, B. Wang, and S. Sato, "Liquid-crystal lens with a focal length that is variable in a wide range.," *Appl. Opt.*, vol. 43, no. 35, pp. 6407–6412, Dec. 2004.

[73] M. Kawamura, K. Nakamura, and S. Sato, "Liquid-crystal micro-lens array with two-divided and tetragonally hole-patterned electrodes.," *Opt. Express*, vol. 21, no. 22, pp. 26520–6, Nov. 2013.

[74] M. Kawamura and H. Goto, "Liquid crystal lens with two divided and double circularly hole-patterned electrodes," in *2010 International Symposium on Optomechatronic Technologies*, 2010, pp. 1–5.

[75] Y. Li and S.-T. Wu, "Polarization independent adaptive microlens with a blue-phase liquid crystal.," *Opt. Express*, vol. 19, no. 9, pp. 8045–50, Apr. 2011.

[76] C. J. Hsu and C. R. Sheu, "Using photopolymerization to achieve tunable liquid crystal lenses with coaxial bifocals.," *Opt. Express*, vol. 20, no. 4, pp. 4738–46, Feb. 2012.

[77] X. Zhao, C. Liu, D. Zhang, and Y. Luo, "Tunable liquid crystal microlens array using hole patterned electrode structure with ultrathin glass slab.," *Appl. Opt.*, vol. 51, no. 15, pp. 3024–30, May 2012.

[78] V. Urruchi, J. F. Algorri, J. M. Sánchez-Pena, M. A. Geday, X. Q. Arregui, and N. Bennis, "Lenticular arrays based on liquid crystals," *Opto-Electronics Rev.*, vol. 20, no. 3, pp. 71–77, May 2012.

[79] H. Ren and S.-T. Wu, "Adaptive liquid crystal lens with large focal length tunability.," *Opt. Express*, vol. 14, no. 23, pp. 11292–98, Nov. 2006.

[80] J. Harrold, D. J. Wilkes, and G. J. Woodgate, "Switchable 2D/3D display–solid phase liquid crystal microlens array," in *Proc. IDW*, 2004, vol. 11.

[81] B. Wang, M. Ye, and S. Sato, "Lens of electrically controllable focal length made by a glass lens and liquid-crystal layers," *Appl. Opt.*, vol. 43, no. 17, pp. 3420–3425, 2004.

[82] L. G. Commander and S. E. Day, "Variable focal length microlenses," *Opt. Commun.*, no. April, pp. 157–170, 2000.

[83] O. H. Willemsen, S. T. de Zwart, W. L. IJzerman, M. G. H. Hiddink, and T. Dekker, "2D/3D switchable displays," in *Proceedings of SPIE*, 2006, vol. 6135.

[84] D. K. G. de Boer, M. G. H. Hiddink, M. Sluijter, O. H. Willemsen, and S. T. de Zwart, "Switchable lenticular based 2D/3D displays," *Proc. SPIE*, vol. 6490, no. 1, p. 64900R–64900R–8, Feb. 2007.

[85] J. Flack, J. Harrold, and G. J. Woodgate, "A prototype 3D mobile phone equipped with a next-generation autostereoscopic display," in *Proceedings of SPIE*, 2007, vol. 6490, p. 64900M–64900M–12.

[86] E. G. Abramochkin, A. A. Vasiliev, P. V. Vashurin, L. I. Zhmurova, V. A. Ignatov, and A. F. Naumov, "Controlled liquid crystal lens," *Prepr. P. N. Lebedev Phys. Inst.*, vol. 194, p. 18, 1988.

[87] G. D. Love and A. F. Naumov, "Modal liquid crystal lenses," *Liq. Cryst. Today*, vol. 10, no. 1, pp. 1–4, Mar. 2000.

[88] N. Fraval and J. L. de Bougrenet, "Low aberrations symmetrical adaptive modal liquid crystal lens with short focal lengths.," *Appl. Opt.*, vol. 49, no. 15, pp. 2778–2783, May 2010.

[89] M. Y. Loktev, V. N. Belopukhov, F. L. Vladimirov, G. V. Vdovin, G. D. Love, and A. F. Naumov, "Wave front control systems based on modal liquid crystal lenses," *Rev. Sci. Instrum.*, vol. 71, no. 9, pp. 3290–3297, 2000.

[90] A. K. Kirby, P. J. Hands, and G. D. Love, "Liquid crystal multi-mode lenses and axicons based on electronic phase shift control," *Opt. Express*, vol. 15, no. 21, pp. 13496–13501, Oct. 2007.

[91] A. F. Naumov, G. D. Love, M. Y. Loktev, and F. L. Vladimirov, "Control optimization of spherical modal liquid crystal lenses.," *Opt. Express*, vol. 4, no. 9, pp. 344–52, Apr. 1999.

[92] P. J. W. Hands and A. K. Kirby, "Adaptive modally addressed liquid crystal lenses," *Proc. SPIE*, vol. 44, no. 0, 2004.

[93] "Flexible Optical B. V.," 2012. [Online]. Available: www.okotech.com/lc.

[94] J. H. Mcleod, "Axicons and Their Uses," *J. Opt. Soc. Am.*, vol. 50, no. 2, p. 166, Feb. 1960.

[95] M. Rioux, R. Tremblay, and P. A. Bélanger, "Linear, annular, and radial focusing with axicons and applications to laser machining.," *Appl. Opt.*, vol. 17, no. 10, pp. 1532–6, May 1978.

[96] O. Ren and R. Birngruber, "Axicon: a new laser beam delivery system for corneal surgery," *IEEE J. Quantum Electron.*, vol. 26, no. 12, pp. 2305–2308, 1990.

[97] R. A. Leitgeb, M. Villiger, A. H. Bachmann, L. Steinmann, and T. Lasser, "Extended focus depth for Fourier domain optical coherence microscopy," *Opt. Lett.*, vol. 31, no. 16, p. 2450, 2006.

[98] R. Arimoto, C. Saloma, T. Tanaka, and S. Kawata, "Imaging properties of axicon in a scanning optical system.," *Appl. Opt.*, vol. 31, no. 31, pp. 6653–7, Nov. 1992.

[99] S. Cabrini, C. Liberale, D. Cojoc, A. Carpentiero, M. Prasciolu, S. Mora, V. Degiorgio, F. De Angelis, and E. Di Fabrizio, "Axicon lens on optical fiber forming optical tweezers, made by focused ion beam milling," *Microelectron. Eng.*, vol. 83, no. 4–9, pp. 804–807, Apr. 2006.

[100] J. Arlt, T. Hitomi, and K. Dholakia, "Atom guiding along Laguerre-Gaussian and Bessel light beams," *Appl. Phys. B Lasers Opt.*, vol. 71, no. 4, pp. 549–554, Oct. 2000.

[101] R. Grunwald and M. Bock, “Spatially encoded localized wavepackets for ultrafast optical data transfer,” *J. Eur. Opt. Soc. - Rapid Publ. vol 7 12009*, vol. 7, 2012.

[102] R. Grunwald, U. Griebner, F. Tschirschwitz, E. T. J. Nibbering, T. Elsaesser, V. Kebbel, H.-J. Hartmann, and W. Jüptner, “Generation of femtosecond Bessel beams with microaxicon arrays,” *Opt. Lett.*, vol. 25, no. 13, p. 981, Jul. 2000.

[103] M. Bock, S. K. Das, and R. Grunwald, “Programmable ultrashort-pulsed flying images,” *Opt. Express*, vol. 17, no. 9, p. 7465, Apr. 2009.

[104] X.-F. Lin, Q.-D. Chen, L.-G. Niu, T. Jiang, W.-Q. Wang, and H.-B. Sun, “Mask-Free Production of Integratable Monolithic Micro Logarithmic Axicon Lenses,” *J. Light. Technol.*, vol. 28, no. 8, pp. 1256–1260, Apr. 2010.

[105] R. Grunwald, S. Woggon, R. Ehlert, and W. Reinecke, “Thin-film microlens arrays with non-spherical elements,” *Pure Appl. Opt. J. Eur. Opt. Soc. Part A*, vol. 6, no. 6, pp. 663–671, Nov. 1997.

[106] Q. Peng, Y. Guo, B. Chen, J. Du, J. Xiang, and Z. Cui, “LCD real-time mask technique for fabrication of arbitrarily shaped microstructure,” in *Symposium on Design, Test, Integration, and Packaging of MEMS/MOEMS 2002*, 2002, pp. 748–754.

[107] N. Weber, D. Spether, A. Seifert, and H. Zappe, “Highly compact imaging using Bessel beams generated by ultraminiaturized multi-micro-axicon systems.,” *J. Opt. Soc. Am. A. Opt. Image Sci. Vis.*, vol. 29, no. 5, pp. 808–16, May 2012.

[108] R. Grunwald and M. Bock, “Programmable microoptics for ultrashort pulses,” in *SPIE Photonics Europe*, 2010, p. 77160P–77160P–8.

[109] M. Padgett and R. Bowman, “Tweezers with a twist,” *Nat. Photonics*, vol. 5, no. 6, pp. 343–348, Jun. 2011.

[110] K. Ladavac and D. G. Grier, “Microoptomechanical pumps assembled and driven by holographic optical vortex arrays,” *Opt. Express*, vol. 12, no. 6, p. 1144, 2004.

[111] J. W. R. Tabosa and D. V. Petrov, “Optical Pumping of Orbital Angular Momentum of Light in Cold Cesium Atoms,” *Phys. Rev. Lett.*, vol. 83, no. 24, pp. 4967–4970, Dec. 1999.

[112] J. Wang, J.-Y. Yang, I. M. Fazal, N. Ahmed, Y. Yan, H. Huang, Y. Ren, Y. Yue, S. Dolinar, M. Tur, and A. E. Willner, “Terabit free-space data transmission employing orbital angular momentum multiplexing,” *Nat. Photonics*, vol. 6, no. 7, pp. 488–496, Jun. 2012.

[113] N. Bozinovic, Y. Yue, Y. Ren, M. Tur, P. Kristensen, H. Huang, A. E. Willner, and S. Ramachandran, “Terabit-scale orbital angular momentum mode division multiplexing in fibers.,” *Science*, vol. 340, no. 6140, pp. 1545–8, Jun. 2013.

[114] Y.-H. Huang, M.-S. Li, S.-W. Ko, and A. Y.-G. Fuh, “Helical wavefront and beam shape modulated by advanced liquid crystal q-plate fabricated via photoalignment and analyzed by Michelson’s interference.,” *Appl. Opt.*, vol. 52, no. 26, pp. 6557–61, Sep. 2013.

[115] N. R. Heckenberg, R. McDuff, C. P. Smith, and A. G. White, “Generation of optical phase singularities by computer-generated holograms,” *Opt. Lett.*, vol. 17, no. 3, p. 221, Feb. 1992.

[116] I. Zeylikovich, H. I. Sztul, V. Kartazaev, T. Le, and R. R. Alfano, "Ultrashort Laguerre-Gaussian pulses with angular and group velocity dispersion compensation," *Opt. Lett.*, vol. 32, no. 14, p. 2025, 2007.

[117] K. Crabtree, J. A. Davis, and I. Moreno, "Optical Processing with Vortex-Producing Lenses," *Appl. Opt.*, vol. 43, no. 6, p. 1360, 2004.

[118] J. Albero, P. Garcia-Martinez, N. Bennis, E. Oton, B. Cerrolaza, I. Moreno, and J. A. Davis, "Liquid Crystal Devices for the Reconfigurable Generation of Optical Vortices," *J. Light. Technol.*, vol. 30, no. 18, pp. 3055–3060, Sep. 2012.

[119] V. Urruchi, "Micropantallas de cristal liquido sobre silicio basadas en materiales esmecticos quirales con respuesta en V," Universidad Politécnica de Madrid, 2004.

[120] J. M. Sánchez Pena, "Caracterización de Pantallas de Cristal Líquido Ferroeléctrico," Universidad Politécnica de Madrid, 1993.

[121] V. R. Brown, "Colorimetric temperature sensor," US3651695 A, 28-Mar-1972.

[122] C. M. Luk, "Liquid crystal temperature indicator for measuring human body temperature," US4302971 A, 01-Dec-1981.

[123] V. M. Balasubramaniam and S. K. Sastry, "Use of liquid crystals as temperature sensors in food processing research," *J. Food Eng.*, vol. 26, no. 2, pp. 219–230, Jan. 1995.

[124] H. Kikuchi, M. Yokota, Y. Hisakado, H. Yang, and T. Kajiyama, "Polymer-stabilized liquid crystal blue phases.," *Nat. Mater.*, vol. 1, no. 1, pp. 64–8, Sep. 2002.

[125] Y. Chen, J. Yan, J. Sun, S.-T. Wu, X. Liang, S.-H. Liu, P.-J. Hsieh, K.-L. Cheng, and J.-W. Shiu, "A microsecond-response polymer-stabilized blue phase liquid crystal," *Appl. Phys. Lett.*, vol. 99, no. 20, p. 201105, Nov. 2011.

[126] S. Gauza, X. Zhu, W. Piecek, R. Dabrowski, and S.-T. Wu, "Fast Switching Liquid Crystals for Color-Sequential LCDs," *J. Disp. Technol.*, vol. 3, no. 3, pp. 250–252, 2007.

[127] Y. Liu, Y. Lan, H. Zhang, R. Zhu, D. Xu, C.-Y. Tsai, J.-K. Lu, N. Sugiura, Y.-C. Lin, and S.-T. Wu, "Optical rotatory power of polymer-stabilized blue phase liquid crystals," *Appl. Phys. Lett.*, vol. 102, no. 13, p. 131102, Apr. 2013.

[128] J. F. Algorri, V. Urruchi, and J. M. Sánchez-Pena, "Reflective sidewall electrodes for low voltage and high transmittance blue-phase liquid crystal displays," *Liq. Cryst.*, 2015.

[129] S. Matsumoto, I. Kadota, and S. Matsumoto, *Liquid Crystals Fundamentals and Applications*. Tokyo, Japan: Kogyochosa-kai, 1991.

[130] P. Yeh and C. Gu, *Optics of Liquid Crystal Displays*. Wiley-Interscience, 1999.

[131] D. A. Usanov, S. A. Nikitov, A. V. Skripal', M. Y. Kulikov, and D. V. Ponomarev, "Measuring the parameters of solid and liquid dielectrics at microwave frequencies with the use of microstrip photonic structures," *J. Commun. Technol. Electron.*, vol. 57, no. 2, pp. 209–214, Feb. 2012.

[132] C.-S. Yang, C.-J. Lin, R.-P. Pan, C. T. Que, K. Yamamoto, M. Tani, and C.-L. Pan, "The complex refractive indices of the liquid crystal mixture E7 in the terahertz frequency range," *J. Opt. Soc. Am. B*, vol. 27, no. 9, p. 1866, Aug. 2010.

[133] M. Davies, *Dielectric and Related Molecular Processes*. Royal Society of Chemistry, 1975.

[134] G. Meier and A. Saupe, "Dielectric Relaxation in Nematic Liquid Crystals," *Mol. Cryst.*, vol. 1, no. 4, pp. 515–525, Jan. 1966.

[135] L. M. Blinov, *Structure and Properties of Liquid Crystals*, vol. 0. Springer, 2010.

[136] Evgenij Barsoukov and J. Ross Macdonald, Eds., *Impedance Spectroscopy: Theory, Experiment, and Applications*. Wiley-Interscience, 2005.

[137] I. Szymańska, H. Radecka, J. Radecki, and R. Kaliszan, "Electrochemical impedance spectroscopy for study of amyloid beta-peptide interactions with (-) nicotine ditartrate and (-) cotinine.," *Biosens. Bioelectron.*, vol. 22, no. 9–10, pp. 1955–1960, 2007.

[138] P J Riu, R Bragós, and J Rosell, "Broadband quasi-differential multifrequency electrical impedance imaging system," *Physiol. Meas.*, vol. 17, no. 4A, p. A39, 1996.

[139] D. A. McRae and M. A. Esrick, "The dielectric parameters of excised EMT-6 tumours and their change during hyperthermia," *Phys. Med. Biol.*, vol. 37, no. 11, pp. 2045–2058, Nov. 1992.

[140] S. Freitas, M. M. Malacarne, W. Romão, G. P. Dalmaschio, E. V. R. Castro, V. G. Celante, and M. B. J. G. Freitas, "Analysis of the heavy oil distillation cuts corrosion by electrospray ionization FT-ICR mass spectrometry, electrochemical impedance spectroscopy, and scanning electron microscopy," *Fuel*, May 2012.

[141] G. Derfel and A. Lipiński, "Charge Carrier Mobility Measurements in Nematic Liquid Crystals," *Mol. Cryst. Liq. Cryst.*, vol. 55, no. 1, pp. 89–100, Jan. 1979.

[142] G. Barbero and A. L. Alexe-Ionescu, "Role of the diffuse layer of the ionic charge on the impedance spectroscopy of a cell of liquid," *Liq. Cryst.*, vol. 32, no. 7, pp. 943–949, Jul. 2005.

[143] *Electrochemical Measurement System, Hardware Operator's Manual*. Gamry Instruments, 2005.

[144] I. Abdulhalim and D. Menashe, "Approximate analytic solutions for the director profile of homogeneously aligned nematic liquid crystals," *Liq. Cryst.*, vol. 37, no. 2, pp. 233–239, Feb. 2010.

[145] B. de Oliveira, P. Avelino, F. Moraes, and J. Oliveira, "Nematic liquid crystal dynamics under applied electric fields," *Phys. Rev. E*, vol. 82, no. 4, pp. 1–7, Oct. 2010.

[146] C. S. MacDonald, J. A. Mackenzie, A. Ramage, and C. J. P. Newton, "Robust adaptive computation of a one-dimensional -tensor model of nematic liquid crystals," *Comput. Math. with Appl.*, vol. 64, no. 11, pp. 3627–3640, Dec. 2012.

[147] C. W. Oseen, "Beiträge zur Theorie anisotroper Flüssigkeiten," *Ark. Math. Fys.*, vol. 19A, pp. 1–19, 1925.

[148] H. Zocher, "ber die Einwirkung magnetischer, electrischer und mechanischer Kräfte auf Mesophasen," *PhysZ*, vol. 28, pp. 790–796, 1927.

[149] F. C. Frank, "On the theory of liquid crystals," *Discuss. Faraday Soc.*, vol. 25, pp. 19–28, 1958.

[150] C. W. Oseen, "The theory of liquid crystals," *Trans. Faraday Soc.*, vol. 29, pp. 883–900, 1933.

[151] J. L. Ericksen, "Conservation Laws for Liquid Crystals," *J. Rheol. (N. Y. N. Y).*, vol. 5, no. 1, p. 23, Mar. 1961.

[152] F. M. Leslie, "Some constitutive equations for liquid crystals," *Arch. Ration. Mech. AMI.*, vol. 28, pp. 265–283, 1968.

[153] H. Mori, E. C. Gartland, J. R. Kelly, and P. J. Bos, "Multidimensional Director Modeling Using the Q Tensor Representation in a Liquid Crystal Cell and Its Application to the π Cell with Patterned Electrodes," *Jpn. J. Appl. Phys.*, vol. 38, no. Part 1, No. 1A, pp. 135–146, Jan. 1999.

[154] Z. Ge, T. X. Wu, R. Lu, and X. Zhu, "Comprehensive three-dimensional dynamic modeling of liquid crystal devices using finite element method," *Disp. Technol.*, vol. 1, no. 2, pp. 194–206, 2005.

[155] F. A. Fernandez, S. E. Day, P. Trwoga, H. F. Deng, and R. James, "Three-Dimensional Modelling of Liquid Crystal Display Cells using Finite Elements," *Mol. Cryst. Liq. Cryst.*, vol. 375, pp. 291–299, 2002.

[156] S. L. Subota, V. Y. Reshetnyak, S. P. Pavliuchenko, and T. J. Sluckin, "Numerical Modeling of Tunable Liquid-Crystal-Polymer-Network Lens," *Mol. Cryst. Liq. Cryst.*, vol. 489, no. 1, p. 40/[366]–53/[379], Sep. 2008.

[157] D. J. Higham and N. J. Higham, "Numerical methods: Part 2," in *Matlab guide*, SIAM, 2005, pp. 195–202.

[158] J. F. Algorri, V. Urruchi Del Pozo, P. J. Pinzón, and J. M. Sánchez Pena, "Modeling electro-optical response of nematic liquid crystals by numerical methods," *Opt. pura y Apl.*, vol. 46, no. 4, pp. 327–336, 2013.

[159] S. Sato, "Applications of Liquid Crystals to Variable-Focusing Lenses," *Opt. Rev.*, vol. 6, no. 6, pp. 471–485, Nov. 1999.

[160] G. V. Vdovin, I. R. Guralnik, and S. P. Kotova, "Liquid-crystal lenses with a controlled focal length. I. Theory," *Quantum Electron.*, vol. 29, no. 3, pp. 256–260, 1999.

[161] G. V. Vdovin, I. R. Guralnik, O. A. Zayakin, N. A. Klimov, S. P. Kotova, M. Y. Loktev, A. F. Naumov, V. V. Patlan, and S. A. Samagin, "Modal liquid crystal wavefront corrector," *Bull. Russ. Acad. Sci.*, vol. 72, no. 1, pp. 71–77, 2008.

[162] X. Liu, X. Jin, and J.-H. Lee, "A compact model of fringing field induced parasitic capacitance for deep sub-micrometer MOSFETs," *Solid. State. Electron.*, vol. 53, no. 9, pp. 1041–1045, Sep. 2009.

[163] A. Levy, R. Shavit, and L. Habib, "Optimisation of a microstrip left-handed transmission line using circuit modelling," *IET Microwaves, Antennas Propag.*, vol. 4, no. 12, p. 2133, Dec. 2010.

[164] R. Igreja, "Analytical evaluation of the interdigital electrodes capacitance for a multi-layered structure," *Sensors Actuators A Phys.*, vol. 112, no. 2–3, pp. 291–301, 2004.

[165] O. G. Vendik, S. P. Zubko, and M. A. Nikol'skii, "Modeling and calculation of the capacitance of a planar capacitor containing a ferroelectric thin film," *Tech. Phys.*, vol. 44, no. 4, pp. 349–355, Apr. 1999.

[166] M. R. Costa, R. A. C. Altafim, and A. P. Mammana, "Electrical modeling of liquid crystal displays-LCDs," *IEEE Trans. Dielectr. Electr. Insul.*, vol. 13, no. 1, pp. 204–210, Feb. 2006.

[167] J. F. Algorri, V. Urruchi, and J. M. Sánchez-Pena, "Reflective sidewall electrodes for low voltage and high transmittance blue-phase liquid crystal displays," *Liq. Cryst.*, 2015.

[168] M. Hövel, B. Gompf, and M. Dressel, "Dielectric properties of ultrathin metal films around the percolation threshold," *Phys. Rev. B*, vol. 81, no. 3, pp. 1–8, Jan. 2010.

[169] A. I. Oliva Arias and J. Lugo-Quintal, "¿Podemos conocer el espesor real de las capas delgadas metálicas?," *Ing. Rev. Académica*, vol. 14, no. 2, pp. 77–86, 2010.

[170] D. Lienhard and F. Heepmann, "Thin nickel films as absorbers in pyroelectric sensor arrays," *Microelectron. Eng.*, vol. 29, pp. 101–104, 1995.

[171] S. Giurgola, A. Rodriguez, L. Martinez, P. Vergani, F. Lucchi, S. Benchabane, and V. Pruneri, "Ultra thin nickel transparent electrodes," *J. Mater. Sci. Mater. Electron.*, vol. 20, pp. S181–84, Dec. 2009.

[172] H. Qiu, G. Safran, B. Pecz, P. B. Barna, and A. Kosuge, "Structural and electrical properties of Ni films grown on Si (100) and SiO2 by dc bias sputtering," *Thin Solid Films*, vol. 229, pp. 107–112, 1993.

[173] R. M. Hill, "Electrical conduction in ultra thin metal films. I. Theoretical," *Proc. R. Soc.*, vol. 309, no. 1498, pp. 377–395, 1969.

[174] B. N. J. Persson and J. E. Demuth, "Determination of the frecuency-dependent resisitivity of ultrathin metallic films on Si(111)," *Phys. Rev. B*, vol. 31, no. 4, pp. 1856–62, 1985.

[175] P. Smilauer, "Thin metal films and percolation theory," *Contemp. Phys.*, vol. 32, no. 2, pp. 89–102, 1991.

[176] A. Khakifirooz and S. Haji, "UV-assisted nickel-induced crystallization of amorphous silicon," *Thin Solid Films*, vol. 383, pp. 241–243, 2001.

[177] M. A. Mohiddon, K. Lakshun Naidu, M. Ghanashyam Krishna, G. Dalba, and F. Rocca, "Growth, optical, and electrical properties of silicon films produced by the metal-induced crystallization process," *J. Nanoparticle Res.*, vol. 13, no. 11, pp. 5999–04, Jun. 2011.

[178] J. K. Wassei and R. B. Kaner, "Graphene, a promising transparent conductor," *Mater. Today*, vol. 13, no. 3, pp. 52–59, Mar. 2010.

[179] E. Otón, S. López-Andrés, N. Bennis, J. M. Otón, and M. Geday, "Silicon oxides as alignment surfaces for vertically-aligned nematics in photonic devices," *Opto-Electronics Rev.*, vol. 22, no. 2, pp. 92–100, Jan. 2014.

[180] V. Urruchi, J. F. Algorri, J. M. Sánchez-Pena, N. Bennis, M. A. Geday, and J. M. Otón, "Electrooptic characterization of tunable cylindrical liquid crystal lenses," *Mol. Cryst. Liq. Cryst.*, vol. 553, no. 1, pp. 211–219, Feb. 2012.

[181] J. F. Algorri, V. Urruchi Del Pozo, J. M. Sánchez-Pena, N. Bennis, and M. Geday, "Liquid crystal microlenses with gradient refraction index control," *Opt. pura y Apl.*, vol. 45, no. 2, pp. 71–78, 2012.

[182] J. Li, C.-H. Wen, S. Gauza, R. Lu, and Shin-Tson Wu, "Refractive Indices of Liquid Crystals for Display Applications," *J. Disp. Technol.*, vol. 1, no. 1, pp. 51–61, 2005.

[183] *1260 Impedance/Gain-Phase Analyzer. Operating Manual*. Solartron Analytical, 2001.

[184] S. Analytical, *Zplot for Windows. Electrochemical impedance Software. Operating Manual*. Scribner Associates Inc., 2001.

[185] P. Perkowski, D. Łada, K. Ogrodnik, J. Rutkowska, W. Piecek, and Z. Raszewski, "Technical aspects of dielectric spectroscopy measurements of liquid crystals," *Opto-Electronics Rev.*, vol. 16, no. 3, pp. 271–276, May 2008.

[186] G. Wang, Y. J. Li, and H. C. Zhou, "Application of the radial basis function interpolation to phase extraction from a single electronic speckle pattern interferometric fringe.," *Appl. Opt.*, vol. 50, no. 19, pp. 3110–7, Jul. 2011.

[187] M. Takeda and H. Ina, "Fourier-transform method of fringe-pattern analysis for computer-based topography and interferometry," *J. Opt. Soc. Am*, vol. 72, no. 1, pp. 156–160, 1982.

[188] M. A. Gdeisat, D. R. Burton, and M. J. Lalor, "Spatial carrier fringe pattern demodulation by use of a two-dimensional continuous wavelet transform.," *Appl. Opt.*, vol. 45, no. 34, pp. 8722–32, Dec. 2006.

[189] H. Wang and Q. Kemao, "Frequency guided methods for demodulation of a single fringe pattern.," *Opt. Express*, vol. 17, no. 17, pp. 15118–27, Aug. 2009.

[190] S. K. Ghorai, D. Kumar, and B. K. Hura, "Strain measurement in a Mach–Zehnder fiber interferometer using genetic algorithm," *Sensors Actuators A Phys.*, vol. 122, no. 2, pp. 215–221, Aug. 2005.

[191] ISO 14880-1:, "Microlens Array. Part 1," 2001.

[192] A.A. Camacho, C. Solano, M. Cywiak, G. Martínez-Ponce, and R. Baltazar, "Method for the determination of the focal length of a microlens," *Opt. Eng.*, vol. 39, no. 8, pp. 2149–2152, 2000.

[193] L. Erdmann and R. Kowarschik, "Testing of refractive silicon microlenses by use of a lateral shearing interferometer in transmission," *Appl. Opt.*, vol. 37, no. 4, pp. 676–682, 1998.

[194] B.-Z. D. J. Liu, B-Y. Gu, and G.-Z. Yang, "Entirely electromagnetic analysis of microlenses without a beam shaping aperture," *Appl. Opt.*, vol. 40, no. 10, pp. 1686–1691, 2001.

[195] D. Montgomery, G. Woodgate, and A. Jacobs, "Analysis of the performance of a flat panel display system convertible between 2D and autostereoscopic 3D modes," in *Proc. SPIE, Stereoscopic Displays*, 2001.

[196] P. Boher, T. Leroux, and T. Bignon, "A new way to characterize autostereoscopic 3D displays using Fourier optics instrument," in *Proceedings of SPIE, Electronic Imagin*, 2009.

[197] P. Boher, "Characterization of autostereoscopic 3D displays using Fourier optics viewing angle instrument," in *IDW'08*, 2008, no. September.

[198] T. T. Alkeskjold, J. Lagsgaard, A. Bjarklev, D. S. Hermann, A. Anawati, J. Broeng, J. Li, and S.-T. Wu, "All-optical modulation in dye-doped nematic liquid crystal photonic bandgap fibers," *Opt. Express*, vol. 12, no. 24, p. 5857, 2004.

[199] K. Milenko, T. R. Wolinski, P. P. Shum, and D. J. J. Hu, "Temperature-Sensitive Photonic Liquid Crystal Fiber Modal Interferometer," *IEEE Photonics J.*, vol. 4, no. 5, pp. 1855–1860, Oct. 2012.

[200] D. J. J. Hu, K. Milenko, P. P. Shum, and T. Wolinski, "Fabrication and Characterization of a Highly Temperature Sensitive Device Based on Nematic Liquid Crystal-Filled Photonic Crystal Fiber," *IEEE Photonics J.*, vol. 4, no. 5, pp. 1248–1255, Oct. 2012.

[201] J. F. Algorri, B. García-Cámara, A. García-García, V. Urruchi, and J. M. Sánchez-Pena, "Theoretical modeling of a Localized Surface Plasmon Resonance (LSPR) based fiber optic temperature sensor," in *OFS2014 23rd International Conference on Optical Fiber Sensors*, 2014, p. 915738.

[202] M. Bray, "Orthogonal polynomials: a set for square areas," in *Optical Systems Design*, 2004, pp. 314–321.

[203] V. N. Mahajan and G. Dai, "Orthonormal polynomials in wavefront analysis: analytical solution," *J. Opt. Soc. Am. A*, vol. 24, no. 9, p. 2994, 2007.

[204] W. Swantner and W. W. Chow, "Gram-Schmidt orthonormalization of Zernike polynomials for general aperture shapes.," *Appl. Opt.*, vol. 33, no. 10, pp. 1832–7, Apr. 1994.

[205] G. Dai and V. N. Mahajan, "Orthonormal polynomials in wavefront analysis: error analysis," *Appl. Opt.*, vol. 47, no. 19, p. 3433, Jun. 2008.

[206] F. Liu, "Analyzing optics test data on rectangular apertures using 2-D Chebyshev polynomials," *Opt. Eng.*, vol. 50, no. 4, p. 043609, Apr. 2011.

[207] R. Zhu, S. Xu, Q. Hong, S.-T. Wu, C. Lee, C.-M. Yang, C.-C. Lo, and A. Lien, "Polymeric-lens-embedded 2D/3D switchable display with dramatically reduced crosstalk.," *Appl. Opt.*, vol. 53, no. 7, pp. 1388–95, Mar. 2014.

[208] B.-J. Mun, J.-H. Baek, J. H. Lee, B. K. Kim, H. C. Choi, J.-H. Kim, and G.-D. Lee, "Low Cell Gap Polymeric Liquid Crystal Lens for 2-D/3-D Switchable Auto-Stereoscopic Display," *IEEE Trans. Electron Devices*, vol. 60, no. 10, pp. 3430–3434, Oct. 2013.

APPENDICES

APPENDIX 1
PROPOSED ALGORITHM TO SOLVE THE MOLECULAR POSITION OF NEMATIC LIQUID CRYSTAL

Firstly, the algorithm transforms the BVP into an initial value problem.

$$Y'' = f(z, Y, Y'), \quad Y(0) = \alpha, \quad Y'(0) = \upsilon \tag{78}$$

The value of α is a 3x1 vector with the applied voltage (V), the pretilt angle (θ_1) and the twist angle (φ_1). The value of the boundary condition, ν, that is also a vector, has to be determined for Y'. A simple algorithm can do this, by a trial-error iterative process, starting with one arbitrary ν value, and solving the initial problem in the [0, d] range. If the solution is $Y(d) = \beta$, the estimated initial condition (v) is right, if not, the process starts again. However, this simple method is very inefficient. So, an improvement has been made by solving the problem of the unknown initial condition as a root of the following equation:

$$r(\upsilon) = g(\upsilon) - \beta = 0 \tag{79}$$

where r is the residual, that is, the difference between the estimation of the solution in d (with the initial condition (v) and the solution in d (β). This equation has been solved with the Newton-Raphson method, because it is simpler and faster than other methods such as the Brent or bisection algorithm. In addition, it is the best method for nonlinear equations. The differential equations are solved by an adaptive fourth order Runge-Kutta algorithm. The three second order equations system has been transformed to a six first order equations system by substitution ($y_1 = \theta$, $y_2 = \theta'$, $y_3 = \varphi$, $y_4 = \varphi'$, $y_5 = V$, $y_6 = V'$) in order to be able to use the Runge-Kutta algorithm.

$$F(z,y) = Y' = \begin{bmatrix} y_1' \\ y_2' \\ y_3' \\ y_4' \\ y_5' \\ y_6' \end{bmatrix} = \begin{bmatrix} y_2 \\ \theta'' \\ y_4 \\ \varphi'' \\ y_6 \\ v_1'' \end{bmatrix} \tag{80}$$

The complete algorithm, to solve the system, is depicted in Figure 128, and it is described by the following steps:

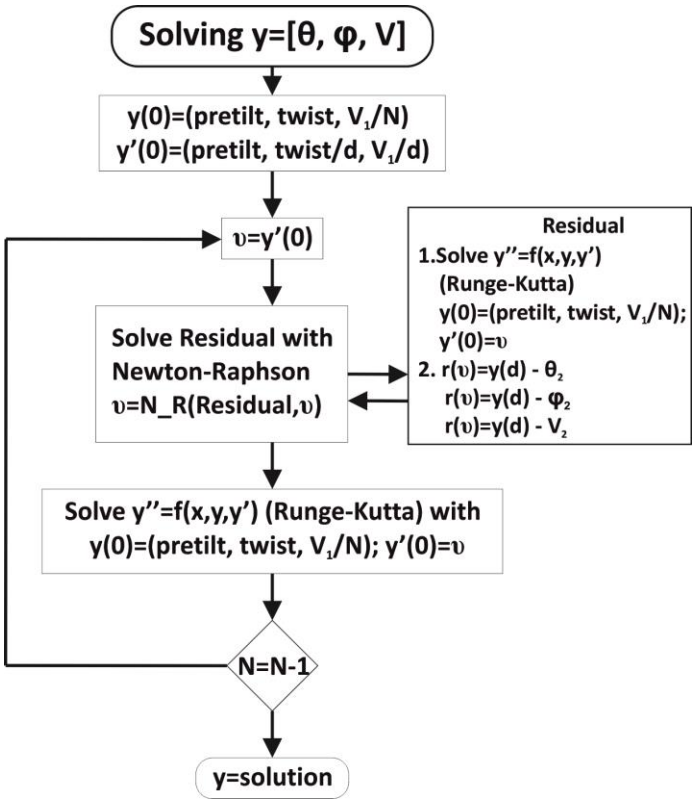

Figure 128. Algorithm flow chart.

Two initial conditions for each equation of the system are set. For the θ'' equation, the pretilt; for φ'', the twist, and for V/N, the voltage corresponding to the current step. For the unknown parameters θ', φ', V' an approximation is made: θ'= pretilt, φ'= totaltwist/d_{LC}, and V'=volts/d_{LC}, (d_{LC}=sample thickness).

- The initial condition v takes the value of the previous $Y'(0)$.
- Eq. 79 is solved by the Newton-Raphson method, giving the initial condition, v, which produces the minimum residual, $r(v)$.
- Once these values are known the differential equations are solved and the results are obtained.
- The step, N, is reduced by one, such that voltage is increased one portion.

- The process is repeated until N = 1 and the initial voltage has its final value. For this voltage the solution is $\theta(z)$, $\varphi(z)$, $V(z)$.

The algorithm solves the two angles θ, φ and the voltage across the dimension z. With these solutions, parameters such as birefringence or permittivity can be easily estimated.

Comparison with previous methods

The proposed algorithm has been compared with two other methods: the classic FDM, with central approximation, and the proprietary algorithm of MATLAB, Bvp4c. As noted above, the last algorithm is known for its minimal error in BVP solutions. So, the comparison between the three methods has been done in terms of computational cost and errors, taking as reference the Bvp4c results. A device with parallel alignment has been chosen for the comparison; this configuration is one of the most used in the newest experimental applications (optical filters, microwave devices, active zoom, etc.). The twist angle is 0° and the elastic constant K_{22} is not taken into account. The LC chosen is MDA-98-1602 (Table 8) with a device of 6.5μm thickness and 5° of pretilt caused by the alignment.

Elastic Constants	Birefringence	Permittivity
K_{11}=15.7 pN	n_e=1.7779	ε_e=16.2
K_{22}=8 pN	n_o=1.5113	ε_o=12
K_{33}=13.6 pN	Δn=0.2666	Δε=4.3

Table 8. MDA-98-1602 nematic LC characteristics

The previous parameters are considered for a 589.3nm wavelength and 1 kHz frequency AC electrical signal and are extracted from the datasheet provided by Merck. The three algorithms have been programmed in MATLAB. The calculation of the voltage and the angle profiles has been made with: 20 steps for the shooting and Bvp4c methods and an incremental number (10^4-10^2) for the FDM method. Both profiles are shown in Figure 129. It is advertised that, for different voltages (2V, 4V and 6V), the number of errors is very small to distinguish between methods in the graphs.

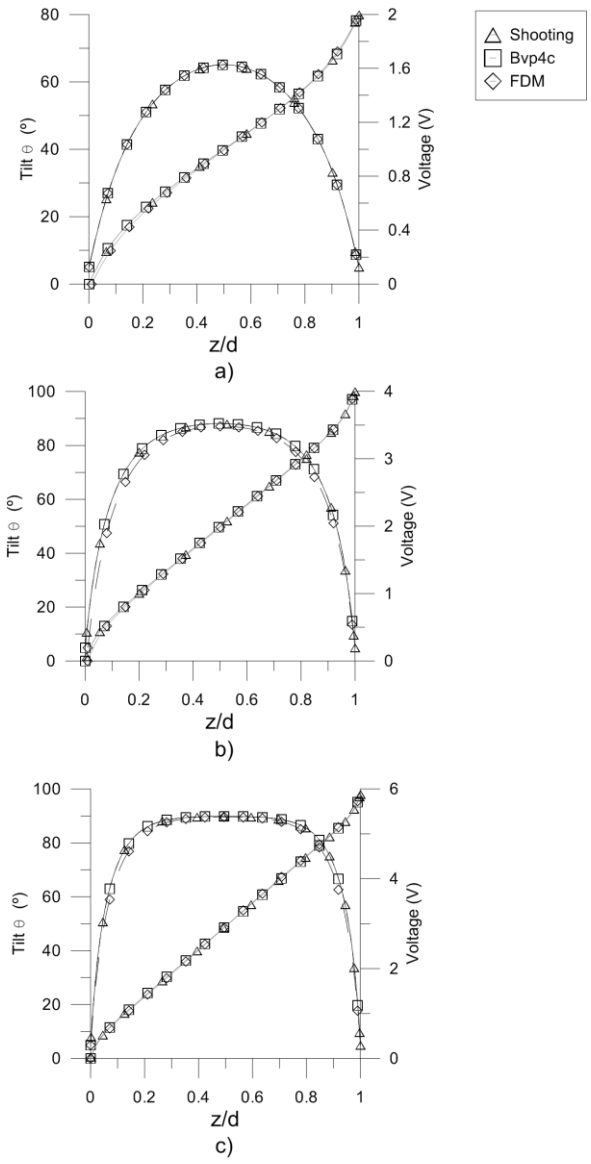

Figure 129. Simulations of LC director with three different methods: (a) 2V, (b) 4V and (c) 6V.

The maximum tilt angle estimated is also similar between algorithms (Table 9). However, the CPU time consumption has been measured on the basis of the three alternative methods of simulation (Table 10). The results demonstrate that the proposed algorithm is faster than Bvp4c and FDM (for low voltages), with the accuracy of the proprietary algorithm of MATLAB, Bvp4c. FDM shows good behaviour for high voltages, when the critical angle is almost ninety.

Voltage	Shooting	Bvp4c	FDM
$2V_{RMS}$	65.11°	65.12°	61.55°
$4V_{RMS}$	88.10°	88.10°	87.14°
$6V_{RMS}$	89.93°	89.95°	89.73°

Table 9. Voltage dependence of maximum tilt angle estimation

On the other hand, FDM has a clear problem to find the optimal step size. There is a critical compromise between error and time consumption. The number of steps in the proposed algorithm is always 20, demonstrating ease of use (there is no need to estimate the step for different supply voltages).

Voltage	Shooting	Bvp4c	FDM(Steps)
$2V_{RMS}$	2.09s	6.55s	$6s(5\cdot10^4)$
$4V_{RMS}$	1.80s	7.53s	$1.8s(10^4)$
$6V_{RMS}$	2.60s	7.37s	$0.3s(2\cdot10^3)$

Table 10. Voltage dependence of CPU time consumption

The minimization of Gibbs free energy has been solved for a LC molecular arrangement. A novel, accurate, fast and reliable algorithm has been proposed and the initial prediction compared with experimental data has been presented. The comparison between experimental and simulated data shows close results. These simulations can be easily extended to other experimental devices where voltage distribution is known.

APPENDIX 2
ESTIMATION OF THE RESISTIVITY R_{SQ}

The analytical study of Eq. 55 require the use of trigonometric functions. The imaginary component can be extracted from the hyperbolic cosine. Considering the module of alpha,

$$|\alpha| = \left| cosh\left(\sqrt{R_{\square} C_2 \omega i} \cdot r\right) \right| \tag{81}$$

and the imaginary solution of the hyperbolic cosine,

$$cosh\left(\sqrt{R_{\square} C_2 \omega i} \cdot r\right) = cosh\left(m + mi\right) \tag{82}$$

$$where\ m = \frac{\sqrt{2 R_{\square} C_2 \omega} \cdot r}{2} \tag{83}$$

the solution of Eq. 81 is:

$$\begin{aligned} |\alpha| &= \left| cosh(m) \cdot cos(m) - i \cdot senh(m) \cdot sen(m) \right| = \\ &\sqrt{\left(cosh(m) \cdot cos(m)\right)^2 + \left(senh(m) \cdot sen(m)\right)^2} = \\ &\sqrt{cosh^2(m) - sen^2(m)} \end{aligned} \tag{84}$$

Considering that the sine of m is limited between [-1,1] and that $\cosh^2(m)$ is an exponential function, the error would be only considerable for low values of m so alpha can be simplified to Eq. 85.

$$|\alpha| \approx \cosh\left(\frac{\sqrt{2 R_{\square} C_2 \omega} \cdot r}{2}\right) \tag{85}$$

The final analytical solution is Eq. 55:

$$R_{\square} \approx \frac{d \cdot 2 \cdot a cosh^2(|\alpha|)}{r^2 \varepsilon_0 \varepsilon'_2 \omega} \tag{55}$$

APPENDIX 3

SOLVING EQUATIONS FOR MODAL DEVICES WITH TWO HIGH RESISTIVITY LAYERS

As commented in previous sections, modal lens theory has been widely studied since it was first reported. Vdovin *et al.* conducted the first studies of the physical processes occurring in the resultant distributed resistive-capacitive system. For describing this type of system, the voltage distribution equation across the lens diameter is derived by considering the EEC of a LC at mid-range frequencies (a distributed parallel-plate capacitor). One of the layers is considered an equipotential surface, while the other contains non-uniformly distributed free charges. Following the law of charge conservation and Ohm's law and ignoring the electrical field outside the lens diameter, the resulting voltage distribution equation is a second-order two-dimensional PDE.

$$\nabla_s U^2 = R_{sq}\left(G - j\omega C\right)\cdot U \tag{86}$$

This equation is strongly dependent on the boundary conditions (voltage at diameter ends). Considerably different analytical expressions are obtained when complex boundary conditions (described in terms of voltage amplitude and phase) are employed. In recent years, other types of modal controls have been proposed. Some of these are based on the use of two high-resistivity layers, one of them instead of the equipotential layer on the ground plane. The latter has been demonstrated to reduce lens aberrations if electrodes of one substrate are placed parallel to each other. On the other hand, if substrates are arranged so that their electrodes are oriented orthogonal to each other, a tunable focusing device can be achieved. The voltage distribution in these two structures can be easily explained with a system using two versions of Eq. 86, one for each layer. As noted above, the two high-resistivity layers result in a two second-order two-dimensional coupled PDE with six initial conditions corresponding to each electrode,

$$\begin{cases} \nabla_s U_1^2 = R_{sq1}\left(G - j\omega C\right)\cdot\left(U_1 - U_2\right) \\ \nabla_s U_2^2 = R_{sq2}\left(G - j\omega C\right)\cdot\left(U_2 - U_1\right) \end{cases} \tag{87}$$

where U_1 and U_2 correspond to the voltage distribution in each high-resistivity layer and R_{sq1} and R_{sq2}, the sheet resistances of the two high resistivity layers. To solve this problem, a finite difference method could be implemented; however, issues such as Neumann boundary conditions or the need for initial values very close to the final result in order to converge correctly, may make this approach inaccurate. For better results, the finite element method is employed. Despite being a more complex method, MATLAB software has some useful functions such as mesh generation and

PDE solvers for treating certain cases. MATLAB is used in order to develop a simulation program with six initial conditions, mixed boundary conditions (Dirichlet and Neumann) and a refined mesh. This one also includes a molecular liquid crystal distribution simulation program that minimizes the Gibbs free energy, F_G. This energy comprises the contribution of two energies: electric energy, F_e, given by the dot product of the displacement vector (D) and the electric field (E), and the deformation free energy, F_d, determined by the Frank-Oseen equation. By combining the voltage distribution and molecular director, the simulation program estimates the interference pattern and the unwrapped phase generated by the modal device. As the LC reorients the permittivity changes, affecting the electric field. The coupling between director and electric field makes it almost impossible to get a direct solution of the problem. In this case, this is solved by an iterative process. The software also provides aberration tests, obtaining the 36 Zernike coefficients of each individual optical element for a specific arrangement, to quantify the optical quality in terms of the phase deviation from a reference sphere.